amU
Aix Marseille Université

NNT : 2025AIXM0250

THÈSE DE DOCTORAT

Soutenue à AMU — Aix-Marseille Université
le 22 Septembre 2025 par

Brieuc Collet

Titre de la thèse: Comprendre la microphysique des émissions radio aurorales de Jupiter avec Juno

Understanding the microphysics of Jovian auroral radio emissions with Juno

Discipline
Physique et Sciences de la Matière

Spécialité
Astrophysique et Cosmologie

École doctorale
ED352 Physique et Sciences de la Matière

Laboratoire
Laboratoire d'Astrophysique de Marseille

Composition du jury

Catriona JACKMAN DIAS, Dublin (Irlande)	Rapporteure
Patrick GALOPEAU LATMOS, CNRS, Guyancourt	Rapporteur
Sebastien HESS ONERA, Toulouse	Examinateur
Nicolas ANDRE IRAP, CNRS, Toulouse	Examinateur
Karine ISSAUTIER LIRA, CNRS, Observatoire de Paris	Présidente du jury
Laurent LAMY LAM, Université d'Aix-Marseille/LIRA, Observatoire de Paris	Directeur de thèse
Mathieu BERTHOMIER LPP, CNRS, Palaiseau	Membre invité

LAM
LABORATOIRE D'ASTROPHYSIQUE DE MARSEILLE

Affidavit

I, undersigned, Brieuc Michel Collet, hereby declare that the work presented in this manuscript is my own work, carried out under the scientific supervision of Laurent Lamy, in accordance with the principles of honesty, integrity and responsibility inherent to the research mission. The research work and the writing of this manuscript have been carried out in compliance with both the french national charter for Research Integrity and AMU charter on the fight against plagiarism.

This work has not been submitted previously either in this country or in another country in the same or in a similar version to any other examination body.

Marseille, July 11, 2025



This work is licensed under Creative Commons Attribution-NonCommercial-NoDerivatives 4.0 International Public License

List of publications and participation to conferences

List of publications produced as part of the thesis project:

1. B. Collet et al. (2023). "Characterization of Jovian hectometric sources with Juno: statistical position and generation by shell-type electrons". In: *Planetary, Solar and Heliospheric Radio Emissions IX*. ed. by C. K. Louis, C. M. Jackman, G. Fischer, A. H. Sulaiman, and P. Zucca, 103095, p. 103095. DOI: 10.25546/103095

2. B. Collet et al. (2024a). "A New Type of Jovian Hectometric Radiation Powered by Monoenergetic Electron Beams". In: *Journal of Geophysical Research: Space Physics* 129.5, e2024JA032422. ISSN: 2169-9380, 2169-9402. DOI: 10.1029/2024JA032422

3. B. Collet, L. Lamy, C. K. Louis, V. Hue, and T. K. Kim (2025). "In Situ Analysis of Jupiter's Broadband Kilometric Auroral Radio Emissions With Juno". In: *Geophysical Research Letters* 52.9, e2024GL114447. ISSN: 0094-8276, 1944-8007. DOI: 10.1029/2024GL114447

4. S. Al Saati et al. (2022). "Magnetosphere-Ionosphere-Thermosphere Coupling Study at Jupiter Based on Juno's First 30 Orbits and Modeling Tools". In: *Journal of Geophysical Research (Space Physics)* 127.10, e2022JA030586, e2022JA030586. DOI: 10.1029/2022JA030586

5. L. Lamy et al. (2023a). "Re-exploring the radio spectrum of Uranus in orbit: science case and digital high-frequency receiver". In: *Planetary, Solar and Heliospheric Radio Emissions IX*. ed. by C. K. Louis, C. M. Jackman, G. Fischer, A. H. Sulaiman, and P. Zucca, 103105, p. 103105. DOI: 10.25546/103105

6. C. K. Louis et al. (2023b). "Source of Radio Emissions Induced by the Galilean Moons Io, Europa and Ganymede: In Situ Measurements by Juno". In: *Journal of Geophysical Research: Space Physics* 128.12. ISSN: 2169-9380, 2169-9402. DOI: 10.1029/2023JA031985

7. N. Heidari et al. (2024). "The SOPHIE search for northern extrasolar planets: XIX. A system including a cold sub-Neptune potentially transiting a V = 6.5 star HD

88986". In: *Astronomy and Astrophysics* 681, A55, A55. DOI: 10.1051/0004-6361/202347897

8. J. Rabia et al. (2025). "In situ and remote observations of the ultraviolet footprint of the moon Callisto by the Juno spacecraft". In: *Nature Communications* 16.1. ISSN: 2041-1723. DOI: 10.1038/s41467-025-62520-4

Participation in conferences and summer schools during the thesis period:

1. Planetary, Solar, and Heliospheric Radio Emissions IX (Oral), Dublin, Ireland, 26-28 September 2022
2. Chapman on Advances in Understanding Alfvén Waves in the Sun and the Heliosphere (Oral), Berlin, Germany, 28 May-2 June 2023
3. PNST : colloque scientifique et de prospective (Oral), Marseille, France, 8-12 January 2024
4. Semaine de la SF2A, Marseille (Attending), France, 4-7 June 2024
5. Astroradiofr24, Astrophysique française aux fréquences radio, vers SKA (Poster), Paris, France, 12-15 November 2024
6. Conference on Magnetospheres of the Outer Planets, Minneapolis (Oral and Poster),USA, 8-12 July 2024
7. EGU General Assembly (Poster), Vienna, 27 April - 2 May 2025 https://doi.org/10.5194/egusphere-egu25-2775
8. Planetary, Solar, and Heliospheric Radio Emissions X (Oral), Marseille, France, 11-13 June 2025

Résumé et mots clés

Jupiter est la source d'émissions radio aurorales la plus intense du Système Solaire. Ces émissions sont émises perpendiculairement au champ magnétique dans un cône creux à une fréquence proche de la fréquence cyclotron locale. Ces émissions ont été observées et caractérisées par des mesures depuis le sol et l'espace et sont maintenant divisées en 4 catégories : les émissions décamétriques (DAM) dont on distingue celles induites par les lunes galiléennes (Moon-DAM), hectométriques (HOM), kilométriques à large bande (bKOM). Elles sont produites dans les régions polaires de la magnétosphère de Jupiter, qui constitue un laboratoire naturel d'une taille et d'une complexité remarquables. Ces émissions sont générées par une instabilité onde-plasma : l'Instabilité Maser Cyclotron (CMI). Elle requiert un plasma dépleté et magnétisé ainsi qu'une inversion de population électronique.

Cette thèse a pour but de confirmer la CMI en tant que mécanisme de génération pour les émissions radio aurorales joviennes. Pour cela, j'utilise les mesures in situ radio, plasma et magnétiques de Juno le premier orbiteur polaire à traverser les régions aurorales de Jupiter.

À partir de spectres radio, j'ai établi un catalogue des traversées candidates de sources radio ensuite confirmées par une analyse du taux de croissance à partir des mesures d'électrons par Juno et d'une nouvelle expression de ce taux.

J'ai pu montrer que les sources HOM et DAM sont principalement générées par des distributions electroniques présentant un cône de perte, et dans une moindre mesure par des distributions de type conique et de type coquille identifiées pour la première fois en tant que sources d'énergie à Jupiter. Les sources bKOM sont produites par des coniques et des coquilles et peuvent être localisées dans des cavités.

Ces résultats confirment l'universalité du CMI pour la génération d'émissions radio aurorales et pourraient être appliqués à d'autres planètes magnétisées.

Mots clés : radio, Jupiter, Juno, plasma, ondes

Abstract and keywords

Jupiter is the most intense source of auroral radio emissions in the Solar System. These emissions are emitted perpendicular to the magnetic field in a hollow cone at a frequency close to the cyclotron frequency. These emissions have been observed and characterized by ground- and space-based observations and are now divided into four categories: the decametric emissions (DAM), including those induced by the Galilean moons (Moon-DAM), the hectometric emissions (HOM), and the broadband kilometer emissions (bKOM). They are produced in the polar regions of Jupiter's magnetosphere, a unique laboratory due to its size and internal processes. These emissions are generated by a wave-plasma instability: the Cyclotron Maser Instability (CMI). It requires a depleted and magnetized plasma and an electronic population inversion.

The aim of this thesis is to confirm CMI as the generation mechanism for Jovian auroral radio emissions. To do this, I use in situ radio, plasma, and magnetic measurements from Juno, the first polar orbiter to cross Jupiter's auroral regions.

From radio spectra, I have compiled a catalog of candidate radio source crossings, which were then confirmed by a growth rate analysis based on Juno's electron measurements and a new expression of the growth rate.

I found that HOM and DAM sources were generated mainly by electron distributions showing a loss cone, and marginally by conics, and shells which I identified for the first time at Jupiter. The bKOM sources were produced by conics and shells, and could be located in cavities.

These results confirm the universality of CMI for the generation of auroral radio emissions and could be applied to other magnetized planets.

Keywords: radio, Jupiter, Juno, plasma, waves

Résumé étendu en Francais

Contexte : La magnétosphère de Jupiter

La magnétosphère est la région autour d'une planète magnétisée, telle que Jupiter, dans laquelle la dynamique est contrôlée par le champ magnétique de la planète. Cette magnétosphère sépare la région d'influence du champ magnétique planétaire de celle du vent solaire.

Jupiter, de par son intense champ magnétique a la magnétosphère la plus étendue du système solaire (jusqu'à 90 rayons Joviens côté jour et 5 unités astronomiques côté nuit).

Cette magnétosphère se démarque également de celles des autres planètes par sa dynamique particulière contrôlée par des processus internes. En effet, le plasma qui compose cette magnétosphère provient en majorité de l'activité volcanique d'Io, lune de Jupiter se situant dans sa magnétosphère. Ce plasma iogénique forme une couche de courant qui déforme le champ magnétique de Jupiter rendant l'usuelle approximation dipolaire invalide.

De plus, cette immense magnétosphère tourne avec Jupiter à une période de 9 h 55. Le plasma est ainsi entrainé en corotation grâce à un système de courant transportant le plasma radialement et se refermant dans l'ionosphère au niveau des pôles grâce à des courants le long des lignes de champ magnétiques.

Au niveau des pôles, le plasma accéléré permet la génération d'émissions aurorales sur une large gamme du spectre électromagnétique et notamment dans le spectre radio.

Cette magnétosphère a été découverte en 1955, grâce à des observations radio depuis le sol et est depuis étudiée par des radiotélescopes, des télescopes spatiaux dans la gamme Ultra violette, et des missions spatiales qui ont survolé Jupiter(Pioneer 10 et 11-1973, Voyager-1973, Ulysses-1992, Cassini-2000, New Horizons-2007) ou des sondes dédiées à Jupiter (Galileo-1995 à 2003). Depuis 2016, l'orbiteur polaire Juno explore pour la première fois les régions aurorales de Jupiter grâce à notamment ses instruments qui mesure les ondes radio (Waves), les électrons (JADE-E et JEDI) et le champ magnétique (MAG).

La magnétosphère de Jupiter est donc un laboratoire de physique des plasmas naturel grâce auquel on peut enrichir notre compréhension du transport et de la dissipation de l'énergie portée par le plasma. De par sa dynamique régie par des processus internes plutôt qu'externes, le cas jovien complète notre compréhension des magnétosphères.

Émissions radio aurorales de Jupiter

Une partie des émissions radio de Jupiter ont été interprétés comme étant générées dans les régions aurorales par des électrons à la fréquence cyclotron f_{ce} proportionnelle à l'intensité du champ magnétique. Ces émissions radio aurorales sont séparées en 4 catégories à Jupiter selon leurs fréquences : les émissions décamétriques (DAM) dont on distingue celles induites par l'interaction avec les lunes de Jupiter (Lunes-DAM pour Io, Ganymède, Europe), les émissions hectométriques (HOM) et les émissions kilométriques à large bande (*broadband kilometric*, bKOM). Elles sont toutes émises le long d'un cône perpendiculaire à la direction du champ magnétique principalement sur le mode X. Les premières orbites de Juno ont confirmé qu'elles étaient générées sur des lignes de champ connectées aux aurores UV. Ces caractéristiques sont similaires à celles observées pour les émissions radio aurorales terrestres (*Auroral Kilometric Radiation*, AKR) et kroniennes (*Saturn Kilometric Radiation*, SKR) et ont donc mené à penser qu'elles étaient toutes générées par l'Instabilité Maser Cyclotron (IMC). Cette instabilité, introduite initialement pour l'AKR par WU et LEE (1979) puis vérifiée in situ pour l'AKR et le SKR, requiert a) des électrons de quelques keV dans b) un plasma déplété présentant c) une inversion de population. Cette inversion de population est habituellement observée dans des distributions de type cône de perte, coniques et coquilles générées dans les magnétosphères.

Les distributions de type cône de perte sont caractérisées par une déplétion des électrons montants dû à la perte d'électrons dans l'atmosphère de Jupiter. Les distributions de type conique par une déplétion en dehors de ce cône de perte. Les distributions coquilles présentent une intensification de la fonction de distribution en forme d'une coquille due à des faisceaux d'électrons propagés adiabatiquement.

Alors que les 2 premiers types ont été observées et confirmées comme source d'énergie par la sonde Juno pour le HOM et le Io-DAM, les distributions de type coquille, source principale à la Terre et Saturne, restaient à identifier à Jupiter.

Le but de cette thèse est donc de confirmer que les émissions radio aurorales de Jupiter sont bien générées par l'IMC, de caractériser les sources de ces émissions et de comparer la génération des différentes composantes du spectre jovien.

Pour cela, j'ai développé une nouvelle expression du taux de croissance. Alors que les expressions utilisées précédemment supposaient un plasma dominé soit par des électrons froids soutenant la propagation de l'onde ou uniquement des électrons chauds instables, cette nouvelle expression rassemble ces deux hypothèses afin de l'appliquer au contexte de Jupiter sans hypothèse sur la composition du plasma jovien.

Le taux de croissance permet de quantifier à quel point des électrons sont instables pour une instabilité onde-plasma et donc à quel point l'onde est amplifiée. Dans le cadre de l'IMC, son expression se base sur l'intégration du gradient perpendiculaire de la fonction de distribution électronique le long d'un cercle de résonance. Ce cercle de résonance permet de caractériser la population électronique instable (énergie, direction des électrons instables) et d'obtenir des propriétés sur l'onde amplifiée (fréquence, angle d'émission).

J'ai ensuite développé une méthode pour appliquer cette expression du taux de

croissance aux mesures de Juno lors de traversées de source radio.

Caractérisation des sources HOM/DAM

J'ai donc analysé les spectres radio lors des 70 premières orbites de Juno (mi-2016 à mi-2025). J'y ai identifié 116 sources HOM et DAM à l'aide du critère de LOUIS et al. (2019) qui identifie une source lorsqu'une émission intense est vue en dessous de $f_{ce} + 1\%$. Ces sources n'étaient en majorité pas connectée aux émissions UV les plus intenses, mais aux aurores diffuses ou le bord équatorial de l'ovale auroral. J'ai confirmé que ces sources étaient générées par des distributions de type cône de perte et coniques de quelques keV partiellement associées à des ondes d'Alfvén. J'ai également identifié 21 sources émises sous la fréquence cyclotron locale qui ne pouvait être générés que par des distributions de type coquille. Ces sources étaient associées à des courants alignés vers le haut et des signatures monoénergétiques dans les spectres en énergie des électrons et un élargissement du cône de perte.

Grâce à mon analyse du taux de croissance, j'ai pu confirmer que ces émissions étaient générés par des distributions de type coquille de 0.2 à 5 keV, identifiant ce type de distributions comme source d'énergie secondaire pour le HOM et le DAM. Ces résultats ont été publiés dans COLLET et al. (2023, 2024a)

Comme le HOM/DAM n'étaient générés que par des électrons de quelques keV alors que des électrons de quelques centaines de keV précipitent dans l'atmosphère pour créer les émissions aurorales UV principales, j'ai analysé le taux de croissance des électrons entre 30 et 1200 keV lors d'un cas connecté à ces émissions UV principales, mais où aucune émission radio n'était vu proche de la fréquence cyclotron. J'ai obtenu que des électrons de quelques centaines de keV pouvaient être instables et peuvent présenter des distributions de types coniques, cône de perte et coquille. Néanmoins, ces distributions n'étant pas assez instables, ne permettent pas de générer des ondes détectables par l'instrument radio de Juno.

J'ai aussi découvert des harmoniques des émissions HOM lors de deux cas que je prévois d'étudier en détail pour mieux comprendre les processus de dissipation de l'énergie portée par les électrons en énergie radio dans les régions aurorales.

Caractérisation des sources Lunes-DAM

Lors de collaborations (LOUIS et al. 2023b ; RABIA et al. 2025), je me suis intéressé à la génération du Lunes-DAM lors de traversées des tubes de flux d'Io et de celui de Callisto, nouvellement identifié.

Grâce à ma méthode, j'ai donc montré lors de 3 traversées de tube de flux d'Io que les émissions radio aurorales induites par Io étaient bien générées par l'IMC par des électrons de type cône de perte de 0.2 à 15 keV. Ces sources étaient localisées dans des zones de courants remontants associés à des ondes d'Alfvén et connectés à l'empreinte UV du satellite. Dans le cas de Callisto, RABIA et al. (2025) a identifié l'empreinte UV associée à la lune, mais aucune émission radio y était associée. Je me

suis tout de même intéressé à l'éventualité qu'une émission soit produite sous le seuil de sensibilité de Waves. J'ai identifié des électrons instables de type cône de perte de 1-5 keV, mais dont le taux de croissance était trop faible pour générer des émissions détectables par Waves.

Caractérisation des sources bKOM

Ensuite, je me suis intéressé à la composante bKOM. J'ai cette fois étudié les 60 premières orbites et ai identifié 5 cas entre 10 et 300 kHz où les mesures radio et électron étaient en haute résolution permettant ainsi d'appliquer mon analyse du taux de croissance. Ce faible nombre s'explique par le fait que ces émissions sont émises à des altitudes plus élevées où l'ovale principal n'est pas souvent traversé par Juno. Parmi ces 5 traversées, j'ai identifié 3 cas de soudaines déplétions électroniques rappelant les cavités aurorales dans lesquelles l'AKR est émis. Les traversées de sources étaient également partiellement associées avec des compressions de la magnétosphère et des *dawn storms* qui sont des intensifications de l'aurore UV liées à une reconfiguration de la magnétosphère. J'ai ensuite appliqué mon analyse du taux de croissance à ces sources. Malheureusement, le cône de perte n'était pas résolu par l'instrument électron JADE-E, je n'ai donc pas pu vérifier si les distributions de type cône de perte étaient instables pour cette composante.

Néanmoins, j'ai pu obtenir que le bKOM est généré par des distributions de type coniques et parfois coquilles de 1-30 keV. Certaines sources présentaient des caractéristiques proches de celles identifiées dans les traversées de sources HOM/DAM ce qui pourrait signifier qu'une partie du bKOM est en fait l'extension à basse fréquence du HOM/DAM.

Ces résultats ont été publiés dans COLLET et al. (2025).

Conclusion

Cette thèse a donc permis de vérifier l'IMC en tant que mécanisme de génération d'ondes radio aurorales dans la magnétosphère de Jupiter grâce aux instruments de la sonde Juno. Chaque composante du spectre radio auroral de Jupiter a été caractérisée et les résultats obtenus ont permis d'améliorer la compréhension des phénomènes de dissipation d'énergie dans les magnétosphères.

En particulier, l'identification de cône de perte en tant que source d'énergie libre principale et les coquilles en tant que source secondaire confirme que les processus d'accélérations à Jupiter ne sont pas liées à un système de courant stable contrôlé par l'interaction avec le vent solaire comme c'est le cas à la Terre, mais par des processus stochastiques complexes mettant en jeu des interactions avec des ondes d'Alfvén et/ou des potentiels de basses fréquences liés à la mise en corotation du plasma par la rotation rapide de Jupiter.

Cette thèse permet dans un contexte plus général de comparer les processus d'émissions radio et d'accélération du plasma dans les magnétosphères, ce qui permettra de

mieux caractériser d'autres planètes et objets magnétisés du système solaire (la Terre, Saturne, mais aussi Mercure, Ganymède, Uranus et Neptune, voire le Soleil) et au-delà (exoplanètes, étoiles, voire pulsars et blazars).

Remerciements

Merci aux membres de mon Jury en particulier aux rapporteurs pour leurs commentaires utiles qui ont permis d'améliorer ce manuscrit. Merci à Catriona d'avoir accepté que la soutenance puisse se dérouler en français afin que mes parents puissent comprendre ce sur quoi j'ai travaillé.

Merci à toi Laurent pour ces 3 années de thèse pendant lesquelles j'ai pu bénéficier de tes conseils et de ta passion pour ce sujet et pour l'histoire de Marseille. Merci de m'avoir laissé du temps et de la liberté pour developper mes idées, d'avoir eu confiance et d'avoir été rigoureux là où j'étais chaotique et de t'être accomodé de mon fameux flegme. Je me rappelle encore quand je t'ai rencontré lors de ma recherche de stage en M1 juste après les confinements, une période où j'étais clairement perdu quant à mon intérêt pour la recherche. Merci aussi à Léna de m'avoir filé ton contact et merci donc à toi pour ces 2 stages qui ont précédés cette thèse. Je suis vraiment heureux d'avoir eu un directeur de thèse avec qui je me suis aussi bien entendu.

Bien évidemment, merci aux compagnons de thèse qui m'ont accompagnés sur ce voyage de 3 ans. Ceux rencontrés au départ et que je précède de peu à l'arrivée : Salomé, Tom et Alizée avec lesquels j'ai découvert Marseille, ses calanques, ses poissons, ses restaus, ses bars (et bien sûr le Makeda). Merci à vous pour cette amitié, ces discussions et ses réconforts quand les deadlines se faisaient courtes, les résultats incohérents et l'avenir incertain. Merci pour ces nombreux fous rires autour d'un café, d'un thé, d'un cocktail (ou rien : ça tue, après tout).

Merci à ceux arrivés plus tôt à destination et partis pour d'autres voyages : James, Max, Antoine, Hugo et Sarah. Ce fut un plaisir de partager ces bières et ces parties endiablées de jeux de société.

Merci aussi à Yannis, Alan, Paul, Tom, Paul, Shinosuke, ceux arrivés entre temps avec qui j'ai partagé le titre de doctorant GSP ces quelques années.

Merci aux permanents de GSP et à tous les autres du LAM. Merci pour ces discussions sur tous ces sujets de recherche fascinants, sur la sphéricité d'une boule de pétanque d'intérieur, et sur les arcanes du fonctionnement de la recherche en France. En particulier, merci à Vincent, Laurent, Audrey, Olivier et Sofia, qui ont aussi nourri mes travaux et mon parcours à venir. Merci à tout le personnel du labo que ce soit administratif, technique, informatique, logistique ou d'entretien. Il en faut du monde pour faire tourner un labo !

Merci aux équipes du LIRA et de l'IRAP avec lesquels ça a été un plaisir de collaborer. J'espère pouvoir continuer à travailler avec vous sur des sujets au moins aussi passionnants. En particulier, merci à Philippe Zarka et Corentin Louis d'avoir co-encadré mes premières expériences dans la recherche et pour leurs discussions au fil de cette thèse. Merci à toi Corentin d'avoir été un super "grand frère" de thèse, de m'avoir payé de nombreuses bières et d'avoir apporté autant de conseils complémentaires à ceux de Laurent.

Merci aux équipes Juno en particulier à Bill Kurth pour m'avoir permis d'accéder aux données de cette sonde et aux réunions d'équipe.

Merci à tous ceux qui m'ont aidé à porter les casquettes d'enseignant, d'enseigné, de membre du CL, d'organisateur de séminaires, de vulgarisateur, de conférencier, de manifestant,... face au vent de Marseille.

Merci à Pierre et Isabelle d'avoir accepté de faire partie de mon comité de suivi de thèse chaque année. Merci aussi à Sofia et Marceau d'avoir parrainé notre génération de thésards au LAM.

Merci à tous ces scientifiques, tous ces exemples qui m'ont permis de sculpter quel scientifique je voulais être. J'espère pouvoir être fier du scientifique que je serai peu importe la forme que cela prendra.

Merci aux copains de PPF que ce soit Etienne, Didi, Marin, mais aussi Emilie et Adam. Très heureux d'avoir survécu à ces cours avec vous et à l'anxiété de trouver une thèse. Merci pour toutes ces idées loufoques, ces fous rires. Bien joué à nous. Tortue escargot laser.

Merci aux Gastronomes, ou aux Magiciens ou je sais plus, en particulier merci à Élo & Lolo pour ces aventures avec qui ça PTSMR. Vous avez été ce rayon de soleil necessaire pendant ces études balotées par la sortie de prépa, l'ambition de la thèse et bien sûr les confinements. C'est grâce à vous que j'ai pu me faire progressivement à être physicien, à se sentir scientifique. Merci pour ces révisions dans les bu avec le cerveau qui fume, les doigts plein d'encre, les tableaux remplis de quantités que je penerai à comprendre aujourd'hui, les esprits embrumés par le desespoir parfois mais toujours chassés par tous ces moments ensemble.

Merci à Jack, mon camarade et prof, pour toutes ses discussions qui me rappellent à quel point notre métier est politique, critiquable, important et donc important à critiquer.

Merci aux choubidous, mes points d'ancrage à *ma Breizh, ma Bro*. Merci pour ces 10 années de soirées, de jeux de société, de cartes yu gi oh, de plages,... Je suis heureux

que notre amitié soit ce qu'elle est aujourd'hui. Merci aux autres copains de BZH, notamment toi Valentin qui a fait toute la route et qui j'en suis sûr va se faire un plaisir de lire ces 200 pages et quelques parce que pourquoi pas. Merci à Émile, je garde précieusement le projet du carton temporel et du découpeur laser de pizza infini pour plus tard.

Merci à ceux que j'appelle trop souvent les amis de mes proches que ce soit ceux que je connais par mon frère ou ceux que je connais par ma chérie. Vous avez bien évidemment une grande place dans mon cœur et avez, vous aussi, contribuer à cette thèse par nos discussions, nos soirées et tous ces moments. Donc merci à Emma, Mathilde, Oihanna, Élodie, JB, Brendan, Nico, Hugo, Maëlla, Manon, et tous les autres.

Merci à tous les profs que j'ai eu lors de ce long parcours. Merci pour vos conseils, vos encouragements, et tous vos efforts. Merci à tous ces profs du lycée à la faac qui continuent de m'inspirer pour parler de science.

Merci à ceux croisés et perdus de vue (souvent par ma faute), que ce soit les copains de lycée et d'avant, les copains de prépa (notamment ceux du 32) et tous ceux rencontrés autour d'une bière, d'un jeu de société,... Vous restez des étapes essentielles du chemin que j'ai mené. J'espère vous recroiser.

Merci à mes parents, à mon très cher frère de m'avoir soutenu émotionnellement (et financièrement) toutes ces années, de m'avoir encouragé sur cette voie, d'y avoir cru parfois plus que moi et d'être si fier de moi. Je me souviens encore de ces tout premiers livres qui parlaient de devenir astronaute que je vous faisais acheter et qui continue de nourrir ce rêve de chaque jour être plus proche des étoiles. Ça y est je suis officiellement astrophysicien, c'est toujours étrange de le réaliser, alors qu'il y a quelques années j'avais peur de l'avouer ne serait-ce qu'à moi même et c'était presque difficile de le prononcer quand on me demandait ce que je voulais faire, ou pourquoi je faisais ces études. J'avais raison à l'époque, c'est exaltant. Merci Maman d'avoir ramené 2 *kouign-amann* qui ont ravi les papilles marseillaises. Merci à mes Mamies notamment pour la tenue que j'ai porté à ma soutenance. Merci à Olaba pour sa chaleur et sa douceur.

Merci à celle qui me soutient et qui me supporte, celle qui me rappelle souvent pourquoi je fais ça, celle dont la juste révolte et la plume font trembler les puissants et mon cœur. Sans toi, je me serais perdu 100 fois et me serais effondré 1000 fois. Je t'aime.

Enfin, j'ai eu la chance de pouvoir étudier dans des conditions confortables, je n'ai eu ni à avoir un emploi pendant mes études, ni à me poser la question de quel repas j'allais sauter, ni à contracter un prêt pour m'inscrire à chacune de ces nombreuses années d'études. Même si ce n'était pas toujours rose, j'ai pu m'amuser, sortir, rencontrer les

belles personnes mentionnées dans ces paragraphes, voir des belles choses, avoir des enseignants passionnés et compétents. Bien que je fusse parfois loin de mes parents, je n'ai pas eu à changer de pays pour avoir les compétences pour entrer en thèse. Et le but ici n'est pas de remercier un système universitaire français en train de couler, mais bien de pointer que pour quelques rêveurs qui comme moi ont pu faire ce qu'ils voulaient combien de compétents ont dû arrêter pour nourrir ses proches ou soi-même ? Combien ont échoué fautes de conditions économiques, sociales, physiques ou mentales ? À combien de lycéens a-t-on caché ces études par discrimination raciale, sexiste, validiste et classiste ? L'épanouissement par le savoir et la curiosité font partie des nombreuses priorités qui manque à nos sociétés face à la poursuite de l'excellence, illusion qui cache une récurrente reproduction sociale.

Contents

Affidavit 2

List of publications and participation to conferences 3

Résumé et mots clés 5

Abstract and keywords 6

Résumé étendu en Francais 7

Remerciements 12

Contents 16

List of Figures 20

List of Tables 24

Acronyms List 25

Symbols 27

1. The Jovian magnetosphere as a laboratory to investigate auroral physics 29

1.1. The Magnetosphere of Jupiter 30

1.1.1. Dynamics in the Jovian magnetosphere 32

1.2. Jupiter: an auroral emitter 33

1.2.1. Jovian auroral radio emissions 33

1.2.1.1. History 33

1.2.1.2. Characteristics of the Jovian auroral radio emissions . . 35

1.2.1.3. Moon-DAM 37

1.2.1.4. DAM and HOM 38

1.2.1.5. bKOM 38

1.2.2. Jupiter's UV aurora to characterize auroral acceleration processes 39

1.2.2.1. Correlation between UV and radio emissions 41

1.3. The Juno era 42

1.3.1. Description of Juno 42

1.3.1.1. Magnetospheric Science Objectives 42

1.3.1.2. Trajectory 42

1.3.2. New constraints on Jupiter's magnetosphere . . . 44
1.3.2.1. Magnetosphere dynamics and structure . . . 44
1.3.2.2. UV aurora . . . 45
1.3.2.3. Radio auroral emissions . . . 45
1.4. Open questions . . . 46

2. Generation of auroral radio emissions 48
2.1. The Cyclotron Maser Instability . . . 49
2.2. Resonance curves . . . 49
2.2.1. Weakly relativistic case . . . 50
2.2.2. General (fully) relativistic case . . . 51
2.3. Growth rate expressions . . . 54
2.3.1. Dispersion relation . . . 54
2.3.2. Cold plasma modes . . . 54
2.3.3. Dispersion relation in the case of CMI . . . 57
2.3.4. Growth rates in the semi-relativistic approach . . . 58
2.3.4.1. Hot plasma assumption . . . 58
2.3.4.2. Effect of a Cold plasma population . . . 59
2.3.4.3. Properties of the expressions of the growth rate . . . 60
2.3.5. CMI applicability to Jupiter . . . 61
2.3.5.1. Hot or cold plasma assumption . . . 61
2.3.5.2. Semi-relativistic approximation . . . 62
2.3.5.3. f_{pe}/f_{ce} range . . . 62
2.4. CMI-unstable electrons . . . 62
2.4.1. Useful formulae to characterize a resonance circle . . . 63
2.4.2. Loss Cone EDF . . . 64
2.4.3. Conics EDF . . . 65
2.4.4. Shell EDF . . . 65
2.4.5. Trapped electrons . . . 65
2.5. Wave intensity . . . 66
2.5.1. Group Velocity . . . 67
2.5.1.1. Group velocity in a cold plasma . . . 68
2.5.1.2. Group velocity in a hot plasma . . . 69
2.5.1.3. Group velocity derived in a plasma with both populations 71
2.5.1.4. Thermal effects . . . 73

3. Instruments and Methods 78
3.1. Juno . . . 78
3.1.1. Waves . . . 79
3.1.2. JADE-E . . . 81
3.1.3. JEDI . . . 82
3.1.4. MAG . . . 83
3.1.5. UVS . . . 83
3.2. Identification of CMI radio source crossings . . . 83

3.3. Growth rate computation . . . 84
3.3.1. EDF processing . . . 84
3.3.2. Set of resonance circles . . . 84
3.3.3. Selection of resonance circle . . . 85
3.4. Computation of relevant observables . . . 86
3.4.1. Theoretical Loss Cone Angle . . . 86
3.4.2. Field Aligned Current Computation . . . 86
3.4.3. Alfvénic perturbations . . . 86

4. In situ characterization of HOM/DAM sources 88
4.1. Radio survey of HOM and DAM sources . . . 89
4.1.1. Description of the studied interval . . . 90
4.1.2. Tracking HOM/DAM source candidates . . . 90
4.1.2.1. Location and plasma context of the candidate sources . 90
4.1.2.2. Comparative characterization of the radio emission regions during the first 10 perijoves . . . 92
4.1.3. The case of sources below f_{ce} . . . 96
4.2. CMI growth rate analysis . . . 97
4.2.1. Case study: PJ32S . . . 97
4.2.1.1. Radio source and auroral context . . . 97
4.2.2. Predicted growth rates . . . 100
4.2.2.1. Wave intensity . . . 106
4.2.3. CMI generation of all HOM/DAM crossed sources . . . 106
4.3. CMI generation of HOM/DAM by highly relativistic electrons . . . 108
4.3.1. Case study: PJ32S . . . 109
4.3.2. Growth rate analysis . . . 111
4.3.3. Summary for the PJ32S case . . . 115
4.4. Discovery of HOM harmonic emission . . . 115
4.4.1. Two harmonic detection examples . . . 116
4.4.2. Plasma context . . . 118
4.5. The case of moon-induced radio emissions . . . 120
4.5.1. The source of Io-induced radio emissions . . . 121
4.5.1.1. The case of PJ5S . . . 121
4.5.2. Callisto-induced radio emissions . . . 124
4.6. Summary of HOM/DAM/Moon-DAM source properties . . . 126

5. Extension to the case of bKOM 128
5.1. Radio Survey of bKOM sources . . . 129
5.1.1. Description of the studied interval . . . 129
5.1.2. Tracking bKOM source candidates . . . 130
5.1.2.1. Location and plasma context of the candidate sources . 130
5.1.2.2. Auroral cavities for bKOM generation . . . 133
5.1.2.3. Solar wind influence . . . 134

5.2. Case study: PJ4S . . . 135
5.2.1. Radio source and auroral context . . . 136
5.2.2. Predicted growth rates . . . 136
5.2.2.1. Emission angles . . . 138
5.3. Case study: PJ5N . . . 140
5.4. Overall properties of bKOM sources . . . 143
5.5. Summary of bKOM source properties . . . 143

6. The CMI in the context of the Jovian magnetosphere and beyond 145
6.1. Discussion on the generation of auroral radio emissions at Jupiter . . . 146
6.1.1. Sources of free energy . . . 146
6.1.2. Efficiency of the CMI at weakly relativistic energies: comparison between the resonant and the precipitating electrons . . . 147
6.2. An updated view of the Jovian radio spectra . . . 148
6.2.1. Limitations of the used CMI growth rate analysis . . . 148
6.3. Comparing the Jovian auroral radio emissions with the Terrestrial and Kronian cases . . . 149
6.3.1. Source properties . . . 150
6.3.2. Sources of free energy . . . 150
6.3.3. O-mode and harmonics . . . 151
6.4. Extension to the case of Mercury . . . 152

Conclusion 155
6.1. Perspectives . . . 156
6.1.1. The case of Ganymede . . . 157
6.1.2. The case of Uranus . . . 157

Bibliography 158

APPENDIXES 173
A. Expression of the relativistic dispersion tensor . . . 174
B. Influence of the parallel gradient term . . . 174
C. Expression of θ_{chara} and v_{chara} for an ellipse . . . 176
D. Comparison between growth rate expressions on a case study . . . 177
E. List of HOM/DAM sources in the first 70 Juno orbits . . . 179

List of Figures

1.1. Timeline of the space missions to Jupiter 30
1.2. Schematics of Jupiter's magnetosphere 31
1.3. Diagram of the dynamics of currents in Jupiter's magnetosphere. 32
1.4. Schematics of the currents propagating in the Alfvén wings. Credits: Louis (2018) 33
1.5. Jovian auroral components locations and properties 35
1.6. Schematics explaining the arc shape in time-frequency spectrogram of auroral emissions 37
1.7. Hubble Space Telescope observations of UV aurora on Jupiter 41
1.8. Juno spacecraft and its science instruments. Image credit: NASA/JPL. 42
1.9. Juno's orbits orbital coverage from PJ1 (2016-08-27) to PJ77 (2025-10-17) 43
1.10. Graphic illustrating the average picture of the fields, particles, and plasma waves in Jupiter's low-altitude 44

2.1. Resonance circle and ellipse at $\Delta\omega = 1\%$ and $k_{\parallel} = 0.2\frac{\omega_{ce}}{c}$ or $k_{\parallel} = 0.4\frac{\omega_{ce}}{c}$ (i.e. $\theta_{(\vec{\mathbf{k}},\vec{\mathbf{B}})} = 78°$ and $66°$ if $N \sim 1$) 52
2.2. Diagram of the different modes obtained from the Altar-Appleton-Hartree relation 56
2.3. Dispersion relation for $k_{\parallel} = 0$ in a cold highly-magnetized plasma for different values of $\epsilon_c = \frac{f_{pe}}{f_{ce}}$ 57
2.4. Illustration of $v_charа$ and θ_{chara} associated with a resonance ellipse and a resonance circle. 63
2.5. Illustration of the different unstable distribution functions 66
2.6. Galactic low-frequency model radio spectrum derived from Dulk et al. (2001) (continuous line) and Manning and Dulk (2001) (diamonds). Figure from Zarka (2004). 67
2.7. a) Dispersion relation and Group velocity for $k_{\parallel} = 0$ in a cold highly-magnetized plasma for different values of $\frac{\omega_{pe}}{\omega_{ce}}$ 68
2.8. Dispersion relation for purely cold or purely hot plasma with $k_{\parallel} = 0$ for $\frac{\omega_{pe}}{\omega_{ce}} = 3 \times 10^{-2}$ and for either $v_0 = 0.015$ or $v_0 = 0.15$ 70
2.9. Dispersion relations for a cold and hot plasma population for $\frac{\omega_{pe}}{\omega_{ce}} = 3 \times 10^{-3}$ and 1×10^{-2} 72
2.10. Group velocities for the same cases as Figure 2.10 73
2.11. Distribution function observed by JADE-E on 2017-03-27 06:52:10 (PJ6S) on anode 4 ($\theta = 35°$), fitted Maxwellians for the cold and supra-thermal population and isotropic DGH for the shell 75

2.12. Dispersion relation obtained for the model at $\frac{f_{pe}}{f_{ce}} = 2 \times 10^{-3}$. The color bar indicates the growth rate ω_i. The continuous horizontal lines indicate f_{ce} and $\frac{f_{ce}}{\Gamma_{peak}}$. Dash lines indicate the cold plasma approximation Right eXtradordinary (RX)-mode modified to fit the data and a model to illustrate the boundaries of the trapped mode. 77

3.1. Example of Waves Survey measurements during PJ6S 79
3.2. Waves noise level. Credits: Kurth et al. (2017) and Louis et al. (2021) . . 80
3.3. Example of Waves Burst measurements during PJ6S on HFR High band (HFR-High) and HFR Low band (HFR-Low) channels. Black lines represent f_{ce} and $f_{ce} = 1\%$. 81
3.4. Density as a function of time during PJ41S. 82
3.5. JADE-E measurement of a smoothed EDF displayed in the normalized velocity space. The red line shows theoretical loss cone aperture angle (computed as explicited in section 3.4). The colored circles display a subset of centered (green) and non-centered (orange, blue) CMI resonance circles. The green circles correspond to shell- (or trapped-) EDF, the blue ones to loss cone ones and the oranges circle test other possible unstable portions of the EDF. 85

4.1. Time-frequency spectrogram from Waves/HFR-Low measurements in Burst mode. 90
4.2. Juno's trajectory for $f_{ce} \geq 300\,\text{kHz}$ and identified candidate HOM/DAM sources. 91
4.3. Occurrence of HOM/DAM source crossings candidates. 92
4.4. Comparison between a source crossing and Diff. A./ZI/ZII. From top to bottom: Waves/Burst mode time-frequency spectrogram the black oblique lines are f_{ce} and $f_{ce} + 1\%$, the black (resp red) box delimits the source identified below $f_{ce} + 1\%$ (resp f_{ce}); Upward (resp downward) electron energy flux in black (resp in red) averaged over 30s intervals; Same but averaged over 5s; Electron energy spectra for downward directions ($\theta < 22°$ averaged at a 1s cadence. The green box delimits the 3-30 keV energy flux peak identified by Allegrini et al. (2020). Credits: Mauk et al. (2020). 94
4.5. Juno radio and particle measurements obtained during PJ32S on day 2021-02-21. 99
4.6. UV image and color ratio during PJ32S. The orange trajectory shows the $f < f_{ce} + 1\%$ candidate source, and the pink trajectory shows the interval studied in section 4.3. Courtesy: Bertrand Bonfond. 101
4.7. CMI growth rate analysis of the EDF measured by JADE-E on 2021-02-21 18:42:46 UT (PJ32S). 102

4.7. For the latter category, the '+' and 'x' symbols distinguish between circles intercepting positive $\frac{\partial F_e}{\partial v_\perp}$ for electrons propagating downward or upward, respectively. For this time interval, the largest growth rates were obtained for upward electrons, such as for the loss cone resonance circles. 103
4.8. CMI growth rate analysis applied to the full-time interval of Figure 4.5. 104
4.9. Superposition of Figure 4.5c and Figure 4.8b 105
4.10. Characteristic pitch angle $\theta_{chara} = \arcsin(v_r / v_0)$ 106
4.11. PJ32S Waves and plasma context 110
4.12. Illustration of resonance ellipses chosen for the growth rate computation on PJ32S. 112
4.13. 2 cases of unstable EDF measured by JEDIin PJ32S. 113
4.14. Growth rate analysis during the regions of PJ32S connected to the MAO in the same format as Figure 4.8 114
4.15. Spectrograms of the harmonic seen during PJ66S 117
4.16. Spectrograms of the harmonic seen during PJ73S 118
4.17. Plasma context during PJ66S 120
4.18. JADE-E electron measurements during PJ5S Io flux tube crossing . . . 122
4.19. Waves/Burst mode time-frequency spectrogram of PJ5S Io flux tube crossing 122
4.20. Example of a measured EDF and associated growth rate during PJ5S Io flux tube crossing. 123
4.21. Example of a measured EDF and associated growth rate during PJ22N Callisto flux tube crossing. 125

5.1. Juno trajectory in bKOM frequency range 129
5.2. Time-frequency spectrogram of PJ5N bKOM candidate source 132
5.3. UV auroral maps derived from UVS during or near bKOM source crossing candidates 133
5.4. Hourly-averaged solar wind parameters for each radio source 135
5.5. In situ measurements and growth rate analysis as a function of time for the PJ4S bKOM source 137
5.6. Unstable Electron Distribution Functions (EDFs) from PJ4S bKOM radio source below Figure 5.5b on top of which red lines indicate the intervals corresponding to the shown EDF. 138
5.7. Emission angle associated with the unstable resonance circles during PJ4S source crossing. Top (resp. bottom) panel shows the angles deduced from circles intercepting upward (downward) electrons yielding upward (downward) waves. The color bar indicates the growth rate corresponding to the associated resonance circle. Blue dashed lines enclose the values associated with resonance circles yielding $\gamma > 5 \times 10^{-5}$. . . . 140
5.8. In situ measurements and growth rate analysis as a function of time for the PJ5N bKOM source 142

6.1. Spatial amplification (proportional to the growth rate) as a function of $\frac{f_{pe}}{f_{ce}}$ computed in the case of beam distribution for the fundamental in X-mode (X1) and O-mode (O1) and for the 1st harmonic in X-mode (X2) and O-mode (O2). Credit: Chen et al. (2002) 151
6.2. Geometry of the flybys from Bepi-Colombo in the Mercury solar orbital (MSO) coordinate system with average Bow Shock and Magnetopause models displayed with dashed gray lines. Credits: Rojo et al. (2024) . . 153
6.3. $\frac{f_{pe}}{f_{ce}}$ obtained during Bepi flybys in the Hermetian magnetosphere. Courtesy: M. Rojo 154

1. Comparison of the growth rate provided by Equations 2.23 and B.3 (respectively without and with the contribution of $\frac{\partial F_e}{\partial v_\parallel}$) applied to Juno/JADE-E measurements obtained on 2017-05-19 06:52:10 175
2. Comparison of the growth rate with and without taking into account the parallel gradient term on 2017-05-19 between 06:52:00 and 06:52:10. . 176
3. Comparison of the different growth rate expressions for the bKOM case of PJ5N a) $\frac{f_{pe}}{f_{ce}}$ and $\frac{n_h}{n_{tot}}$ b-d) Computed growth rates for the different expressions e)Electron flux f-h)Associated characteristic energy 178
4. Comparison of the different growth rate expression. Same as Figure 3 for the HOM source crossing of PJ32S. 179

List of Tables

1.1. Jupiter's characteristics 31
1.2. Characteristics of Jovian auroral components. 46

4.1. Characteristics of the Moon-DAM, DAM, HOM components. 89
4.2. HOM and DAM sources identified during the 10 first perijoves and associated auroral regions. 95
4.3. Catalog of $f < f_{ce}$ HOM emissions 98
4.4. Comparison between the characteristics of the Jovian auroral radio components with the other planetary auroral radio emissions 127

5.1. Catalog of bKOM source crossings identified from Juno/Waves observations over PJ1-60 131

6.1. Characteristics of the Jovian auroral radio components obtained in situ. Callisto's radio emission was not detected. 146
6.2. Characteristics of AKR and SKR 149

1. 184

Acronyms List

AKR Earth's Auroral Kilometric Radiation 36, 41, 49, 58, 61, 64, 65, 107, 108, 119, 141, 143, 145, 148–151, 156

bKOM Jovian brodband Kilometric emission 34, 38, 39, 41, 47, 80, 127, 128, 147, 148, 150, 151, 156

CMI Cyclotron Maser Instability 35, 38, 45–47, 51, 53, 57, 59, 61, 62, 64, 65, 71, 73, 75, 78, 83, 107, 115, 119, 120, 145, 147–153, 155–157

DAM Jovian Decametric emission 34, 37–39, 41, 45, 47, 62, 80, 88–90, 92, 94, 96, 97, 105, 107, 108, 120, 126, 143, 147–152, 155, 156

Diff. A Diffuse Aurora Zone 93, 94, 97, 100, 107

EDF Electron Distribution Function 22, 49, 58, 61, 62, 64–66, 68, 69, 71, 73–75, 81–85, 89, 96, 100, 105, 107, 108, 112, 115, 123, 126, 127, 136, 138, 141, 146–149, 155, 156, *also* F_e

EEF Electron Energy Flux 82

FAC Field Aligned Current 32, 33, 40, 44, 86, 107, 108, 118, 119, 123, 124, 126, 136, 143, 146, 147

HFR High Frequency Receiver 79

HFR-High HFR High band 21, 79–81, 89, 96, 116, *see also* HFR

HFR-Low HFR Low band 21, 79–81, 89, 116, 129, *see also* HFR

HOM Jovian Hectometric emission 34, 36, 38, 39, 41, 45, 47, 62, 64, 80, 88–90, 92, 94, 96, 97, 105, 107–109, 115, 116, 119, 120, 126, 127, 143, 147, 148, 150–152, 155, 156

HST Hubble Space Telescope 43

JADE-E Jovian Auroral Distributions Experiment Electron sensors 81, 82, 84, 85, 89, 96, 100, 109, 111, 112, 115, 118, 121, 124, 132, 136, 144, 156, 177

JEDI Jupiter Energetic particle Detector Instrument 82, 109, 111, 112, 115, 156

JRM33+CON20 Internal field model complemented by a current sheet model 38, 64, 86

LFR Low Frequency Receiver 79

LFR-High LFR High band 79, 116, 129, *see also* LFR

LFR-Low LFR Low band 79, *see also* LFR

LO Left Ordinary 53, 55, 57, 58

MAG Magnetometer 83, 86, 87, 89, 96, 177
MAO Main Auroral Oval 40, 44, 45, 90–94, 96, 98, 100, 107–109, 124, 127, 130, 143, 146–148, 150, 155, 156
MAW the Main Alfvén Wing 40, 41, 46, 89, 146
Moon-DAM Jovian Moon-induced Decametric emissions 34, 37, 38, 41, 47, 88, 89, 126, 147, 155
M-SHELL distance at which a field line cross the equator (equivalent to L-Shell for non dipolar magnetic field) 38, 40, 41, 45, 90, 92, 107, 130, 132

PJ Perijove 43

RAW Reflected Alfvén Wing 40, 41, 46, 89, 146
RX Right eXtradordinary 21, 49, 53, 55–61, 67, 68, 72, 77

SKR Saturn's Kilometric Radiation 36, 58, 72, 107, 108, 116, 117, 119, 145, 149–151, 156, 157

TEB Transhemispheric Electron Beam 40, 146

UKR Uranus' Kilometric Radiation 157
UV DA UV Diffuse Aurora 40, 44, 45, 93, 94, 100, 107, 108
UVS Ultraviolet Spectrograph 83, 96, 132

ZI Zone I 44, 93, 94, 97, 100, 107, 108
ZII Zone II 44, 93, 94

Symbols

f_{ce} Cyclotron frequency, $f_{ce} = \frac{eB}{m_e}$

f_{pe} Plasma frequency, $f_{pe} = (2\pi)^{-1}(\frac{e^2 n_e}{m_e \epsilon_0})^{\frac{1}{2}} \simeq 8.967\sqrt{n_e}$

ω Angular frequency $\omega = 2\pi f$

$\vec{B}$ Magnetic field. $B = \left\|\vec{B}\right\|$ is the magnetic field amplitude, $\parallel$ and $\perp$ subscripts indicate directions parallel and perpendicular to this magnetic field.

$\parallel$, $\perp$ Subscripts indicating the quantity component in the direction parallel or perpendicular to the magnetic field.

$R_{\mathbf{J}}$ Jupiter equatorial radius $1R_{\mathrm{J}} = 71\,492\,\mathrm{km}$

F_e Electron Distribution Function

$\theta_{(\vec{k},\vec{B})}$ Beaming angle: angle between $\vec{k}$ and $\vec{B}$

$\vec{v}$ Electron velocity. $v = c\sqrt{1-(\frac{E}{m_e c^2}+1)^{-2}}$

$\vec{\beta}$ Normalized electron velocity $\vec{\beta} = \frac{\vec{v}}{c}$

$\vec{u}$ Normalized electron momentum $\vec{u} = \Gamma\vec{v}$

E Energy of the electrons. $E = 2m_e c^2 \frac{1}{\sqrt{1-\beta^2}} - 1$

θ Electron pitch angle: angle between $\vec{v}$ and $\vec{B}$

m_e Electron mass $m_e = 9.11 \times 10^{-31}\,\mathrm{kg}$ or $m_e c^2 = 255.5\,\mathrm{keV}$

n_e Electron density

Γ Lorentz factor $\Gamma = \frac{1}{\sqrt{1-\frac{v^2}{c^2}}} = \frac{1}{\sqrt{1-\beta^2}} = \sqrt{1+u^2}$

γ Normalized wave growth rate $\gamma = \frac{\omega_i}{\omega_{ce}}$

$\vec{k}$ Wavenumber

$\vec{N}$ Refraction index $\vec{N} = \frac{\vec{k}c}{\omega}$

β_0 Center of a resonance circle

r Radius of a resonance circle

β_{0e} Center of a resonance ellipse

$r_{\parallel}$ Semi minor axis of a resonance ellipse
$r_{\perp}$ Semi major axis of a resonance ellipse

$\Delta\omega$ Algebraic difference between ω and ω_{ce}: $\Delta\omega = \frac{\omega - \omega_c e}{\omega_{ce}}$
$\delta\omega$ Ratio between ω and ω_{ce}: $\delta\omega = \frac{\omega}{\omega_{ce}}$

$\overline{k_{\parallel}}$ Normalized parallel wavenumber $\overline{k_{\parallel}} = k_{\parallel} \frac{c}{n\omega_{ce}}$

θ_{SysIII} Jupiter Latitude in System III coordinates

1. The Jovian magnetosphere as a laboratory to investigate auroral physics

If you have access of knowing the ways of the plasma then you will have access of knowing the way of the past. If you can merit yourself the frequencies you can also guess the future.

JCVD

Contents

1.1. The Magnetosphere of Jupiter . . . 30
1.1.1. Dynamics in the Jovian magnetosphere . . . 32
1.2. Jupiter: an auroral emitter . . . 33
1.2.1. Jovian auroral radio emissions . . . 33
1.2.1.1. History . . . 33
1.2.1.2. Characteristics of the Jovian auroral radio emissions . . . 35
1.2.1.3. Moon-DAM . . . 37
1.2.1.4. DAM and HOM . . . 38
1.2.1.5. bKOM . . . 38
1.2.2. Jupiter's UV aurora to characterize auroral acceleration processes 39
1.2.2.1. Correlation between UV and radio emissions . . . 41
1.3. The Juno era . . . 42
1.3.1. Description of Juno . . . 42
1.3.1.1. Magnetospheric Science Objectives . . . 42
1.3.1.2. Trajectory . . . 42
1.3.2. New constraints on Jupiter's magnetosphere . . . 44
1.3.2.1. Magnetosphere dynamics and structure . . . 44
1.3.2.2. UV aurora . . . 45
1.3.2.3. Radio auroral emissions . . . 45
1.4. Open questions . . . 46

1.1. The Magnetosphere of Jupiter

Jupiter is not only the largest and heaviest planet of our Solar System, but also the planet with the most intense magnetic field which is 20 times larger at the 1-bar level than it is at Earth's surface. The magnetic field $\vec{\mathbf{B}}$ of a planet such as Jupiter interacts with the solar wind (the flow of charged particles that escape from the Sun) to form a cavity within the solar wind, known as the magnetosphere wherein the planetary magnetic field dominates. The Jovian magnetosphere (illustrated in Figure 1.2) is the largest in the Solar system. Indeed, its magnetopause, which delimits the magnetosphere in the dayside (defined as the equilibrium points between the pressures of the solar wind and the internal magnetic field), is located between 60 and 90 R_J (depending on the solar wind activity see Feng et al. 2023) while in the nightside, a magnetotail extends up to Saturn's orbit 5 au (1 au = Sun-Earth distance = 149.6×10^6 km) further away (Desch 1983).

The Jovian magnetic axis is tilted by 10.3° relative to Jupiter's axis of rotation at a longitude of 196.4° (Connerney et al. 2022) and rotates at the very short period of 9h 55min 30s.

This magnetosphere has been studied since the 1950s when it was discovered with ground-based radio emissions (Burke and Franklin 1955, see also Section 1.2.1). The planet was then studied from UV space telescopes (Prange 1992; Grodent et al. 2003) and in situ thanks to the flybys of Pioneer 10 and 11 (1973-1974) who gave the first measurements of the magnetic field, of Voyager (1979–1980) who discovered the current sheet and encountered the Io plasma torus (see next paragraphs), of the solar orbiter Ulysses (1992), of Cassini (2000) and of New Horizons (2007) who investigated the magnetotail. The Galileo space probe orbited Jupiter from 1995 to 2003 and investigated the equatorial magnetosphere. Before describing the polar orbiter Juno (at Jupiter since 2016) and its measurements that changed our view of this magnetosphere, I present the understanding of the Jovian magnetosphere before Juno (Khurana et al. 2004). I chose to firstly address the dynamics and plasma sources of the magnetosphere, prior the auroral emissions from which these properties were initially derived.

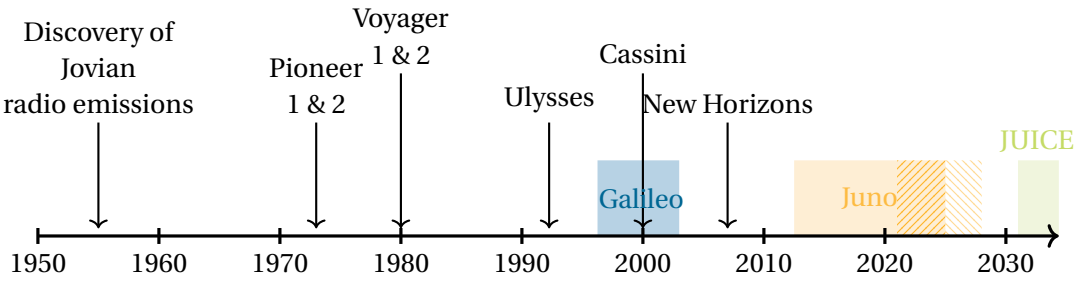


Figure 1.1.: Timeline of the space missions to Jupiter

A magnetosphere is composed of a *soup* of charged particles (electrons and ions) called a **plasma**. In the case of Jupiter, this plasma originates mostly from internal

sources, the main one being the volcanic activity of Io, one of its 97 satellites (as of May 2025), injecting mostly neutral matter (SO_2) in the magnetosphere. This matter is then ionized, producing ions at a rate of 100-1000 $\mathrm{kg \cdot s^{-1}}$ (Bagenal and Delamere 2011) which is then trapped by the magnetic field to form the Io plasma torus, which roughly corotates with Jupiter's magnetic field at 6 R_J.

The other Galilean moons also inject matter into the magnetosphere with a lower contribution of 20 $\mathrm{kg \cdot s^{-1}}$ ions (Cooper et al. 2001). The ionosphere is the main source of proton injecting 20 $\mathrm{kg \cdot s^{-1}}$. The external solar wind is thought to contribute marginally as the source of the proton seen in the outer magnetosphere (r>60 R_J).

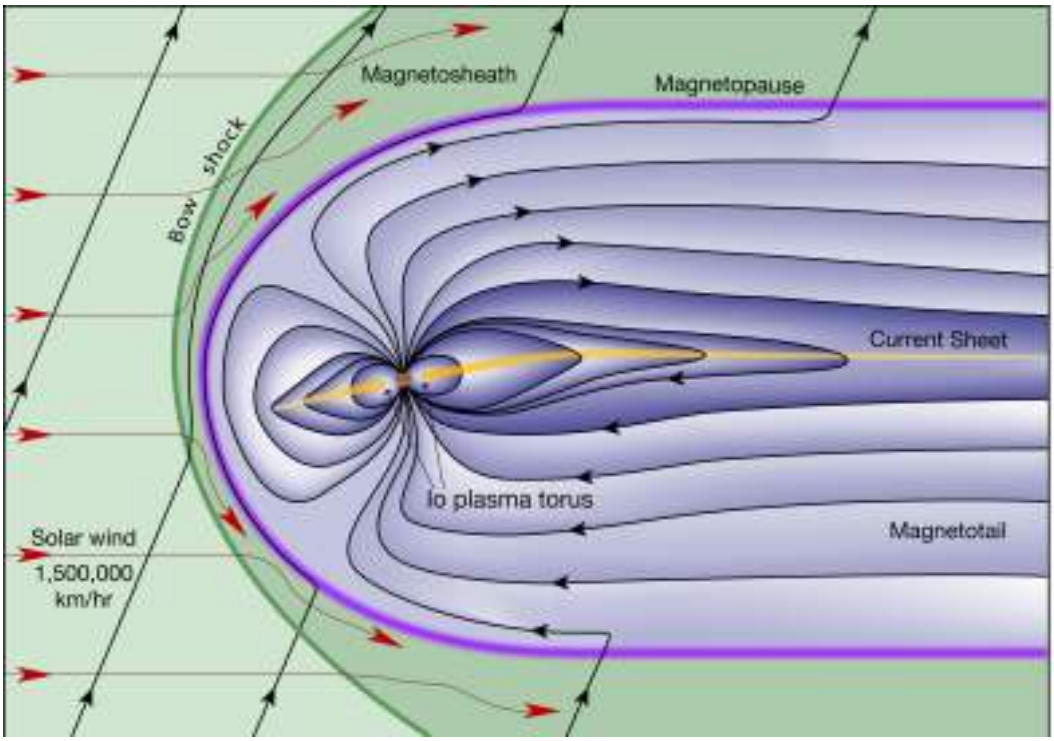


Figure 1.2.: Schematics of Jupiter's magnetosphere

Equatorial radius	$1\,R_J = 71\,492$ km
Mass	1.8986×10^{27} kg
Rotation period	9h55min
Orbital period	11.862 year
Flattening	0.06487
Average distance from Sun	5.2 au = 778.479×10^6 km
Dipole tilt	10°

Table 1.1.: Jupiter's characteristics Credits: Blanc et al. (2005)

1.1.1. Dynamics in the Jovian magnetosphere

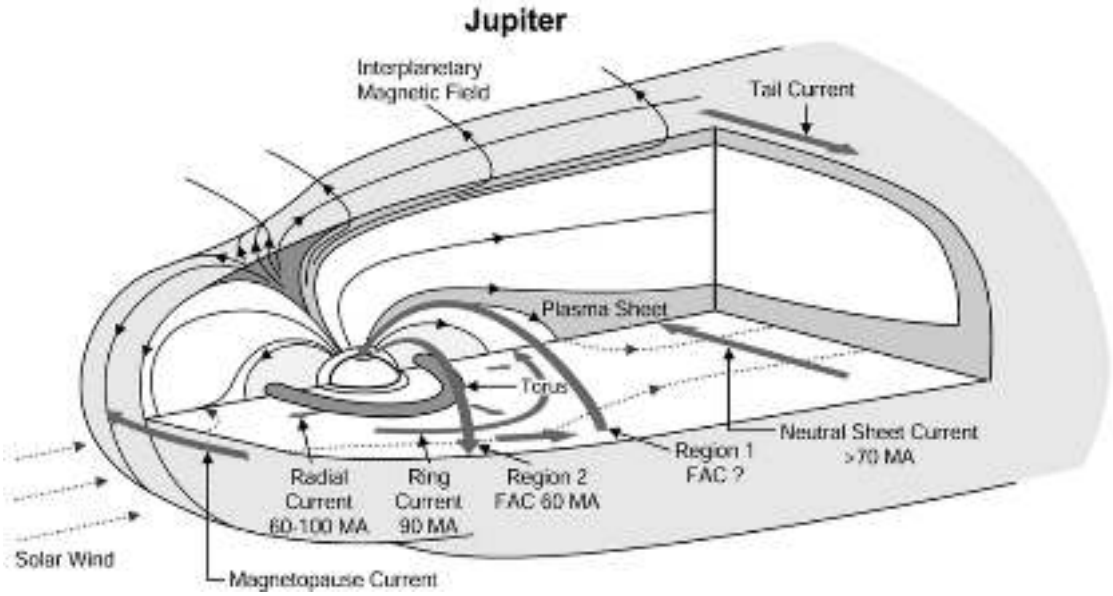


Figure 1.3.: Diagram of the dynamics of currents in Jupiter's magnetosphere. Credits: Khurana et al. (2004)'s Figure 24.16

Contrary to the case of Earth's magnetosphere, which is controlled by the interaction with the solar wind, the dynamics in the Jovian magnetosphere is heavily controlled by the planet rotation. The Io plasma torus is extended by the centrifugal force to form a plasma sheet (yellow in Figure 1.2) from 5 R_J to 60 R_J. The Lorentz force $\vec{\mathbf{J}} \times \vec{\mathbf{B}}$, associated with this radial current $\vec{\mathbf{J}}$, accelerates the equatorial plasma to corotation speed. From 10 R_J, the plasma sheet rotation starts to lag behind Jupiter's rotation because the poorly conducting ionosphere not able to impart sufficient angular momentum to the outflowing plasma. This **corotation breakdown** stretches the magnetic field lines. As a result, the magnetic field cannot be approximated by a dipole. This also cause a large extension of the magnetosphere.

The radial currents close into the Jovian ionosphere by propagating along magnetic field lines (illustrated in Figure 1.3). These Field Aligned Currents (FACs) peak at $\sim 20\,R_J$ to $50\,R_J$ close to the region where the system becomes unable to maintain full corotation with the planet (Cowley and Bunce 2001; Hill 1979). This radial current was also shown to be dependent on the local time for $R > 30\,R_J$, suggesting an influence of the solar wind convection.

Similarly to Earth, an azimuthal current enhanced locally in the midnight sector is seen at Jupiter. This partial ring current appears to be the result of a global convection system driven by the solar wind. The FAC noted as region 2 n Figure 1.3 is introduced to feed and evacuate this Jovian partial ring current.

Knight (1973)'s law showed that to maintain a current $\vec{\mathbf{J}} = n_e \vec{\mathbf{v}}$ the density must decrease when the speed of the electrons accelerated by a FAC increases. In the

electron flux energy spectrum, this phenomenon is exhibited by inverted V shaped features.

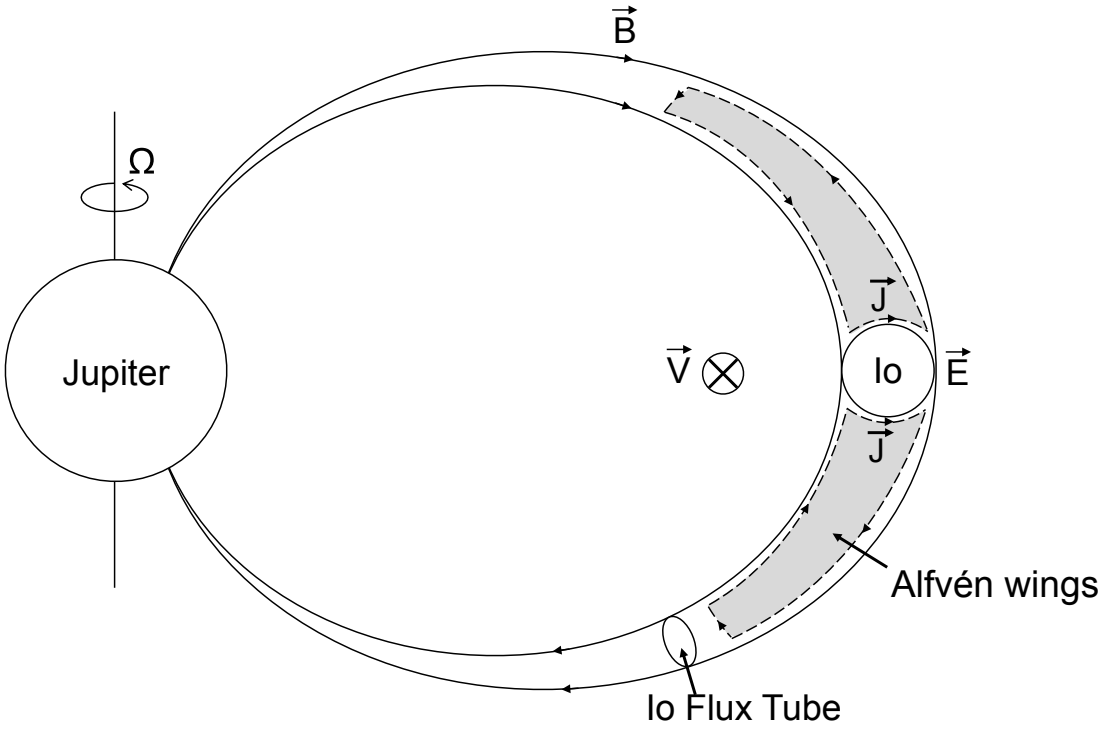


Figure 1.4.: Schematics of the currents propagating in the Alfvén wings. Credits: Louis (2018)

In addition, Io rotates inside the Io plasma torus at a rotation speed different from it. This motion perturbs the magnetic field and generates a current carried by Alfvén waves. These waves propagate along Alfvén wings in the Io flux tube as illustrated in Figure 1.4. Some of these waves are amplified and reflected when they reach the ionospheric Alfvén resonator (a depletion above the ionosphere described in Lysak 1993). These waves thus create bidirectional FAC along the Io flux tube.

1.2. Jupiter: an auroral emitter

1.2.1. Jovian auroral radio emissions

1.2.1.1. History

Strong non-thermal radio emissions have been detected by Burke and Franklin (1955) using ground-based measurements. They were early interpreted as driven in the auroral regions by the motion of electrons at the electron gyrofrequency $f_{ce} = \frac{eB}{2\pi m_e}$ (where $e = 1.6 \times 10^{19}$ C is the electron charge, m_e the electron mass). These **auroral radio emissions** were therefore the first evidence of a magnetic field at Jupiter and allowed

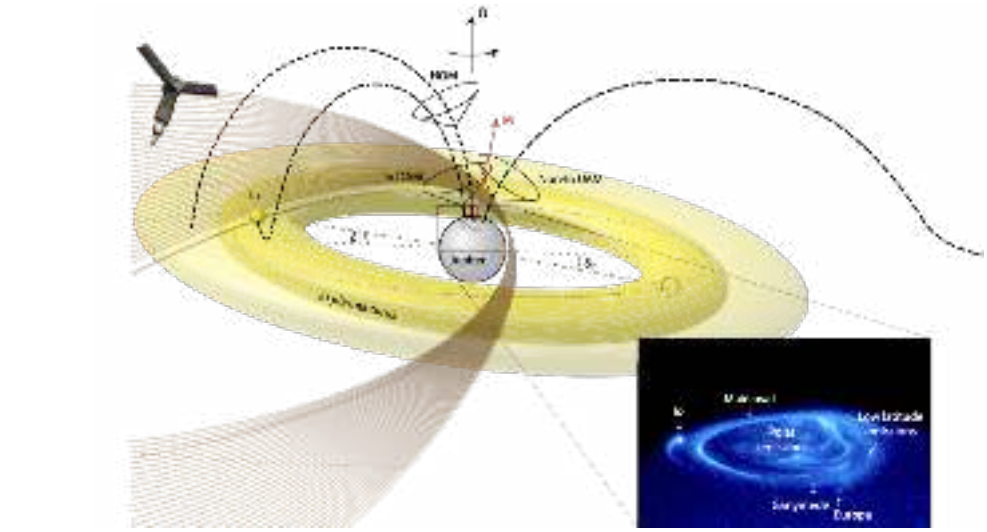
for the estimation of Jupiter's rotation period (Carr et al. 1983; Genova et al. 1989). Later, space probes equipped with a radio instruments (Voyager, Galileo, Ulysses and Cassini) allowed a better characterization of the Jovian auroral radio spectrum (Scarf et al. 1979; Zarka 1998). This led to the separation of these complex emissions into 4 components illustrated in Figure 1.5 (Boischot et al. 1981, and references therein):

- The Jovian Moon-induced Decametric emissions (Moon-DAM), which have the particularity to be corotating with Io, Europa or Ganymede (Bigg 1964; Menietti et al. 1998; Higgins et al. 2006) $f > 3\,\mathrm{MHz}$ up to 40 MHz
- The Jovian Decametric emission (DAM) $f > 3\,\mathrm{MHz}$
- The Jovian Hectometric emission (HOM) $0.3 < f < 3\,\mathrm{MHz}$
- The Jovian brodband Kilometric emission (bKOM) $10 < f < 300\,\mathrm{kHz}$ (up to 1 MHz)

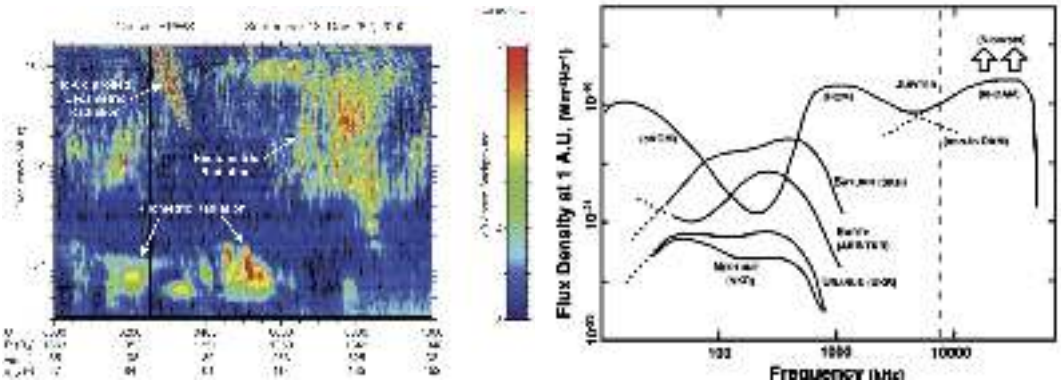
These frequency ranges are porous as bKOM often extends on the HOM range.

Quasi-periodic bursts from 1 kHz to 30 kHz were also reported by Kurth et al. (1989) using Voyager measurements and MacDowall et al. (1993) using Ulysses measurements. However, there is no consensus on the generation mechanism and origin of these QP bursts. Similarly, narrow lower frequency (nLF or VLF or escaping continuum) and narrow band kilometric (nKOM) emissions have been reported since Voyager 2 fly by (Warwick et al. 1979). These emissions were shown to be emitted from the Io torus (thus not auroral and out of scope see also Boudouma et al. 2024, for the most recent review and study on the generation processes).

Strong Jovian radio emissions were reported to be generated in the radiation belts of Jupiter in the decimetric range (synchrotron radiation). These emissions, not being auroral, are therefore outside the scope of this thesis.



(a)



(b) (c)

Figure 1.5.: Jovian auroral components locations and properties a)Schematics of the field lines hosting Jovian auroral sources b)Time-frequency spectrogram of the different components of Jovian radio seen by Cassini (Figure from Kurth et al. 2017) c) Comparative spectra of auroral radio emissions. Average emissions are sketched, normalized to a distance of 1 au from the source based on Voyager measurements (Figure 1 from Zarka (1998))

1.2.1.2. Characteristics of the Jovian auroral radio emissions

All these emissions are beamed along a thin (1°) hollow-cone at large angles (70°-90°) from the direction of the local magnetic field, which is responsible for the arc-shaped structures observed in time-frequency radio spectrograms (Fig. 1.6)

This characteristic, the mostly circular polarization and the observed dominantly Right Hand (RH) polarization in the North and dominantly Left Hand (LH) polarization in the South, suggesting preferential emission on the X-mode (and marginal on the O-mode), early led to considering the Cyclotron Maser Instability (CMI) as a generation

mechanism (detailed in Chap 2). In brief, this instability coherently amplifies waves at a frequency f close to the gyration frequency of the electrons f_{ce}, requires a highly magnetized plasma, and an inversion population for electrons of a few keV. This theory was proposed to explain the Earth's Auroral Kilometric Radiation (AKR) (Wu and Lee 1979) and was later verified with in situ measurements in monoenergetic acceleration regions at Earth (Louarn 1992; Ergun et al. 2000) and for the Saturn's Kilometric Radiation (SKR) (Mutel et al. 2010; Lamy et al. 2010). This instability was also verified in laboratory experiments where it was shown to have a 2% conversion efficiency (McConville et al. 2008; Ronald et al. 2008; Bingham et al. 2013).

At these planets, harmonics of AKR and SKR were observed (Wu et al. 2022; Benson 1982; Hosotani et al. 2003; Mellott et al. 1986), whereas at Jupiter, only poorly convincing observations of harmonics of the Io-DAM and HOM were reported (Menietti 1995; Menietti and Curran 1990; Menietti et al. 1998).

These emissions often exhibit fine structures (Zarka 1998). At Jupiter, S-bursts in the decameter range are discrete quasi periodic features drifting mainly negatively in time-frequency plane ($-10\,\mathrm{MHz}\cdot\mathrm{s}^{-1}$ to $-30\,\mathrm{MHz}\cdot\mathrm{s}^{-1}$) in a few tens to a few hundred milliseconds. These bursts are thought to be generated by the modulation of the unstable electrons at the period of Alfvén waves (Hess et al. 2007, 2009). Initially, these bursts were thought to be only generated in the Io flux tube but Mauduit et al. 2023 showed that emissions controlled by Ganymede and auroral (non-moon) decametric emissions generate also these fine structures. They also developed a method to deduce the energy of the unstable electrons from these drifts.

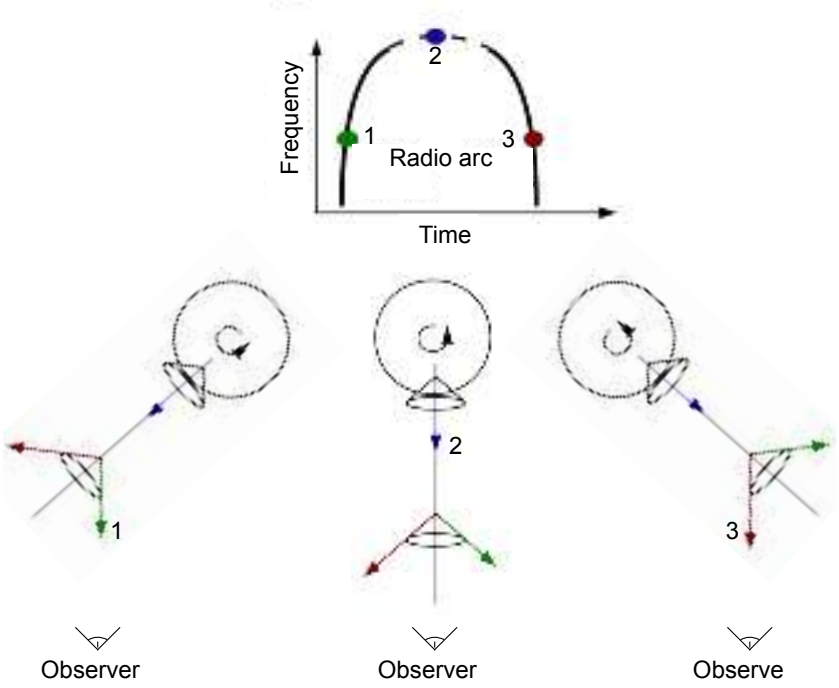


Figure 1.6.: Schematics explaining the arc shape in time-frequency spectrogram of auroral emissions. In this simplistic case of a totally dipolar and axisymmetric magnetic field, the edges of the conical emission sheet will sweep across the observer throughout the movement of the magnetic field line relative to the observer, at each frequency and at each time step. In case 1, the conical emission sheet is located on the morning side relative to the observer: the shape of the arc is vertex early; in case 2, the conical emission sheet is located opposite the observer; in case 3, the conical emission sheet is located on the morning side relative to the observer: the shape of the arc is vertex late. Credits: Louis (2018)

1.2.1.3. Moon-DAM

Decametric emissions above 10 MHz were the first components to be observed from Earth. They were soon divided in Io-DAM and non-Io DAM to account for the dependence of some emissions to the Io phase (Bigg 1964). Nowadays, Io, Ganymede, and Europa are known to induce radio emissions (Bigg 1964; Louis et al. 2017, 2020; Zarka et al. 2017) so the term Moon-DAM is more accurate and I will use DAM to describe the non-Moon (auroral) component (described in the next subsection).

Remote observations of subsecond burst by Mauduit et al. (2023) and Hess et al. (2007, 2008) inferred that these emissions were generated by electrons of 0.1-10 keV for the case of Ganymede and of mostly 2-10 keV for the case of Io. Lamy et al. (2022, 2023b) observed the beaming angles for each Moon-DAM (70°-80° for Io ;79°-81° for Europa ; 71°-87° for Ganymede) and estimated these energies at 3-16 keV for Io ; 1-3 keV for Europa ; 0.5-15 keV for Ganymede.

This component and the DAM both have elliptic polarization that have been in-

terpreted as the source being highly depleted. Also, Galopeau and Boudjada (2016) suggested that an oblate beaming cone is more accurate for Io-DAM.

Hints for Callisto-induced radio emissions were observed from Voyager and Galileo (Menietti et al. 2001; Higgins 2007) but have later been attributed to biases in data selection and processing (Jácome et al. 2022).

1.2.1.4. DAM and HOM

DAM and HOM were first observed from ground-based radio telescopes. The first Jupiter flybys by Voyager, Ulysses, and Cassini provided a better constraint on the source locations. This location is expressed in terms of magnetic apex, either L-SHELL or M-SHELL (in R_J). Both these quantities designate the maximal distance a field line (here on which radio emission is produced) extends from Jupiter. L-SHELL is the magnetic apex supposing a dipolar magnetic field and M-SHELL is the counterpart for a modeled magnetic field taking into account the current sheet (most often Connerney et al. (2022, 2020)'s Internal field model complemented by a current sheet model (JRM33+CON20) or Connerney et al. (2018, 2020)'s JRM09+CON20).

Genova and Aubier (1987) inferred the source location at $L > 6\,R_J$ in the case of the DAM component, whereas the HOM component was identified on different sets of L-shells: either $7\,R_J$ to $11\,R_J$ (Ladreiter et al. 1994), $5\,R_J$ or $8\,R_J$ to $10\,R_J$ (Zarka et al. 2001).

While the connection between HOM and DAM had long been debated, Zarka et al. (2021) confirmed that HOM was indeed the lower frequency extension of DAM using both Cassini and Nançay Decameter Array data. In this study, HOM was shown to be preferentially emitted from the dusk side (Boudouma et al. 2023, and confirmed in).

Mauduit et al. (2023) inferred that the DAM components was produce by electrons of 0.1-10 keV.

1.2.1.5. bKOM

Contrary to the case of HOM, DAM and Moon-DAM, bKOM is emitted from 10 kHz to 300 kHz and so below the terrestrial ionosphere cut off of 1 MHz. Then, it was not until Voyager 1's approach that Jupiter's kilometric emissions were discovered (Warwick et al. 1979). These kilometric emissions are decomposed into two components differentiated by their spectral properties: the narrowband kilometric (nKOM) and the broadband kilometric (bKOM). Sometimes, a third component is added the smooth kilometric (sKOM) emissions. Initially, it was unclear whether the bKOM was emitted in the auroral regions or in the Io plasma torus. (Warwick et al. 1979; Kurth et al. 1979). Only direction finding measurements from the Ulysses mission during its Jupiter fly by allowed to show that bKOM was emitted from auroral field lines (Ladreiter et al. 1994). The generation of this component by the CMI was also confirmed from the observed circular polarization predominantly right-handed in the North and left-handed in the South, thus coherent with RX mode (Barrow et al. 2001; Leblanc and Daigne 1985) and also the observed emission cone with half-angles of 40° to 80°(Ladreiter et al. 1994).

The sKOM was only reported by Reiner et al. (1994) with the Ulysses radio instrument. This component is fairly weak (2 orders of magnitude weaker than bKOM) and probably requires a very sensitive instrument to be detected. Since these emissions have the opposite polarization to those of bKOM, Kimura et al. (2008) theorized these emissions could be bKOM converted to the O-mode by mode conversion processes.

The emission from auroral field lines was also theorized from the longitudinal preference of bKOM near 200° (close to the Northern magnetic pole) (Desch and Kaiser 1980; Kurth et al. 1979, 1980; Leblanc and Daigne 1985; Galopeau and Boudjada 2005; Kimura et al. 2008; Louis et al. 2021; Fischer et al. 2025). Ladreiter et al. (1994) and Zarka et al. (2001) predicted sources to be located on magnetic apexes from 9 R_J to > 50 R_J using Ulysses measurements,

In addition to the frequency range, there are two major differences between HOM/DAM and bKOM. First, the intensity flux is twice as low for bKOM as it is for the other components. Second, this component is less controlled by the corotation breakdown than by solar wind, as it is for HOM/DAM. Indeed, bKOM has been shown to correlate with the start of solar wind density enhancements (Louarn et al. 1998; Louis et al. 2023a; Reiner et al. 2000; Zarka et al. 2021).

Measurements from Voyager (Boischot et al. 1981, and refs therein), Ulysses (Lecacheux et al. 1992), Cassini (Zarka et al. 2021), and Juno (Louis et al. 2021; Fischer et al. 2025) all showed that bKOM is mainly observed at longitudes in antiphase with those where HOM and DAM are observed. Indeed, bKOM is more observed at longitudes near 200° in the North (sometimes referred to as the "Main component") while a secondary occurrence peak, attributed to Southern emissions, is seen at 25°-40° (sometimes refer to as the Intermittent component").

1.2.2. Jupiter's UV aurora to characterize auroral acceleration processes

An aurora is defined as a light emission produced by the impact on a planet's atmosphere of any charged energetic particles traveling along magnetic field lines. Due to their larger mass, the ions are less accelerated than the electrons, so their contribution to the auroral emissions is negligible. These collisional emissions are observed from visible to Far Ultraviolet wavelengths depending on the composition of the atmosphere. On top of these, emissions due to ro-vibrational transitions of H_3^+ in the infrared and X-ray bremsstrahlung emissions can be observed in the precipitation regions. These aurorae act like a giant screen, responding to acceleration processes in the magnetosphere (Clarke et al. 2004; Badman et al. 2015).

At Earth, the aurorae are well known as *northern lights* or *aurora borealis* and *aurora australis*. They are produced in the visible spectrum (red green and blue) due to the Oxygen and Nitrogen-rich atmosphere below 100 km and in the red (H_α line at 656.3 nm) due to the Hydrogen rich above 100 km.

At Jupiter, the auroral emissions are emitted in the visible and UV range (H Lyman α and H_2 Lyman and Werner bands) and infrared (H_3^+ ro-vibrational transitions) due to the Helium and Hydrogen-rich atmosphere (Prange 1992). These aurorae are the most

powerful in the solar system (emitted power of 10^{12} W), are always active and rotate with the magnetosphere. They were discovered by Voyager and the International UV Explorer in 1979 (Broadfoot et al. 1981; Clarke et al. 1980)

Among these various auroral emissions, I will hereafter refer to the UV aurorae to monitor the auroral context, as they probe the instantaneous response of the neutral atmosphere to particle precipitation.

These UV emissions are structured into 4 categories (see Figure 1.7):

- The Main Auroral Oval (MAO): an almost continuous curtain of auroral emissions around the magnetic pole,
- The UV Diffuse Aurora (UV DA) equatorward the MAO,
- The footprint of Io, Europa, and Ganymede,
- The polar emissions whose origin is still debated.

In the North Pole, the MAO has a "kidney-bean" shape (Pallier and Prangé 2001) which is thought to be due to a magnetic anomaly located at a latitude of 75° and a longitude of 115° that pushes the main aurora poleward. These emissions are magnetically connected to M-SHELL typically ranging from 20 to 60 R_J. They are then thought to be produced by the FACs enforcing the plasma corotation.

The Io footprint has four features explained by the Alfvén wing theory (see Figure 1.4): (1) the Main Alfvén Wing (MAW) spot, which is caused by Io's interaction with Jupiter's corotating magnetosphere (Bonfond et al. 2008; Saur et al. 2013) (2) a Transhemispheric Electron Beam (TEB) spot, which is probably caused by conjugate electron beams from the opposite hemisphere's MAW, (3) Reflected Alfvén Wing (RAW) spots, which are probably a result of Alfvén wave reflections across density gradients in the Io torus and (4) a long auroral tail.

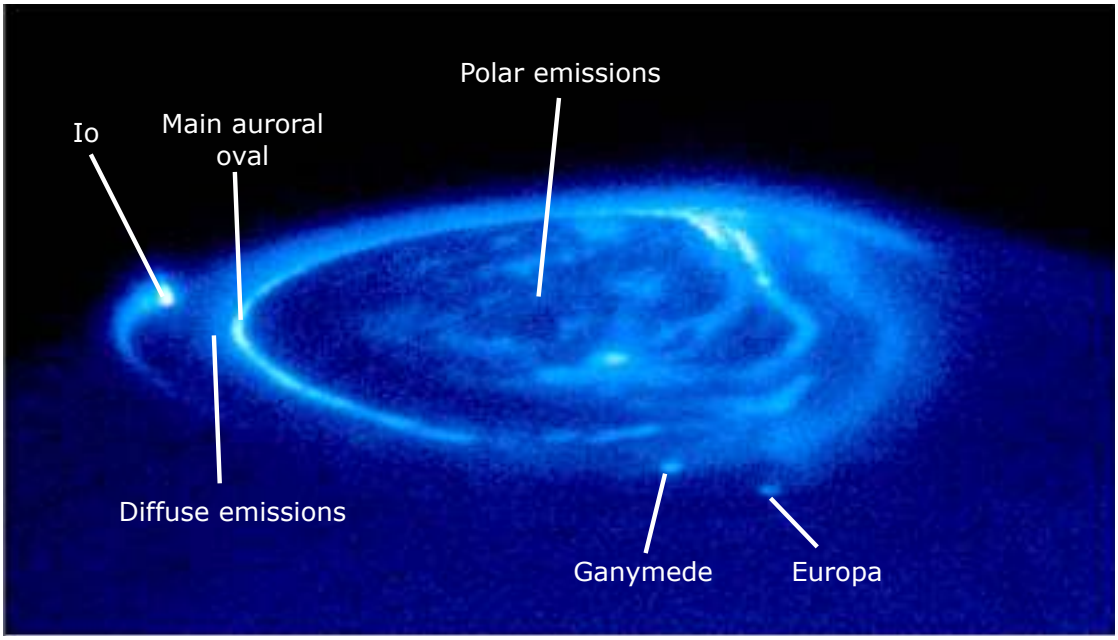


Figure 1.7.: Hubble Space Telescope observations of UV aurora on Jupiter

1.2.2.1. Correlation between UV and radio emissions

At Earth,AKR sources are located on the same field lines on which electrons precipitate in the atmosphere to produce aurora. (Huff et al. 1988; Menietti et al. 2011)

A similar association was then expected at Jupiter. Indeed, the M-SHELL where DAM, HOM, and bKOM have been predicted to be located at seem coherent with the field lines connected to the aurora. In addition, a direct correlation was found between the bKOM observed by Galileo and the UV auroral activity observed by the International Ultraviolet Explorer (Prangé et al. 2001). Prange et al. (1993) showed that the power of Far UV and DAM auroral emissions have a similar longitudinal variability.

Hess et al. (2010) predicted that the UV footprint of a satellite and the radio emissions associated with the satellite should be produced on the same field lines. In the case of Io, radio emissions are produced on field lines connected to the MAW and RAW. No simultaneous observation of UV and Moon-DAM have been reported before Juno.

1.3. The Juno era

1.3.1. Description of Juno



Figure 1.8.: Juno spacecraft and its science instruments. Image credit: NASA/JPL.

1.3.1.1. Magnetospheric Science Objectives

Juno is a NASA space mission aimed at studying the polar Jovian magnetosphere and, in particular, the auroral regions. Indeed, Jupiter had been characterized from observations made in the equatorial regions. Bagenal et al. (2017) compiled the objectives of the missions, which include understanding:

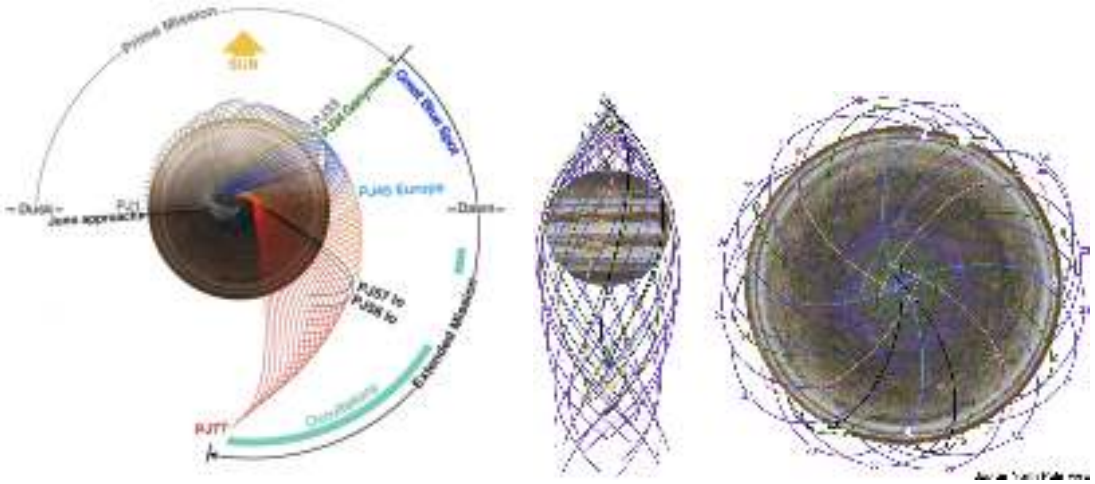
- The acceleration processes precipitating particles in the atmosphere,
- The link between the aurora and the solar wind and magnetosphere dynamics
- The generation of auroral radio emissions.

1.3.1.2. Trajectory

The polar trajectory of the spacecraft is unprecedented, and was designed to probe both the northern and southern auroral regions surrounding the magnetic poles once

per orbit, at low altitudes (down to 0.1 R_J). At apojove, the distance is of the order of 100 R_J. Initially planned to last for 35 orbits (hereafter Perijove (PJ)), from 2016 to 2021, the mission will have completed its 76th orbit on September 15th, 2025, as per its extended mission, and a second mission extension is currently in discussion.

These numerous orbits brought Juno from the dusk side to the dawn side of Jupiter (see Figure 1.9. This precession resulted in the sampling of auroral field lines on a broad range of radial distances and longitude mapping to all components of the Jovian aurorae.



(a) (b)

Figure 1.9.: Juno's orbits orbital coverage from PJ1 (2016-08-27) to PJ77 (2025-10-17). Credits: Bolton et al. (2017).

In this work, I have used observations acquired from within the auroral regions by three instruments, namely the Waves radio experiment (Kurth et al. 2017), the JADE-E electron spectrometer (McComas et al. 2013), and the MAG flux gate magnetometer (Connerney et al. 2017), whose characteristics are briefly reminded below. I have also occasionally used high-energy electron measurements from JEDI and UV auroral observations from Juno/UVS or from Hubble Space Telescope (HST). These instruments will be described in Chapter 3.

1.3.2. New constraints on Jupiter's magnetosphere

1.3.2.1. Magnetosphere dynamics and structure

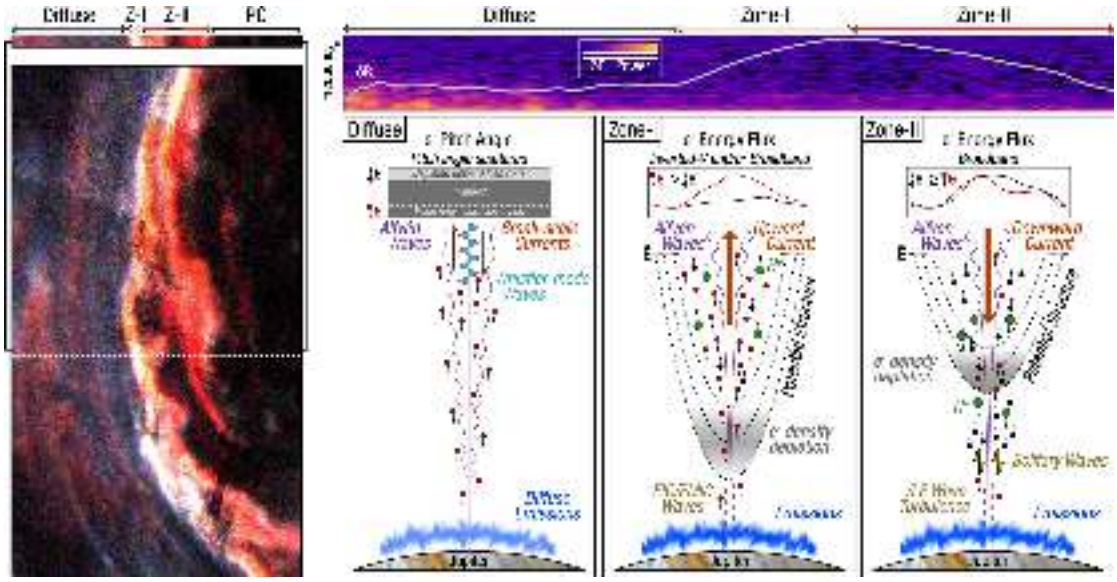


Figure 1.10.: Graphic illustrating the average picture of the fields, particles, and plasma waves in Jupiter's low-altitude Diff. A, ZI, and ZII. Credits: Sulaiman et al. (2022)

In situ measurements from Juno allowed to better constrain the origin of the plasma in the Jovian magnetosphere. The ionosphere was shown to produce $5\,\mathrm{kg\cdot s^{-1}}$ (Szalay et al. 2021). Szalay et al. (2024) estimated that 6-41% of the $(0.16 \pm 0.04)\,\mathrm{kg\cdot s^{-1}}$ Europa espaping H_2 were ionized and injected into the magnetosphere.

The auroral region was shown to be organized into three main zones, the Diffuse Aurora (Diff. A.), mapping to the UV DA equatorward of the main oval, characterized by small-scale FAC and Alfvén waves, the Zone I (ZI) connected to the MAO with mostly downward electron acceleration, generally at intermediate latitudes, and the Zone II (ZII) connected to polar emissions at higher latitudes with bidirectional acceleration (Mauk et al. 2018; Sulaiman et al. 2022). This is very unexpected and still not well understood, as the brightest emissions are produced in regions where electrons are accelerated anti-planetward. These currents are also not stable, as the prominence of each zone differs from one orbit to another. In addition, Allegrini et al. (2017) reported a recurring 3 to 30-keV electron energy flux peak equatorward the MAO and Gershman et al. (2019) identified Alfvén waves in auroral acceleration regions that are known to be the acceleration driver in the Io flux tube that lead to Io-DAM emissions.

Juno's first orbits revealed that mono energetic accelerations characterized by inverted Vs and more generally mono energetic distributions are not prominent in Jupiter's auroral regions compared to the broadband distributions (Salveter et al. 2022). These mostly broadband distributions are associated with stochastic particle

acceleration (opposed to electrostatic potentials generating monoenergetic distributions). Proposed mechanisms include dissipation of turbulent Alfvénic fluctuations (Saur et al. 2003, 2018), resonance with whistler mode waves (Elliott et al. 2018; Kurth et al. 2018), and magnetospheric ultralow frequency (1–60 min) Alfvénic waves (Pan et al. 2021).

1.3.2.2. UV aurora

Jupiter's aurorae present an equivalent to Earth substorms: **dawn storms** (Gerard et al. 1994). During these events, bright UV emissions rotates dawnward. They were first thought to be generated by the Solar activity, but are now explained by magnetosphere reconfiguration in the magnetotail, not necessarily due to active solar wind (Nichols et al. 2009).

Energies of the precipitating electrons have now been better constrained by Benmahi et al. (2024). They showed that in the North the polar emissions were generated by electrons of 300-500 keV, the MAO by energies up to 550 keV, the UV DA by energies between 5 and 50 keV. In the south, the polar emissions are much fainter and generated by electrons of 100 keV and the MAO by electrons of 150-600 keV.

The MAO was also shown to vary with local time. Indeed, in both hemispheres, the MAO dusk side is more contracted and 4 times brighter than the dawn side (Head et al. 2024). In addition, solar-wind compressions induces main auroral brightenings (Yao et al. 2022) These observations (and other arguments presented in Bonfond et al. 2020) led to the reconsideration of the enforcement of the MAO by corotation breakdown. An alternative scenario for the MAO generation based on Alfvén waves has also been proposed (Saur et al. 2003, 2018). These waves originate from Alfvénic perturbations in the middle magnetosphere, which propagate to the auroral regions where they stochastically accelerate electrons to form broadband distributions. Currently, neither the proposed FAC nor the Alfvénic models are fully consistent with observation, and require further analysis.

1.3.2.3. Radio auroral emissions

In terms of radio auroral emissions, Juno allowed the first source crossings of HOM radio sources where the CMI was verified (Louarn et al. 2017, 2018). They analyzed the growth rate by computing $\frac{\partial F_e}{\partial v_\perp}$ estimated solely with $\frac{\partial F_e}{\partial v}$ and showed that HOM sources were generated by loss cone and conics.

Louis et al. (2019) and Imai et al. (2019) identified source crossings during the first 15 orbits of Juno. DAM was shown to be located on field lines with M-SHELL of 7 R_J to 61 R_J and HOM for M-SHELL of 48 R_J to 58 R_J in the Southern hemispheres and down to 12 R_J in the Northern Hemisphere. Note that this location is slightly biased by Juno's trajectory, which favored the dawn side for these orbits.

In the same study, the radio sources were shown to be connected with the equatorward part of the MAO rather than the brightest auroral spots.

The generation of Ganymede-DAM was also studied in a flux tube crossing (Louis

Component		Frequency	M-SHELL	Local time preference	Longitude preference	Emission angle (°)	Power (W)	UV Association	Drivers	Source of free energy
Moon-DAM	Io	1-40 MHz	6 R_J	-	-	70°-80°	$\simeq 10^{11}$	MAW/RAW	Moon-Jupiter interaction	?
	Ganymede	up to 20 MHz	15 R_J			76°-83°				Loss cone
	Europa	up to 25 MHz	9 R_J			79°-81°		?		?
DAM		~1-35 MHz	7-61 R_J	None	120° & 330°	55°-85°	8×10^{10}	Diffuse Aurora	Rotation	?
HOM		0.3- ≥ 3 MHz	North: 12-58 R_J South: 48-58 R_J	Dusk	40°-130°	30°-90°	4×10^{10}			Loss cone and Conics
bKOM		10-300 kHz (up to ~ 1 MHz)	14-66 R_J	Midnight to Dawn	200° 25°-40°	40°-80°	5×10^8		Solar wind	?

Table 1.2.: Characteristics of Jovian auroral components.

et al. 2020) in which the CMI was verified. The emission was produced by 4–15 keV, with a wave propagation angle from 83° to 76°.

The properties of each radio component are summarized in Table 1.2.

1.4. Open questions

The previous paragraphs described the specificities of the Jovian magnetosphere in the Solar System, making it a unique laboratory to understand fundamental plasma acceleration processes, auroral emissions and the CMI. Auroral emissions and in particular auroral emissions are a powerful diagnostic of this magnetosphere.

In this thesis, I was interested in deepening the **understanding of the microphysics of the generation of Jovian auroral emissions** by seeking to address several unresolved inquiries, such as:

- Does the CMI systematically drive the DAM, HOM, and bKOM emissions, and in which conditions does it operate for each of those?
- What are the sources of free energy and the underlying acceleration process for these radio sources?
- What are the magnetic flux tubes hosting the various auroral radio components?
- How do Jovian radio emissions relate to (and in turn diagnose) the underlying acceleration processes ?
- How do they connect to the UV auroral components down into the atmosphere?
- Do the HOM and DAM indeed form a single component ?
- How do these emissions compare with those observed at other planets?
- What are the implications of the understanding of the generation of Jovian auroral radio emissions on the search for more distant auroral radio sources, such as exoplanets and stars?

To describe my approach to tackle these questions, I will first remind the basics of the CMI theory in Chapter 2, then Chapter 3 will explain the methods I developed and used to test it in situ with Juno electron and radio measurements acquired within the auroral radio emissions regions. The investigations I conducted on the generation of HOM, DAM, and Moon-DAM components will be described in Chapter 5. These investigations are then extended to the bKOM component in Chapter 5. Finally, in Chapter 6, I will discuss the results obtained for the different Jovian auroral radio components and compare those in the Jovian context and in the more general solar system one.

2. Generation of auroral radio emissions

Do not disturb my circles

Archimedes

Contents

2.1. The Cyclotron Maser Instability . . . 49
2.2. Resonance curves . . . 49
2.2.1. Weakly relativistic case . . . 50
2.2.2. General (fully) relativistic case . . . 51
2.3. Growth rate expressions . . . 54
2.3.1. Dispersion relation . . . 54
2.3.2. Cold plasma modes . . . 54
2.3.3. Dispersion relation in the case of CMI . . . 57
2.3.4. Growth rates in the semi-relativistic approach . . . 58
2.3.4.1. Hot plasma assumption . . . 58
2.3.4.2. Effect of a Cold plasma population . . . 59
2.3.4.3. Properties of the expressions of the growth rate . . . 60
2.3.5. CMI applicability to Jupiter . . . 61
2.3.5.1. Hot or cold plasma assumption . . . 61
2.3.5.2. Semi-relativistic approximation . . . 62
2.3.5.3. f_{pe}/f_{ce} range . . . 62
2.4. CMI-unstable electrons . . . 62
2.4.1. Useful formulae to characterize a resonance circle . . . 63
2.4.2. Loss Cone EDF . . . 64
2.4.3. Conics EDF . . . 65
2.4.4. Shell EDF . . . 65
2.4.5. Trapped electrons . . . 65
2.5. Wave intensity . . . 66
2.5.1. Group Velocity . . . 67
2.5.1.1. Group velocity in a cold plasma . . . 68
2.5.1.2. Group velocity in a hot plasma . . . 69
2.5.1.3. Group velocity derived in a plasma with both populations 71
2.5.1.4. Thermal effects . . . 73

2.1. The Cyclotron Maser Instability

The Cyclotron Maser Instability was first introduced by Wu and Lee (1979) to account for AKR and was extensively reviewed by Treumann (2006) in a larger astrophysical context (see also Wu 1985; Bingham et al. 2013). This theory is based on the resonance of a wave with non-thermal electrons.

In particular, this wave-plasma instability occurs in a depleted and highly magnetized plasma so that $\frac{f_{pe}}{f_{ce}} \ll 1$ with $f_{pe} = (2\pi)^{-1}(\frac{e^2 n_e}{m_e \epsilon_0})^{\frac{1}{2}} \simeq 8.967\sqrt{n_e}$ the plasma frequency (with $\epsilon_0 = 8.85 \times 10^{-12}$ F/m, the vacuum permittivity). The unstable electrons for this instability must be non-thermal and have weakly relativistic energies. The wave amplification also requires an inversion population characterized by a positive gradient of the Electron Distribution Function (EDF) in the direction perpendicular to the magnetic field.

The amplified wave is emitted quasi-perpendicularly to $\vec{\mathbf{B}}$ on circularly polarized modes, mainly the Right-handed eXtradordinary (RX) mode and marginally the Left-handed Ordinary (LO) mode. These modes are usual plasma modes and will be described in Section 2.3.1.

The wave is emitted at the frequency of gyration of the unstable electrons along magnetic field lines in their proper frame of reference. This frequency of gyration f_{ce} writes $\frac{f_{ce}}{\Gamma}$ with $\Gamma = \frac{1}{\sqrt{1-\beta^2}}$ the Lorentz factor with $\beta = v/c$ the normalized velocity of the unstable electron and is shifted by a Doppler term $k_\parallel v_\parallel$, where $\vec{\mathbf{k}} = (k_\parallel, k_\perp) = \left(k\cos(\theta_{(\vec{\mathbf{k}},\vec{\mathbf{B}})}), k\sin(\theta_{(\vec{\mathbf{k}},\vec{\mathbf{B}})})\right)$ is the wave number of the amplified wave, with $\parallel, \perp$ subscripts indicating the direction parallel and perpendicular to the local magnetic field $\vec{\mathbf{B}}$. Note that while I'm mostly interested in the fundamental ($n = 1$), this instability can produce emissions at harmonics $f_n = nf$ with $n \in \mathbb{N}$.

The resonance equation of this instability is given in Equation 2.1.

$$\omega - k_\parallel v_\parallel = n\frac{\omega_{ce}}{\Gamma} \tag{2.1}$$

where $\omega = 2\pi f$ is the angular frequency,

On top of these fundamental conditions, complementary sets of hypotheses were made on the resonant electrons, thus affecting the expression of the dispersion relation and growth rate.

In this chapter, I will remind the theory of this instability by describing its resonance equation and conditions. I will then derive different expressions of the growth rate for Right eXtradordinary (RX)-mode waves and present the typical CMI-unstable electron populations. Finally, I will discuss the group velocity and the wave source term, which associated with the wave growth rate, are needed to achieve the final wave amplitude.

2.2. Resonance curves

The key difference that Wu and Lee (1979) introduced compared to the basic electron-wave cyclotron resonance was to consider the effect of relativistic correction in the

treatment of the resonant electrons, even for the case of very weakly relativistic electrons. This resulted in the addition of the Γ parameter in Equation 2.1. I will describe below the resonance equation in the case of the weakly relativistic and in the general fully relativistic approach.

First, note that if no relativistic effects are taken into account, the resonance equation 2.1 is then reduced to $v_\parallel = \frac{\omega - n\omega_{ce}}{k_\parallel}$ for finite $k_\parallel$. This equation transposes into a vertical line in the $(v_\parallel, v_\perp)$ phase space. Along this line, only very few resonant electrons contribute to radiation, making this instability poorly efficient. Such non-relativistic cyclotron theory was shown to be able to generate radio emissions, but requires unrealistically high temperature anisotropies to explain radio auroral emissions.

2.2.1. Weakly relativistic case

In the case of Earth's magnetosphere, the accelerated, out-of-equilibrium electrons that prevail in the auroral regions have typical kinetic energies of a few keV. The Lorentz factor Γ can then be approximated by its first order approximation $\Gamma^{-1} = 1 - \frac{1}{2}\beta^2$. This so-called semi-relativistic approximation should be a good approximation up to $\frac{v^2}{c^2} = 0.1 \Rightarrow v \simeq 0.3c \Rightarrow E \simeq 30\,\text{keV}$. In this approximation, the resonance equation can be developed into Equations 2.2. Using $\overline{k_\parallel} = k_\parallel \frac{c}{n\omega_{ce}}$ the normalized wavenumber and $\Delta\omega = \delta\omega - 1 = \frac{\omega - \omega_{ce}}{n\omega_{ce}}$ the algebraic frequency difference between ω and ω_{ce}. This resonance equation turns into the equation of a circle (Equation 2.3a) with radius r and center $(\beta_0, 0)$ in the $(\beta_\parallel, \beta_\perp)$ phase space (Equations 2.3).

$$\begin{aligned} n\omega_{ce}\left(1 - \frac{1}{2}\frac{v^2}{c^2}\right) &= \omega - k_\parallel v_\parallel \\ \frac{v_\perp^2}{c^2} + \frac{v_\parallel^2}{c^2} - 2\frac{k_\parallel c}{n\omega_{ce}}\frac{v_\parallel}{c} + 2\left(\frac{\omega}{n\omega_{ce}} - 1\right) &= 0 \\ \beta_\perp^2 + \beta_\parallel^2 - 2\overline{k_\parallel}\beta_\parallel + 2\Delta\omega &= 0 \\ \beta_\perp^2 + \left(\beta_\parallel - \overline{k_\parallel}\right)^2 &= \overline{k_\parallel}^2 - 2\Delta\omega \end{aligned} \tag{2.2}$$

Resonance circle in the semi-relativistic case

$$\frac{\beta_\perp^2}{r^2} + \frac{(\beta_\parallel - \beta_0)^2}{r^2} = 1 \tag{2.3a}$$

with

$$\beta_0 = \overline{k_\parallel} = \frac{k_\parallel c}{n\omega_{ce}} \qquad \text{Center of the circle} \tag{2.3b}$$

$$r^2 = \beta_0^2 - 2\Delta\omega \qquad \text{Circle radius} \tag{2.3c}$$

where $\Delta\omega$ can be expressed as function of r and β_0

(2.3d)

$$\Delta\omega = \frac{1}{2}(\beta_0^2 - r^2) \tag{2.3e}$$

2.2.2. General (fully) relativistic case

The importance of the relativistic effects exhibited by Wu and Lee (1979) led to the consideration of the general fully relativistic approach for the CMI. This fully relativistic resonance equation can be developed (Equations 2.4) to obtain a resonance ellipse given by Equation 2.5a with a center $(\beta_{0e}, 0)$, a semi major axis $r_\perp$, and a semi minor axis $r_\perp$ (See Equations 2.5).

$$\begin{aligned}
n\omega_{ce}\sqrt{1-\beta^2} &= \omega - k_\parallel v_\parallel \\
\sqrt{1-\beta^2} &= \delta\omega - \overline{k_\parallel}\beta_\parallel \\
\beta_\perp^2 + \beta_\parallel^2 + \beta_\parallel^2\overline{k_\parallel}^2 - 2\delta\omega\overline{k_\parallel}\beta_\parallel + \delta\omega^2 - 1 &= 0 \\
\beta_\perp^2 + \left(1+\overline{k_\parallel}^2\right)\left(\beta_\parallel - \frac{\delta\omega k_\parallel}{1+\overline{k_\parallel}^2}\right)^2 &= \frac{1+\overline{k_\parallel}^2 - \delta\omega^2}{1+\overline{k_\parallel}^2} \\
\frac{\beta_\perp^2}{r_\perp^2} + \frac{\left(\beta_\parallel - \beta_0\right)^2}{r_\parallel^2} &= 1
\end{aligned} \tag{2.4}$$

Resonance ellipse in the fully relativistic case

$$\frac{\beta_\perp^2}{r_\perp^2} + \frac{(\beta_\parallel - \beta_0)^2}{r_\parallel^2} = 1 \tag{2.5a}$$

with

$$\beta_{0e} = \frac{\overline{k_\parallel}\delta\omega}{1+\overline{k_\parallel^2}} = \frac{k_\parallel c}{\omega}\frac{1}{1+\left(\frac{k_\parallel c}{n\omega_{ce}}\right)^2} \qquad \text{Center of the ellipse} \tag{2.5b}$$

$$r_\perp^2 = \frac{1+\overline{k_\parallel}^2 - \delta\omega^2}{1+\overline{k_\parallel}^2} = 1 - \frac{\omega^2}{n^2\omega_{ce}^2}\frac{1}{1+\left(\frac{k_\parallel c}{n\omega_{ce}}\right)^2} \qquad \text{Semi major axis } (\perp) \tag{2.5c}$$

$$r_\parallel^2 = r_\perp^2\frac{1}{1+\overline{k_\parallel}^2} = r_\perp^2\frac{1}{1+\left(\frac{k_\parallel c}{n\omega_{ce}}\right)^2} = r_\perp^2\left(1 - \frac{\beta_{0e}^2}{1-r_\perp^2}\right) \qquad \text{Semi minor axis } (\parallel) \tag{2.5d}$$

where $\delta\omega$ and $\overline{k_\parallel} = \frac{k_\parallel c}{\omega_{ce}}$ can be expressed as

$$\overline{k_\parallel}^2 = k_\parallel^2 \left(\frac{c}{n\omega_{ce}}\right)^2 = \frac{\beta_{0e}^2}{1 - r_\perp^2 - \beta_{0e}^2} \tag{2.5e}$$

$$\delta\omega^2 = \frac{\omega^2}{\omega_{ce}^2} = \frac{(1 - r_\perp^2)^2}{1 - r_\perp^2 - \beta_{0e}^2} \tag{2.5f}$$

Both resonance curves give a relationship between the properties of the wave $k_\parallel$, ω and those of the curves (radius and center).

It is worth mentioning that, contrary to the resonance circle, the resonance ellipse ensures $v < c$. Moreover, the ellipse corresponds to physical waves only for :

$$\beta_{0e}^2 + r_\perp^2 < 1 \tag{2.6}$$

The resonance ellipse is shrunken in the parallel direction and degenerates into a circle at $k_\parallel = 0$. Moreover, the expression of the resonance circle obtained in the semi-relativistic approximation can be retrieved by using the first order approximation of $k_\parallel^2 \ll \left(\frac{n\omega_{ce}}{c}\right)^2$ (i.e. $\overline{k_\parallel}^2 \ll 1$) and $\Delta\omega \ll 1$. Hence, the semi-relativistic approximation should be valid for $\Delta\omega < 10\%$ and $k_\parallel^2 < 0.1\left(\frac{n\omega_{ce}}{c}\right)^2$, which gives $70° \lesssim \theta_{(\vec{\mathbf{k}},\vec{\mathbf{B}})} \lesssim 110°$ for a wave light ($\frac{kc}{\omega} \sim 1$).

This merging of the resonance ellipse with the resonance circle for quasi-perpendicular emission close to nf_{ce} is illustrated by Figure 2.1 left panel. The right panel of this figure shows that at higher $k_\parallel$ the resonance circle intercepts the same electrons as the resonance ellipse only for $v_\parallel \sim 0$. Note that on this figure, the red circles are the resonance ellipse (degenerated into a circle) for the same ω as the 2 other curves but for $k_\parallel = 0$.

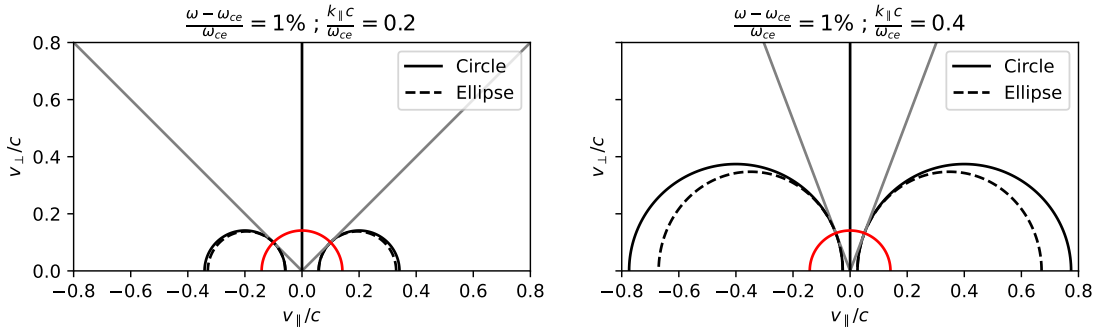


Figure 2.1.: Resonance circle and ellipse at $\Delta\omega = 1\%$ and $k_\parallel = 0.2\frac{\omega_{ce}}{c}$ or $k_\parallel = 0.4\frac{\omega_{ce}}{c}$ (i.e. $\theta_{(\vec{\mathbf{k}},\vec{\mathbf{B}})} = 78°$ and $66°$ if $N \sim 1$)

For both the resonance ellipse and circle, the expressions of r^2 and $r_\perp^2$ can be negative for a range of $(k_\parallel, \omega)$. This implies that no physical emissions for a resonance

ellipse with $\delta\omega^2 < 1 - k_\parallel^2 \frac{c}{\omega_{ce}}$ or for resonance circles with $\delta\omega < 1 + \frac{1}{2}\sqrt{k_\parallel \frac{c}{\omega_{ce}}}$.

Equation 2.3e gives that in the case of a resonance circle, the emission is produced below f_{ce} only if $r > \beta_0$, i.e., if the circle intercepts both sides of the origin, i.e., downward and upward electrons. In the case of a resonance ellipse, Equation 2.5f gives that $\delta\omega < 1$ only if $r_\perp^2 > \beta_{0e}^2 + r_\perp^4$. Supposing $r_\perp^4 \ll r_\perp^2 - \beta_{0e}^2$, the same result as in the semi-relativistic approximation is obtained. This inequality has solution if $\beta_{0e} < 0.5$ and either $r_\perp^2 < \frac{1}{2}(1 - \sqrt{1 - 4\beta_{0e}^2})$ or $r_\perp^2 > \frac{1}{2}(1 + \sqrt{1 - 4\beta_{0e}^2})$.

CMI in a nutshell

The CMI is a wave-plasma instability amplifying waves
-at $f \simeq n f_{ce}$
-quasi-perpendicularly to $\vec{\mathbf{B}}$
-circularly polarized
-Mainly on the RX-mode (marginally Left Ordinary (LO)-mode)
Conditions:
- $\frac{f_{pe}}{f_{ce}} \ll 1$
-Inversion population of weakly relativistic electrons ($\frac{\partial F_e}{\partial v_\perp} > 0$)
Resonance equation:

$$\omega = \omega_{ce}\Gamma^{-1} + k_\parallel v_\parallel$$

where the relativistic effect must be taken into account
In $(\beta_\parallel, \beta_\perp)$ the resonance equation turns into
- a circle in the weakly relativistic case:

$$\beta_\perp^2 + (\beta_\parallel - \beta_0)^2 = r^2$$

$$\text{with } \beta_0 = \frac{k_\parallel c}{\omega_{ce}} \qquad \text{and } r^2 = \beta_0^2 - \Delta\omega$$

- an ellipse in the general (fully) relativistic case:

$$\frac{\beta_\perp^2}{r_\perp^2} + \frac{(\beta_\parallel - \beta_{0e})^2}{r_\parallel} = 1$$

$$\text{with } \beta_{0e} = \frac{k_\parallel c}{\omega} \frac{1}{1 + \left(\frac{k_\parallel c}{n\omega_{ce}}\right)^2}, \quad r_\perp^2 = 1 - \delta\omega^2 \frac{1}{1 + \left(\frac{k_\parallel c}{n\omega_{ce}}\right)^2} \text{ and } r_\parallel^2 = r_\perp^2 \left(1 - \frac{\beta_{0e}^2}{1 - r_\perp^2}\right)$$

In the rest of this chapter, I assume emission on the fundamental ($n = 1$).

2.3. Growth rate expressions

2.3.1. Dispersion relation

The growth rate ω_i (or its unitless expression $\gamma = \frac{\omega_i}{\omega_{ce}}$) is a physical quantity used to quantify at what rate radio waves are amplified and, in turn, how unstable electrons are. If $\gamma > 0$, the wave is amplified and the electrons are unstable, and if $\gamma < 0$, the wave is dampened and the electrons are stable. For the sake of clarity, I will not treat the absorption of waves by the plasma.

The expression of the growth rate depends on the propagation modes and is obtained from **the wave dispersion relation**. The latter is derived from the equations governing the dynamics of a plasma: the Maxwell (Equation 2.7) and Vlasov (Equation 2.8) equations.

These equations describe a dilute plasma where the collisions of the particles are neglected, which is adapted for magnetospheres.

$$\vec{\nabla}\cdot\vec{\mathbf{E}} = \frac{n}{\epsilon_0} \tag{2.7a}$$

$$\vec{\nabla}\cdot\vec{\mathbf{B}} = 0 \tag{2.7b}$$

$$\vec{\nabla}\times\vec{\mathbf{E}} = \frac{\partial\vec{\mathbf{B}}}{\partial t} \tag{2.7c}$$

$$\vec{\nabla}\times\vec{\mathbf{B}} = \frac{1}{\epsilon_0 c^2}\left(\vec{\mathbf{j}} + \epsilon_0\frac{\partial\vec{\mathbf{E}}}{\partial t}\right) \tag{2.7d}$$

$$\frac{\partial\mathscr{F}_\alpha}{\partial t} + \vec{\mathbf{v}}\cdot\vec{\nabla}\mathscr{F}_\alpha + \frac{q_\alpha}{m_\alpha}\left(\vec{\mathbf{E}} + \vec{\mathbf{v}}\times\vec{\mathbf{B}}\right)\cdot\vec{\nabla}_{\vec{\mathbf{v}}}\mathscr{F}_\alpha = 0 \tag{2.8}$$

where $\vec{\mathbf{E}}$ is the electric field, $\mathscr{F}_\alpha$ is the distribution function normalized in the $\vec{\mathbf{u}} = \Gamma\vec{\mathbf{v}}$ space, $\vec{\nabla}_{\vec{\mathbf{u}}} = \dfrac{\partial}{\partial\vec{\mathbf{u}}}$ is the gradient in velocity space, $n_\alpha = \int du^3\mathscr{F}_\alpha$ the density, $\vec{\mathbf{j}_\alpha} = \int du^3\vec{\mathbf{v}}\mathscr{F}_\alpha$ the current density, where the α subscript designate the different species ($\alpha = i$ for ions and $\alpha = e$ for electrons) of the plasma.

Note that in the rest of the thesis, F_α, the distribution function normalized in $\vec{\mathbf{v}}$ phase space, is used with $n_\alpha = \int dv^3 F_\alpha$.

2.3.2. Cold plasma modes

By linearizing these equations, in the case of a non-collisional homogeneous magnetized plasma, we can obtain the dispersion relation in the tensor form shown in Equation 2.9. In the case of a cold, therefore non-relativistic plasma, this relation dispersion simplifies into the Altar-Appleton-Hartree dispersion relation 2.10 (Appleton 1932).

$$D = \left|(1-N^2)\overleftrightarrow{\mathbf{1}} + \vec{\mathbf{N}}\otimes\vec{\mathbf{N}} + \frac{\overleftrightarrow{\boldsymbol{\sigma}}(\omega,\vec{\mathbf{k}})}{i\omega\epsilon_0}\right| = 0 \tag{2.9}$$

where $\vec{\mathbf{N}}$ is the refraction index, $\overleftrightarrow{\mathbf{1}}$ the unit tensor, $\otimes$ the tensor product, $\overleftrightarrow{\boldsymbol{\sigma}}$ the conductivity tensor whose expression is given in Appendix A.

$$N^2 = \left(\frac{kc}{\omega}\right)^2 = 1 - \frac{2X(1-X)}{2(1-X) - Y_\perp^2 \pm \sqrt{Y_\perp^4 + 4Y_\parallel^2(1-X)^2}} \tag{2.10}$$

with

$$X = \frac{\omega_{pe}^2}{\omega^2} \text{ and } Y_\perp = \frac{\omega_{ce}}{\omega}\sin\left(\theta_{(\vec{\mathbf{k}},\vec{\mathbf{B}})}\right) \text{ and } Y_\perp = \frac{\omega_{ce}}{\omega}\cos\left(\theta_{(\vec{\mathbf{k}},\vec{\mathbf{B}})}\right)$$

From this equation, 5 regions can be delimited corresponding to 5 modes (illustrated in Figure 2.2):

- The RX mode (in blue) has a right-handed polarization and has $f_X = f_{ce}/2 + \sqrt{f_{pe}^2 + f_{ce}^2/4}$ as low cutoff frequency. This mode tends toward a high-frequency light wave. This mode is therefore capable of escaping the plasma and propagating in a vacuum.
- The LO mode (in red) has a left-handed polarization and has f_{pe} as a low cutoff frequency. This mode tends toward a high-frequency light wave.
- The Z mode (in green) has a right-handed polarization. This mode is trapped between its low cutoff frequency at the plasma frequency f_{pe} and its high resonance frequency at the upper hybrid frequency $f_{uh} = \sqrt{f_{ce}^2 + f_{pe}^2}$.
- The Left eXtradordinary (LX) mode (in green) has a left-handed polarization and has f_L as a low cutoff frequency and f_{pe} as a high cutoff frequency.
- The "whistler" (in yellow) have f_{pe} as high cutoff frequency.

Only RX-mode and LO-mode can propagate in the void and escape the plasma, but I will only focus on the RX-mode in the rest of this work as it was shown to be dominant by 1–2 orders of magnitude (Louarn and Le Quéau 1996). This corroborates the observed weaker LO-mode for Jovian radio auroral emissions.

Note that the RX cutoff frequency f_X reduces to $f_X = f_{ce} + \frac{1}{2}\frac{f_{pe}^2}{f_{ce}^2}$ for $\frac{f_{pe}}{f_{ce}} \ll 1$. So in the depleted plasma, this cutoff is close but above f_{ce}.

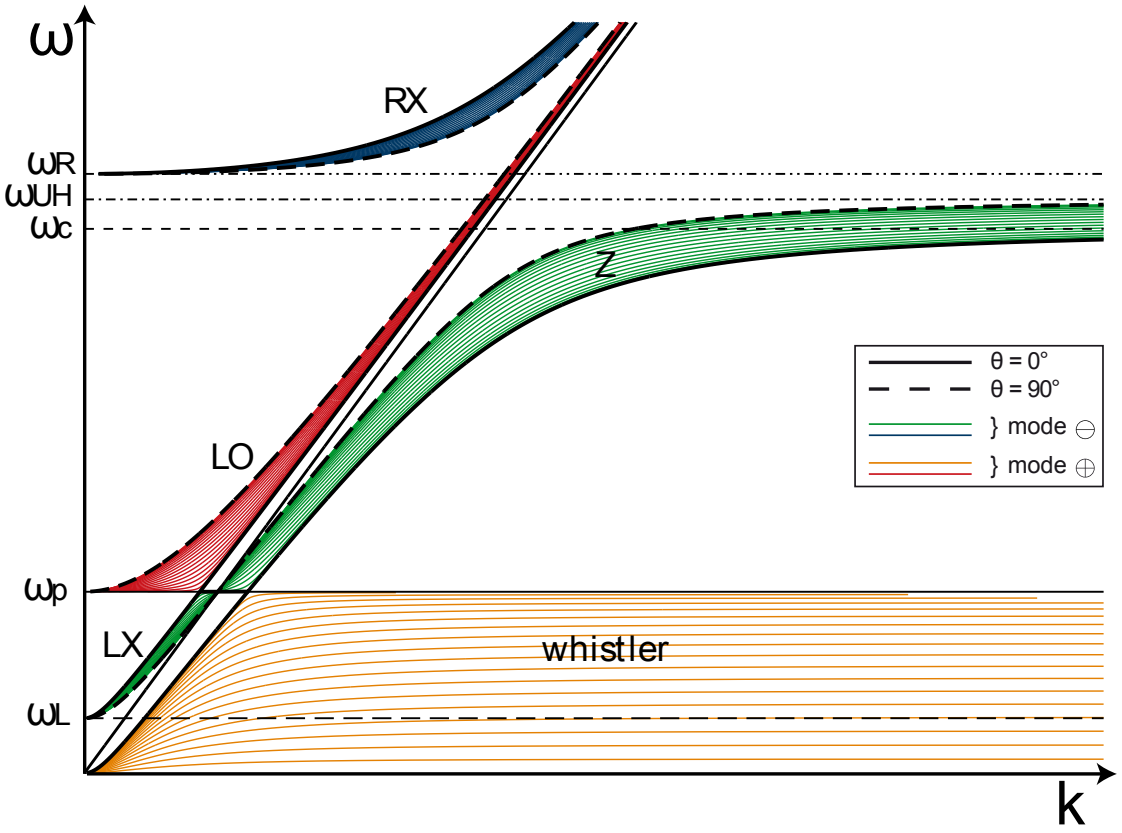


Figure 2.2.: Diagram of the different modes obtained from the Altar-Appleton-Hartree relation. The dispersion curves in parallel propagation are represented by thick black solid lines, those in perpendicular propagation by thick black dashed lines. The dispersion curves in oblique propagation for different $\theta_{(\vec{\mathbf{k}},\vec{\mathbf{B}})}$ are represented by thin colored lines. The cutoff and resonance frequencies are represented, respectively, by thin solid lines for plasma cutoff, thin wide dashed lines for L-mode cutoff, double dotted lines for R-mode cutoff, thin dashed lines for cyclotron resonance, and thin dotted lines for upper hybrid resonance. Credit: Gautier (2013)

Note that for $\frac{f_{pe}}{f_{ce}} \ll 1$, $f \simeq f_{ce}$ and $\theta_{(\vec{\mathbf{k}},\vec{\mathbf{B}})} \sim 90°$ we can obtain a RX-mode cold expression of the refractive index given in Equation 2.11.

$$N^2_{cold} = 1 - \frac{\frac{\omega^2_{pc}}{\omega^2_{ce}} \sin^2(\theta_{(\vec{\mathbf{k}},\vec{\mathbf{B}})})}{2\Delta\omega(\Delta\omega + 1)} \tag{2.11}$$

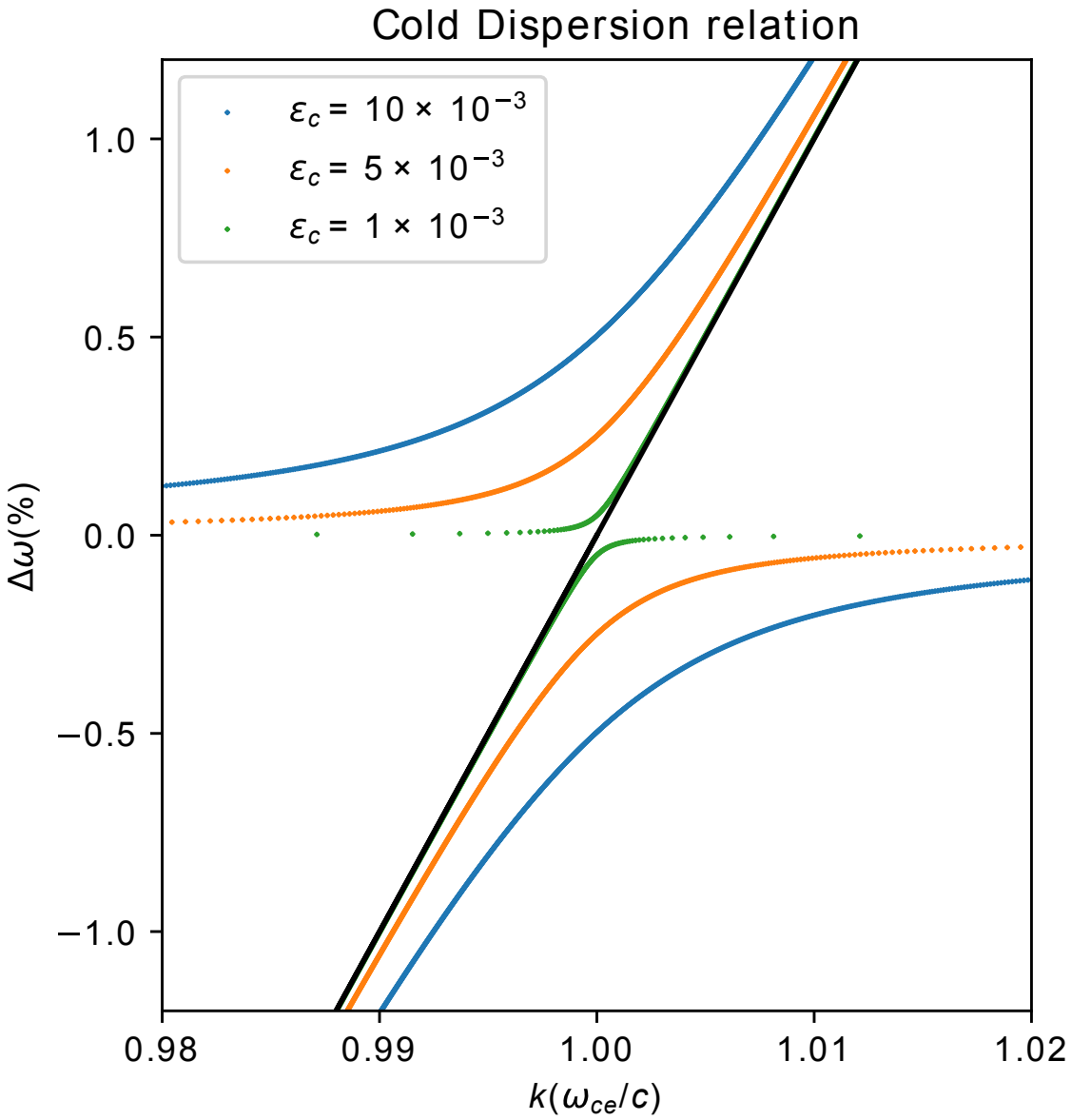


Figure 2.3.: Dispersion relation for $k_{\parallel} = 0$ in a cold highly-magnetized plasma for different values of $\epsilon_c = \frac{f_{pe}}{f_{ce}}$

This simplified cold plasma dispersion relation is illustrated in Figure 2.3. N_{cold} gives the 2 usual cold plasma modes: the RX-mode for $f > f_{ce}$, which can escape the plasma, and the trapped Z mode for $f < f_{ce}$.

2.3.3. Dispersion relation in the case of CMI

In the case of CMI, the relativistic effects must be taken into account not only for the resonance equation but also for the dispersion relation. In the CMI conditions, two modes are obtained bearing similarities to the cold plasma RX and LO modes, so the

RX-mode and LO-mode designations are retained. The dispersion relation obtained for X-mode is given in Equation 2.12.

$$D = 1 - N^2 + (1 - N_\perp^2/2) J(\omega, \vec{\mathbf{k}}) = 0 \tag{2.12}$$

where $J(\omega, \vec{\mathbf{k}})$ is a current term which describes the influence of the plasma on the wave. Its expression depends on assumptions that will be described in the next sections.

(2.13)

Numerical and analytical solving of this dispersion relation showed that the cutoff of this mode is shifted below f_{ce} in the presence of a hot relativistic plasma (Wong et al. 1982; Pritchett 1984). The shifted cutoff frequency was evaluated at $f_x \simeq f_{ce}(1 + \frac{1}{2}\frac{f_{pe}^2}{f_{ce}^2} - \frac{1}{2}\frac{v_r^2}{c^2})^{\frac{1}{2}}$ in the case of a ring characterized by v_r (see also Section 2.5.1). This result is consistent with the anterior observations of AKR and SKR emitted on the RX-mode below the local f_{ce}.

2.3.4. Growth rates in the semi-relativistic approach

The most common approach to *treat* Cyclotron Maser Instability is to suppose the plasma is homogeneously composed of a cold stable component and a hot semi-relativistic unstable component. The current term J thus separates into J_c and J_h to account for the contribution to the current of both populations (Le Quéau et al. 1984).

2.3.4.1. Hot plasma assumption

In the first derivations of the growth rate by Wu and Lee (1979), the contribution of the cold plasma was neglected. The expression of J_h is given by:

$$J_h = -\pi \frac{\omega_{ph}^2}{\omega^2} \frac{1}{n_e} \int dv_\perp dv_\parallel v_\perp^2 \frac{(\omega - k_\parallel v_\parallel)\frac{\partial F_e}{\partial v_\perp} + k_\parallel v_\perp \frac{\partial F_e}{\partial v_\parallel}}{\omega - k_\parallel v_\parallel - \omega_{ce}/\Gamma} \tag{2.14}$$

with ω_{ph} the plasma frequency of the hot electrons and F_e the EDF normalized in $\vec{\mathbf{v}}$ space

In the semi-relativistic approximation ($\Gamma^{-1} \simeq 1 - \frac{v^2}{c^2}$), Plemelj formula (Equation 2.15) allows the simplification of this expression into Equation 2.16a.

$$\int_{-\infty}^{+\infty} \frac{f(x)}{x - x_0} dx = \text{P.V.} \int_{-\infty}^{+\infty} dx \frac{f(x)}{x - x_0} + i\pi \int_{-\infty}^{+\infty} dx f(x) \delta(x - x_0) \tag{2.15}$$

with P.V. the Cauchy principal value obtained from Plemelj's formula.

I obtain

$$J_h = i\pi^2 \frac{\omega_{ph}^2}{\omega_{ce}^2} \frac{1}{n_e} \int_0^\pi d\phi c^2 v_r^2 \sin^2\phi \frac{\partial F_e}{\partial v_\perp} + \mathrm{Re}(J_h) \tag{2.16a}$$

where the integral is computed over a resonance circle ($v_0 = c\beta_0, v_r = cr$)
and $\mathrm{Re}(J_h)$ designates the real part of J_h which can be expressed as

$$\mathrm{Re}(J_h) = -\pi \frac{\omega_{ph}^2}{\omega_{ce}} c^2 \frac{1}{n_e} \mathrm{P.V.} \int dv d\theta \frac{v^3 \sin^2\theta}{v^2 - v_r^2} \frac{\partial F_e}{\partial v_\perp} \tag{2.16b}$$

Note that J_h depends on the distribution type of hot electrons (see Section 2.4).

For the sake of simplicity, Wu and Lee (1979) supposed perpendicular propagation with $\frac{k^2c^2}{\omega_{ce}} = 1$ and $\Delta\omega \ll 1$ so that N^2 was expressed as $N^2 = 1 - 2\Delta\omega$. In these assumptions, $\mathrm{Re}(J_h)$ is a negligible quantity.

From these simple assumptions, Wu and Lee (1979) obtained the RX-mode **hot plasma** expression of the growth rate:

Hot plasma expression of the growth rate

$$\gamma_{hot} = \frac{\omega_i}{\omega_{ce}} = \left(\frac{\pi c \omega_{ph}/\omega_{ce}}{2}\right)^2 \frac{1}{n_e} \int_0^\pi d\phi c^2 v_r^2 \sin^2\phi \frac{\partial F_e}{\partial v_\perp} \tag{2.17}$$

This expression has been used at Earth for numerous papers and at Saturn by Mutel et al. (2010).

2.3.4.2. Effect of a Cold plasma population

To include the effect of a cold stable population, Le Quéau et al. (1984) introduced J_c. In the CMI approximations, this cold term simplifies into (Bekefi 1969):

$$J_c = \frac{\omega_{pc}^2}{\omega(\omega - \omega_{ce})} \tag{2.18}$$

with ω_{pc} the plasma frequency of the cold electrons.

Similarly to the treatment of the hot plasma approximation, they supposed $\mathrm{Re}\{J_h\}$ to be a small quantity that can be neglected with respect to J_c. However, they supposed $N^2 = 1$ instead of $N^2 \simeq 1 + 2\Delta\omega$. The obtained dispersion relation writes:

$$D = \frac{1}{2}(J_c + i\,\mathrm{Im}(J_h)) = 0 \tag{2.19}$$

The RX-mode **cold plasma** expression of the growth rate (Equation 2.21) was then

derived from Equation 2.20 which assumes $\gamma \ll \frac{\omega}{\omega_{ce}}$.

$$\omega_i = -\left.\frac{\mathrm{Im}(D)}{\frac{\partial \mathrm{Re}(D)}{\partial \omega}}\right|_{\omega_i=0} \tag{2.20}$$

This expression was used on in situ measurements in Louarn et al. (2017, 2018) and Louis et al. (2020)

Cold plasma expression of the growth rate

$$\gamma_{cold} = \frac{\omega_i}{\omega_{ce}} = \left(\pi \frac{\omega_{ph}}{\omega_{pc}} \Delta\omega\right)^2 c^2 \frac{1}{n_e} \int_0^\pi d\phi c^2 v_r^2 \sin^2\phi \frac{\partial F_e}{\partial v_\perp} \tag{2.21}$$

To determine a generalized expression of the RX-mode growth rate that would be applicable to a regime dominated either by hot or cold plasma, I assembled both hypotheses used to obtain Equation 2.17 and Equation 2.21. The resulting dispersion relation is expressed in Equation 2.22a [a]:

$$D = 2\Delta\omega + \frac{1}{2} J_c + \frac{1}{2} i\,\mathrm{Im}\{J_h\} = 0 \tag{2.22a}$$

which can be used to obtain:

$$\frac{\partial \mathrm{Re}(D)}{\partial \omega} = \frac{2}{\omega_{ce}} + \frac{1}{2\omega_{ce}} \frac{\omega_{pc}/\omega_{ce}^2}{\delta\omega^2} \tag{2.22b}$$

The resulting growth rate writes:

New **expression of the growth rate**

$$\gamma = \frac{\omega_i}{\omega_{ce}} = \frac{\left(\frac{\pi\omega_{ph}/\omega_{ce}}{2}\right)^2}{1 + \left(\frac{\omega_{pc}/\omega_{ce}}{2\Delta\omega}\right)^2} c^2 \frac{1}{n_e} \int_0^\pi d\phi v_r^2 \sin^2\phi \frac{\partial F_e}{\partial v_\perp} \tag{2.23}$$

2.3.4.3. Properties of the expressions of the growth rate

All these expressions of the growth rate are proportional to an integral along a resonance circle of $\frac{\partial F_e}{\partial v_\perp}$. The growth rate is positive only if the integral intercepts positive gradients, illustrating the required inversion population characterized by a $\frac{\partial F_e}{\partial v_\perp} > 0$ region that can be intercepted by a resonance curve.

[a] I obtained the same expression in Collet et al. (2023) by wrongly assuming $\frac{\partial k}{\partial \omega} = 0$. This mistake had no repercussions on the rest of my work.

Also, this integral is weighted by $\sin^2(\theta)$, implying a more important contribution from the circle portion where $v_\perp$ is large.

From this new expression, the cold expression of the growth rate (Equation 2.21) can be retrieved for $\Delta\omega \ll \frac{\omega_{pc}}{2\omega_{ce}}$ and the hot expression of the growth rate for $\Delta\omega \gg \frac{\omega_{pc}}{2\omega_{ce}}$.

The comparison of these different formulae is discussed in the next subsection and Appendix D.

In some expressions used in the literature (like the one from Mutel et al. 2010), the $k_\parallel v_\perp \frac{\partial F_e}{\partial v_\parallel}$ term in Equation 2.14 is not neglected with respect to the $\omega \frac{\partial F_e}{\partial v_\perp}$ term. I checked in a case study (Appendix B) that this term does not have a significant influence on the growth rate.

2.3.5. CMI applicability to Jupiter

The applicability of the CMI for Jovian auroral radio emissions has been discussed early by Zarka (1998), Galopeau et al. (2004), Treumann (2006), Hess et al. (2007, 2008, 2009, 2010), Mottez et al. (2010), and Louarn (1992) and refs therein. I will compare below the CMI conditions with the Jovian auroral regions.

2.3.5.1. Hot or cold plasma assumption

As shown in Section 2.3.4, the expression of the RX mode CMI growth rate depends strongly on the inclusion of the cold plasma in the relation dispersion. While Equation 2.21 appears to be more precise than Equation 2.17 since it takes into account the effect of the cold plasma, Pritchett (1984, 1986) demonstrated through numerical simulations that in the case of AKR radio sources where the plasma is predominantly composed of a hot population (Delory et al. 1998), the cold-plasma theory is a poor approximation to describe the CMI wave growth. In these works, the authors numerically computed the growth rate without any assumption on the temperature of the plasma. They showed that these growth rates were larger than those obtained with the cold plasma assumption. In particular, they showed that the $\Delta\omega$ dependence of γ is simply diminished by 30% when $\frac{n_h}{n_{tot}} = 0.50$ and 40% for $\frac{n_h}{n_{tot}} = 0.10$ with Equation 2.17. In the Jovian auroral radio source regions (see Chapters 4 and 5), I have shown that the $\frac{n_h}{n_{tot}}$ lies between 0.6 and 0.9, confirming the prominence of the hot electron population and the invalidity of the cold plasma expression of the growth rate in these regions. The expression I developed (Equation 2.23) allows for transition between the hot and cold plasma assumptions.

Fully taking into account the hot plasma relativistic correction requires numerically computing J_h without Plemelj's formula by using an analytical model of the hot EDF. This was done by Pritchett (1984), and I used a similar approach in section 2.5.1. The resulting improvement of the expression of the growth rate would then not be directly applicable to EDF measurements without requiring fitting the measured EDF to a model. An alternative approach, that I did not pursue, would be to analytically express $\mathrm{Re}(J_h)$ as a function of $\frac{\partial F_e}{\partial v_\perp}$ or to compute it numerically.

As shown in the case study of Appendix D (and since $\frac{\omega_{pc}}{\omega_{ce}}\frac{1}{2\Delta\omega}$ rarely exceeds 1 in HOM/DAM radio sources), the use of Equation 2.23 is equivalent to the use of the hot plasma approximation(Equation 2.17) in regions where $\frac{n_h}{n_{tot}}$ is large. Moreover, in Appendix D, I showed that the cold plasma expression (Equation 2.21) overestimates the growth rates at large $\Delta\omega$ in hot plasma regions, which in the case of a perfect loss cone leads to unphysically high growth rates at large $\Delta\omega$.

2.3.5.2. Semi-relativistic approximation

From the properties of X-ray aurorae at Jupiter, electrons up to a few MeV were predicted to precipitate at Jupiter. Thanks to Juno, these precipitating electrons were indeed detected in situ, and the dominance of electrons of hundreds keV in regions connected to the main auroral emissions was established (Allegrini et al. 2017; Mauk et al. 2018). However, the first HOM and Ganymede-DAM sources Juno crossed were reported to have unstable electrons of only a few keV, the same range as the unstable electrons seen at Earth and Saturn. Thus confirming the use of the semi-relativistic approximation, at least for these cases.

2.3.5.3. f_{pe}/f_{ce} range

The remotely observed elliptical polarization of DAM and pre-Juno magnetic field and plasma density models suggested that $\frac{f_{pe}}{f_{ce}}$ values as low as 10^{-3} in the auroral regions (Barrow and Morrow 1968; Mottez et al. 2010).

The first Jovian source crossings by Juno reported in Louarn et al. (2017, 2018) confirmed the electrons of a few keV can generate HOM in a highly magnetized plasma with $\frac{f_{pe}}{f_{ce}} = 10^{-3} - 10^{-2}$.

In the next chapters, I detail the plasma conditions of the radio sources I identified and the energy of the unstable populations.

2.4. CMI-unstable electrons

As the different expressions of the growth rate showed, the amplification of waves by the CMI requires regions $\frac{\partial F_e}{\partial v_\perp} > 0$ that would be intercepted by a resonance circle. In this section, I will describe the types of unstable distribution functions that are commonly observed in the auroral regions of planetary magnetospheres.

To describe such unstable EDFs, I introduce the pitch angle θ such that $v_\parallel = v\cos(\theta), v_\perp = v\sin(\theta)$. Hereafter, electrons at "large pitch angles" designate electrons with a velocity in the quasi-perpendicular direction to the magnetic field, while electrons at "low pitch angles" designate those quasi-(anti-)parallel. It is important to mention that in the northern hemisphere, downward electrons have $v_\parallel < 0$ and upward electrons have $v_\parallel > 0$, and inversely in the southern hemisphere.

2.4.1. Useful formulae to characterize a resonance circle

To characterize the unstable population, it is useful to retrieve the characteristic energy E_{chara} and pitch angle θ_{chara} associated with a resonance curve. For non-centered resonance circles, these quantities are defined from the intersection between the resonance circle and its tangent that passes through the origin, namely where $\frac{\partial F_e}{\partial v_\perp}$ maximizes along the resonance circle (Hess et al. 2008).

The calculation in the case of a resonance circle was explicited in Hess et al. (2008), I demonstrated the expressions of v_{chara} and θ_{chara} in the case of an ellipse in Appendix C.

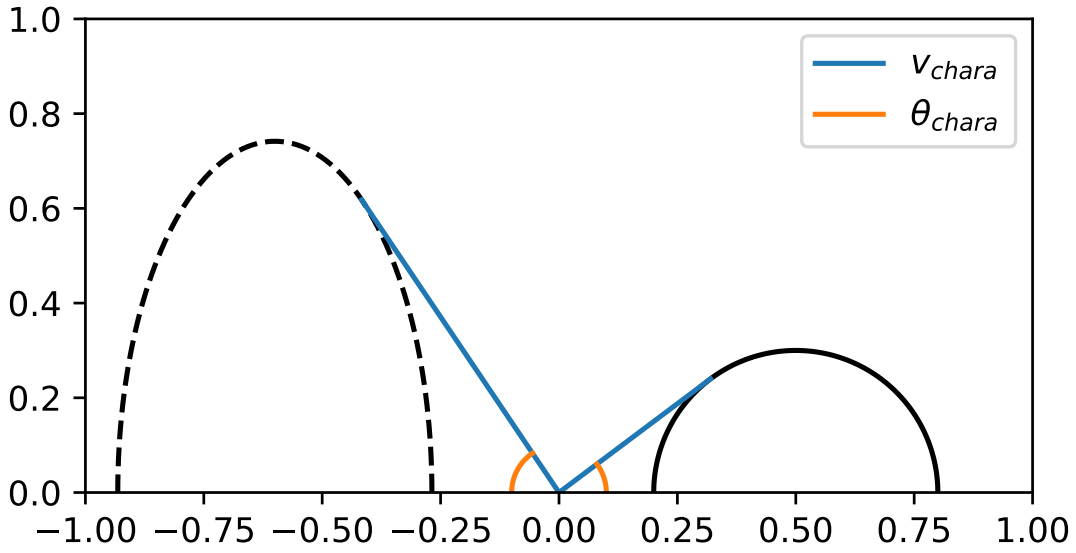


Figure 2.4.: Illustration of v_chara and θ_{chara} associated with a resonance ellipse and a resonance circle.

In the fully relativistic case (ellipse)

$$\frac{v_{chara}^2}{c^2} = \left| \frac{\beta_{0e}^2}{(1-r_\perp^2)^2} - \frac{r_\perp^2}{1-r_\perp^2} \right| \qquad = |1-\delta\omega^{-2}| \tag{2.24a}$$

$$\sin^2\theta_{chara} = \frac{r_\perp^2}{\beta_{0e}^2}(1-r_\perp^2) \qquad = 1 - \frac{\delta\omega^2-1}{\overline{k_\parallel}^2} = 1 - \frac{(\omega-\omega_{ce})(\omega+\omega_{ce})}{k_\parallel^2 c^2} \tag{2.24b}$$

In the semi-relativistic case (circle)

$$\frac{v_{chara}^2}{c^2} = |\beta_0^2 - r^2| \qquad = 2|\Delta\omega| \tag{2.24c}$$

$$\sin^2(\theta_{Chara}) = \frac{r^2}{\beta_0^2} \qquad = 1 - \frac{2\Delta\omega}{\overline{k_\parallel}^2} = 1 - \frac{2\omega_{ce}(\omega - \omega_{ce})}{k_\parallel^2 c^2} \tag{2.24d}$$

(2.24e)

Note here that θ_{chara} and v_{chara} are only defined for resonance curves amplifying waves with $\Delta\omega > 0$ (cf Section 2.2).

In the case of resonance circles centered on 0, v_{chara} can be extended as the radius of the circle, and θ_{chara} can be taken as 90°.

2.4.2. Loss Cone EDF

The Loss cone EDF was identified as a possible source of free energy for CMI by Wu and Lee (1979). This type of EDF is CMI unstable because it displays a depletion in a cone in the upward (anti-planetward) direction due to the loss of electrons in the atmosphere. Indeed, for a non-uniform magnetic field, such as along the magnetic field lines of a magnetosphere, electrons propagating toward increasing value of B (downward here) are reflected at their *mirror point* where $B = B_{max}$ (B_{max} depends on the initial velocity and pitch angle of electrons, the magnetic field model and the assumed loss altitude). In the case of a magnetosphere, electrons whose mirror point is below the ionosphere are then lost by collisions.

The angle of this cone θ_{LC} is defined by Equation 2.25.

$$sin^2(\theta_{LC}) = \frac{B}{B_{max}}(1 - \frac{e\Delta\phi}{E}) \tag{2.25}$$

where B and $E = \frac{m_e v^2}{2}$ are the local magnetic field amplitude and energy. $\Delta\phi = \phi - \phi_m$ accounts for any electric potential difference between the atmosphere and the observation point and was neglected. I used JRM33+CON20 as a model for the magnetic field and assumed all electrons to be lost below 300 km above the 1 bar level. These resonance circles intercepting the unstable loss cone have $\theta_{chara} \sim \theta_{LC}$.

This distribution is illustrated by a thermal EDF modified by a loss cone at $\theta = 120°$ in Figure 2.5.

As the unstable electrons are only in the upward direction, the associated CMI resonance circle corresponds to oblique waves emitted above f_{ce}.

This CMI source of free energy was first thought to be the prominent one for AKR, but was later shown not to lead to high enough growth rates. At Jupiter, loss cone was early thought to drive Io-DAM arcs (Hess et al. 2008; Mottez et al. 2010), and was identified in the first HOM sources crossed by Juno (Louarn et al. 2017).

2.4.3. Conics EDF

Conics EDF (see Figure 2.5.b) were first reported at Earth by Menietti and Burch (1985) with the Dynamics Explorer 1 (DE 1) satellite and were then regularly observed by Viking (André and Eliasson 1992; Eliasson et al. 1996) in the auroral regions, but were seldom considered as an efficient driver of the CMI.

They are characterized by an enhancement of the EDF at pitch angles larger than the loss cone so that resonance curves intercepting them have θ_{chara} above θ_{LC}. At Jupiter, Louarn et al. (2018) identified conics (in both the upward and downward directions) as efficient drivers of the CMI coincidently with the loss cone. Such conics are regularly observed by Juno outside radio sources (Muñoz et al. 2022).

Conics are thought to be generated from wave-particle interactions, most notably by Alfvén waves (Louarn et al. 2018) and low frequency electric field fluctuations (André and Eliasson 1992).

2.4.4. Shell EDF

Shell type EDF were then first proposed by Pritchett (1984) as a source of free energy for the CMI. They were later observed in the terrestrial auroral regions and showed that they, rather than the loss cone, form the main CMI source of free energy, able to account for the observed AKR intensity (Roux et al. 1993; Louarn and Le Quéau 1996). Such distributions appear after an electron beam has formed (often by parallel potentials) and evolved adiabatically along the flux tube. While doing so, the electrons are scattered to larger pitch angles, thus forming a shell in the $(v_\parallel, v_\perp)$ phase space (see Fig. 2.5.c). If the particles are accelerated near the ionosphere, the pitch angle scattering due to adiabatic motion covers only a limited range of pitch angle. In this case, when the particles are reflected and the loss cone is created, the distribution obtained is a ring in velocity space.

This source of free energy is particularly CMI unstable as the resonance circle fitting the inner shell boundary continuously matches positive gradients.

Since the resonance circle along a shell has its center at the origin, this type of unstable population thus generates waves perpendicularly to $\vec{\mathbf{B}}$ below f_{ce}.

Extrapolating the Earth's example, shell EDF were expected to drive auroral radio emissions of Jupiter (Ergun et al. 2000) and Saturn, where they have indeed been observed to locally drive SKR with 6-12 keV shell-type electrons (Mutel et al. 2010).

2.4.5. Trapped electrons

The trapped electrons have been identified by Louarn et al. (1990) as a source of free energy for AKR. These EDF show positive gradients on a broad range of $v_\parallel$ close to $v_\parallel = 0$. As so, they should be intercepted by centered resonance circles. In this paper, Louarn et al. (1990) also showed that this trapped electron amplification occurred simultaneously with loss cone amplification, but that the former was more efficient.

These trapped electrons are generated by varying parallel electric fields. They were not identified as a source of free energy outside Earth.

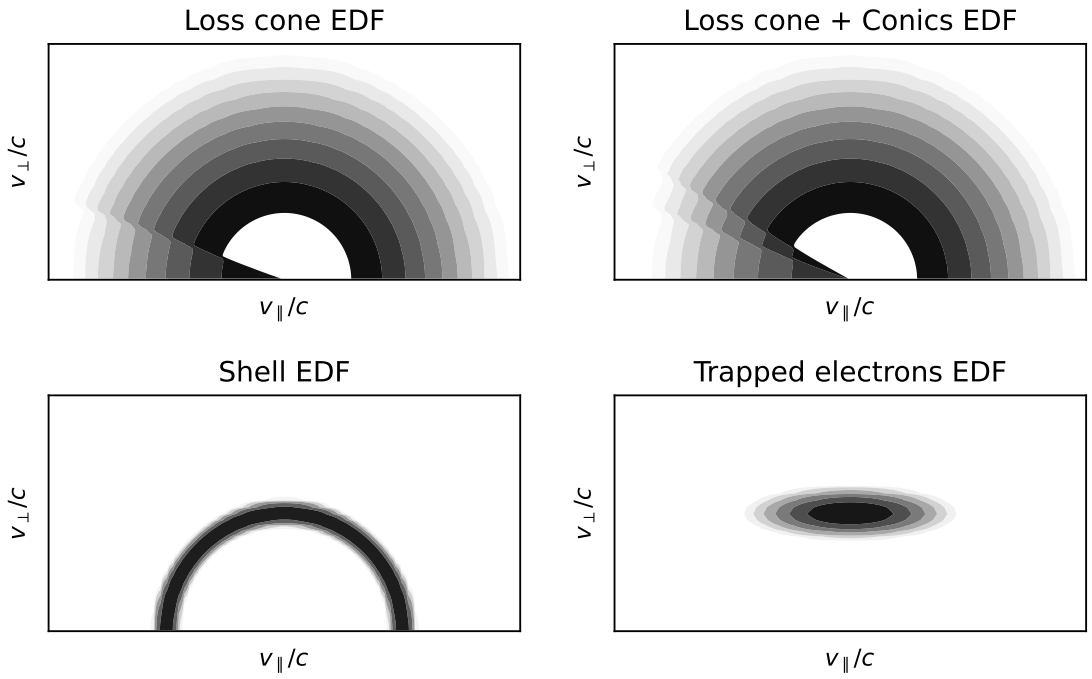


Figure 2.5.: Illustration of the different unstable distribution functions

In a given EDF measurement, different parts of the distribution can be simultaneously CMI unstable, yielding different growth rates from different resonance circles. For instance, shell-type EDF are observed simultaneously with the thermal population cut by the loss cone.

2.5. Wave intensity

Now that I presented different expressions of the growth rate and which types of EDFs can lead to positive growth rates, it is useful to remind how to use these to determine the final wave intensity S (in $\mathrm{W \cdot m^{-2} \cdot Hz^{-1}}$), a key observable to be compared to the radio wave intensity measured by Waves within any source region

S can be expressed as $S = G\, S_0$ with S_0 the amplitude of source radio waves and G the gain factor associated with the wave growth. The expression of G can be written as (Mutel et al. 2010):

$$G = \exp\left(\frac{4\pi f_{ce} \gamma L_c}{v_g}\right) \tag{2.26}$$

where L_c is the convective length along which the wave grows and v_g is the RX-mode wave group velocity.

A fair estimate of L_c is provided by the length of the crossed radio source.

The choice of S_0 and v_g is further discussed below.

For the sake of simplicity, I suppose the source term to be the galactic noise. This noise was estimated from radio measurements in Dulk et al. (2001) on the range of frequencies where Jovian radio emissions are emitted. I then used the values shown in Figure 2.6 to estimate the source term to compute the intensity.

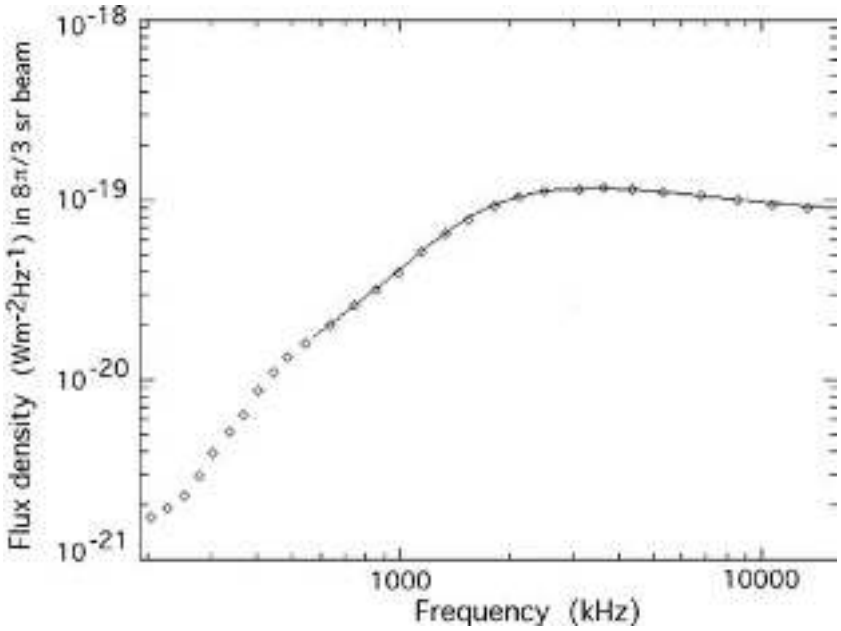


Figure 2.6.: Galactic low-frequency model radio spectrum derived from Dulk et al. (2001) (continuous line) and Manning and Dulk (2001) (diamonds). Figure from Zarka (2004).

An alternate approach to estimate S_0 proposed by Zarka et al. (1986) consists of estimating, with quasi-linear analytical calculation, the source term from the bulk incoherent noise resulting from the local motion of electrons.

2.5.1. Group Velocity

In the literature, the group velocity is often assumed to be constant, with values generally equal to c or $0.1c$. This quantity is nonetheless essential to the determination of S. Hereafter, I remind how it can be retrieved from the dispersion equation with various assumptions. Equation 2.27 defines v_g from N.

$$v_g = \frac{\partial \omega}{\partial k} \simeq c \left(\frac{\partial N \omega}{\partial \omega} \right)^{-1} \tag{2.27}$$

In this section, the approach is different from the one of Section 2.3.4. In that section, I derived expressions of J_h for a general EDF so that the obtained quantities could be computed with measured EDF, whereas in this section, I compute J_h by using analytical models of unstable EDF.

2.5.1.1. Group velocity in a cold plasma

The simplest hypothesis is to suppose the RX-mode wave freely propagates: $N \simeq 1$, and therefore $v_g = c$.

A more precise way to obtain v_g is to suppose that the plasma is dominated by a cold plasma. Thus, N can be retrieved from the Altar-Appleton-Hartree relation (Equation 2.10) and gives Equation 2.11 (recalled below).

$$N^2_{cold} = 1 - \frac{\frac{\omega^2_{pc}}{\omega^2_{ce}} \sin^2(\theta_{(\vec{\mathbf{k}},\vec{\mathbf{B}})})}{2\Delta\omega(\Delta\omega + 1)}$$

From this expression of N_{cold}, I can thus derive v_g. Figure 2.7 illustrates that the dependence of v_g on $\frac{\omega_{pc}}{\omega_{ce}}$ and $\Delta\omega$ for $\theta_{(\vec{\mathbf{k}},\vec{\mathbf{B}})} = 90°$. v_g additionally depends on the angle of propagation $\theta_{(\vec{\mathbf{k}},\vec{\mathbf{B}})}$, and Equation 2.11 shows that its influence consists of reducing the value of $\frac{\omega_{pc}}{\omega_{ce}}$ by a factor of $\sin^2(\theta)$.

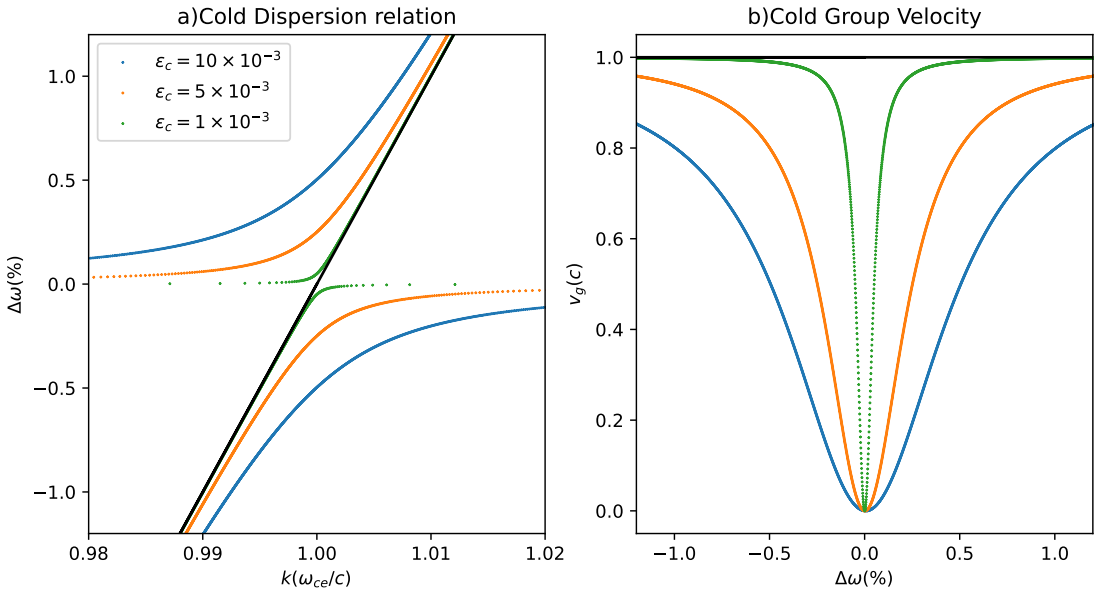


Figure 2.7.: a) Dispersion relation and Group velocity for $k_\parallel = 0$ in a cold highly-magnetized plasma for different values of $\frac{\omega_{pe}}{\omega_{ce}}$

For instance $\frac{\omega_{pc}}{\omega_{ce}} = 10^{-2}$, at$\Delta\omega = 0.5\%$, $v_g \simeq 0.5c$, whereas for $\frac{\omega_{pc}}{2\omega_{ce}} = 10^{-3}$, $v_g \simeq c$. The approximation $v_g \simeq c$ is therefore only verified for a cold plasma where $\frac{\omega_{pe}}{\omega_{ce}}$ is particularly small.

2.5.1.2. Group velocity in a hot plasma

To consider how v_g is affected by assuming that the source region is dominated by a hot plasma, I used the analytical approach described in Le Queau and Louarn (1989) to obtain N for $k_\parallel = 0$. At the time of the paper, loss cone was still considered the main source of energy at Earth, and shell was not studied. In the next paragraphs, I summarize the results they obtained and complete them by using EDF models to account for shell-type EDF.

This work uses the dispersion relation given by Equation 2.12 with $k_\parallel = 0$ and the semi-relativistic approximation. The dispersion relation can then be expressed as Equation 2.28a. The derivation of this relation thus requires computing J_h (Equation 2.28b) for a model of the EDF.

$$-\frac{1-N^2}{1-N^2/2} = J_h(\omega, k_\parallel = 0) \tag{2.28a}$$

$$J_h(\omega, k_\parallel = 0) = \pi \left(\frac{\omega_{pe}}{\omega_{ce}}\right)^2 \int v_\perp^2 \, dv_\perp \int dv_\parallel \frac{\partial f}{\partial v_\perp} \frac{1}{\Gamma - \frac{\omega_c}{\omega}} \tag{2.28b}$$

In this approach, ω is assumed to be complex and N to be real. These assumptions thus correspond to the conditions 2.29.

$$\mathrm{Im}(J_h(\omega, k_\parallel = 0)) = 0 \tag{2.29a}$$

$$1 < \mathrm{Re}(J_h(\omega, k_\parallel = 0)) < 2 \tag{2.29b}$$

From these conditions and the derivation of J_h (Equation 2.28b), a relationship between ω and ω_i can be derived and injected into Equation 2.28a to obtain the dispersion relation, which is often too complex to be given in mathematical terms.

In the next paragraphs, I'll derive different expressions of J_h, and since the expression of N can be complex to write, I will only show plots of the dispersion relation obtained numerically.

Idealized Ring Distribution

Le Queau and Louarn (1989) first investigated the case of an idealized ring EDF (Equation 2.30a) to explore the dispersion relation. This expression being a Dirac allows for easy simplification of J_h given in Equation2.30b.

$$F_e(v_\parallel, v_\perp)1 = \frac{\delta(v_\parallel)\delta(v_\perp - v_0)}{2\pi v_0} \tag{2.30a}$$

$$J_h(\omega, k_\parallel = 0) \approx -\left(\frac{\omega_{pe}}{\omega_{ce}}\right)^2 \frac{1}{\delta} \frac{Z}{(1+Z)^2} \tag{2.30b}$$

with $\delta(x)$ the Dirac function, $\delta = \frac{\beta_0^2}{2}$, $Z = \frac{\Delta\omega}{\delta}$

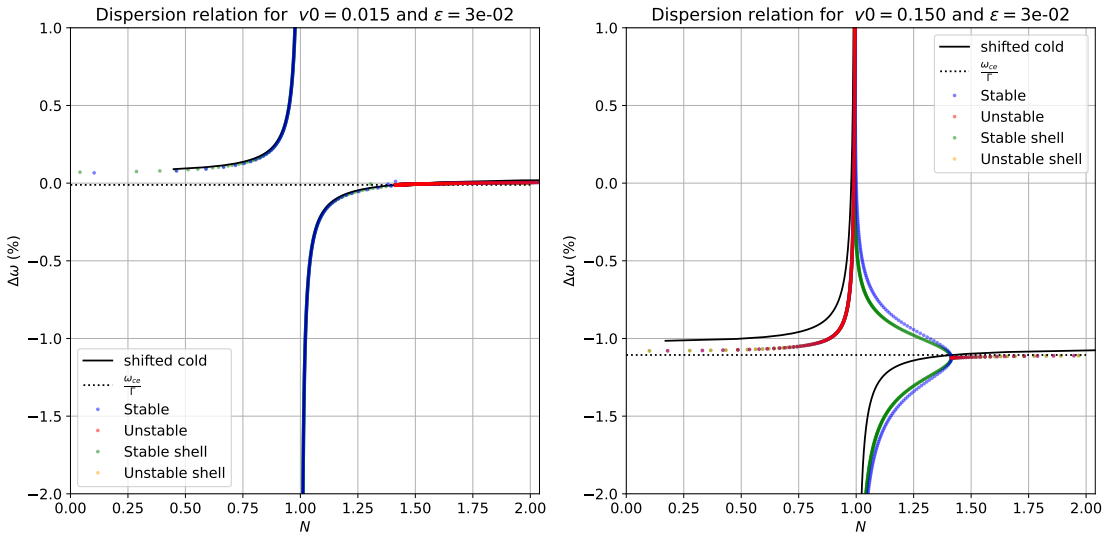
Condition 2.29a yields two relations:

$$\omega_i = 0 \tag{2.31}$$

$$Im(Z)^2 + Re(Z)^2 = 1 \tag{2.32}$$

The obtained expression of J_h (thus the expression of N) strongly depends on the ratio $\frac{\omega_{pe}/\omega_{ce}}{\beta_0}$.

This dispersion relation is shown in Figure 2.8 where the unstable ($\omega_i > 0$) branch is shown in red and the stable ($\omega_i \leq 0$) one in blue. In panel a), the black line represents the cold dispersion, whereas in panel b) this line represents a cold plasma dispersion shifted toward frequencies lower than f_{ce}, where I substituted $\Delta\omega$ by$1 - \frac{\omega}{\omega_{ce}/\Gamma_0 - 1}$ to account for the relativistic electrons.



(a) (b)

Figure 2.8.: Dispersion relation for purely cold or purely hot plasma with $k_\parallel = 0$ for $\frac{\omega_{pe}}{\omega_{ce}} = 3 \times 10^{-2}$ and for either $v_0 = 0.015$ or $v_0 = 0.15$

Panel a shows that the dispersion relation for small $\frac{\omega_{pe}/\omega_{ce}}{\beta_0}$ is reminiscent of the cold plasma X-mode. Panel b) shows that the dispersion relation for large $\frac{\omega_{pe}/\omega_{ce}}{\beta_0}$ exhibits a X-mode shifted at $\frac{f_{ce}}{\Gamma_0}$, an infraluminous ($N > 1$) branch tends to $N = 1$ at high and low frequencies and a branch is seen for large N at $f \lesssim \frac{f_{ce}}{\Gamma_0}$.

As described by Le Queau and Louarn (1989), in a dense or low energy plasma (low $\frac{\omega_{pe}/\omega_{ce}}{\beta_0}$), panel a), only the infraluminous waves ($N > 1$) can be unstable, while in a sparse or high energy plasma, the cutoff is shifted below f_{ce} at f_{ce}/Γ_0. In that case, waves are emitted near this shifted cutoff on a mode connected to a stable $N = 1$ mode at high frequencies.

Idealized Shell Distribution

In order to apply this method to the shell EDF rather than the ring EDF, I derived a dispersion relation for a perfect shell $f(v) = \frac{\delta(v-v_0)}{4\pi v_0^2}$.

$$J_h \approx -\left(\frac{\omega_{pe}}{\omega_{ce}}\right)^2 \frac{1}{\delta} \frac{Z+\frac{1}{3}}{(Z+1)^2} \tag{2.33}$$

$$\omega_i = 0 \tag{2.34a}$$

$$Im(Z)^2 + (Re(Z) + \frac{1}{3})^2 = (\frac{2}{3})^2 \tag{2.34b}$$

The obtained dispersion relations are shown in Figure 2.8 in orange for the unstable branches and in green for the stable branches. For a cold plasma, there are almost no differences between the dispersion relations derived from an idealized ringlike EDF and from a perfect shell EDF. For a hot plasma, the differences are visible only for the stable branch, where the shell-derived dispersion relation is slightly closer to the $\omega = \omega_{ce}/\Gamma_0$ line.

Figure 2.8a shows that this approach allows to retrieve the results obtained in the cold plasma approximation for a ring or shell with a sufficiently low $\frac{\omega_{pe}/\omega_{ce}}{\beta_0}$ (i.e., sufficiently low energy at a fixed $\frac{\omega_{pe}}{\omega_{ce}}$).

Figure 2.8a shows that for a sufficiently hot plasma, the dispersion relation is shifted by a factor Γ_0^{-1}. This also confirms that the presence of hot relativistic electrons shifts the X-mode cutoff frequency below f_{ce}.

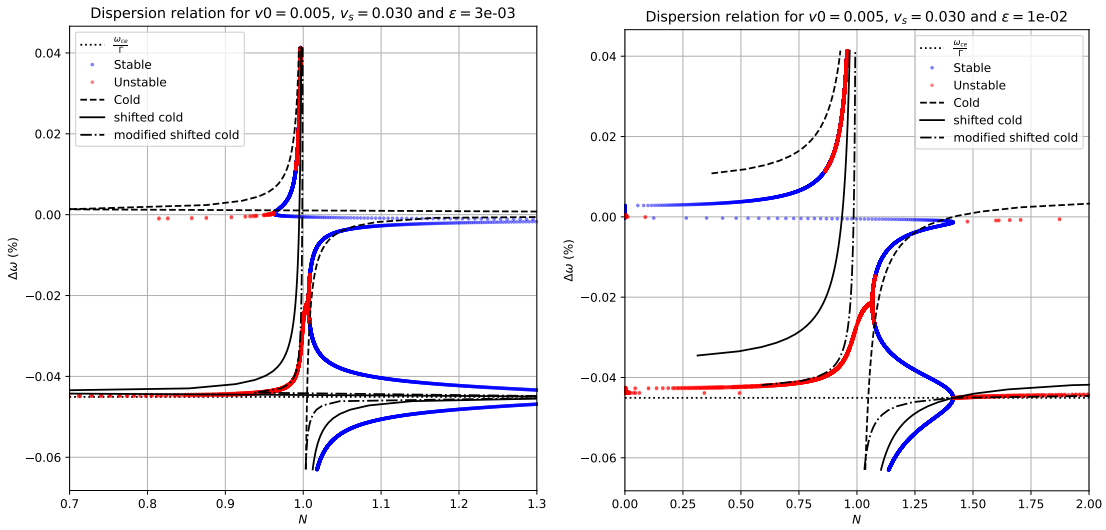
2.5.1.3. Group velocity derived in a plasma with both populations

As mentioned in Section 2.3.1, CMI radio sources are supposed to be composed of a hot and cold population. I modeled this intermediate case with 2 shells, each representing either the cold or hot population represented by Equation 2.35.

$$F_e = \frac{1}{2}\frac{\delta(v-v_{th})}{4\pi v_{th}^2} + \frac{1}{2}\frac{\delta(v-v_r)}{4\pi v_r^2} \tag{2.35}$$

I solved the obtained dispersion relation numerically for the arbitrarily chosen case of $v_r = 0.03c \Rightarrow 239\,\text{eV}$ and $v_{th} = 0.008c \Rightarrow 16\,\text{eV}$, which are sufficiently separated to not yield the same result as in the previous section. While v_r is low compared to the energy of the measured shell at Earth, it is sufficiently high to have a relativistic shift of the dispersion relation.

The obtained dispersion relation can be summarized by the 2 cases $\frac{\omega_{pe}}{\omega_{ce}} = 3\times10^{-3}$ and 1×10^{-2} shown in Figure 2.9.



(a) (b)

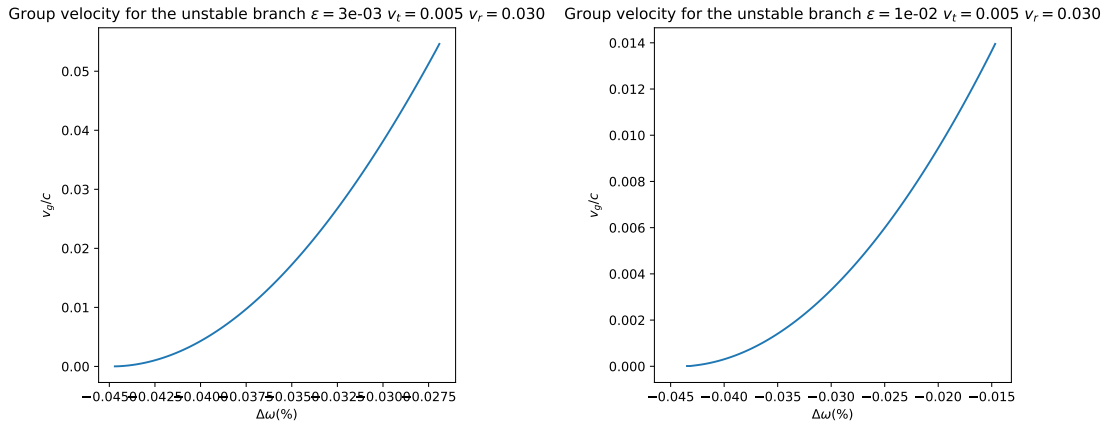
Figure 2.9.: Dispersion relations for a cold and hot plasma population for $\frac{\omega_{pe}}{\omega_{ce}} = 3\times10^{-3}$ and 1×10^{-2}

In both cases, I obtained 4 different branches. For $f > f_{ce}$, I identify a stable mode reminiscent of the cold plasma RX-mode. Between $\simeq f_{ce}/2\Gamma_r$ and f_{ce}, an equivalent to the Z mode is seen. This mode is connected to the RX-mode (and the shifted Z mode) when $\frac{v_{th}}{\omega_{pe}/\omega_{ce}}$ becomes important. Similarly, a shifted Z-mode is seen below f_{ce}/Γ_r. Contrary to the cases of a purely hot or purely cold population, an unstable trapped branch appears between f_{ce}/Γ_r and $\simeq f_{ce}/2\Gamma_r$. This mode has a steeper slope than a shifted X-mode. I graphically found that this mode can be modeled with an expression of J_{steep} given in Equation 2.36.

$$J_{steep} = -\frac{\left(\frac{\omega_{pe}}{\omega_{ce}}\right)^2}{1-(\frac{\omega}{\omega_{ce}/\Gamma_r})^4} \tag{2.36}$$

These branches are similar to the ones described in Ning et al. (2023) appendix, which revisited the calculations of Mutel et al. (2010) and to the results of the simulations of Pritchett (1984). Le Queau and Louarn (1989) also described this configuration using a DGH distribution (Dory et al. 1965). As described in Ning et al. (2023), the unstable mode below f_{ce} merges with the RX-mode when there are no cold electrons.

Ning et al. (2023) hypothesized that if the observed SKR are emitted from this trapped mode, only mode conversion would allow this mode to escape, but further work is needed to understand this configuration.



(a) (b)

Figure 2.10.: Group velocities for the same cases as Figure 2.10

Figure 2.10 presents the group velocities obtained on the unstable branch below f_{ce} for the 2 cases $\frac{\omega_{pe}}{\omega_{ce}} = 3 \times 10^{-3}$ and 1×10^{-2} This figure shows that in the case of unstable shell distributions on top of a cold plasma, the CMI amplifies waves on a trapped mode with a small group velocity ($v_g \simeq 10^{-2}c$ for $\frac{\omega_{pe}}{\omega_{ce}} \simeq 10^{-3}c$ and $v_g \simeq 10^{-3}c$ for $\frac{\omega_{pe}}{\omega_{ce}} \simeq 10^{-2}$) which depends on $\frac{\omega_{pe}}{\omega_{ce}}$ and v_r.

I did not conduct a complete parameter study on the dependence on $\frac{\omega_{pe}}{\omega_{ce}}$ and v_r and $\frac{n_{hot}}{n_{cold}}$, as I was only interested in characterizing plasma conditions similar to those observed in HOM and DAM sources.

2.5.1.4. Thermal effects

In the previous sections, I assumed that the distribution functions could be modeled by Dirac functions. This is equivalent to assuming a zero temperature for these populations. To account for the thermal effects resulting from assuming a finite temperature, Le Queau and Louarn (1989) assumed the EDF to be a DGH (Dory et al. 1965) defined by its thermal speed α and parameter $l \in \mathbb{N}$. This distribution was introduced to describe electron distribution with an empty loss cone. Note that for l=0, the DGH becomes a Maxwellian.

$$f_l(v_\parallel, v_\perp) = \frac{1}{l!\pi^{3/2}\alpha^3}\left(\frac{v_\perp}{\alpha}\right)^{2l} e^{-\frac{v^2}{\alpha^2}} \tag{2.37}$$

They obtained

$$J = \frac{\left(\omega_{pe}/\omega_{ce}\right)^2}{\alpha^2/2}\left((l+1)I_{l+2}\left(\frac{\Delta\omega}{\alpha^2/2}\right) - lI_{l+1}\left(\frac{\Delta\omega}{\alpha^2/2}\right)\right) \tag{2.38a}$$

with,

$$I_l(x) = -i \int dt \frac{e^{itZ}}{(1-it)^{l+\frac{1}{2}}} \tag{2.38b}$$

$$I_l(x) = \frac{\pi^{\frac{1}{2}}}{\Gamma(l)}(-x)^{l-1}(-\sqrt{-x}F(-\sqrt{-x})) + \sum_{k=0}^{l-1}(-x)^k \frac{\Gamma(l+\frac{1}{2}-1-k)}{\Gamma(l+\frac{1}{2})} \tag{2.38c}$$

where $\Gamma(x) = \int dt\, t^{x-1}e^{-t}$ is the gamma function. $\Gamma(n) = (n-1)!$ for $n \in \mathbb{N}$ and F(x) the plasma dispersion function analytically prolonged on C.

Similarly, I derived J for a EDF model more adapted to describe shell using the isotropic DGH defined in Strangeway (1986).

$$f_l(v) = \pi^{-\frac{3}{2}}\alpha^{-3}\frac{\Gamma(\frac{3}{2})}{\Gamma(l+\frac{3}{2})}(\frac{v}{\alpha})^{2l}e^{-\frac{v^2}{\alpha^2}} \tag{2.39}$$

$$J = \frac{2}{3}\frac{\left(\omega_{pe}/\omega_{ce}\right)^2}{\frac{\alpha^2}{2}}\left((l+\frac{3}{2})I_{l+2}(\frac{\Delta\omega}{\alpha^2/2}) - lI_{l+1}(\frac{\Delta\omega}{\alpha^2/2})\right) \tag{2.40}$$

In these cases, the relation between ω_i and $\Delta\omega$ cannot be obtained analytically; I thus solved this relation numerically.

For a purely hot and purely cold plasma, the obtained dispersion relations are quite similar to those for the idealized ringlike or shell cases (see Le Queau and Louarn (1989)).

For the sake of brevity, I will only show the more realistic case of a cold and hot population superposed. In particular, I will show the dispersion relation obtained from parameters obtained by fitting measured EDF to the model of a cold Maxwellian and a hot shell defined by an isotropic DGH (Equation 2.39).

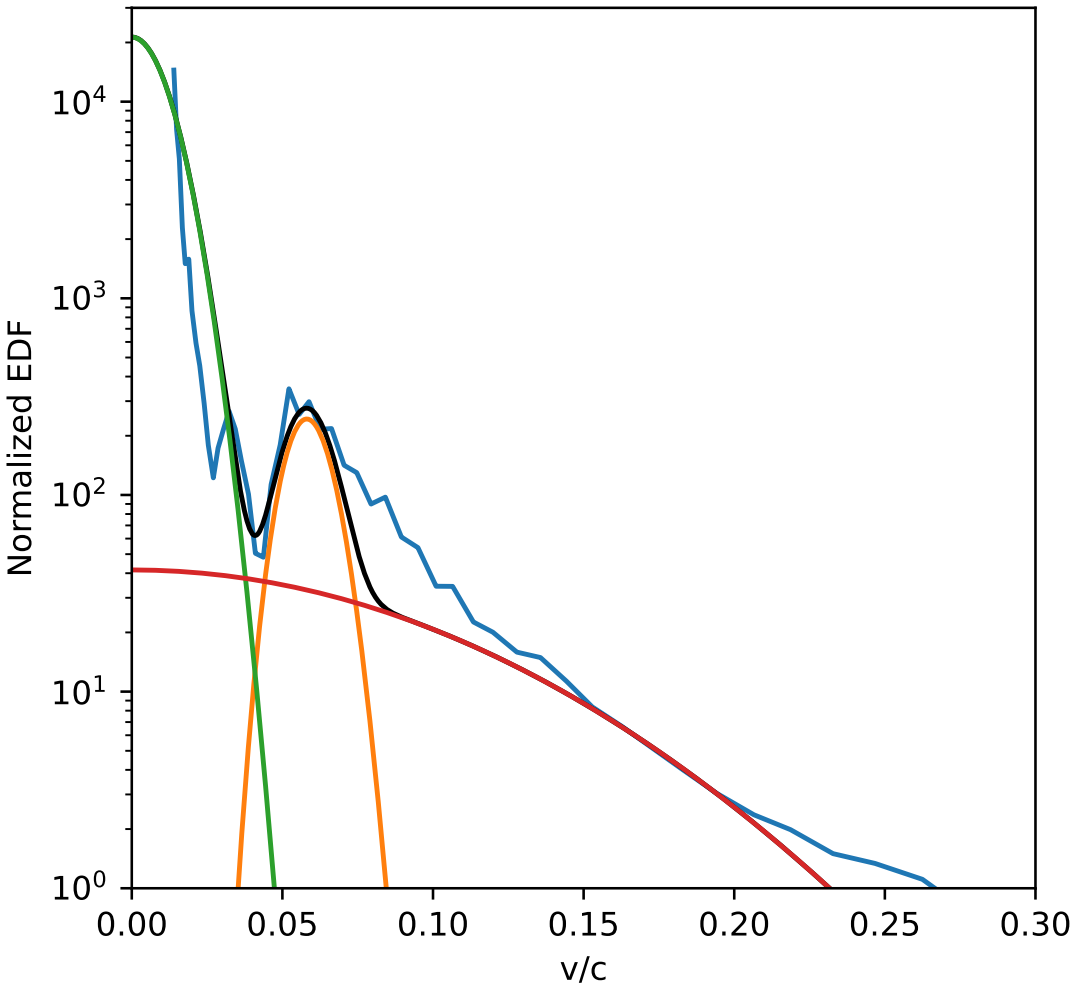


Figure 2.11.: Distribution function observed by JADE-E on 2017-03-27 06:52:10 (PJ6S) on anode 4 ($\theta = 35°$), fitted Maxwellians for the cold and supra-thermal population and isotropic DGH for the shell

I chose the JADE-E EDF measurement obtained on 2021-02-21 at 18:42:45 (see Chapter 4) as a representative case of a $f < f_{ce}$ source. This event is described extensively in Chapter 4.

The distribution observed at $\theta = 37.5°$ is displayed in Figure2.11, by the blue curve. I then fitted this distribution using a least squares method with 2 Maxwellians to account for the cold EDF for $v = 0.05c$ (green curve) and the supra-thermal tail $v > 0.10c$ (red curve), and an isotropic DGH for the shell (orange curve). The black curve shows the total modeled distribution. Although this model does not take into account some features of the EDF (especially the tail of the shell), it fits the data fairly well. Indeed, the most important parts of the EDF to drive CMI are the positive gradient of the EDF and the cold population, which determines the properties of the amplified wave.

During this time interval, JADE-E measured an electron density of 0.091 cm^{-3} and

HOM was observed at f_{ce} =2 MHz, thus resulting $\frac{\omega_{pe}}{\omega_{ce}} = 1.3 \times 10^{-3}$. To account for the underestimation of the density, I supposed $\frac{\omega_{pe}}{\omega_{ce}} = 2 \times 10^{-3}$

I then solve numerically $J(\omega)$ for values of ω_r and ω_i close to ω_{ce} to obtain N and the dispersion relation.

The obtained dispersion relation is shown in Figure 2.12 with the color bar indicating the growth rate γ. This relation is strongly similar to the case shown in Figure 2.9a). This confirms that the group velocity obtained from the zero temperature distributions can be applied to an actual source crossing. In that case, we can assume a group velocity of the order of 10^{-2}. This value is therefore much lower than the ones previously used in the literature and results in larger wave amplification.

To conclude, I still chose 0.1c as the value of v_g for the purpose of facilitating a comparison with results previously published. The consideration of the dependence of v_g on $\frac{\omega_{pe}}{\omega_{ce}}$ and the energy of the unstable population will be addressed posteriorly in Chapter 6.

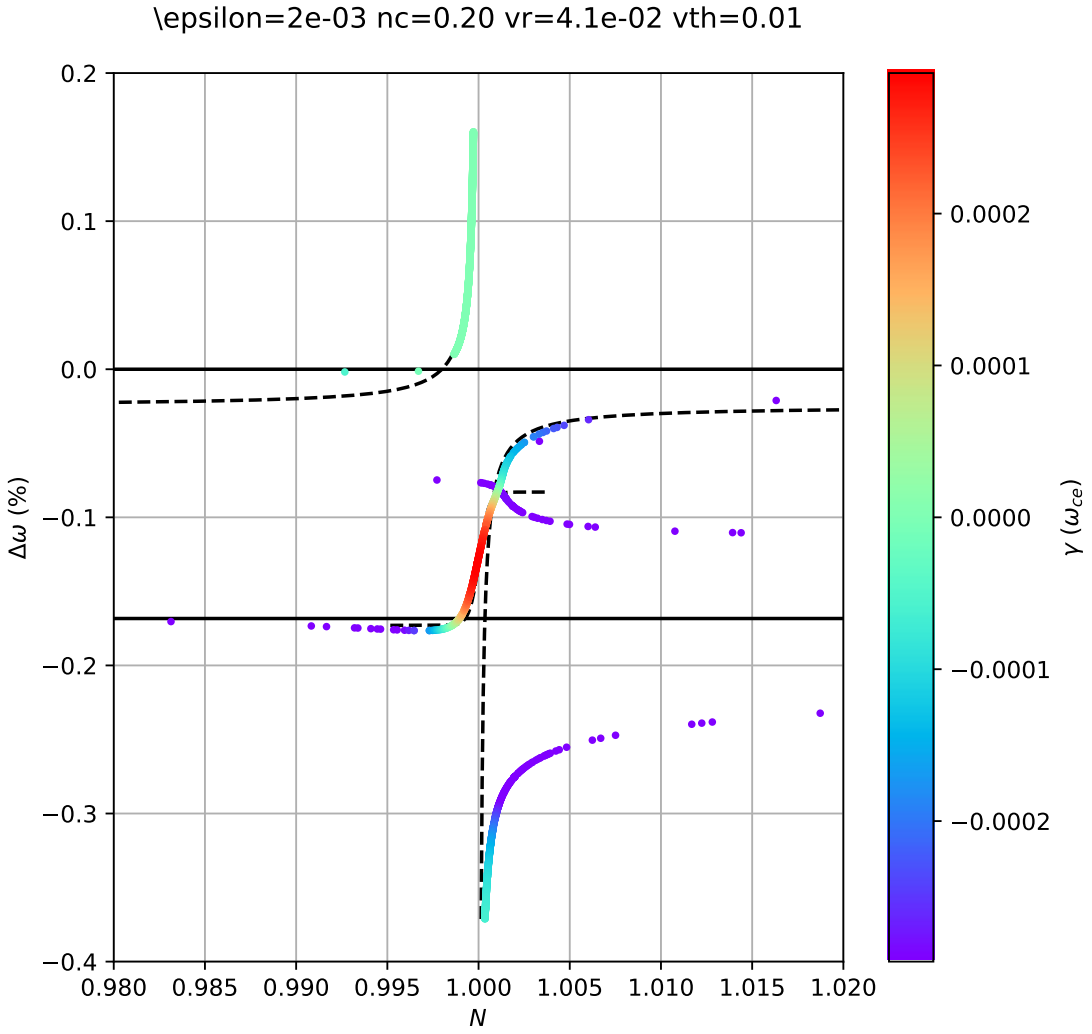


Figure 2.12.: Dispersion relation obtained for the model at $\frac{f_{pe}}{f_{ce}} = 2 \times 10^{-3}$. The color bar indicates the growth rate ω_i. The continuous horizontal lines indicate f_{ce} and $\frac{f_{ce}}{\Gamma_{peak}}$. Dash lines indicate the cold plasma approximation RX-mode modified to fit the data and a model to illustrate the boundaries of the trapped mode.

3. Instruments and Methods

All we hear is radio ga ga

Queen

Contents

3.1. Juno . . . 78
3.1.1. Waves . . . 79
3.1.2. JADE-E . . . 81
3.1.3. JEDI . . . 82
3.1.4. MAG . . . 83
3.1.5. UVS . . . 83
3.2. Identification of CMI radio source crossings . . . 83
3.3. Growth rate computation . . . 84
3.3.1. EDF processing . . . 84
3.3.2. Set of resonance circles . . . 84
3.3.3. Selection of resonance circle . . . 85
3.4. Computation of relevant observables . . . 86
3.4.1. Theoretical Loss Cone Angle . . . 86
3.4.2. Field Aligned Current Computation . . . 86
3.4.3. Alfvénic perturbations . . . 86

This chapter describes the methodology I developed to assess the validity and operation conditions of the CMI from in situ measurements within the source of Jovian auroral radio emissions.

As the **radio** auroral emissions are produced by a wave-**electron** instability in highly **magnetized** plasma, I used in situ **radio**, **electron** and **magnetic** measurements acquired by Juno, sometimes complemented by ultraviolet observations of the auroral context provided by Juno or the Hubble Space Telescope.

3.1. Juno

As described in Chapter 1, Juno is a polar spacecraft equipped with different instruments. In this work I mainly used the measurements from the **Waves** radio experiment (Kurth et al. 2017), the JADE-E electron spectrometer (McComas et al. 2013), and the **MAG** flux gate magnetometer (Connerney et al. 2017). I have also occasionally used

high energy electron measurements from JEDI and UV auroral observations from UVS or from the Hubble Space Telescope.

3.1.1. Waves

Waves measures electric field over a wide radio frequency range (50 Hz to 41 MHz) with a single electric dipole antenna made of two 2.8 m monopoles and two Low and High Frequency Receivers (LFR and HFR). Both receivers sample two bands:

- The Low Frequency Receiver (LFR) subdivides into:
  - The LFR Low band (LFR-Low) which samples frequencies between 50 Hz and 20 kHz, at a rate of 50×10^6 samples per second transferred in blocks of 6144 samples,
  - The LFR High band (LFR-High) scans frequencies between 10 and 150 kHz, at rate of 375×10^6 samples per second transferred in blocks of 6144 samples.
- The High Frequency Receiver (HFR) also subdivides into :
  - The HFR Low band (HFR-Low): 150 kHz to 3 MHz at rate of 7000×10^6 samples per second in blocks of 4096 samples,
  - The HFR High band (HFR-High): 3 MHz to 41 MHz at rate of 1312×10^6 samples per second in blocks of 4096 samples.

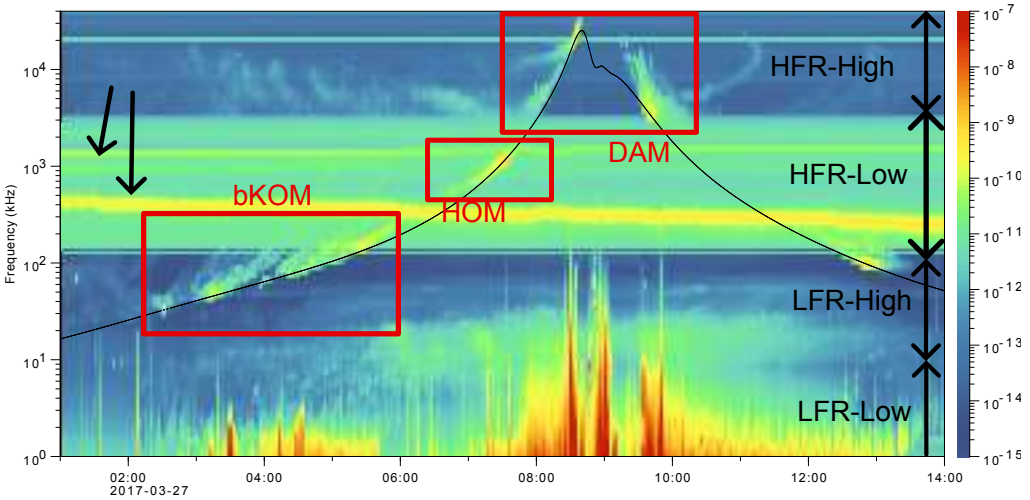
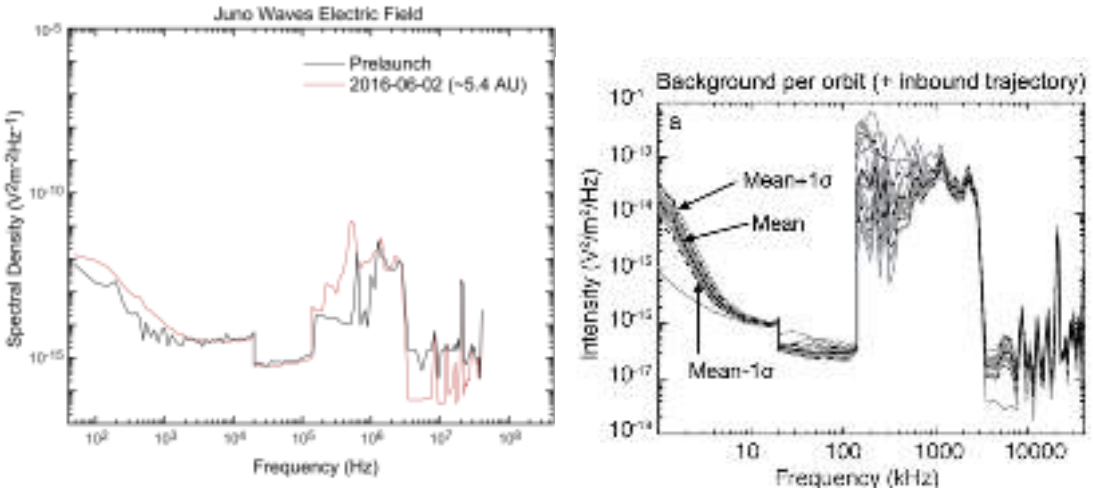


Figure 3.1.: Example of Waves Survey measurements during PJ6S



(a) (b)

Figure 3.2.: Waves noise level. Credits: Kurth et al. (2017) and Louis et al. (2021)

Unfortunately, the HFR-Low receiver, which intercepts parts of the bKOM and HOM frequency ranges, has a low sensitivity and present a variable parasite (see Kurth et al. 2017; Louis et al. 2021, and Figure 3.2). During perijoves, only intense enough HOM and bKOM can be detected when the parasite is not present. Outside perijoves, this receiver is blind to Jupiter radio waves.

Waves operates either in the Survey or Burst mode. Survey observations consist of time-frequency measurements, sampling the full Waves spectral range at a cadence varying from 1 to 130 s. The 1 s cadence is used for approximately 12 hours around each PJ for the sampling of auroral regions. Outside this window, the survey time cadence is reduced to 10 s, and near apoapsis, it is degraded to 30 s. Figure 3.1 presents an example of Waves Survey time-frequency spectrogram during PJ6S (2017-05-19) where bKOM, HOM and DAM components are visible. The lower sensitivity of HFR-Low channel is exhibited in this Figure and multiple parasites are shown by black arrows.

Burst mode measurements are only collected 2.5 hours before and after near periapsis as waveform data that can be used to reconstruct the dynamic spectra with high spectral and temporal resolutions. HFR-High Burst mode measurements are acquired for periods of time when f_{ce} (derived from measurements of the local magnetic field) falls within the HFR-High range. These spectra are then given in a 1 MHz sliding frequency range near f_{ce}.

Figure 3.3 illustrates the typical spectrogram obtained from HFR-High and HFR-Low measurements in Burst mode.

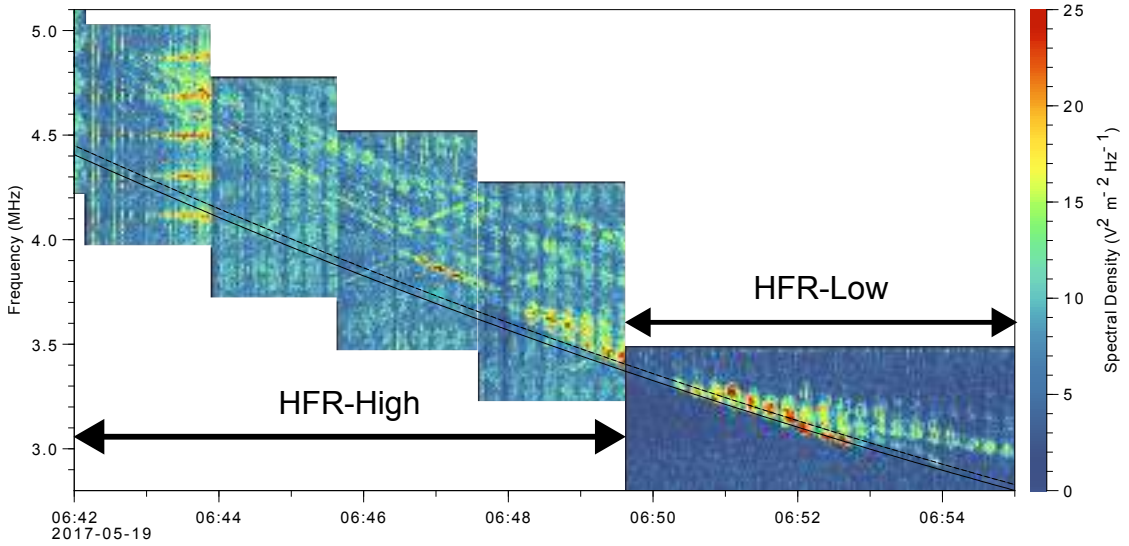


Figure 3.3.: Example of Waves Burst measurements during PJ6S on HFR-High and HFR-Low channels. Black lines represent f_{ce} and $f_{ce} = 1\%$.

While a single dipole antenna cannot perform goniopolarimetric measurements (polarization and direction-finding), they can sometimes be inferred from dipole measurements accumulated during a spin period (Kurth et al. 1975; Lecacheux 1978; Menietti et al. 2023).

Waves measurements can be used to infer f_{pe}, and so the electron density, by tracking the upper frequency cut-off of the whistler-mode emission (Elliott et al. 2021; Sulaiman et al. 2022).

3.1.2. JADE-E

The Jovian Auroral Distributions Experiment (McComas et al. 2013) is an instrument that samples electrons and ions over a wide range of energy and directions. It includes : JADE-E (electron sensor) and JADE-I (ion sensor). As I am solely interested in electrons, I only describe Jovian Auroral Distributions Experiment Electron sensors (JADE-E) here.

JADE-E is a swept-energy electron spectrometer that measures electrons at 64 energies logarithmically spaced from 0.1 to ~100 keV. The spatial coverage was originally ensured by 3 sensors measuring the full sky EDF, out of which 1 stopped operating during the Juno cruise phase. The EDF is measured since then by the 2 remaining sensors, with a total of 64 anodes each sampling a 7.5×120° field-of-view. Similarly to Waves, JADE-E measurements are stored either in high resolution every second or in low resolution where 1 s measurements are stacked for 30 s. As Juno completes a rotation in 30 s, in high resolution, JADE-E samples all directions within a spin period. The signal is recorded successively by adjacent energy channels with a time delay of ~0.1 s. It can therefore significantly change whenever the EDF varies at sub-second timescales, producing a characteristic saw tooth profile (see Louarn et al. 2018). The

maximal energy sampled by JADE-E is lower when the spacecraft spin axis is not parallel to the magnetic field (down to 40 keV when the angle is about 35°).

Out of this, the measured EDFs are biased. Electron measurements are significantly depleted for pitch angles $\theta = (\vec{\mathbf{v}}, \vec{\mathbf{B}})$ (with $\vec{\mathbf{v}}$ the electron velocity and $\vec{\mathbf{B}}$ the local magnetic field) near 90° in strong magnetic field regions because of an instrumental, energy-dependent, masking part of incident electrons (McComas et al. 2013; Allegrini et al. 2017, 2020).

For comparison purposes with the literature, I used time-energy or time-pitch angle Electron Energy Flux (EEF) (in $\mathrm{cm}^2 \cdot \mathrm{sr}^{-1} \cdot \mathrm{s}^{-1}$) spectrograms. With this quantity the acceleration signatures at high energy are more easily identifiable. EEF is defined by (McComas et al. 2013):

$$\mathrm{EEF} = \mathrm{EDF} \times v^4$$

Because of the missing sensor, the instrumental shadowing, and the non-sampling of electrons with energies falling outside the JADE-E range, the derived values of n_e are a lower limit of the real instantaneous electron density. To minimize this bias, I used an envelope of the density using the spin-modulated peaks of this signal. This is illustrated in Fig. 3.4 where JADE-E measurements are shown by dots and the envelope is shown by a continuous line both for the total density in black and the hot electrons (> 1keV) in red.

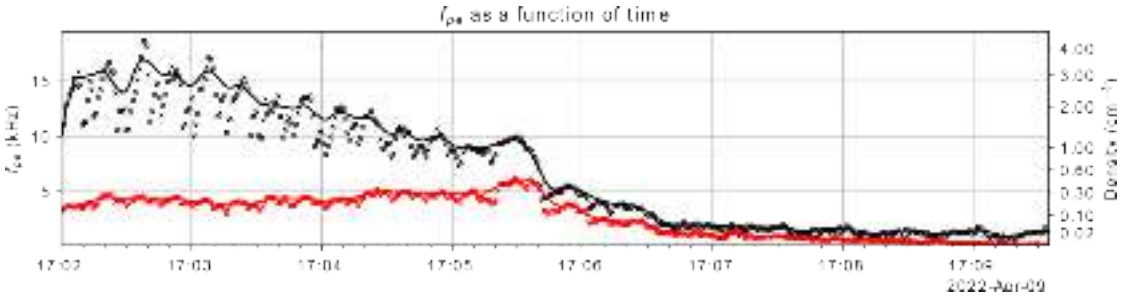


Figure 3.4.: Density as a function of time during PJ41S.
Black dots represent the total density estimated by JADE-E, red dots represent the density of sampled electrons with an energy larger than 1 keV. Solid lines are the envelope of the density used to overcome the underestimation of JADE-E.

3.1.3. JEDI

The Jupiter Energetic particle Detector Instrument (JEDI) suite (Mauk et al. 2017) comprises three nearly identical instruments that samples the energetic electrons within the energy range of 25 to 1200 keV. This suite is equipped with 18 solid state detectors (SSD) which are arranged in a 160° fan for the three instruments, covering a nearly full sky.

The measurements are obtained every 0.5 s but the pitch angle coverage of JEDI depends on the alignment of the magnetic field with the plane perpendicular to the spacecraft. I used measurement averaged on 3 s to ensure a better pitch angle coverage.

3.1.4. MAG

The radio/electron observations introduced above are complemented by Magnetometer (MAG) measurements (Connerney et al. 2017). This instrument is placed at the edge of one of the three solar panels to ensure that the data are least "polluted" by magnetic signals from the spacecraft system. High cadence measurements of $\vec{\mathbf{B}}$ consist of 64 measurements per seconds. f_{ce} can be derived directly from the measured B, and the direction of encountered field-aligned currents (FAC) by the derivative of the azimuthal component B_ϕ.

3.1.5. UVS

The Ultraviolet Spectrograph (UVS) is an imaging spectrometer that observes Jupiter's poles in the ultraviolet range between 68 and 210 nm (Gladstone et al. 2017). Near each PJ, the UVS will scan the auroral region of Jupiter every 30 seconds, and the co-addition of successive images can be used to reconstruct complete maps of the H_2-bands emissions radiated by the Jovian atmospheric aurorae (Bonfond et al. 2017; Greathouse et al. 2021). I have used such images of H_2-bands aurorae, together with maps of the so-called Color Ratio (courtesy of V. Hue and B Bonfond). This color ratio is defined by the ratio between the integrated brightness from 158 to 162 nm and from 126 to 130 nm, which correspond to H_2 emissions respectively unabsorbed and absorbed by atmospheric hydrocarbon layers. Images of this color ratio are used to estimate the penetration depth of the precipitating electrons (Gladstone et al. 2017). This proxy is sensitive to highly energetic (typically >10 keV) precipitating electrons (Gérard et al. 2014, and refs therein).

Occasionally, I have also used UV auroral images of H-Lyman α and H_2 bands obtained by the Space Telescope Imaging Spectrograph onboard the Hubble Space Telescope. These images, which sample either the full northern or southern auroral region, benefit a high spatial resolution. These were processed by and accessed through the APIS service (Lamy et al. 2015).

3.2. Identification of CMI radio source crossings

To identify crossings of radio source amplified by the CMI, I used the criterion proposed for Jupiter by Louis et al. (2019). This criterion considers that the detected radio waves are possibly locally emitted (source candidate) whenever intense radio emissions are detected for $f < f_{ce}+1\%$. Figure 3.3 shows a Waves Burst time-frequency radio spectrogram where f_{ce} and $f_{ce}+1\%$ are shown in black. From 06:50 to 06:54:30, intense emissions with the characteristic arc shape described in Chapter 1 are visible below $f_{ce}+1\%$. This interval is identified as a radio source candidate.

I note here that emissions seen close but below f_{ce} are necessarily emitted locally by shell-type electrons. The identification as source crossings is then directly confirmed. For emissions seen above f_{ce}, this criterion allows the identification of emissions generated by other unstable EDF than shell up to a characteristic energy of 5 keV (see

Equation 2.3a). This low energy limitation makes this criterion ad-hoc as emissions could be generated by electrons of tens keV.

3.3. Growth rate computation

The validation of the CMI as the generation mechanism for the source candidates identified with the above-mentioned approach requires performing a dedicated CMI growth rate analysis based on in situ electron measurements from JADE-E. The derived radio wave properties can then be compared to those observed by Waves.

Recap of the growth rate expression

In Chapter 2, I have derived different analytical expressions of the CMI growth rate for X-mode coherent amplification. The retained expression of this growth rate is expressed as

$$\gamma = \frac{(\frac{\pi}{2}\frac{\omega_{pc}}{\omega_{ce}})^2}{1+(\frac{\epsilon_h}{2\Delta\omega})^2} c^2 \frac{1}{n_e} \oint d\phi v_r^2 \sin^2\phi \frac{\partial F_e}{\partial v_\perp} \tag{3.1}$$

This expression is strongly dependent on the integral of $\frac{\partial F_e}{\partial v_\perp}$ along a resonance circle and on n_{hot}. I used the density derived from electron detected above 1 keV as a proxy for n_{hot}. The integration of $\frac{\partial F_e}{\partial v_\perp}$ is detailed in the next paragraphs.

3.3.1. EDF measurement processing

To mitigate the sub-second variations (described in Section 3.1.2) affecting the EDF measured by JADE-E in (E,θ) phase space, I first smoothed the EDF on a 3 pitch angles × 3 energy channels running boxcar. I then obtained $\frac{\partial F_e}{\partial v_\perp}$ from the decomposition:

$$\frac{\partial F_e}{\partial v_\perp} = \frac{\cos\theta}{v}\frac{\partial F_e}{\partial \theta} + \sin\theta \frac{\partial F_e}{\partial v} \tag{3.2}$$

where $\frac{\partial F_e}{\partial \theta}$ and $\frac{\partial F_e}{\partial v}$ are obtained by the derivation of three-point Lagrangian interpolation polynomials

This method is more precise than the one used in Louarn et al. (2017) and Louis et al. (2020) where the gradient was estimated solely from $\frac{\partial F_e}{\partial \theta}$ as it takes into account the variation in both directions and is applicable on circles that are not confined to low pitch angles.

3.3.2. Set of resonance circles

To blindly analyze each EDF measurement, I tested a wide set of resonance circles aimed at testing upward and downward electrons but also shell-type EDFs. A series of 128 (twice the number of JADE-E energy channels) circles centered on $(0,0)$ and

logarithmically spaced radii in the JADE-E energy range is specifically chosen to test shell-type EDFs. A second series of 4200 non-centered resonance circles, exploring the ranges $v_0 = 0.033\,c$ to $0.367\,c$ ($0.28 - 38.3$keV) and $v_r = 0.2\,v_0$ to $1.25\,v_0$, were aimed at testing either downward of upward part of the EDF.

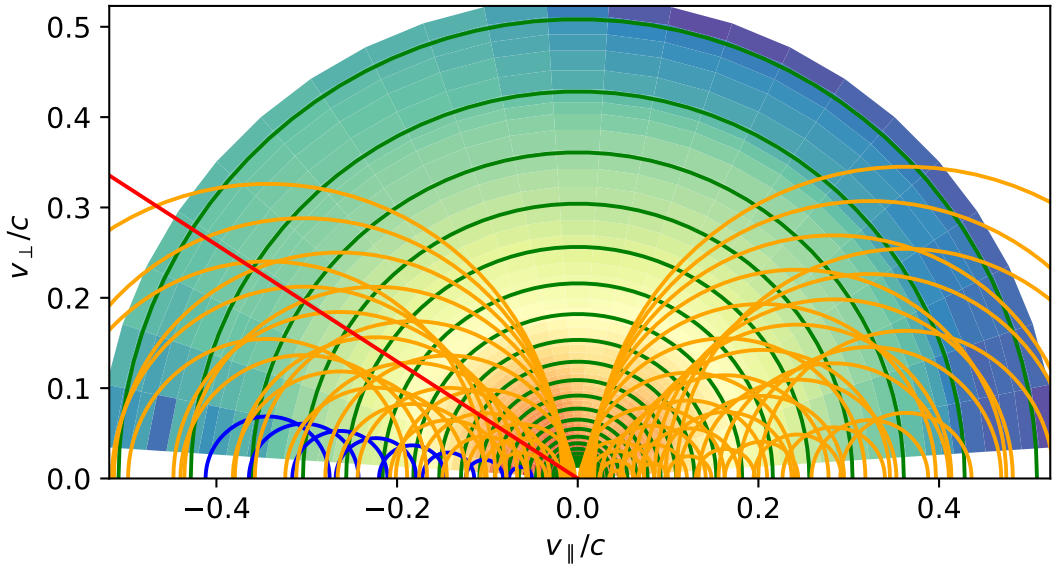


Figure 3.5.: JADE-E measurement of a smoothed EDF displayed in the normalized velocity space. The red line shows theoretical loss cone aperture angle (computed as explicited in section 3.4). The colored circles display a subset of centered (green) and non-centered (orange, blue) CMI resonance circles. The green circles correspond to shell- (or trapped-) EDF, the blue ones to loss cone ones and the oranges circle test other possible unstable portions of the EDF.

The growth rate is then computed by a 1000-point numerical integration along a circle using 6-point bi-linear interpolations of $\frac{\partial F_e}{\partial v_\perp}$.

3.3.3. Selection of resonance circle

To account for incorrect data points (either resulting from original measurements or from the background subtraction step), resonance circles made of more than 13% negative values or including less than 25 pixels are rejected from the analysis. These thresholds were fixed by testing the method on sample dataset. To avoid confusion with sub-second variations, I imposed to the centered resonance circles to yield positive growth rates for at least two consecutive radii.

From this valid set of tested resonance circles, I finally retained the one yielding the largest growth rate per series, assuming that, for an exponential wave growth, the largest growth rate (and associated resonance circle) will dominate the wave amplification process. I could then deduce properties on the amplified wave ($\Delta\omega, k_{\parallel}$ see Chapter 2) and retrieve the characteristics of the unstable electron population ($E_{chara}, \theta_{chara}$ see Chapter 2). By comparing θ_{chara} with θ_{LC}, the non-centered circles were labelled as loss cone if θ_{chara} is below $\theta_{LC} + 7.5°$.

3.4. Computation of relevant observables

3.4.1. Theoretical Loss Cone Angle

The value of the theoretical loss cone angle θ_{LC} (see Chap 2) is needed to disambiguate perpendicular gradients caused by this loss cone from any other accelerations. This angle, defined in Equation 2.25, I used JRM33+CON20 to obtain B at the position of interest and B_{max} at a precipitation altitude of 300 km above the 1 bar level (taken as the average altitude of peak auroral precipitation) and assume $\Delta\phi = 0$.

3.4.2. Field Aligned Current Computation

The auroral regions acceleration processes are strongly linked to FAC and gives an important context in radio sources. These currents and especially their direction can be estimated using MAG measurements. As a first order approximation, I assumed Jupiter's magnetic field to be dipolar, hence $\frac{\partial \vec{\mathbf{B}}}{\partial \phi} = \vec{\mathbf{0}}$. Then supposing stationary electric field ($\frac{\partial \vec{\mathbf{E}}}{\partial t} = 0$), a field aligned current $j_{\parallel}$ can be expressed from Equation 2.7d as:

$$j_{\parallel} = \frac{1}{\mu_0}(\vec{\nabla} \times B)_{\parallel} = \frac{1}{\mu_0 r \sin\theta_{SysIII}} \frac{\partial(\sin\theta_{SysIII} B_{\phi})}{\partial \theta_{SysIII}} \tag{3.3}$$

with r the distance from the planet and θ_{SysIII} the latitude. FACs were directly computed from MAG measurements from which δB_{ϕ} (defined in Equation 3.4) is derived. A positive δB_{ϕ} slope observed above the Northern (res. Southern) aurora corresponds to an upward (resp. downward) FAC and if a negative one is observed, it corresponds to a downward (resp. upward) FAC.

$$\delta B_{\phi} = B_{\phi}|_{MAG} - B_{\phi}|_{JRM33+CON20} \tag{3.4}$$

where $B|_{MAG}$ is the magnetic field measured by MAG and $B|_{JRM33+CON20}$ the JRM33+CON20 modeled magnetic field

3.4.3. Alfvénic perturbations

Along with FACs, Alfvén waves are known to accelerate the plasma through wave-particle interactions and they have been shown to be systematically present along

some auroral magnetic flux tubes. I used the method described in Gershman et al. (2019) to identify the regions where these Alfvénic fluctuations were important. This method use high resolution MAG measurements to compute the transverse power spectral densities from discrete fast Fourier transforms of each component of $\vec{\mathbf{B}}$. I constructed spectrograms of $P_{Tr} = (P_{B_x} + P_{B_y} + P_{B_z})/3$ obtained from successive sets of 30 s samples (25 s overlap). P_{Tr} represents the transverse fluctuation power. Whenever these fluctuations become important, I identified this region as presenting Alfvén accelerations.

4. In situ characterization of HOM/DAM sources

Radio goo goo

Queen

Contents

4.1. Radio survey of HOM and DAM sources . . . 89
4.1.1. Description of the studied interval . . . 90
4.1.2. Tracking HOM/DAM source candidates . . . 90
4.1.2.1. Location and plasma context of the candidate sources . 90
4.1.2.2. Comparative characterization of the radio emission regions during the first 10 perijoves . . . 92
4.1.3. The case of sources below f_{ce} . . . 96
4.2. CMI growth rate analysis . . . 97
4.2.1. Case study: PJ32S . . . 97
4.2.1.1. Radio source and auroral context . . . 97
4.2.2. Predicted growth rates . . . 100
4.2.2.1. Wave intensity . . . 106
4.2.3. CMI generation of all HOM/DAM crossed sources . . . 106
4.3. CMI generation of HOM/DAM by highly relativistic electrons . . . 108
4.3.1. Case study: PJ32S . . . 109
4.3.2. Growth rate analysis . . . 111
4.3.3. Summary for the PJ32S case . . . 115
4.4. Discovery of HOM harmonic emission . . . 115
4.4.1. Two harmonic detection examples . . . 116
4.4.2. Plasma context . . . 118
4.5. The case of moon-induced radio emissions . . . 120
4.5.1. The source of Io-induced radio emissions . . . 121
4.5.1.1. The case of PJ5S . . . 121
4.5.2. Callisto-induced radio emissions . . . 124
4.6. Summary of HOM/DAM/Moon-DAM source properties . . . 126

In this chapter, I will present the in situ characterization of the HOM/DAM and Moon-DAM sources obtained by the methods introduced in Chapter 3. These results

Component		Frequency	M-SHELL	Local time preference	Longitude preference	Emission angle (°)	Power (W)	UV Association	Drivers	Source of free energy
Moon-DAM	Io	1-40 MHz	6 R_J	-	-	70°-80°	$\simeq 10^{11}$	MAW/RAW	Moon-Jupiter interaction	?
	Ganymede	up to 20 MHz	15 R_J			76°-83°				Loss cone
	Europa	up to 25 MHz	9 R_J			79°-81°		?		?
DAM		~1-35 MHz	7-61 R_J	None	120° & 330°	55°-85°	8×10^{10}	Diffuse ~~Aurora~~	Rotation	?
HOM		0.3- ≥ 3 MHz	North: 12-58 R_J South: 48-58 R_J	Dusk	40°-130°	30°-90°	4×10^{10}			Loss cone and Conics

Table 4.1.: Characteristics of the Moon-DAM, DAM, HOM components.

were partially published in Collet et al. (2024a) (see Appendix F2) and further used either for case studies or for statistical analyses (Al Saati et al. 2022; Collet et al. 2023; Louis et al. 2023b; Rabia et al. 2025). In the first section, I will give a description of the plasma and magnetic context of the HOM and DAM identified sources. In the second section, I will survey Juno/Waves measurements to identify candidate radio sources that I will compare with the plasma context derived from JADE-E and MAG measurements. In the third section, I will identify the sources of free energy with the growth rate analysis described in Chapter 3. The fourth section will study the eventual generation of HOM/DAM by highly energetic electrons. The fifth section will detail results on Moon-DAM. The sixth section will describe the first detection of a HOM harmonic.

The open questions on the radio auroral components studied in this chapter have been described in Chapter 1. The results obtained from observations from ground-based measurements and space missions (in particular Galileo and the first flybys of Juno) are summarized in Table 4.1

I still remind that by the start of this thesis, only the generation of HOM and Ganymede-DAM had been studied in situ by Louarn et al. (2017, 2018) and Louis et al. (2020). They analyzed the growth rate by computing $\frac{\partial F_e}{\partial v_\perp}$ estimated solely with $\frac{\partial F_e}{\partial v}$ (see Chapter 3) and showed that HOM sources were generated by loss cone EDF and conics and that Ganymede-DAM were generated by loss cone . Thanks to the progress of the Juno mission and the methods I've developed, these results will be explored in greater depth in the following sections.

4.1. Radio survey of HOM and DAM sources

In order to investigate the generation of HOM/DAM emissions and compare the locus of these sources with the auroral acceleration regions, I surveyed Waves observations above 300 kHz for the first 70 PJ (August 2016 to March 2025). The identification of candidate radio source crossings was conducted using Waves Burst mode time-frequency spectra using HFR-Low (ranging from 150 kHz to 3.5 MHz) and HFR-High (from 3.5 to 40 MHz).

Note that I conducted a study on the first 45 PJ (mid-2016 to Sept 2022) for emissions above 1 MHz that was published in Collet et al. (2024a,b). I completed this survey with

the most up-to-date measurements.

4.1.1. Description of the studied interval

The trajectory of Juno over the first 70 PJ for $f_{ce} > 300$ kHz is shown in black in Figure 4.2. This figure illustrates the biases in LT induced by Juno's trajectory. Local times between 19 and 05 (night sector) are rarely crossed in the Southern Hemisphere, so as LT between 00 and 10 in the Northern Hemisphere. The MAO is crossed at all longitudes but is more often crossed in the dawn side in the South and more near 20h in the North. Also, f_{ce} often reaches the HOM/DAM range when Juno is connected to the polar region (M-SHELL > 60 R_J) where radio source crossings were not observed so far (Louis et al. 2019).

4.1.2. Tracking HOM/DAM source candidates

4.1.2.1. Location and plasma context of the candidate sources

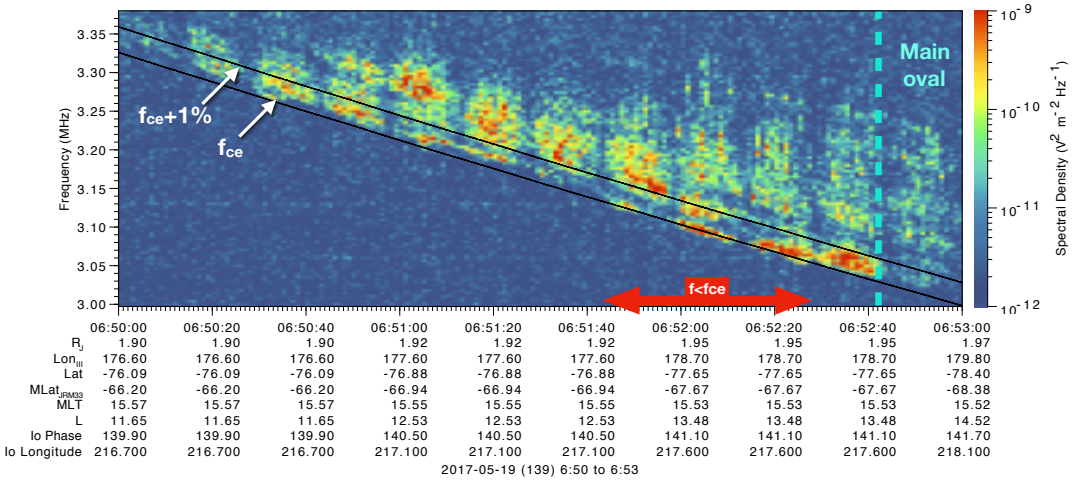


Figure 4.1.: Time-frequency spectrogram from Waves/HFR-Low measurements in Burst mode.

Overall, over the PJ1-70 interval, spanning 9 years, I have identified 115 candidate radio source crossings. These are exhaustively listed in Appendix E and Collet et al. (2024b). The position of the source candidates is superimposed in color onto the Juno trajectory in Figure 4.2 : green for events with $f < f_{ce}$ and orange for those with $f_{ce} < f < f_{ce} + 1\%$. Their statistics are detailed in Figure 4.3. Candidate sources all lie or are confined within flux tubes with M-SHELL between 5 and 55 R_J, consistent with the MAO. These Figures confirm that candidate sources are located continuously at all longitudes of the MAO but are preferentially located at its equatorward boundary. I

notice that source crossings are less seen for LT between 11 and 13 in the North and South with an otherwise homogeneous distribution in LT.

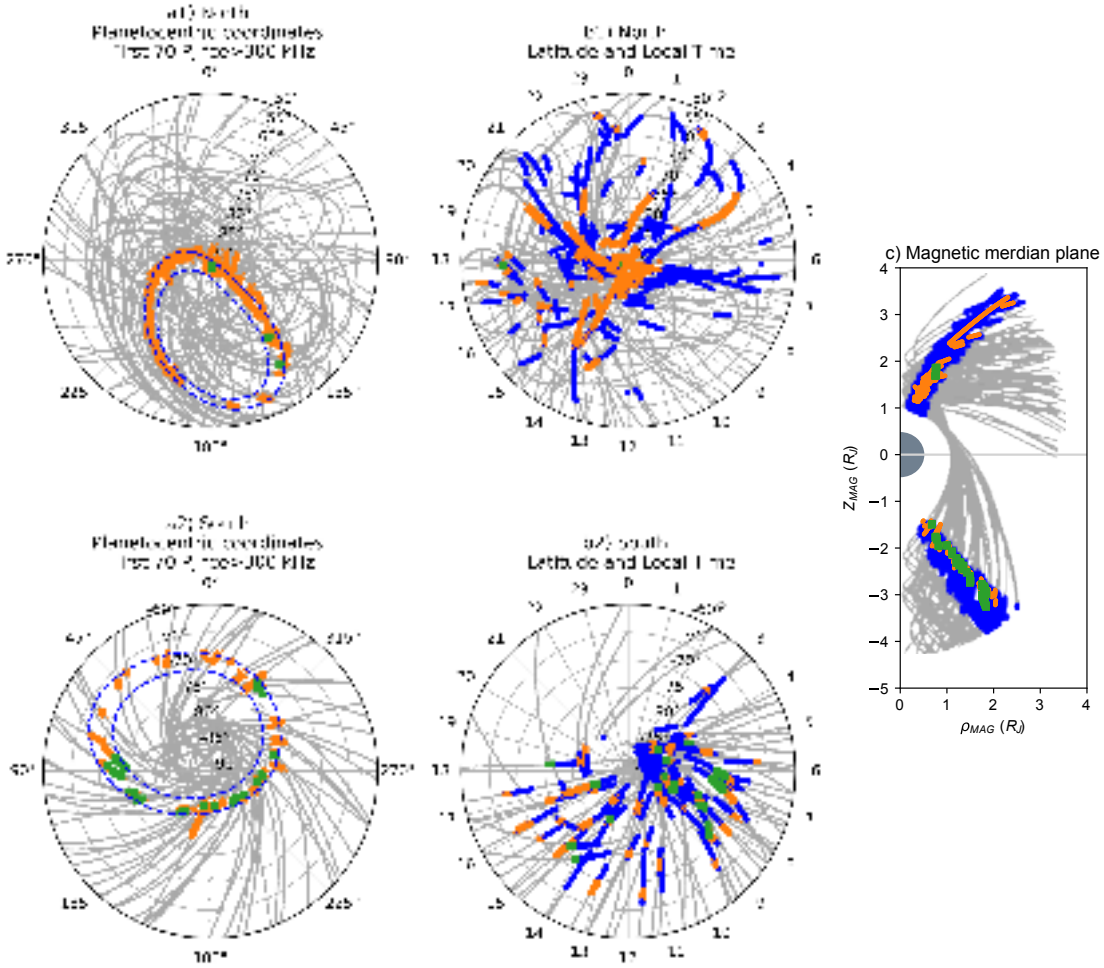
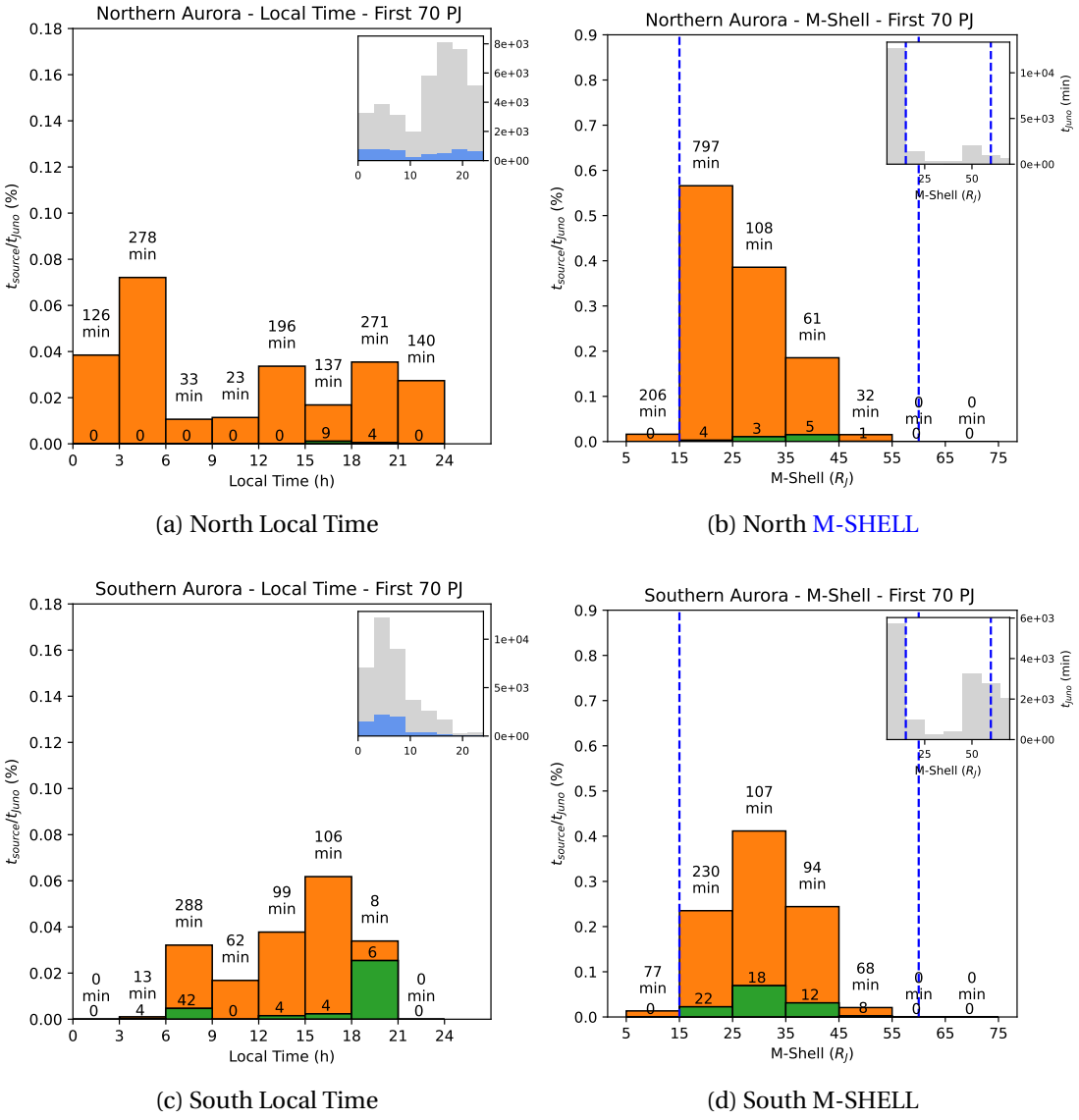


Figure 4.2.: Juno's trajectory for $f_{ce} \geq 300$ kHz and identified candidate HOM/DAM sources.

The northern (a1 and b1) and southern (a2 and b2) polar projections are displayed in planetocentric (Sys III) coordinates (a1 and a2), as a function of latitude and Local Time (b1 and b2) and in a magnetic meridian plane (c) where Z_{MAG} is the planetary dipole axis and ρ_{MAG} the perpendicular radial distance from the axis. The magnetic footprints of field lines mapping to M = 15 and M =60 R_J are taken as boundaries of the MAO. They are indicated by the blue dashed lines in Panels a1 and a2 and by the blue trajectory in Panels b1, b2, and c.



(a) North Local Time

(b) North M-SHELL

(c) South Local Time

(d) South M-SHELL

Figure 4.3.: Occurrence of HOM/DAM source crossings candidates.
Histograms of $\frac{t_{source}}{t_{Juno}}$ (in %) with t_{source} the time spent by Juno in a candidate source crossing and t_{Juno} the total time spent by Juno in the region corresponding to each bin. Panels a and c (b and d, resp.) compare the source candidate LT (M-SHELL, resp.) occurrence in the Northern and Southern Hemispheres. In the top right corner of each panel lies a reference histogram of t_{Juno} (in min).

4.1.2.2. Comparative characterization of the radio emission regions during the first 10 perijoves

From this survey, I first attempted to characterize the HOM/DAM radio sources by comparing their location with the features that were recently identified in the MAO:

- The UV emissions to which the candidate source crossings are associated with

(either MAO or UV DA)

- The zones (Diffuse Aurora Zone (Diff. A)/ZI/ZII)
- The 3 keV to 30 keV electron energy peak
- The peak of Alfvénic perturbations in the auroral regions

Since the articles where these regions were reported were restricted to the first 10 Juno orbits, I chose the same time interval to cross-compare with radio source candidates. The time-frequency spectrogram where I identified candidate radio sources were then superposed with Allegrini et al. (2017), Mauk et al. (2020), and Gershman et al. (2019)'s figures. Figure 4.4 illustrates this comparison on the case of PJ1s with the Waves spectrogram (top), and the 3 panels extracted from Figure 11 of Mauk et al. (2020). In this figure, the source crossing (black box) was identified in the Diff. A along with the 3-30 keV electron energy flux peak(green box). The red box shows event where $f < f_{ce}$ emissions are seen.

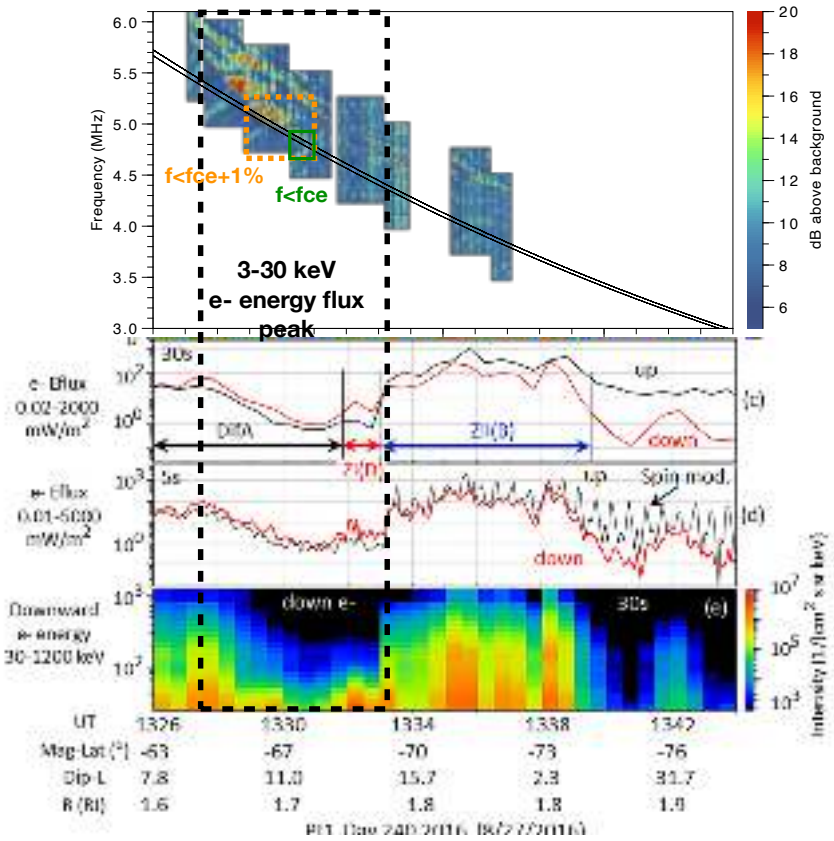


Figure 4.4.: Comparison between a source crossing and Diff. A./ZI/ZII. From top to bottom: Waves/Burst mode time-frequency spectrogram the black oblique lines are f_{ce} and $f_{ce}+1\%$, the black (resp red) box delimits the source identified below $f_{ce}+1\%$ (resp f_{ce}); Upward (resp downward) electron energy flux in black (resp in red) averaged over 30s intervals; Same but averaged over 5s; Electron energy spectra for downward directions ($\theta < 22°$ averaged at a 1s cadence. The green box delimits the 3-30 keV energy flux peak identified by Allegrini et al. (2020). Credits: Mauk et al. (2020).

During the first 10 perijoves, I identified 25 radio source crossings with several cases of multiple source crossings during the same orbit. The result of that comparison is shown in the Table. 4.2. Overall, 17 out of 25 (68%) identified HOM/DAM sources were associated with the 3 – 30 keV electron flux peak. All the HOM/DAM sources were identified within the Diff. A except for 2 cases (22%) which also overlapped with ZI. No HOM source was found to map to the ZII region. Alfvénic perturbations were identified in 9 (25 %), mostly in the Northern Hemisphere.

The survey analysis offers substantiated evidence that HOM sources statistically lie along flux tubes connected to the UV DA sometimes extending to the equatorward boundary of the MAO. It also suggests that HOM sources were associated with 3-30 keV electrons.

	Date (UTC)	f (MHz)	$f < f_{ce}$	UV aurora	<30 keV e^- flux	Acceleration zones	Alfvénic perturbations
South							
PJ1	2016-08-27 13:29:00 to 13:31:00	5		Diffuse	↑↓	Diff A.	X
	2016-08-27 13:30:25 to 13:30:45	5	X	Diffuse	↑↓	Diff A.	
PJ3	2016-12-11 17:36:29 to 17:37:22	6		Diffuse	↑↓		X
PJ4	2017-02-02 13:36:14 to 13:38:30	5		Diffuse	↑↓	Diff A	
	2017-02-02 13:36:31 to 13:37:30	5	X	Diffuse	↑↓	Diff A	
PJ5	2017-03-27 9:36:04 to 9:36:45	4		Diffuse	↓		X
	2017-03-27 9:40:05 to 9:40:40	3.5		Diffuse	↑↓		X
PJ6	2017-05-19 6:50:00 to 6:54:30	3		Main Oval & Diff. A.	↓	Diff A & ZI	X
	2017-05-19 6:51:45 to 6:52:30	3	X	Diffuse	↓	Diff A	
PJ7	2017-07-11 2:30:10 to 2:34:00	5		Diffuse	↑↓	X	
PJ8	2017-09-01 22:26:28 to 22:27:55	5		Diffuse	↓	Diff A & ZI	X
PJ9	2017-10-24 18:27:33 to 18:30:50	15		Diffuse	No		X
North							
PJ3	2016-12-11 16:24:01 to 16:26:17	5		Main Oval & Diff. A.	↑↓	X	
	2016-12-11 16:24:34 to 16:25:15	5	X	Main Oval & Diff. A.	No		X
PJ4	2017-02-02 12:25:00 to 12:26:47	7		Diffuse	No		
PJ5	2017-03-27 8:31:57 to 8:35:07	17-21		Diffuse	No		
PJ6	2017-05-19 5:31:07 to 5:33:36	8		Main Oval & Diff. A.	↓		
	2017-05-19 5:32:40 to 5:33:00	8	X	Diffuse	No		
PJ7	2017-07-11 2:30:24 to 2:33:55	5.5		Diffuse	↑↓	Diff A	
PJ8	2017-09-01 21:16:12 to 21:18:30	6.5		Main Oval & polarward	↓		
PJ9	2017-10-24 17:19:49 to 17:21:03	13		Main Oval & Diffuse	↓		X
	2017-10-24 17:19:55 to 17:20:05		X	Main Oval & Diffuse	↓		
	2017-10-24 17:20:30 to 17:20:50		X	Main Oval & Diffuse	No	X	
PJ10	2017-12-16 16:47:00 to 16:50:06	1.8		Main Oval & Diffuse		Diff A	
	2017-12-16 16:49:10 to 16:50:06		X	Main Oval & Diffuse		Diff A	

Table 4.2.: HOM and DAM sources identified during the 10 first perijoves and associated auroral regions.
The first 2 columns provide the perijove number and the date. The 3rd column is the detected emission frequency. Crosses in the 4th column indicate emissions falling below the local f_{ce} (exact time interval given in an additional row). The 5th column specifies the component of the UV aurora connected to the source crossing. Column 6 specifies the presence of a peak flux for 3-30 keV electrons and their sense of propagation(upward ↑ or downward ↓). Column 7 is a reminder of the classification proposed by Mauk et al. (2018). Blank cells represent cases with no identified acceleration zone or 3-30 keV e^- flux.

4.1.3. The case of sources below f_{ce}

Interestingly, radio sources reaching frequencies below the local f_{ce} were identified in this survey (example Figure 4.1). As explicited in Chapter 2, in the CMI framework, the discovered $f < f_{ce}$ radio emissions can only correspond to centered resonance circle triggered by either shell or trapped EDFs and yielding perpendicular emission. They can thus be considered as verified crossed sources (not candidates) and demonstrate the existence of a new CMI source of free energy at Jupiter on top of the loss cone and conics identified by Louarn et al. (2017, 2018).

Among the 116 candidates, I identified 21 candidate $f < f_{ce}$ source crossings ranging from 450 kHz to 5 MHz. I excluded 7 ambiguous cases identified with HFR-High. The $f < f_{ce}$ source location is shown in green in Figure 4.2 and 4.3 and presented in more detail in Table 4.3. The columns of this table are separated into 3 categories by the vertical double lines. These categories correspond to the different steps of the study: 1) the properties of sources identified from the survey, 2) the description of the auroral plasma context inferred from JADE-E spectra and MAG measurements, and 3) the results of the CMI growth rate analysis (to be presented below). The (unpublished yet) list of $f < f_{ce}$ sources identified from PJ46 to PJ70 lies below the horizontal double line (only the first category could be filled in at the time of writing these lines).

The maximal frequency reached by $f < f_{ce}$ HOM sources of our survey was about 5 MHz. The reason why we did not detect DAM sources beyond 5 MHz likely relates to the altitude at which the auroral flux tubes were crossed, favoring the HOM range. Still, the Jovian auroral radio spectrum peaks in the hectometric range, and HOM/DAM sources were suggested to actually be one unique component in Zarka et al. (2021), so that the studied HOM sources can be taken as representative of both HOM/DAM components.

Overall, out of the 21 $f < f_{ce}$ events, only 3 were observed in the Northern Hemisphere and 18 in the Southern Hemisphere. Contrary to the case of $f_{ce} < f < f_{ce} + 1\%$ sources, the sources identified in the Northern Hemisphere are only seen in the dusk side. In addition, 15 events out of 21 (71%) are located in the dawn side (LT$\in [01-10]$). In terms of longitudes, 18 events are produced on field lines between 80° and 280°, the remaining 3 events are all observed near 330° in the South.

Comparing the footprint of these sources with UVS images (see Column "UV aurorae" in Tables 4.3) revealed that 9 (43%) of these sources are colocated with the diffuse UV auroral emissions, 9 (43%) with the MAO and 2 (10%) poleward of it. Moreover, Figure 4.3 shows that Southern $f < f_{ce}$ sources have the same occurrence peak than the $f < f_{ce} + 1\%$ candidate sources for M-SHELL = 30 R_J.

The study of the auroral plasma context derived from JADE-E spectra and MAG magnetic field measurements (methods described in Chapter 3) is summarized in Table 4.3, Columns 7 to 10. The $f < f_{ce}$ HOM sources are composed of a hot and tenuous plasma with $n_h/n_{tot} \sim 0.6$ and $\frac{\omega_{pe}}{\omega_{ce}} \sim 3.6 \times 10^{-3}$ on average. Only 5 (46%) sources coincide with Alfvénic fluctuations. 18 (86%) sources lie within an upward FAC layer and match a gradual electron depletion. According to the criteria proposed in Mauk et al. (2018) and Sulaiman et al. (2022), most sources are located near the

boundary between Diff. A and ZI (a definite identification of which would have required the analysis of highly energetic electrons sampled by Juno/JEDI, which was not dealt with here). Obvious inverted Vs in JADE-E energy spectra were found in 14 (67%) sources.

4.2. CMI growth rate analysis

To validate and characterize the 15 $f < f_{ce}$ HOM source candidates identified during the first 45 PJ listed in Table 4.3, I used the CMI growth rate analysis described in Chapter 3 and Juno multi-instrumental observations. This work has been published in Collet et al. (2024a), which discusses in detail two case studies. Hereafter, I simply remind below the analysis of one of those as a representative case of a $f < f_{ce}$ HOM source. The results of this growth rate analysis are then generalized to all HOM/DAM sources for the full PJ1-45 (see the right-handed part of table 4.3).

4.2.1. Case study: PJ32S

4.2.1.1. Radio source and auroral context

The case of PJ32S stands as a typical illustration of $f < f_{ce}$ southern HOM sources. Figure 4.5 provides a summary of radio and particle measurements observed between 18:40:00 to 18:45:00 UT on day 2021-02-21.

PJ	Date YYYY-MM-DD HH:mm:ss-mm:ss	f (MHz)	$\frac{f-f_{ce}}{f_{ce}}$	$\frac{f_{pe}}{f_{ce}}$	Estimated intensity ($Wm^{-2}Hz^{-1}$)	UV aurorae	Mono energetic signatures	$\frac{n_h}{n}$	FAC direction	Alfvén waves	Shell energy (keV)	Enlargement of LC	Normalized growth rate ($x10^{-4}$)	Size (10^3km)
1S	2016-08-27 13:29:29-30:51	5	-0.6 %	4×10^{-3}	7.9×10^{-10}	Poleward.		0.5	↑	X	0.2	X	0.3-0.8	0.25
6S	2017-05-19 06:51:45-52:27	3	-0.2%	10^{-3}	8.02×10^{-12}	Diffuse	X	0.8	↑		0.5-3	X	0.2 – 2	2
11N	2018-02-07 12:57:24-36	2.5	-0.3%	2×10^{-3}	1.85×10^{-11}	Main Oval		0.8	↑	X	1	X	0.5 – 1	0.6
11S	2018-02-07 14:44:54-45:19	2.8	-0.25%	3×10^{-3}	2.56×10^{-11}	Main Oval		0.8	↑	X	2	X	0.5 – 3	1.25
21N	2019-07-21 03:08:05-29	2.6	-0.25%	2×10^{-3}	1.20×10^{-11}	Diffuse	X	0.7	↓		3	X	0.2 – 2	1.2
24S	2019-12-26 19:04:04-54	1	-0.3%	3×10^{-3}	2.69×10^{-11}	Diffuse	X	0.15	↑		1	X	0.2 – 0.8	2.5
25S	2020-02-17 19:11:43-57	1.2	-0.2%	3×10^{-3}	4.13×10^{-11}	Poleward		0.5	↑		0.2-0.7	X	2-3	0.75
28S	2020-07-25 07:14:06-51	2.2	-0.3%	2×10^{-3}	4.00×10^{-12}	Main Oval	X	0.5	↑		2	X	0.5	2
31S	2020-12-30 23:08:24-09:20	1.1	-0.25%	2×10^{-3}	8.27×10^{-12}	Main Oval	X	0.6	↑↓		2-3	X	0.3 – 3	2.5
32S	2021-02-21 18:42:13-43	2.2	-0.55%	10^{-3}	1.5×10^{-11}	Diffuse	X	0.7	↑	X	1.5	X	0.1 – 1	0.8
35N	2021-07-21 7:27:30-40	4	-0.2 %	2×10^{-3}	6×10^{-10}	Diffuse		0.7	*	*	0.2	X	0.5	1-10
37S	2021-10-16 18:22:33-25:39	1.6	-0.4%	3×10^{-3}	1.29×10^{-11}	Main Oval		0.4	↓		3	X	2 – 20	(1+) 3
38S	2021-11-29 15:34:35-36:34	1.1	-0.4%	2×10^{-3}	8.27×10^{-12}	Diffuse		0.5	↑		4	X	1 – 20	(0.5+)1.5
41S	2022-04-09 17:05:40-06:35	1.3	-0.3%	5×10^{-3}	3.50×10^{-11}	Diffuse		0.6	↑		5	X	2 – 10	2.75
44S	2022-08-17 16:17:14-34	0.9	-0.8%	4×10^{-3}	2.69×10^{-10}	Diffuse	X	0.5	↑		5	X	0.2 – 1	1.0
48S	2023-01-22 07:09:50-11:38	1	-2%	5×10^{-3}	2.69×10^{-11}	Main Oval	X	0.6	↑		10	X	1	2.4
53S	2023-07-31 10:54:00-56:00	0.6	-1%	6×10^{-3}	5.3×10^{-10}	Main Oval	X	0.7	↑	X	1-5	X	1-10	3.4
63S	2024-07-16 16:14:19-16:43	0.7	-0.5%	1×10^{-3}	1.5×10^{-10}	Diffuse	X	0.6	↑		0.2-2		1	1.4
64S	2024-08-18 08:33:08-48	0.75	-0.6%	7×10^{-3}	2.2×10^{-10}	Main Oval	X	0.6	↑		3	X	0.8	2
65S	2024-09-20 04:20:51-28:23	0.55	-1%	8×10^{-3}	1.3×10^{-10}	Main Oval	X	0.6	↑					
66S	2024-10-22 20:08:20-21:24	0.45	-0.5%	10^{-2}	7×10^{-11}	Main Oval	X	0.8 ?	↑					
Mean				3.6×10^{-3}	1×10^{-11}	Diffuse Main Oval	X	0.6	↑		0.2 to 5	X	2.5	2.1

Table 4.3.: Catalog of $f < f_{ce}$ HOM emissions identified from Waves observations over PJ1-45.

Columns 1 and 2 indicate the perijove and the event time interval. Columns 3, 4, and 5 give the absolute and relative emission frequency at the point where the emissions are the lowest below f_{ce}, together with the $\frac{\omega_{pe}}{\omega_{ce}}$ ratio. Column 6 gives the source peak spectral flux density as observed by Waves. Column 7 indicates whether Juno was magnetically colocated with the MAO or with the Diff. A. zone located from UVS images, column 8 whether the JADE-E spectrum exhibited a mono-energetic signature, column 11 whether I identified Alfvénic perturbations from MAG measurements, and column 10 the upward/downward sense of FAC (not identified on PJ35N). Column 8 indicates the ratio of hot to total electron density. Columns 13-15 provide the radio wave properties derived from my CMI growth rate analysis and the source size along the spacecraft trajectory. Empty colored cells indicate cases part of the study that have not been conducted yet.

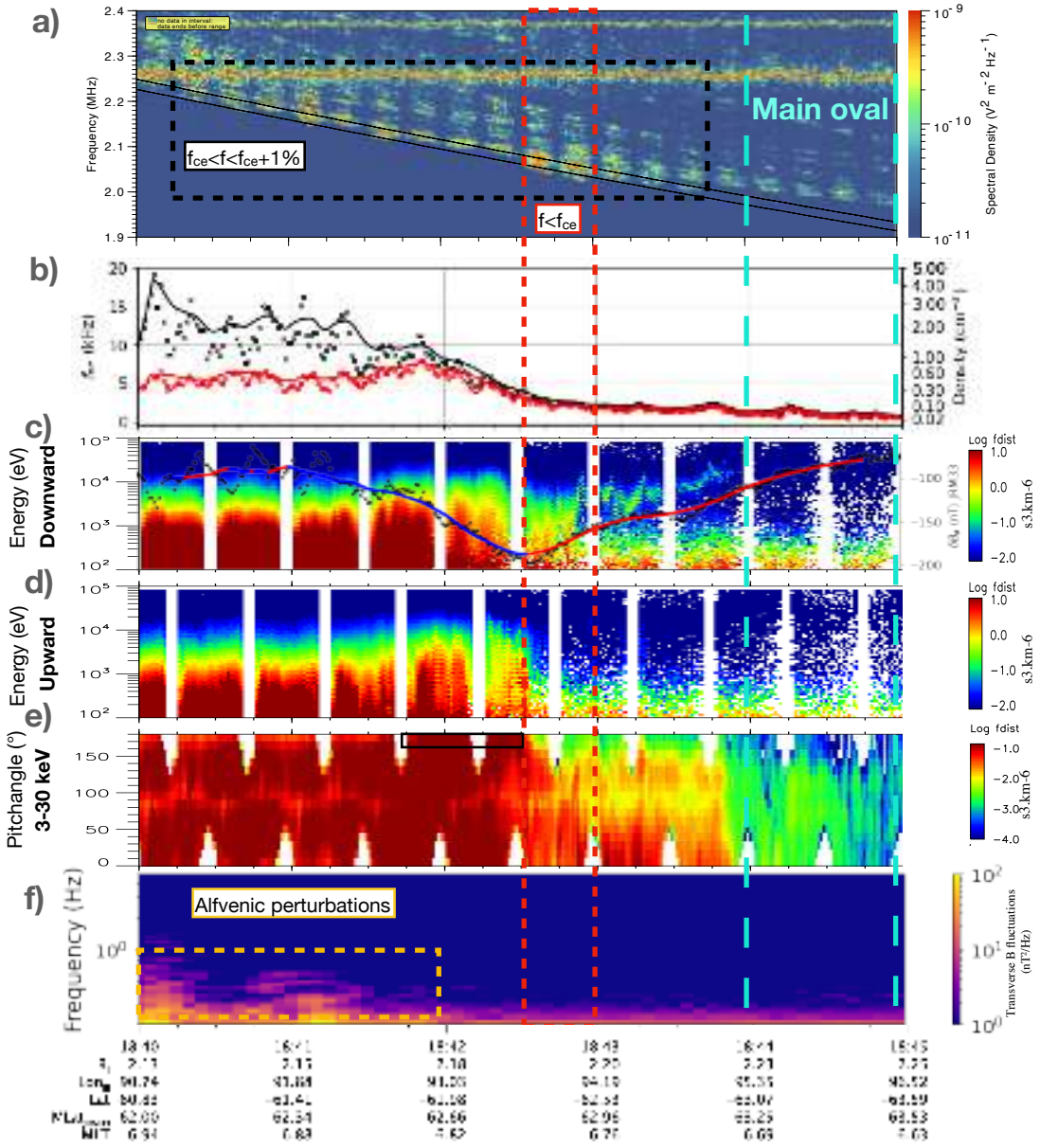


Figure 4.5.: Juno radio and particle measurements obtained during PJ32S on day 2021-02-21.

(a) Waves high resolution time-frequency spectrogram. The two solid black lines plot f_{ce} and f_{ce}+1%. The dashed red (black, resp.) boxes indicate emission at frequencies $f < f_{ce}$ ($f < f_{ce} + 1\%$, resp.). The vertical blue dashed line marks the timing after which Juno was colocated with the main UV auroral oval. The horizontal signal seen near 2.27 MHz is an instrumental radio frequency interference. (b) Electron plasma frequency f_{pe} (left-handed y-axis) or electron plasma density n_e (right-handed y-axis) plotted as a function of time, as derived from JADE-E for all electrons (black crosses) and for those above 1 keV only (red crosses). The solid lines plot the upper envelope of the density. (c) Time-energy spectrogram of the downward electron flux ($\theta < 30°$). The azimuthal magnetic field is superimposed on the panel with the right-handed y-axis. Its blue and red portions indicate downward and upward FAC. (d) Same as (c) for the upward electron flux ($\theta > 150°$). (e) Time-pitch angle spectrogram of the electron flux integrated between 3 and 30 keV. (f) Time-frequency spectrogram of the transverse perturbations of the magnetic field. The yellow box indicates Alfvénic fluctuations (during which no compressive perturbations were observed, supporting their Alfvénic nature).

Figure 4.5a shows a high-resolution radio dynamic spectrum ranging from 1.9 to 2.4 MHz. I observe emissions between f_{ce} and f_{ce} +1% from 18:40:10 to 18:43:45 UT (black dashed rectangle) and emissions strictly below f_{ce}, down to $f_{ce} - 0.5\%$, from 18:42:30 to 18:43:00 UT (red dashed rectangle). Figure 4.5b shows the electron plasma frequency f_{pe} (left-handed y-axis) derived from JADE-E measurements of the total electron density (black crosses). The contribution of energetic (>1 keV) electrons is shown in red.

Overall, n_{tot} is sharply decreasing between 18:42:00 and 18:43:00 from 1.5 cm^{-3} ($f_{pe} \simeq 10$ kHz) to 0.05 cm^{-3} ($f_{pe} \simeq 2$ kHz) resulting in f_{pe}/f_{ce} ratios as low as 1×10^{-3}. The contribution of energetic electrons becomes predominant after 18:42:00 with $\frac{n_h}{n_{tot}} \simeq 0.7$. Figures 4.5c and 4.5d show time-energy electron spectrograms in the downward ($\theta < 30°$) and upward ($\theta > 150°$) direction, respectively, while Figure 4.5e displays the time pitch-angle spectrogram for 3 keV to 30 keV electrons. On top of Figure 4.5c, the azimuthal magnetic field perturbations (see Chapter 3) are superimposed, whose blue and red portions indicate downward and upward FAC. Clear signatures of downward mono-energetic electrons between 1 keV to 20 keV form inverted Vs observed between 18:42:45 to 18:44:15, overlapping both the upward FAC layer starting equatorward of the main UV oval and the $f < f_{ce}$ HOM emission. The density of this mono-energetic population (not visible in the upward direction) is decreasing with increasing energy. Figure 4.5f shows a time-frequency spectrogram of transverse magnetic field fluctuations. Alfvénic fluctuations are visible equatorward of the MAO, from 18:40:00 to 18:42:00 (orange dashed rectangle), reminiscent of those identified by Gershman et al. (2019). These fluctuations coincide with the $f > f_{ce}$ source candidate, but not with the $f < f_{ce}$ one.

From the above results, I can infer the position of the auroral zones. Alfvénic fluctuations are characteristic of the Diff. A region. However, since their amplitude is known to decrease with increasing 3–30 keV electron flux (hereafter 18:41:30), the Diff. A region plausibly ends between 18:42:00 and 18:42:30. The $f < f_{ce}$ HOM emission lies strictly equatorward of the main UV auroral oval while coinciding with a depletion of the total electron density and with the upward FAC layer consistent with region ZI. Moreover, the source is connected to emissions with a low color ratio (up to 4), confirming the association with the UV DA.

The UV image in Figure 4.6 however, shows that the brightest emissions that I identify as the MAO are crossed from 18:47 to 19:00. The source crossings are indeed in the UV DA.

4.2.2. Predicted growth rates

Figure 4.7 illustrates the result of the growth rate analysis applied to one EDF measured at 18:42:46 UT. Figure 4.7a and b display the EDF and $\frac{\partial F_e}{\partial v_\perp}$ in the $(v_\parallel, v_\perp)$ plane on top of which the resonance circles yielding the maximum growth rate are shown for 3 categories: in green the shell type resonance circles, in blue dots circles intercepting the computed theoretical loss cone and in orange circles intercepting the downward and upward regions of the EDF outside the loss cone. Figures 4.7c-d plot all the

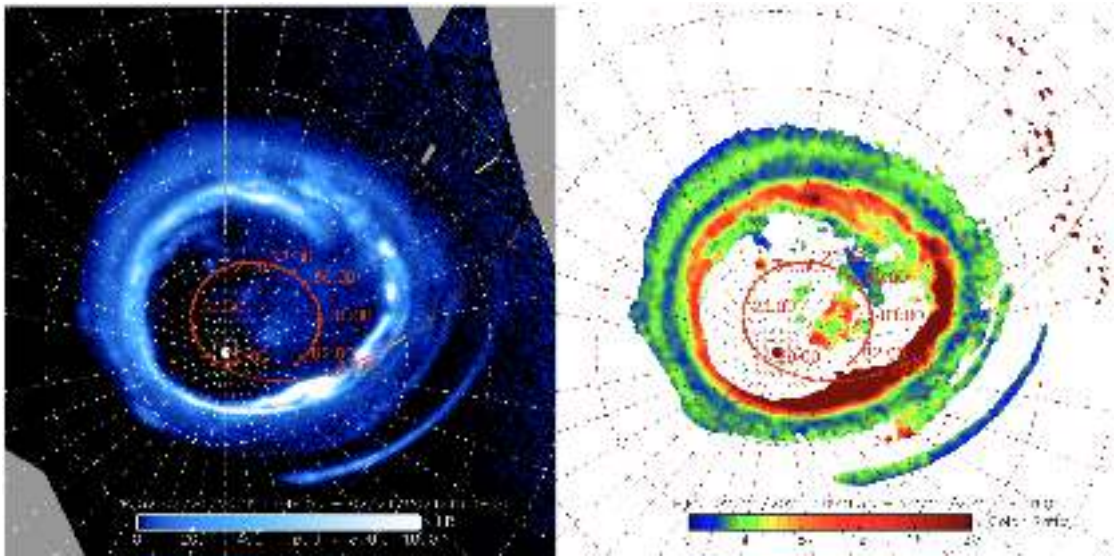


Figure 4.6.: UV image and color ratio during PJ32S. The orange trajectory shows the $f < f_{ce} + 1\%$ candidate source, and the pink trajectory shows the interval studied in section 4.3. Courtesy: Bertrand Bonfond.

calculated growth rates as a function of (v_0, v_r) and as a function of $\Delta\omega = \frac{\omega - \omega_{ce}}{\omega_{ce}}$. In Figure 4.7c, the black lines delimit the area of resonant circles consistent with the loss cone aperture. The maximal growth rate for each of the 3 categories of circles is marked by a symbol (green diamond for shell, blue for loss cone, and orange 'X' (resp '+') for the downward electrons (resp. for the upward electrons outside the loss cone). In Figure 4.7d the growth rates are plotted as a function of their associated $\Delta\omega$, and the same symbols are used for each category of circles.

Overall, two portions of the investigated EDF yield $\frac{\partial F_e}{\partial v_\perp} > 0$ and are therefore simultaneously CMI-unstable. The maximal growth rate $\gamma = 5.4 \times 10^{-5}$ is obtained for the shell resonance circle associated with a weakly energetic electron shell distribution at 0.9 keV and expected emission frequency 0.17% below f_{ce}. The other two circles (loss cone and other) lie close to each other. They yield lower growth rate maxima about 1.2 and 1.1×10^{-6}, respectively. They are associated with upward electrons of 5.3 and 4.6 keV, which should generate emission 1.02% and 0.88% above f_{ce}. Both these predictions are consistent with the observed radio emissions (in Figure 4.5a) at the corresponding frequencies, both below and above f_{ce} simultaneously.

Figure 4.8 presents the growth rate analysis of the full-time interval of Figure 4.5. Figure 4.8a displays the maximal growth rate for the 3 categories of resonance circle as a function of time. Figure 4.8b plots the associated characteristic electron energy. Figure 4.8c shows a high resolution radio dynamic spectrum, here plotted as a function of $\Delta\omega$, on top of which are plotted the emission frequencies derived from the radius of resonance circles yielding large enough growth rates (arbitrarily chosen $\gamma > 10^{-5}$, as a good compromise).

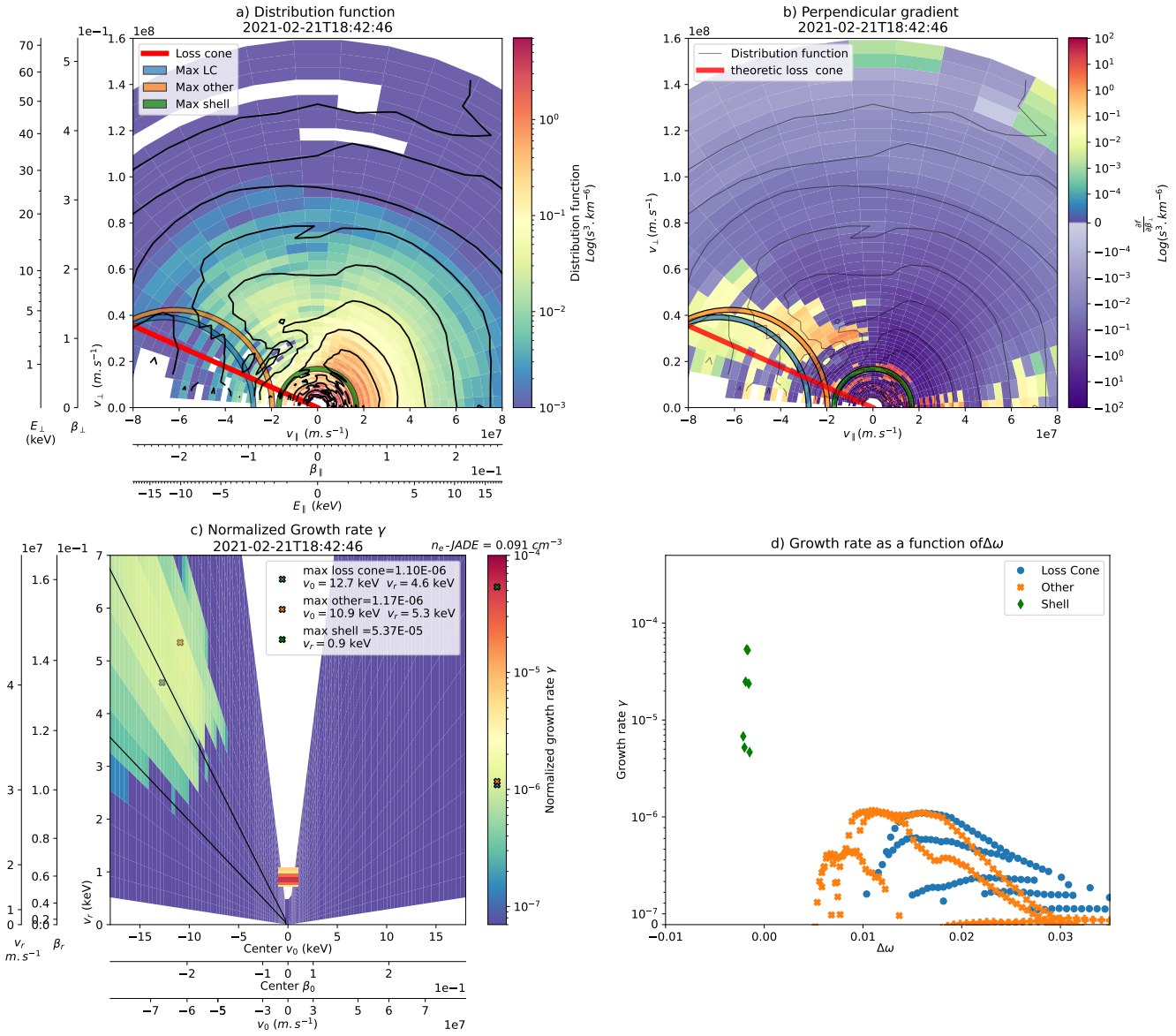


Figure 4.7.: CMI growth rate analysis of the EDF measured by JADE-E on 2021-02-21 18:42:46 UT (PJ32S).
(a) EDF displayed in the $(v_\parallel, v_\perp)$ phase space. For the sake of clarity, each axis displays velocities v in m/s, relative velocities $\beta = \frac{v}{c}$, and associated energies $E = \frac{1}{2} m_e v^2$ in keV. The black lines map isocontours of the EDF smoothed over 3 consecutive energy and pitch angle channels. The red line plots the theoretical loss cone aperture angle. The green, blue, and orange circles correspond to those yielding the maximal growth rates for the categories of CMI resonance circles testing shell-type, loss cone-type, and other (neither shell nor loss cone) unstable electrons. (b) Same as (a) with $\frac{\partial F_e}{\partial v_\perp}$ plotted instead of F_e. (c) CMI growth rate displayed as a function of the center v_0 and the radius v_r. The 2 black lines enclose the area corresponding to loss cone-type resonance circles. (d) CMI growth rate displayed as a function of $(\Delta\omega = \frac{1}{2c^2}(v_0^2 - v_r^2))$. The green, blue, and orange symbols again correspond to shells, loss cones, and other types of resonance circles.

Figure 4.7 *(previous page)*: For the latter category, the '+' and 'x' symbols distinguish between circles intercepting positive $\frac{\partial F_e}{\partial v_\perp}$ for electrons propagating downward or upward, respectively. For this time interval, the largest growth rates were obtained for upward electrons, such as for the loss cone resonance circles.

The 3 categories of circles simultaneously display positive growth rates, with γ ranging from 10^{-7} to a few 10^{-4}, over the whole interval. Before 18:42:20, the loss cone growth rates (blue dots) are prominent, gradually rising from 10^{-7} to 10^{-4}. They correspond to 0.3-30 keV electrons and emission frequencies of a few 0.1% above f_{ce}, consistent with the HOM low frequency envelope observed below f_{ce}+1%. I note at this occasion that the most unstable loss cone circles amplify waves predicted to be emitted on a hollow cone 4° to 8° from the magnetic field in the upward direction. This matches well with the predicted emission angles (Mottez et al. 2010).

Positive shell growth rates (green diamonds) appear after 18:42:10, peaking at a few 10^{-4} before monotonically decreasing down to 10^{-6} at 18:45:00. They correspond to electron energies increasing from 0.2 to 26 keV, and emission frequencies below f_{ce}. The latter matches the $f < f_{ce}$ HOM low frequency cutoff observed down to $f_{ce} - 0.5\%$ between 18:42 and 18:43 (for 1-3 keV electrons). As illustrated in Figure 4.9, the electron characteristic energy of the shell resonance circles gradually increases from 18:42 to 18:45, strikingly matching with the inverted Vs identified in Figure 4.5c. After 18:43:00, shell growth rates predict radio emission below $f_{ce} - 0.5\%$, which is unobserved by Waves.

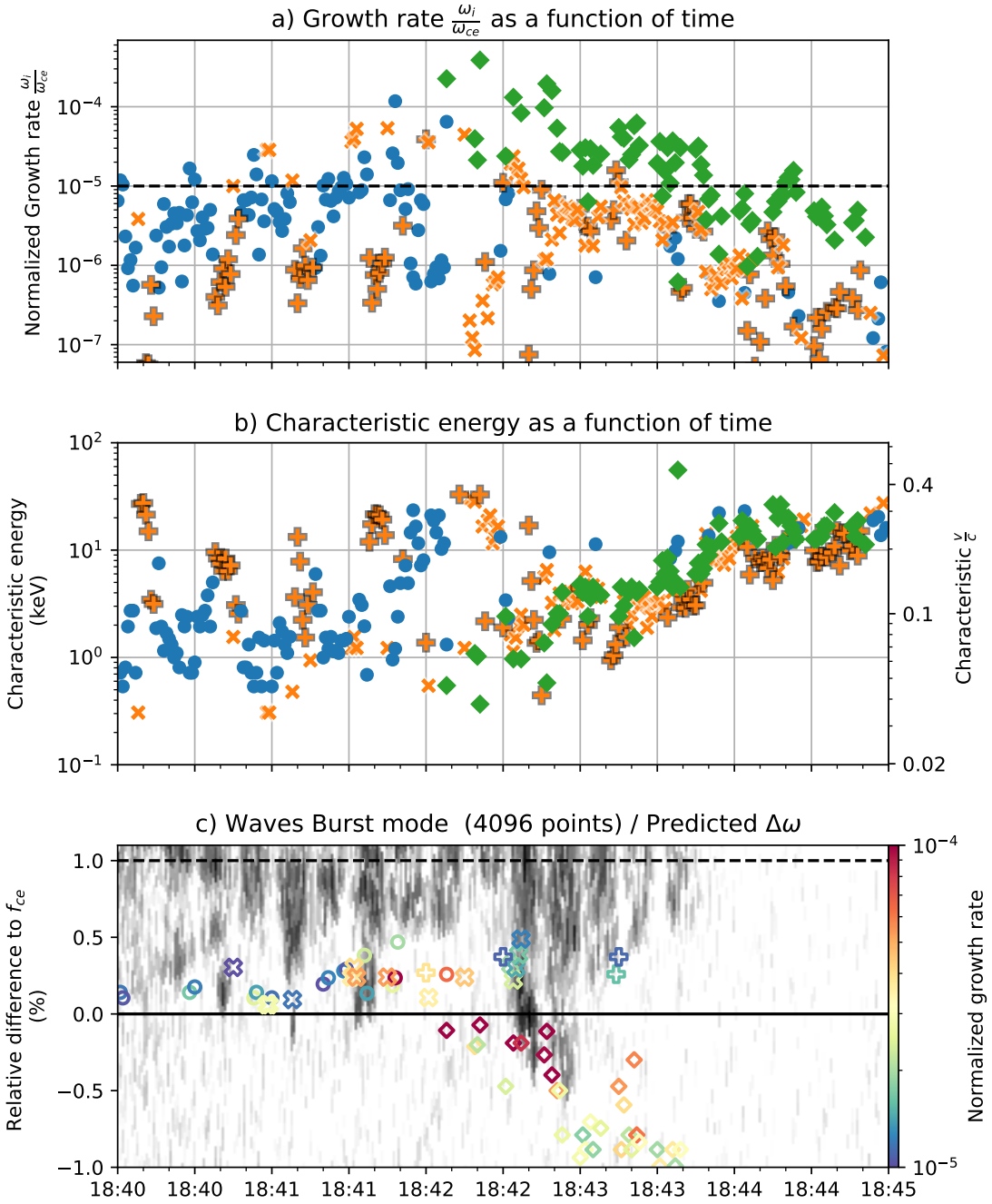


Figure 4.8.: CMI growth rate analysis applied to the full-time interval of Figure 4.5. (a) Maximum growth rate as a function of time for each EDF measurement (1-sec cadence) for the shell (green diamonds), loss cone (blue circle), upward other (orange 'x' crosses), and downward other (orange '+' crosses) types of resonance circles. (b) Associated electron characteristic energy as a function of time. (c) Waves high resolution dynamic spectrum plotted as a function of time and frequency relative to f_{ce}. The colored symbols map the predicted wave emission frequency for positive growth rates $\geq 10^{-5}$.

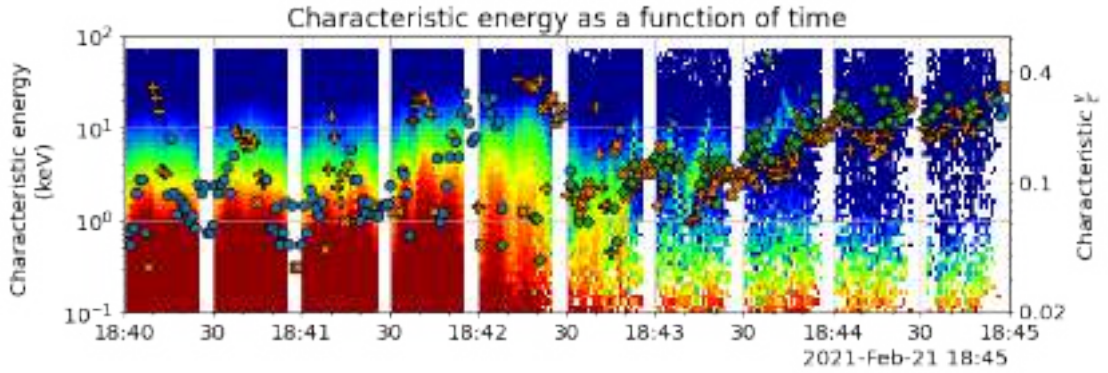


Figure 4.9.: Superposition of Figure 4.5c and Figure 4.8b

Figure 4.10 displays θ_{chara} for both the other and loss cone circles. As defined in Chapter 3, the circles associated with upgoing electrons were classified as loss cone whenever $|\theta_{chara} - \theta_{LC}| < 7.5°$, lying within the two black dashed lines on Figure 4.10a. This condition left circles consistent with an enlarged loss cone, clearly separated from the loss cone ones between 18:42:30 and 18:43:50. This enlargement might probe a downward acceleration experienced by the EDF consistent with the upward FAC layer encountered during this interval and/or a downward potential drop located below the spacecraft. Interestingly, Figure 4.10b also reveals a significant amount of other circles associated with the upgoing portions of the EDF, where $\frac{\partial F_e}{\partial v_\perp} > 0$. Such enlargement of the loss cone fits the definition of "conics" as they were identified as secondary sources of energy by Louarn et al. (2018). Similarly, this identification as "conics" can also be applied to resonance circles intercepting downward electrons. These conics generally yield modest growth rates, corresponding to expected emission near $f_{ce} + 0.2 - 0.3\%$ with emission angles from 84° to 86°, for instance, observed at 18:42:30 and 18:43:20.

The non-observation of radio waves expected to be amplified below $f_{ce} + 0.5\%$ from 18:41:40 and 18:42:30 and below $f_{ce} - 0.5\%$ after 18:43:00 from 2-20 keV electrons may be explained by transient, smaller sized, sources resulting in lower wave spectral flux densities, below the Waves' sensitivity threshold. From 18:42:00 to 18:42:30, the loss cone was generally filled in (black rectangle in Figure 4.5e), and unstable loss cone EDFs were not detected continuously.

Overall, the growth rate analysis of PJ32S validated the CMI as the HOM/DAM generation mechanism, confirming loss cone and conics as the prominent driver of emissions above f_{ce} and demonstrating the newly found shell EDF as being responsible for less frequent, transient, HOM/DAM emission below f_{ce}. HOM/DAM emission observed between $f_{ce} + 0.5\%$ and $f_{ce} + 1\%$ in turn most likely corresponded to a source observed from (slightly) remote distances rather than in situ.

I note that the unstable population sampled from 18:40 to 18:42 corresponds to the typical case for the main source of free energy for HOM/DAM $f < f_{ce} + 1\%$ sources: the loss cone. Hence, the results obtained in this interval also serve to characterize the $f < f_{ce} + 1\%$ sources.

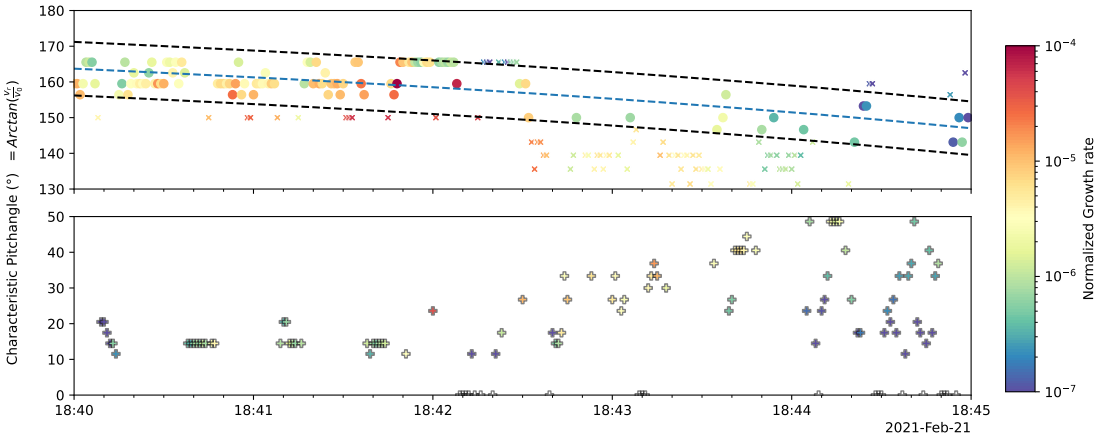


Figure 4.10.: Characteristic pitch angle $\theta_{chara} = \arcsin(v_r / v_0)$ of the loss cone-type (filled circle) and other-type (crosses) resonance circles yielding the maximum growth rate displayed in Figure 4.8a as a function of time for (top) up going and (bottom) downgoing electrons. The blue dashed line on the top panel indicates the theoretical loss cone aperture angle, and the black lines its ±7.5° uncertainty. Loss cone (other) resonance circles therefore lie within (outside) these black lines. The blue-to-red color scale corresponds to increasing growth rates.

4.2.2.1. Wave intensity

The wave intensity can be computed from the growth rate and Equation 2.26. Following the discussion of Section 2.5.1, I chose $v_g = 0.1c$ as a compromise between the result in the hot plasma and the cold plasma approximation at $\frac{\omega_{pe}}{\omega_{ce}} = 10^{-3}$.

The convective length was derived from the overall time interval $\tau_{cross} = 8s$ during which unstable shell-type electrons at energies consistent with the observed emissions are detected, which yields $400km$. I then transpose this source length along the spacecraft trajectory to its equivalent latitudinal extent as a more realistic estimate, so that $L_c \approx 100km$.

I derive a gain $G \approx 10^9$, which in turn provides a theoretical wave intensity of $S = 10^{-10}$ W.m^{-2}.Hz^{-1}, which is only 1 order of magnitude larger than the observed $S_{Waves} = 10^{-11}$ W.m^{-2}.Hz^{-1}.

4.2.3. CMI generation of all HOM/DAM crossed sources

To achieve a full understanding of $f < f_{ce}$ sources, I repeated the same growth rate analysis to the 15 [a]sources identified in the first 45 perijoves.

These sources were accompanied by adjacent sources generating emissions above f_{ce}. This analysis also allowed the study of the more frequent case of emissions $f <$

[a]the number of 15 differs from the total of 21 $f < f_{ce}$ sources discussed in the survey section, as the latter has been completed by the writing of this document, while the growth rate analysis of the last 6 events remains to be done.

$f_{ce}+1\%$. The intervals during which emissions are seen under $f_{ce}+1\%$ are longer and include those during which $f < f_{ce}$ (when present). These emissions were confirmed to be generated by the CMI relying on loss cone and conics as sources of free energy (Louarn et al. 2017, 2018). This is very different from the cases of AKR and SKR where the shell was found to be the main source of free energy.

These sources are often associated with Alfvénic perturbations in cold plasma but are not necessarily associated with any FAC. These sources are mostly associated with the UV DA.

Shell type EDFs was also statistically confirmed to drive CMI with electron energies corresponding well with the frequencies of the waves observed below f_{ce}. This validates that shell EDF constitutes a new, third CMI source of free energy, able to drive HOM at Jupiter, and the robustness of the $f < f_{ce}$ criterion to unambiguously track in situ crossed radio sources.

The plasma region hosting the $f < f_{ce}$ HOM/DAM sources is hot and tenuous with $n_h/n_{tot} \sim 0.6$ and $\frac{\omega_{pe}}{\omega_{ce}} \sim 3\times10^{-3}$ on average and often present mono energetic acceleration signatures. The radio sources are hosted along flux tubes with magnetic apex (M-SHELL) ranging from 17 to 50 R_J. In most cases, the sources are either magnetically connected to the equatorward boundary of to the MAO or connected to UV DA.

This survey revealed a strong north/south asymmetry, with only 3 $f < f_{ce}$ unambiguous sources detected in the north. The northern auroral region proved to host more complex and dynamical FAC systems (Al Saati et al. 2022) which may result in less frequent and/or more transient electron beams producing shell EDF than in the southern auroral region.

Only 4 out of 15 sources (27%) coincide with Alfvénic fluctuations, 12 out of 15 sources (80%) lie within an upward FAC layer, and match a gradual electron depletion. According to the criteria proposed in Mauk et al. (2018) and Sulaiman et al. (2022), the sources are located near the boundary between Diff. A. and ZI. The poor matching between the position of the MAO and upward FAC or the sporadic unexpected coincidence between the MAO and Alfvénic fluctuations renders the identification of auroral ZI and the region of Diff. A ambiguous. However, there is no obvious reason that these regions do not overlap. Note that a definite identification of which would have required the analysis of highly energetic electrons sampled by Juno/JEDI, which I did not include in this study.

The most unstable shell resonance circles correspond to growth rates up to a few 10^{-4} associated with weakly energetic electrons of 0.2 keV to 5 keV. The observed wave spectral flux densities S_{obs} range from 4×10^{-12} to 7.9×10^{-10} W.m^{-2}.Hz^{-1}. The latter, largest, value (observed at 5 MHz during PJ1S) transposes to 4×10^{-20} Wm^{-2}Hz^{-1} at 1 astronomical unit (AU), slightly below the median (50% occurrence level) intensity derived from statistical Waves observations Louis et al. (2021). This means that the crossed HOM/DAM sources corresponded to weak emissions, as observed remotely on average by Waves.

Poleward of the $f < f_{ce}$ observed sources, I regularly identified CMI-unstable shell EDF with large growth rates associated with more energetic, 2 keV to 20 keV, electron

beams but, surprisingly, without any visible radio counterpart. I have also identified on some occasions unstable shell resonance circles at larger (up to 30 keV) energies, yielding growth rates $\gamma \lesssim 10^{-6}$, also without any radio counterpart. A plausible explanation of the lack of emission observed below f_{ce}-0.5% might be that, in spite of reaching growth rates similar to the loss cone ones, a smaller convective length should result in lower radio wave flux, below the Waves (poor) sensitivity.

The HOM/DAM $f < f_{ce}$ sources share common properties with the AKR/SKR ones. They are embedded within an upward FAC and present mono energetic features reminiscent of inverted V signatures, observed in those sources. However, the $\frac{f_{pe}}{f_{ce}}$ ratios I observe are 1 order of magnitude smaller than the one observed at Earth and Saturn. In addition, while the sources are located in or near the ZI electron depletion, the usual $\frac{f_{pe}}{f_{ce}} < 0.1$ condition is verified even outside sources in the HOM range, thus no Earth-type, large-scale, auroral cavities were observed. The energies of the unstable shell (and thus the associated $\Delta\omega$) are in most sources (0.2 keV to 5 keV) lower than those observed in AKR 1 keV to 10 keV and SKR sources ()1 keV to 20 keV). This is quite surprising as the energies of the precipitating electrons at Jupiter can reach 1 MeV while they only reach a few keV at Earth. Nonetheless, it is interesting to note that more energetic (5 – 50 keV) CMI-unstable shell EDFs with large growth rates were systematically detected poleward of the tracked $f < f_{ce}$ sources, but without any radio counterpart. Smaller sources might be a plausible reason for preventing wave amplification beyond the Waves' sensitivity threshold. The increase in energy of the shell EDF toward the pole was correlated with a decrease in the total electron density, as expected from a static current system (Knight 1973).

During the $f < f_{ce}$ sources, different portions of the same EDF could therefore amplify radio emission below and above f_{ce} simultaneously.

4.3. CMI generation of HOM/DAM by highly relativistic electrons

As mentioned above, the contributions of electrons with energies larger than 100 keV to the precipitating budget are an important part of the precipitating electrons, whereas only low energy electrons associated with the UV DA have been found so far to be involved in the generation of Jovian HOM/DAM(see the previous section and Louarn et al. 2017, 2018; Louis et al. 2020). .

This is surprising as for AKR and SKR, the sources are colocated with the main, bright, auroral emissions.

Hereafter, I specifically investigate >30 keV electrons above the MAO as a possible driver for HOM/DAM emissions.

4.3.1. Case study: PJ32S

In section 4.2.1, I analyzed the HOM source observed at and below f_{ce} during PJ32S, focusing on JADE-E electron measurements between 100 eV and 30 keV. Below, I investigate the high energy extension of the EDF with JEDI measurements between 30 and 1200 keV from 18:42:30 to 18:52:00.

During and after this source crossing, a monoenergetic feature extending above 30 keV was identified in JADE-E spectra. As shown in Figure 4.9, the characteristic energy of the unstable resonance circles generating the observed radio emissions followed the energy trend of this monoenergetic event.

The plasma context of the studied event is shown in Figure 4.11. Figure 4.11a shows Waves/Burst mode time frequency spectrogram where the solid lines represent f_{ce} and $f_{ce}+1\%$ while the dashed lines represent $f_{ce}+10\%$, $f_{ce}+20\%$, and $f_{ce}+30\%$. The source crossing below f_{ce} is represented by the red dashed box. No other emissions were detected below $f_{ce}+1\%$ (nor below f_{ce} not shown here). Note that electrons of high energy can produce emissions far from f_{ce}. For instance, resonance circles with characteristic energies of 30 keV and 1000 keV, Equation 2.5f gives that the amplified wave will be emitted 5.4% and 44% above f_{ce}. While emissions are seen below f_{ce}+40%, it is not clear if they are produced locally or from regions where f_{ce} is larger.

Figure 4.11b shows the plasma frequency derived from JADE-E measurements (in black) and JEDI measurements (in purple). The purple boxes highlight intervals where the JEDI-derived density is larger than half the JADE-E-derived density, probing regions where the plasma is dominated by relativistic electrons. For the whole interval, $\frac{f_{pe}}{f_{ce}}$ does not exceed 3×10^{-3}

Figures 4.11d and 4.11f show JADE-E energy and pitch angle spectra in the same format as Figure 4.5. In Figure 4.11d, 3 inverted V can be observed (18:42:30 to 18:45:30 ; 18:45:30 to 18:47:30 ; 18:47:30 to 18:51:58) from 1 keV to the upper JADE-E energy limit (30 keV). Broadband amplifications are seen below 1 keV during the last two inverted Vs. Figure 4.11c extends this energy spectrum to the JEDI energy range where the maxima of these inverted V are seen. The intervals where the hot electrons contribution becomes important (purple boxes in Figure 4.11b) coincide with these maxima. Figures 4.11e and 4.11f show the pitch angle spectra in the 30 keV to 1000 keV energy for JEDI and 3 keV to 30 keV energy for JADE-E. In Figure 4.11f, the enlargement of the loss cone identified in Section 4.2.1 is highlighted by a green box, and several electron beams are highlighted by black boxes. These enlargements and these beams are not observed simultaneously in Figure 4.11f. Indeed, an enlargement of the loss cone is seen only in JEDI measurements from 18:48:00 to 18:49:15 in Figure 4.11e.

Also, the JEDI pitch angle coverage is sometimes not sufficient to observe the loss cone for the whole interval.

Note also that during the studied interval, Juno was connected to the MAO (as shown by the purple trajectory in Figure 4.6). These emissions exhibited a high color ratio, coherently with the observed high energy population.

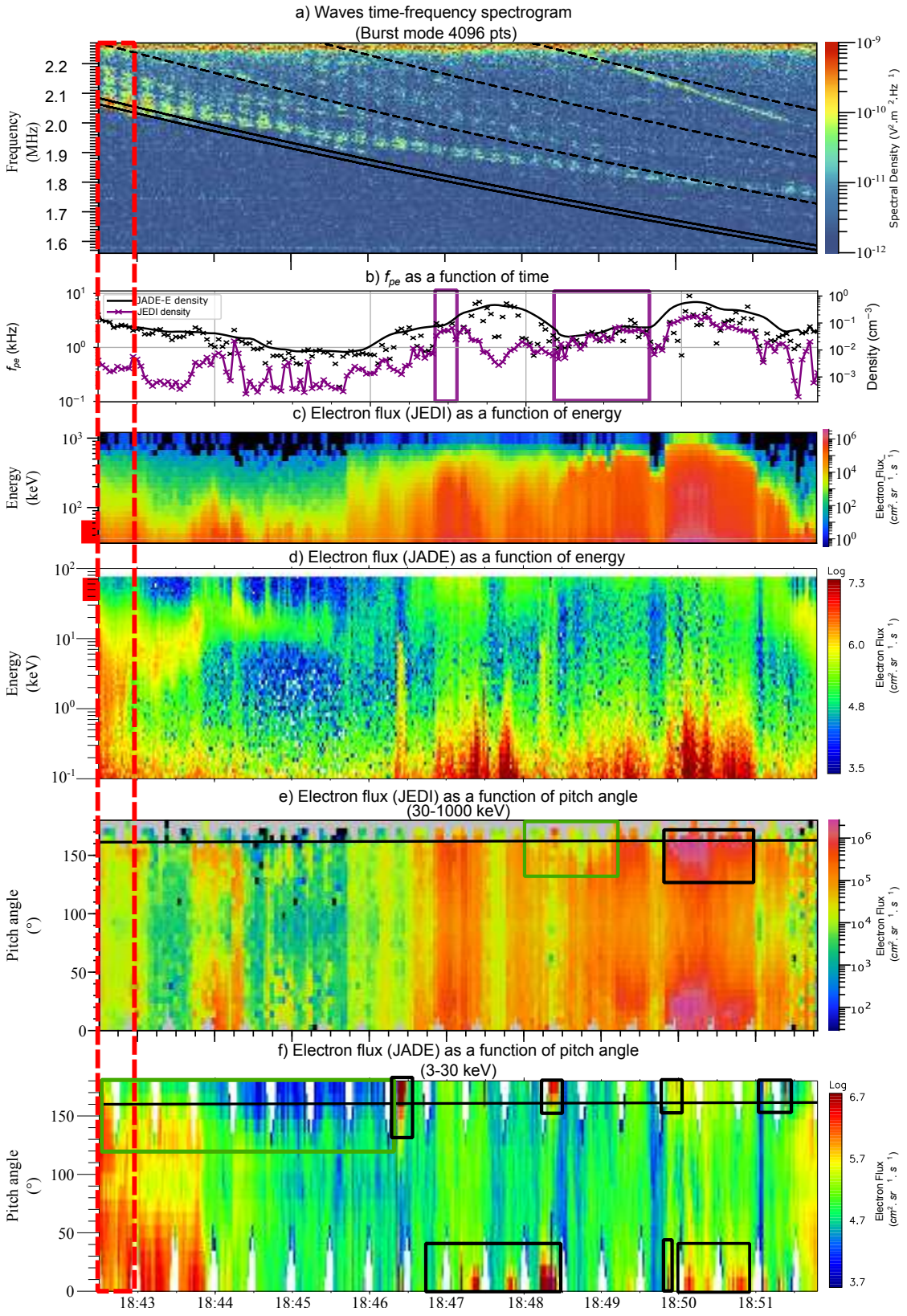


Figure 4.11.: PJ32S Waves and plasma context.
(a) Waves/Burst Time-frequency radio spectrogram (b)Plasma frequency derived from JEDI (purple) and JADE-E (black). (c) and (d) Electron flux energy spectra from (c) JEDI or (d) JADE-E. (e) and (f) Electron flux pitch-angle spectra from (e) JEDI or (f) JADE-E

4.3.2. Growth rate analysis

Even if no radio emissions were clearly identified during this interval, I computed the growth rate for the studied analysis with the same expression as in previous cases (Equation 2.23) but with a relativistic resonance condition yielding an ellipse (instead of a circle, see Chapter 2).

I remind here that a resonance ellipse is described in the $(\beta_\parallel, \beta_\perp) = (v_\parallel/c, v_\perp/c)$ phase space by its semi-minor axis $r_\parallel$, semi-major axis $r_\perp$, and center β_{0e}. Since $r_\parallel$ can be expressed as a function of $r_\perp$ and β_{0e} (Eq. 2.5d reminded in 4.1), an ellipse can then be simply defined solely by the two parameters $r_\perp$ and β_{0e}.

Since $r_\parallel^2 > 0$, the maximum $r_\perp$ value for a set β_{0e} can be retrieved from Equation 4.1 : $\sqrt{1-\beta_{0e}^2}$.

I defined 20 resonance centers β_{0e} in the interval $\beta_{0e} \in [0.067, 0.9]$ for each direction (upward and downward). For each value of β_{0e}, the semi-major axes $r_\perp$ were defined as 20 logarithmically spaced values between $0.2\beta_{0e}$ and $0.6\sqrt{1-\beta_{0e}^2}$. Thus resulting in $20 \times 2 \times 20 = 800$ ellipses. Waves amplified by these ellipses are oblique. A subset of these ellipses is shown in Figure 4.12 in which the eccentricities increase as the ellipses approach the limit $v = c$.

In the case of resonance ellipses with $\beta_{0e} = 0$, Equation 4.1 gives $r_\parallel = r_\perp$ thus transforming the ellipse into a circle.

$$r_\parallel^2 = r_\perp^2 \left(1 - \frac{\beta_{0e}^2}{1 - r_\perp^2}\right) \tag{4.1}$$

For shell resonance circles, I defined 36 (twice the number of used JEDI energy channels) resonance circles logarithmically spaced.

For the sake of simplicity, I took $\frac{n_h}{n_{tot}}$ as the ratio between JEDI and JADE-E derived densities. This rough assumption neglects that the energy ranges of both instruments overlap but compensates for the missed cold electrons.

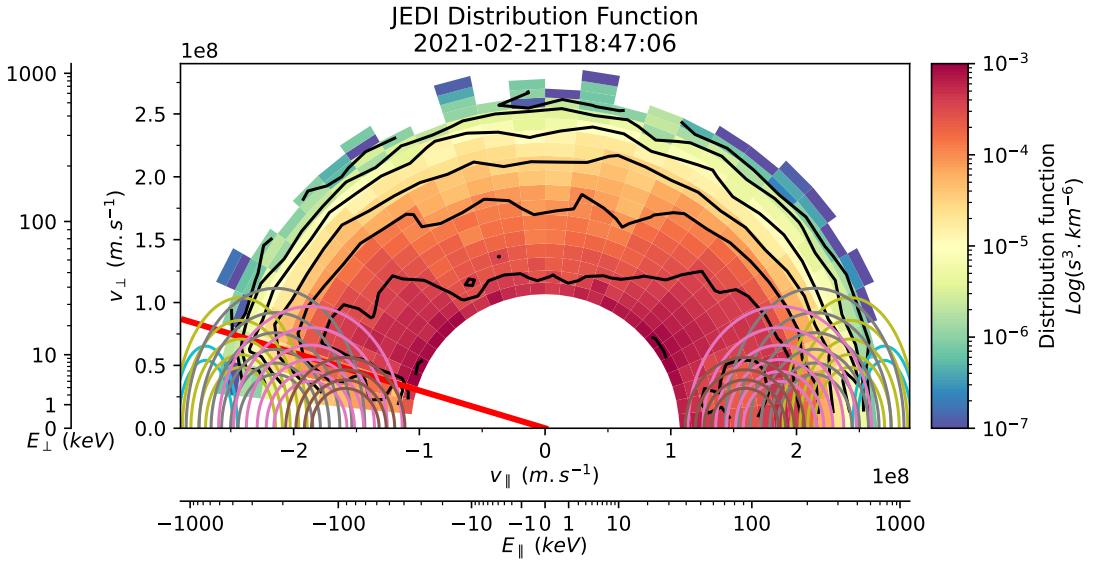


Figure 4.12.: Illustration of resonance ellipses chosen for the growth rate computation on PJ32S.

Figure 4.13 illustrates the method on 2 high-energy EDFs. The EDF shown in Figure 4.13a was measured on 2021-02-21 from 18:47:06 to 18:47:09. A clear depletion is visible below the loss cone while a depletion occurs at large picth angles and in the downward region near $v_\parallel$ =1.5 × 10^8 m · s^{-1}(80 keV). It is unclear if this depletion is due to a cone or 2 parallel beams. Also, the depletion seen at $\theta = 90°$ suggests the possibility of a conic being superimposed on the loss cone. For the sake of simplicity, these features are categorized as loss cone and conics simply using the criterion based on θ_{chara} (see Chapter 3).

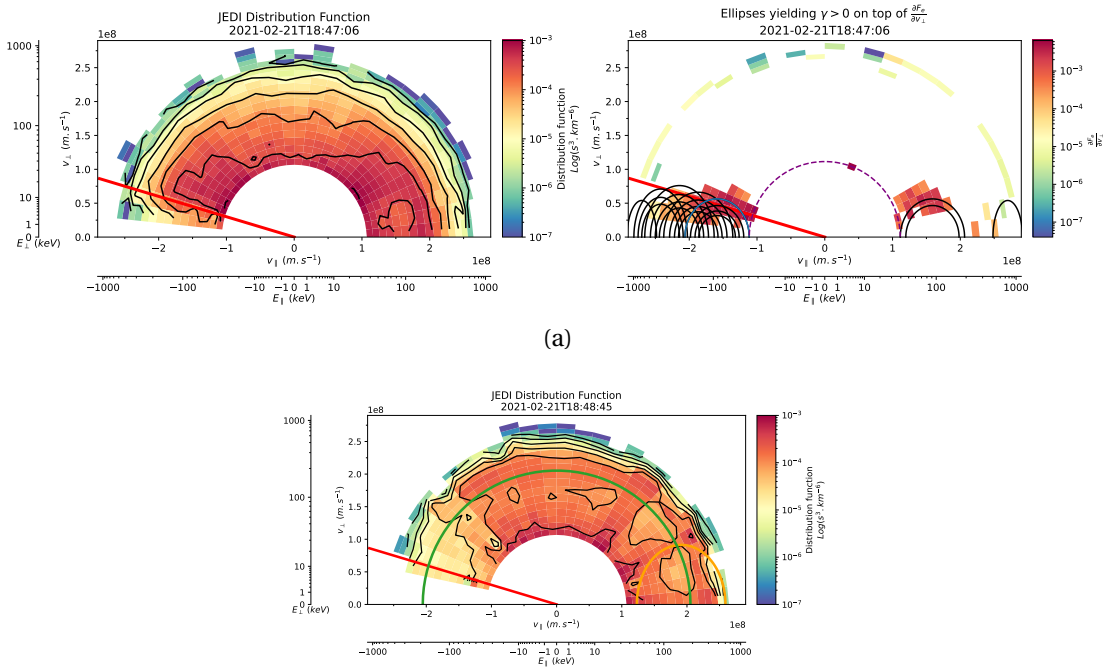
Figure 4.13b shows positive values of $\frac{\partial F_e}{\partial v_\perp}$ and all resonance ellipses yielding positive growth rate values. This figure confirms that the features described are unstable but also that the sole use of JEDI does not allow for covering the whole range $\frac{\partial F_e}{\partial v_\perp} > 0$. Indeed, no ellipses can intercept the $\frac{\partial F_e}{\partial v_\perp} > 0$ values seen at low energy and intermediate pitch angle in both direction (for instance, at 1.1 × 10^8 km · s^{-1} = 38 keV and $\theta = 40°$) without extending below JEDI energy range.

The resonance ellipse yielding maximum growth rate (1 × 10^{-7}) is plotted in blue.

Another example is shown in Figure 4.13b obtained from 18:46:42 to 18:46:45. The upward part of the EDF is depleted beyond the loss cone. However, the ellipse that yields maximum growth rate is in the downward direction and intercepts a conic near $\theta = 45°$. This is likely because no ellipse can intercept the large loss cone without extending to JADE-E energy range or without violating the condition 2.6.

On top of the multiple conics, a radial intensification of the EDF is visible at 2 × 10^8 m · s^{-1} (180 keV) and is more obvious at $\theta = 90°$. This amplification corresponds to a shell and is well-fitted by the green circle that yields growth rates of a few 10^{-7}.

These two figures illustrate that every part of the EDF can be unstable in this interval. These unstable populations should amplify both perpendicular and oblique waves.



(a)

Figure 4.13.: 2 cases of unstable EDF measured by JEDIin PJ32S.
(a) EDF measured from 18:47:06 to 18:47:09. The red line indicates the approximate loss cone. (b) Unstable resonance circles on top of $\frac{\partial F_e}{\partial v_\perp}$ where it is positive. The blue circle designates the circle yielding the maximal growth rate. The purple dashed circle illustrates JEDI lower energy limit. (c EDF measured from 18:42:30 to 18:46:45.)

The results of the growth rate analysis are shown in Figure 4.14 with the same format as Figure 4.8. Figure 4.14a shows that, during two time intervals, ranging from 18:42:30 to 18:46:45 and from 18:47:30 to 18:48:30, modest positive growth rates of γ reaching 1×10^{-7} are produced by various parts of the EDF including the loss cone (blue circles), shell (green diamonds), and upward/downward conics (purple/orange crosses). The associated characteristic energies of the resonance ellipses in these regions (80-200 keV) follow an energy trend strikingly matching the inverted V visible on Figure 4.11. Note that the emissions associated with these resonance ellipses are very oblique (22° to 54°).

Outside these intervals, the highest growth rates mostly correspond to ellipses intercepting downward conics and the loss cone.

Figure 4.14c shows that the most unstable electrons of this interval are predicted to amplify waves at frequencies 15% to 37% above f_{ce}. Some of these frequencies are close to an observed emission (near $f_{ce} + 37\%$). It is unlikely that these waves are produced by these resonance ellipses, as the observed emission does not reach its minimal $\Delta\omega$ usually associated with the source crossing. Note also that the identified shell should produce emissions 37% below f_{ce} where no emissions were observed.

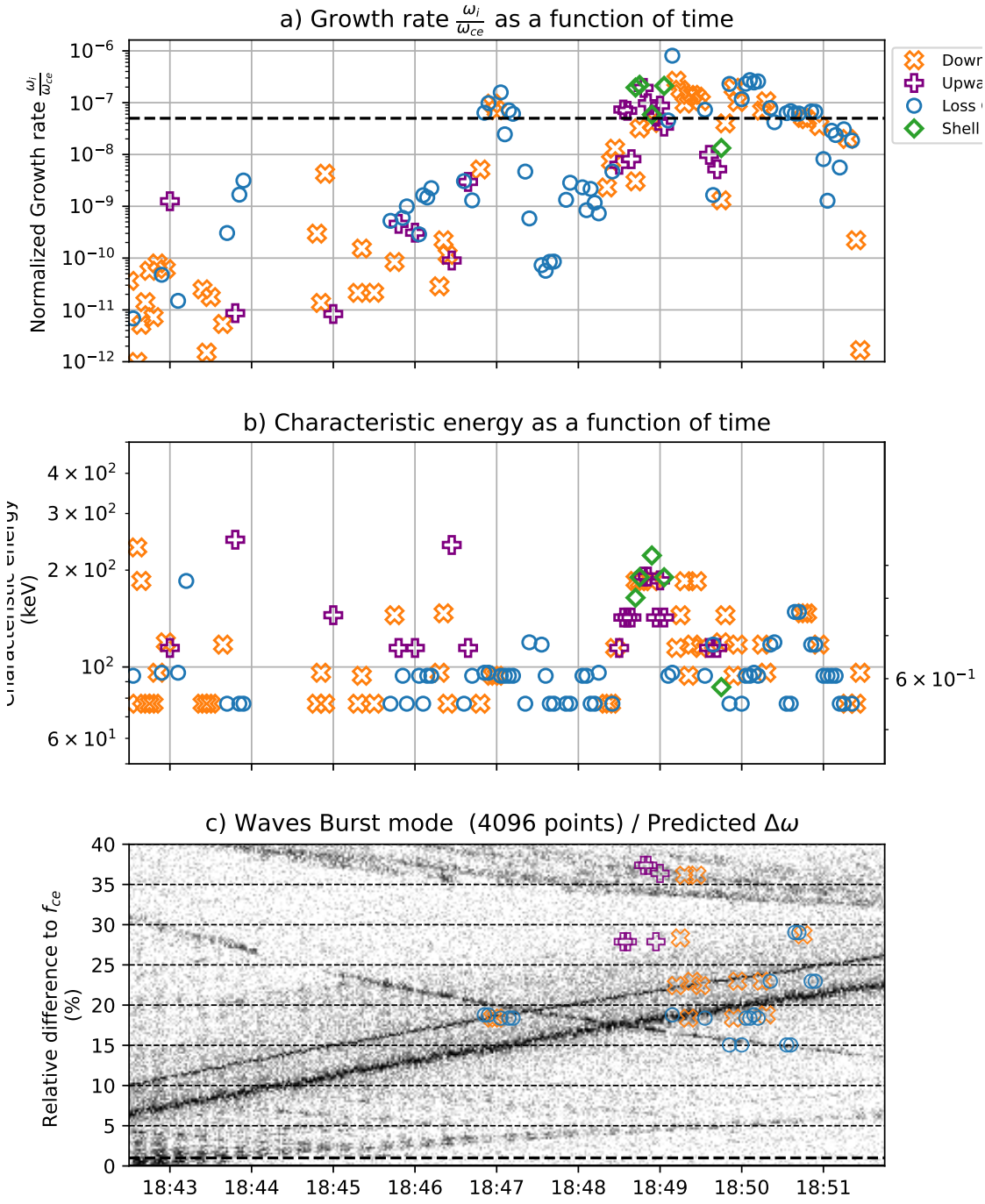


Figure 4.14.: Growth rate analysis during the regions of PJ32S connected to the MAO in the same format as Figure 4.8

From 18:48:45 to 18:49:10, modest positive shell growth rates ($\gamma \sim 10^{-7}$) are identified. For a source size of 3×10^3 km (corresponding to a source crossed for 60 s) and a group velocity of $v_g = 0.1c$, even an overestimated growth rate of 1×10^{-6} can only amplify waves with a gain of 12 leading only to a wave intensity of 1×10^{-18} $Wm^{-2}Hz^{-1}$ which is well below Waves sensitivity (1×10^{-12} $Wm^{-2}Hz^{-1}$ from Figure 3.2).

4.3.3. Summary for the PJ32S case

This case study revealed that electrons of high energy electrons (80-200 keV) can be CMI unstable and present the same types of unstable populations as those observed in the low energy (0.5-5 keV) range. However, these electrons drive much more modest growth rates (up to 1×10^{-7} , typically 2 orders of magnitude less than 0.5-5 keV electrons), so that the associated amplified radio waves are likely not detected by Waves.

This study allows questioning the $f_{ce} < f < f_{ce} + 1\%$ criterion but also showed that the unambiguous detection of oblique emissions generated by high energy electrons is difficult since they can be emitted up to 40% above f_{ce} where they are drowned out in the remote emissions. Conversely, perpendicular emissions would be easy to identify 40% below f_{ce}.

In the CMI formalism used to investigate relativistic electrons, while I used realistic resonance ellipses, I only used the semi-relativistic approximation to derive growth rates.

Zhang et al. (2023) numerically computed the growth rate in the semi and fully relativistic approximations for an analytical power law EDF. They obtained growth rates only 3 times larger with a fully relativistic treatment.

Ideally, JADE-E measurements should be used combined with JEDI measurements to exhaustively test all CMI resonances ellipses from 100 eV to 1.2 MeV.

4.4. Discovery of HOM harmonic emission

This section provides preliminary results about the identification of HOM harmonic.

As reminded in Chapter 1, the literature only reports an attempt detection for the Io-DAM and HOM components, which were never confirmed.

CMI emission at harmonics given by equation 2.1 is possible and helps to refine our understanding of the electron-wave energy conversion process.

As the first harmonics are predicted to be 2 orders of magnitude weaker than the fundamental when $\frac{f_{pe}}{f_{ce}} < 0.3$ (Lee and Wu 1980; Wu and Qiu 1983), the optimal conditions to observe the harmonics requires maximizing the intensity of the fundamental. This can be done by approaching the source. Hence, I will only consider source crossings to identify harmonics. As first harmonics are not distinguishable from the fundamental in the low resolution Survey mode from Waves, we will solely use high resolution Burst mode measurements.

The harmonic is not observable with HFR-High (3.5 to 41 MHz) receiver as its measurements are given on a 1 MHz wide bandwidth around the local f_{ce}.

In the HFR-Low and LFR-High frequency range (150 kHz to 3.5 MHz), HOM harmonics can only be observed if the associated fundamental are between 150 kHz and 1.75 MHz or between 10 kHz and 75 kHz. Thus, only bKOM and HOM harmonics are surveyed.

After the fortuitous detection of a harmonic in one of the cases shown below, I then resurveyed the catalog of HOM sources which fitted the condition f <1.75 MHz or 10 kHz < f < 75 kHz to identify emissions close to $2 \times f_{ce}$. To avoid confusing harmonics and distant sources, I compared the shape of the fundamental and candidate harmonic in a time-frequency spectrogram and in time-$\frac{f-f_{ce}}{f_{ce}}$ and time-$\frac{f-2\times f_{ce}}{2\times f_{ce}}$ spectra.

4.4.1. Two harmonic detection examples

Overall, I only identified 2 sources where the first harmonic was detected: PJ66S (2024-10-22 19:50 to 20:30) and PJ73S (2025-06-08 22:20 to 23:30). This low number can be explained by the fact that in most cases, first harmonics are expected to have a frequency on the HFR-Low band close to a frequency-variable parasite and at intensities close to HFR-Low noise level (1×10^{-12}) and in a spectral range strongly contaminated by a frequency-variable parasite.

Figure 4.15 shows 3 spectrograms of PJ66S source crossing. Figure 4.15a shows a time-frequency spectrogram where f_{ce} and $2 \times f_{ce}$ are shown in black lines while Figure 4.15c and d show radio spectrogram as a function of time and $\frac{f-f_{ce}}{f_{ce}}$ and $\frac{f-2f_{ce}}{2f_{ce}}$, respectively, between -2% and 10%. In Figure 4.15a, a clear and strong emission is detected above and slightly below f_{ce} over a remarkably extended period between 20:08 and 20:20. This long duration can be attributed to the short distance (130×10^3 km) crossed by Juno during this source crossing.

Near $2 \times f_{ce}$, a weaker emission (in yellow) follows the typical arc shape of auroral emissions from 20:00 to 20:10. Comparing the Figure 4.15 c and d panels confirms that the 2 emissions follow the same trend and reach f_{ce} (resp $2 \times f_{ce}$) simultaneously. However, Figure 4.15 c shows that the harmonic has an intensity close to the HFR-Low noise level, which makes part of the emissions absent compared to their corresponding fundamental in Figure 4.15d. This can explain the absence of emissions below $2 \times f_{ce}$ in Figure 4.15c.

Figure 4.15b shows the uncalibrated spectral density at 20:04:01 as a function of the frequency. The ratio between the peak intensities of the fundamental and the harmonic (red lines) is estimated at 1.7×10^{-2} This is coherent with the theoretical predictions and the observed ratio for SKR (Wu et al. 2022).

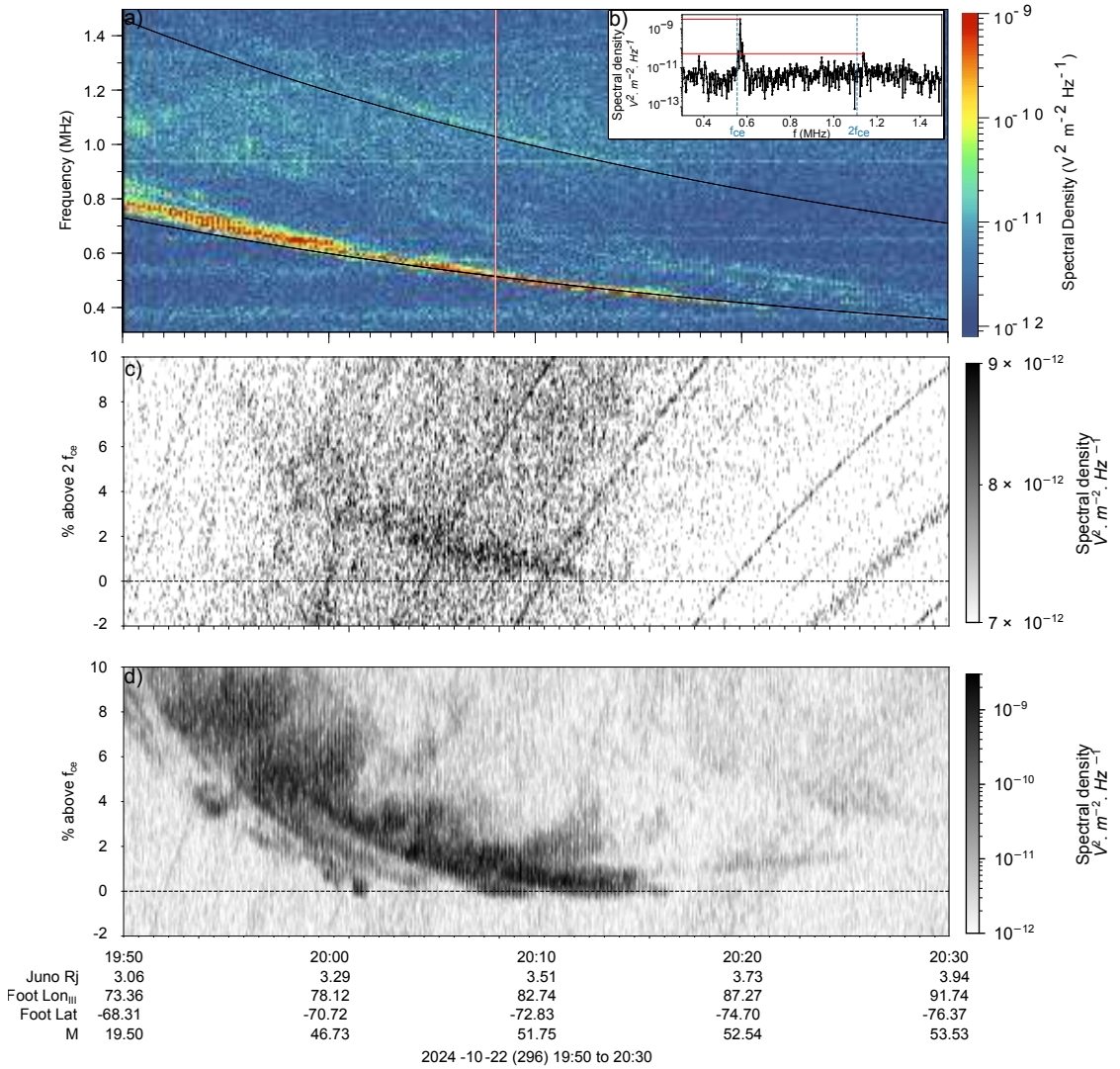


Figure 4.15.: Spectrograms of the harmonic seen during PJ66S in (a) time-frequency and a (c) time-$\frac{f}{2f_{ce}} - 1$ (d)time-$\Delta\omega$ spectrograms. The black lines show f_{ce} and $2f_{ce}$. (b) Spectral density measured at 2024-10-22 20:04:01 (red dashed line).

Similarly, Figure 4.16 has the same format as Figure 4.15 but for the case of PJ73S. In this case, the harmonic rather appears as patches (red boxes). The shapes of the harmonic I observe were reproduced in Figure 4.16d by red curves and illustrate the relevance of the detection. The harmonic/fundamental spectral density ratio reaches here 1.8×10^{-3}

These two examples display low harmonic/fundamental intensity ratios, comparable to those identified routinely for SKR at Saturn.

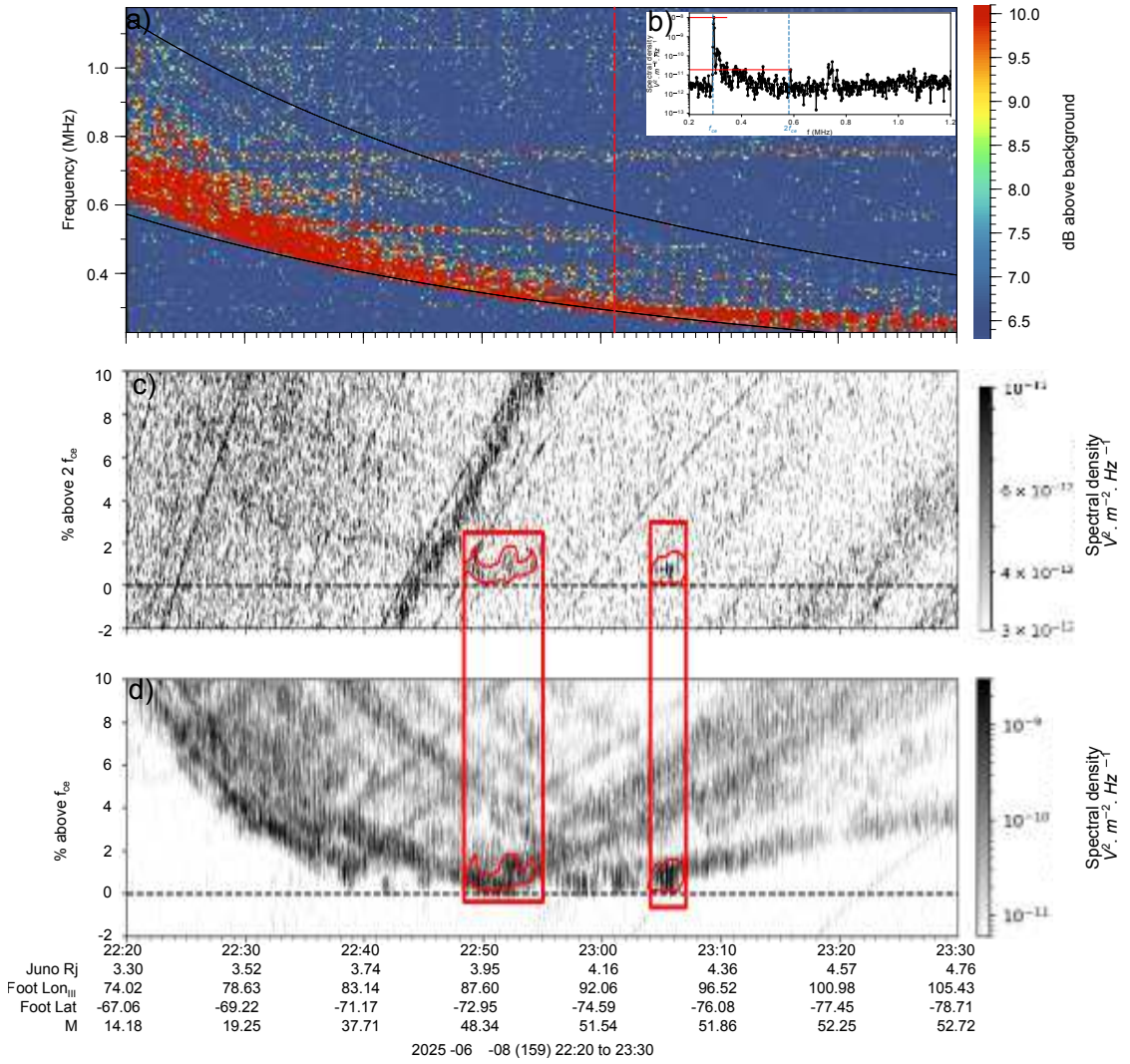


Figure 4.16.: Spectrograms of the harmonic seen during PJ73S
in (a) time-frequency and a (c) time-$\Delta\omega$ (d) time-$\frac{f}{2f_{ce}}-1$ spectrograms. The black lines show f_{ce} and $2f_{ce}$. (b) Spectral density measured at 2025-06-08 23:01:10 (red dashed line).

4.4.2. Plasma context

At the time of writing this section, electron measurements obtained by JADE-E for PJ73S were under *embargo* and for calibration purposes. Figure 4.17 shows the plasma context during PJ66S. Figure 4.17a is in the same format as Figure 4.5c except that the FAC are shown in Figure 4.17e. Figures 4.17b and c are in the same format that 4.5d except these panels are restricted to 0.1 keV to 3 keV and 5 keV to 33 keV respectively. Figure 4.17d is similar to Figure 4.5b except the density is displayed rather than the plasma frequency. This case is reminiscent of the $f < f_{ce}$ sources described in Section 4.2, with similar mono energetic signatures in Figure 4.17a from 20:00 to 20:30 that extend later. This large mono energetic event can be separated into 2. From 20:00

to 20:04, an inverted V is visible, from 20:04 to 20:30, its peak energy ($\sim 100 seV$) remains constant. Surprisingly, this separation is located near the change of FAC direction, which usually coincides with the end of an inverted V. No signs of Alfvénic perturbations were detected during this source crossing. Figures 4.17b-c show that the loss cone (near θ =180°) is empty for the whole interval at high energies and after 19:59 at low energies. The total density decreases from 7 cm^{-3} at 19:50:00 to 0.25 cm^{-3} at 20:05. Similarly to the mono energetic feature, the density remains constant from 20:05 to 20:30. The hot electrons dominate ($\frac{n_h}{n_{tot}} \simeq 0.8$) starting from 20:00 to 20:30. The density measured during the mono energetic event yields $\frac{f_{pe}}{f_{ce}} \sim 10^{-2}$.

The only difference between this case and typical HOM $f < f_{ce}$ source crossings is the duration during which the mono energetic signature is seen and the $\frac{f_{pe}}{f_{ce}}$ ratio that is one order of magnitude larger than usual. This value is close to the range of $\frac{f_{pe}}{f_{ce}}$ measured in AKR and SKR sources. Since the CMI is known to amplify preferentially the first harmonic at large $\frac{f_{pe}}{f_{ce}}$ (Winglee 1985), the low $\frac{f_{pe}}{f_{ce}}$ values reported in the rest of the $f < f_{ce}$ source catalog could explain why this harmonic had not been observed before.

A comparative analysis of the CMI growth rates for X and O-mode emissions at the harmonic frequencies, beyond the scope of this thesis, is needed.

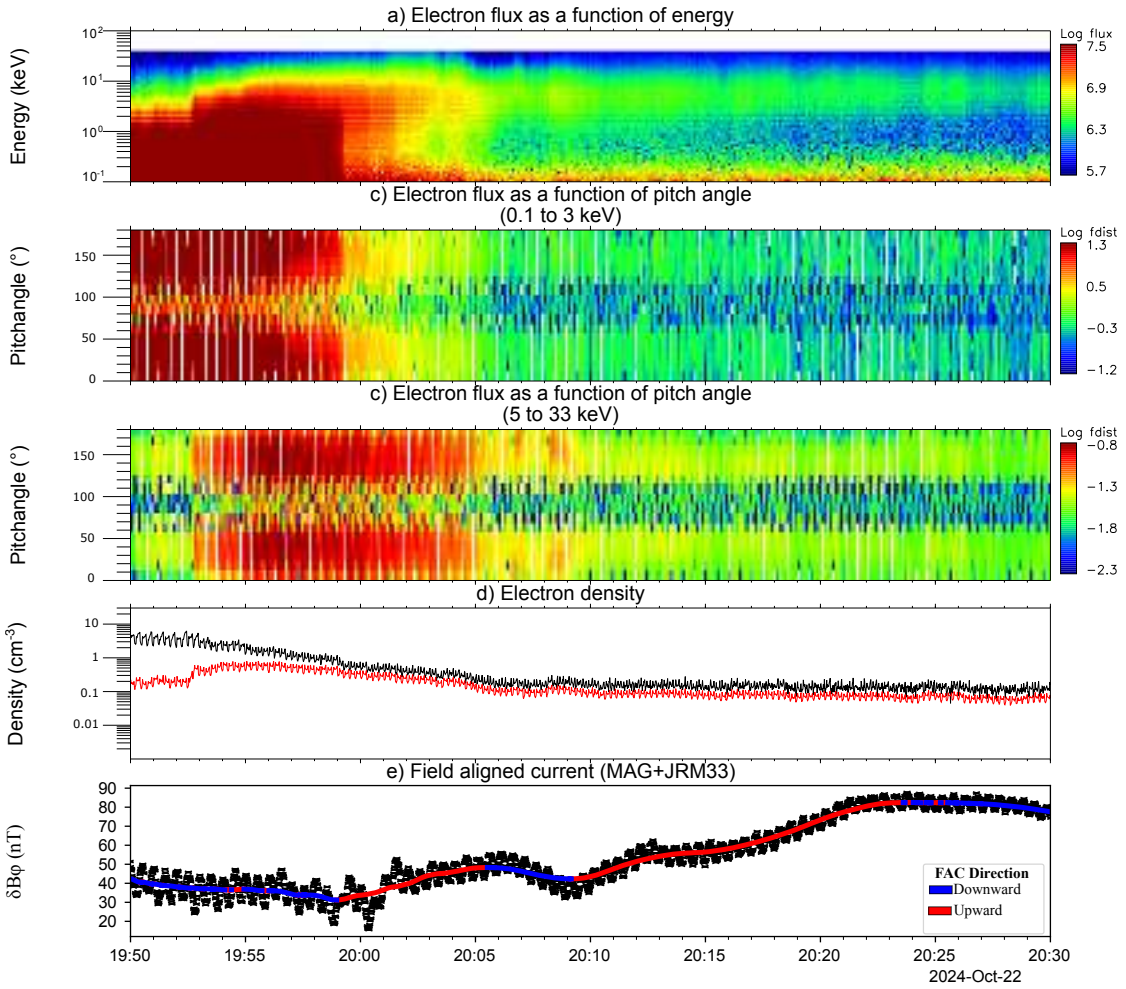


Figure 4.17.: Plasma context during PJ66S.
(a) Electron energy spectrum (b) Pitch angle spectrum for electrons 0.1 to 3 keV (c) Pitch angle spectrum for electrons 5 to 33 keV (d) Electron density. The red line displays the >1 keV electron density (e) δB_ϕ whose gradient indicates the direction of the FAC.

4.5. The case of moon-induced radio emissions

At the start of my PhD, while Io-DAM had been long studied remotely, only radio emissions induced by Ganymede had been studied in situ by Louis et al. (2020), who also confirmed the generation by the CMI.

I had the opportunity to contribute to two investigations on moon-induced aurorae for which I used the above-described growth rate analysis method. Both of these studies improved our understanding of moon-induced aurorae at radio and UV wavelengths and the underlying acceleration processes. Firstly, Louis et al. (2023b) statistically investigated the crossing of HOM/DAM sources associated with the auroral footprint of Io, Ganymede, and Europe radio emissions. Among the 7 identified source

candidates, ranging frequencies from 2 to 28 MHz, only 3 of those, all concerning Io, had electron measurements with the required pitch angle coverage enabling the application of my method (Section 4.5.1). Secondly, Rabia et al. (2025) discovered the Callisto-induced UV emissions, I used my method to discuss the plausibility of (unobserved) associated radio emissions (Section 4.5.2).

4.5.1. The source of Io-induced radio emissions

During the first 31 perijoves, the Io flux tube was crossed twice (one per hemisphere) per orbit (Szalay et al. 2020), but only 23 cases were observed in appreciable amounts by JADE-E. Among these, only 4 cases (PJ5N, PJ5S, PJ6N, and PJ29N) displayed a candidate source crossing established with the $f < f_{ce} + 1\%$ criterion. The analysis of cases PJ5S, PJ6S, and PJ29N, corresponding to flux tubes mapping to the tail of the Io main footprint, revealed positive growth rates. During the fourth case, PJ5N, where only downward electrons were sampled by JADE-E, no positive growth rates were found. I briefly present below the analysis of the representative case of PJ5S.

4.5.1.1. The case of PJ5S

Figure 4.18 shows JADE-E energy and pitch angle spectra in the same format as Figure 4.5b and c during the traversal of the Io flux tube identified in PJ5S (2017-03-27) between 09:30:51 and 09:31:02 (Szalay et al. 2020). This Figure shows the drastic, wideband intensification of the electron flux corresponding to this flux tube. Interestingly, Figure 4.18b shows that the loss cone is empty simultaneously.

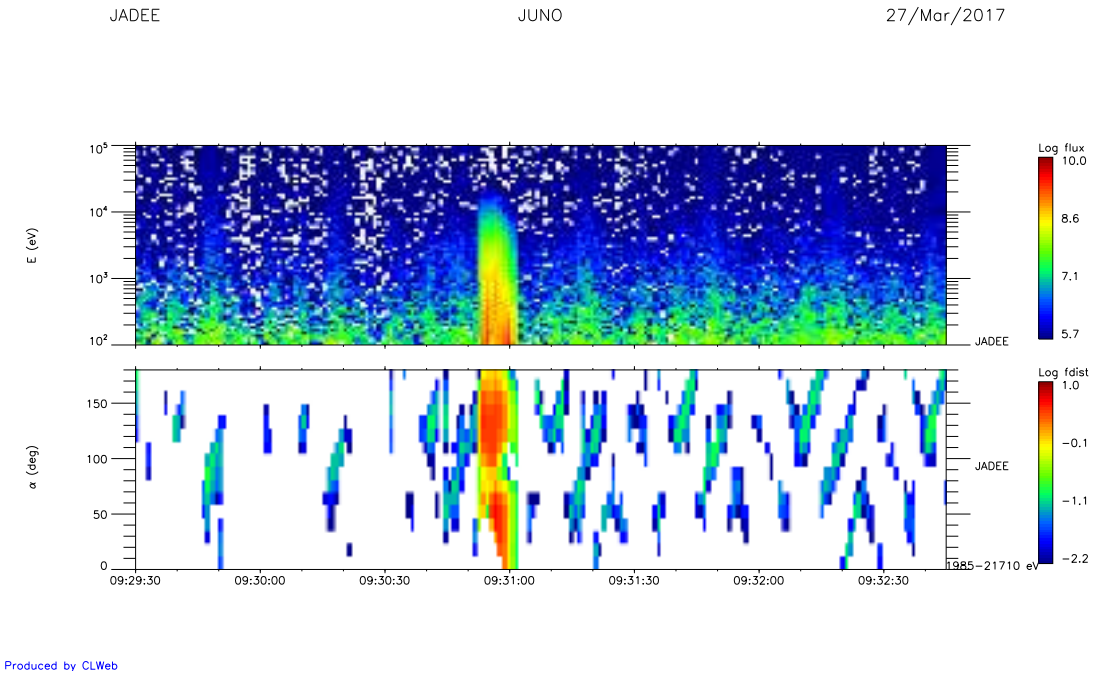


Figure 4.18.: JADE-E electron measurements during PJ5S Io flux tube crossing. (a) Energy spectrum (b) Pitch angle spectrum between 2 and 22 keV.

Figure 4.19 shows the corresponding Waves/Burst time-frequency spectrogram. A candidate source crossing is identified from the $f < f_{ce} + 1\%$ criterion at the same interval as the Io flux tube.

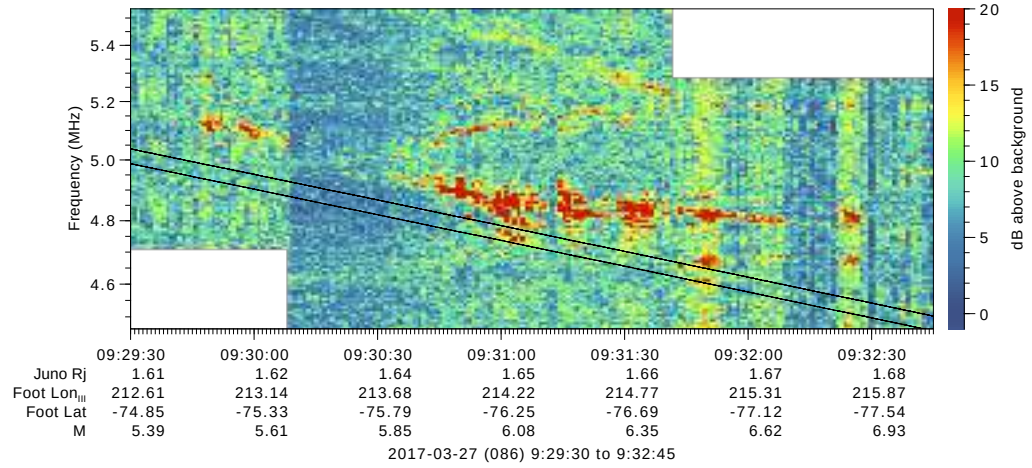


Figure 4.19.: Waves/Burst mode time-frequency spectrogram of PJ5S Io flux tube crossing

I computed the growth rate during the whole flux tube crossing and 2s before and after it. I obtained positive growth rates from 09:30:51 to 09:30:59. Figure 4.20 illustrates this by showing a EDF in the same format as Figure 4.7. The loss cone depletion is well-defined and easily observable from the isocontours in Figure 4.20a and in Figure 4.20b. Positive growth rates are obtained only in the upward direction. The circles yielding maximum growth rates intersect the theoretical loss cone illustrated by the red line. In this plot, the star symbols designate circles inside the loss cone but far below the aperture angle ($\theta_{chara} < \theta_{LC} - 7.5°$).

Throughout the Io source, the energy of the resonant electrons lies in the range 1 keV to 15 keV, generating emissions with $\theta_{(\vec{\mathbf{B}},\vec{\mathbf{k}})} \in [74° - 85°]$.

Note that no positive growth rates were found outside the flux tube crossing, as expected in the investigated CMI framework.

Interestingly, Louis et al. (2023b) showed that unstable electrons were only found during downward FAC, accelerating upward electrons.

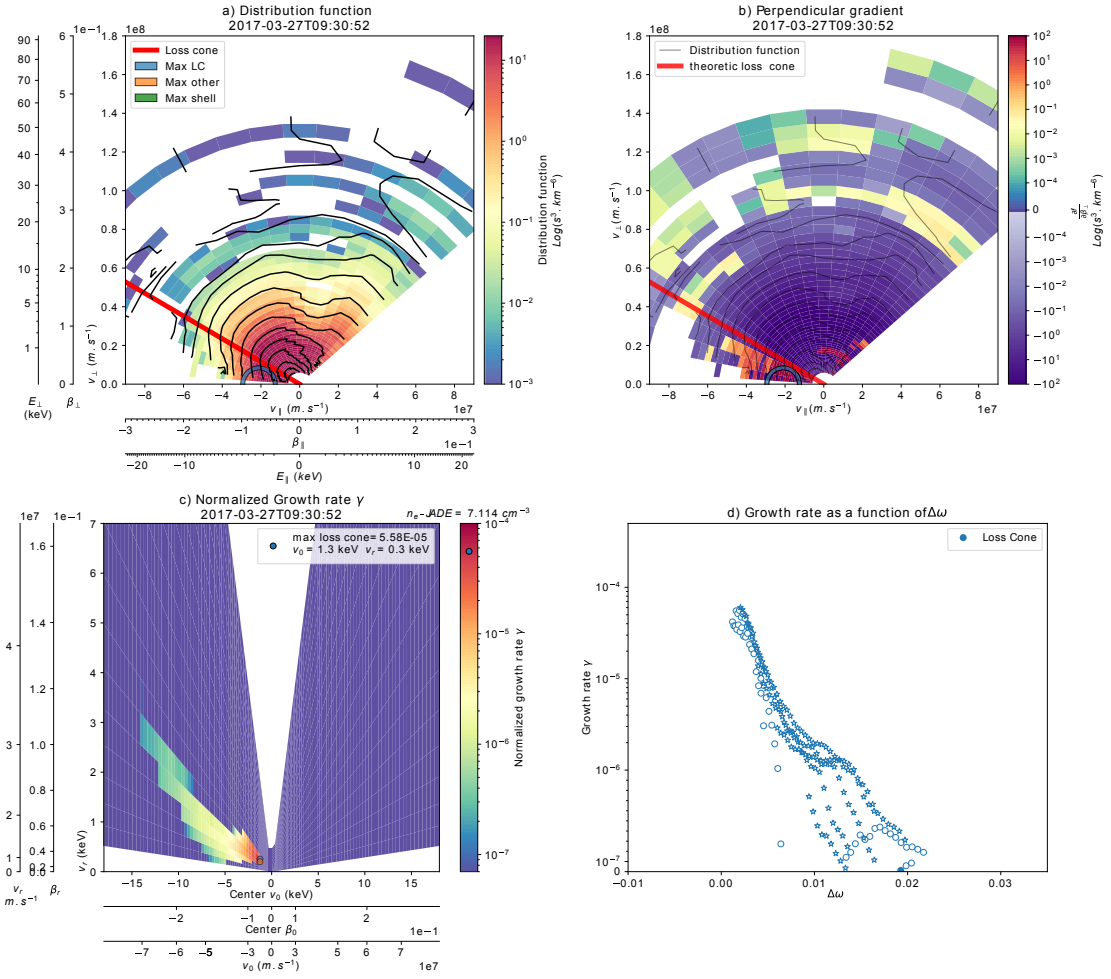


Figure 4.20.: Example of a measured EDF and associated growth rate during PJ5S Io flux tube crossing.

Overall, this paper has shown that Io-induced emissions associated with the Io footprint are driven by the CMI from loss cone EDF with upward electrons of 1 to 15 keV.

This investigation also revealed the constraints of the conditions for generating Io-DAM on top of the usual CMI assumptions. Indeed, Io-DAM generation requires:

- a sufficiently dense, unstable population to obtain growth rates large enough
- either Alfvén waves or downward FAC to accelerate unstable electrons.

4.5.2. Callisto-induced radio emissions

Callisto's UV footprint detection has long been a challenge since this footprint is expected to be colocated with (and therefore embedded in) the MAO (Hess et al. 2009). Moreover, the low velocity of Callisto compared to the surrounding plasma and the weak magnetic field on its orbit, the power dissipated in Callisto's flux tube is expected to be 3 to 4 orders of magnitude below the one of Io (Zarka 2007). Also, due to its tilted orbit, Callisto is often located in the plasma sheet where the plasma conditions are very switching from super- to sub-Alfvénic during a revolution, while the inner moons interact with Jupiter in the sub-Alfvénic regime only. During a compression event of the Jovian magnetosphere by an interplanetary shock that moved the MAO toward lower latitudes, Rabia et al. (2025) identified a double footprint structure in the northern hemisphere, sampled in situ by Juno, and identified as the Callisto footprint. The analysis of JADE-E revealed that the UV emissions were produced by downward electrons of 10 keV. However, no radio emission was visible near the local f_{ce}(=7.5 MHz). Nonetheless, I investigated the possibility of radio generation below the Waves noise level.

Figure 4.21 shows the result of the growth rate analysis applied to a typical EDF measurement sampled during the flux tube crossing, where $\frac{f_{pe}}{f_{ce}} = 7 \times 10^{-4}$ and $\frac{n_h}{n_{tot}} = 0.9$. In Figure 4.21a, a clear depletion is observed in the upward direction below the theoretical loss cone angle (red line). The most unstable loss cone resonance circle (blue) yields growth rates about 7×10^{-7} The EDF also displays two shell-type electron shells at $v \simeq 1.8 \times 10^7\,\mathrm{m \cdot s^{-1}}$ and $v \simeq 3 \times 10^7\,\mathrm{m \cdot s^{-1}}$. These shells do not yield any positive growth rate, probably due to the important shadowing seen at 90°.

Using a growth rate of 1×10^{-6} to overcome the underestimation of the density, a source size of 200 – 300 km and $v_g = 0.1c$ only lead to a an expected intensity in the range $0.6 \times 10^{-18} - 1.6 \times 10^{-18}\,\mathrm{Wm^{-2}Hz^{-1}}$ which is below Waves sensitivity $1.6 \times 10^{-18}\,\mathrm{Wm^{-2}Hz^{-1}}$.

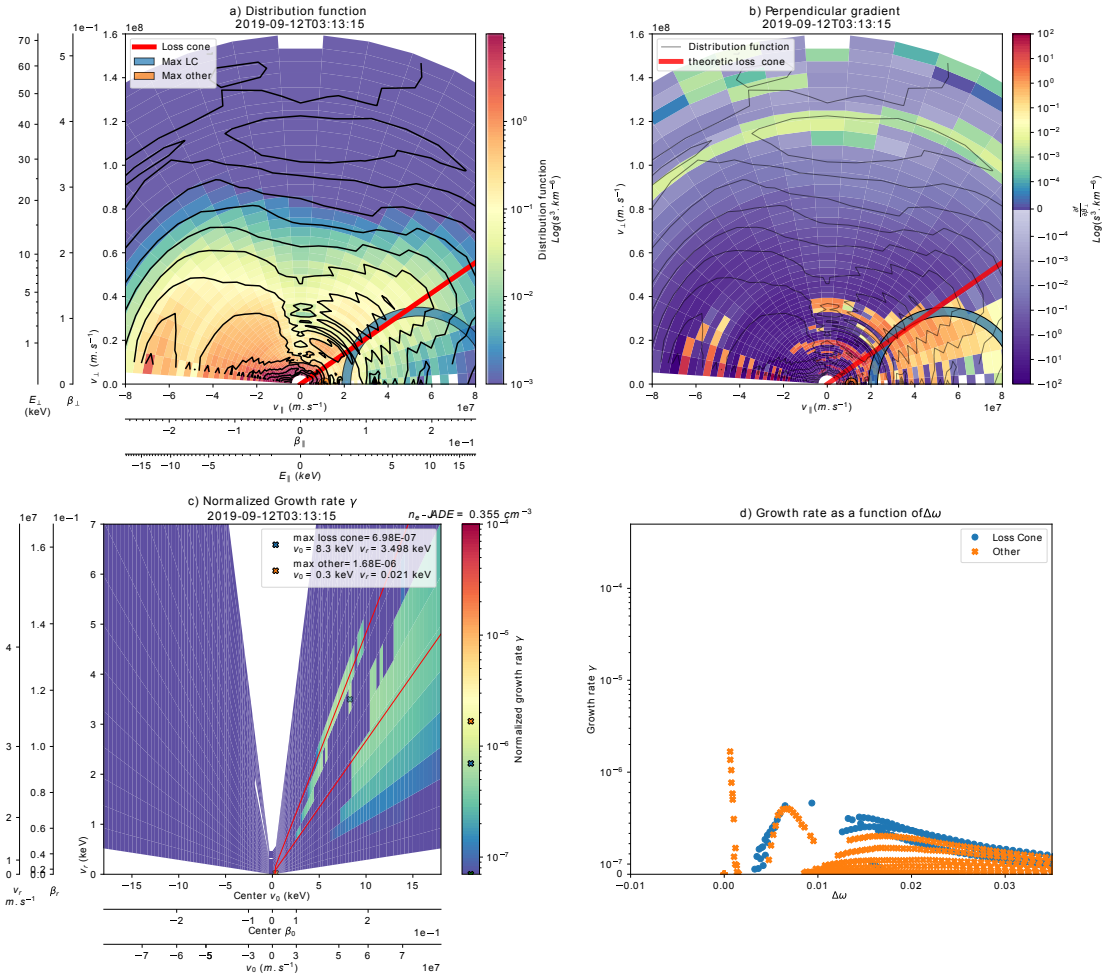


Figure 4.21.: Example of a measured EDF and associated growth rate during PJ22N Callisto flux tube crossing.

This study showed that the CMI can be driven by the Callisto-Jupiter interaction from loss cone EDF of a few keV, but that the wave intensity falls below the Waves' sensitivity.

4.6. Summary of HOM/DAM/Moon-DAM source properties

In this chapter, I studied the location, generation processes, and spectral characteristics of auroral HOM and DAM but also of Moon-DAM.

I surveyed Juno first 70 PJ and identified 116 HOM/DAM source crossings ranging from 0.3 and 15 MHz from Jupiter These sources were

- in highly depleted region $\frac{f_{pe}}{f_{ce}} \sim 10^{-3} - 10^{-2}$
- homogeneously distributed in longitude
- more detected in the dawn side
- magnetically connected the UV Diffuse Aurorae and the equatorward boundary of the Main Auroral Oval
- associated with a recurring peak of 3-30 keV energy flux
- located in highly depleted regions ($\frac{f_{pe}}{f_{ce}} \sim 10^{-3} - 10 - -2$)

Thanks to a growth rate analysis I confirmed loss cone EDF of 0.2-5 keV as the main source of free energy for to HOM/DAM. These sources were partially associated with recurring Alfvénic perturbations. Conics were also confirmed to be a secondary source of free energy with similar properties. Both these sources amplify oblique wave, in line with Mottez et al. (2010) and Hess et al. (2010)'s predictions.

I also identified shell-type EDFs of 0.2-5 keV as a new source of free energy for Jovian radio auroral emissions. Contrary to loss cone and conics the waves amplified by these distributions are purely perpendicular to the magnetic field and emitted below f_{ce} (down to 2%). These were only found in 21 (18%) source crossings Specifically, these unstable monoenergetic distributions were:

- composed of a hot plasma
- associated with monoenergetic signatures such as inverted Vs
- in upward FAC
- paired with an enlargement of the loss cone.

While Juno mostly crossed HOM sources, these characteristics were also commonly observed for both DAM confirming these components are actually a single component.

The generation by > 30 keV electrons connected to the MAO was investigated in a case study by taking relativistic effects in the resonance equation. These electrons were shown to be unstable and to present the same types of unstable distributions than those reported in the 0.2-5 keV range. However, the amplified waves were shown to be emitted below Waves' sensitivity due to the low number of these unstable electrons.

I also reported the first detection of the first harmonic of HOM whose generation conditions remain to be studied.

The generation of Io-DAM was also studied in 3 traversals of the Io flux tubes. These were shown to be generated only by loss cone EDF of 3-8 keV, thus completing the results obtained for the case of Ganymede-DAM.

Unstable loss cone EDF of 1-8 keV were also found in Callisto's flux tube at the occasion of the detection of its footprint. However, these amplified waves were shown to amplify waves below Waves' sensitivity level.

The properties I obtained are summarized in Table 4.4. These properties will be discussed and compared with the results obtained on bKOM source crossings (Chapter 5) and in a broader context in Chapter 6.

Component	Frequency	Emission angle (°)	Source size (km)	UV Association	Source of free energy	Unstable e^- Energy (keV)
Io	2-28 MHz	79°-84°	200-600	footprint tail	Loss cone	3-8 keV
Callisto	Emissions too weak to be detected				Loss cone?	1-8 keV?
DAM/HOM	300 kHz-5 MHz	70°-90°	250–3000	Diffuse aurora	Loss cone Conics Shell	0.2-5 keV

Table 4.4.: Comparison between the characteristics of the Jovian auroral radio components with the other planetary auroral radio emissions

5. Extension to the case of bKOM

Radio ga ga

Radio Ga Ga - Queen

Contents

5.1. Radio Survey of bKOM sources . . . 129
5.1.1. Description of the studied interval . . . 129
5.1.2. Tracking bKOM source candidates . . . 130
5.1.2.1. Location and plasma context of the candidate sources . 130
5.1.2.2. Auroral cavities for bKOM generation . . . 133
5.1.2.3. Solar wind influence . . . 134
5.2. Case study: PJ4S . . . 135
5.2.1. Radio source and auroral context . . . 136
5.2.2. Predicted growth rates . . . 136
5.2.2.1. Emission angles . . . 138
5.3. Case study: PJ5N . . . 140
5.4. Overall properties of bKOM sources . . . 143
5.5. Summary of bKOM source properties . . . 143

In this chapter, I will extend the study to the remaining Jovian radio component: bKOM. The results presented in this chapter were published in Collet et al. (2025)(see Appendix F3). This component has been studied from remote observations since Voyager 1 and while some source crossings were reported during the Juno era (Louis et al. 2019; Ebert et al. 2021; Imai et al. 2019), the generation of these emissions was never studied with in situ measurements.

I will first present a survey of Juno/Waves measurements of bKOM source candidates (Section 1). Two case studies (PJ4S and PJ5N) will be analyzed in Sections 2 and 3 to illustrate the results obtained with my growth rate analysis. Then, I will extend these results to the rest of the source crossings (Section 4) and characterize the bKOM generation conditions in Section 5.

5.1. Radio Survey of bKOM sources

5.1.1. Description of the studied interval

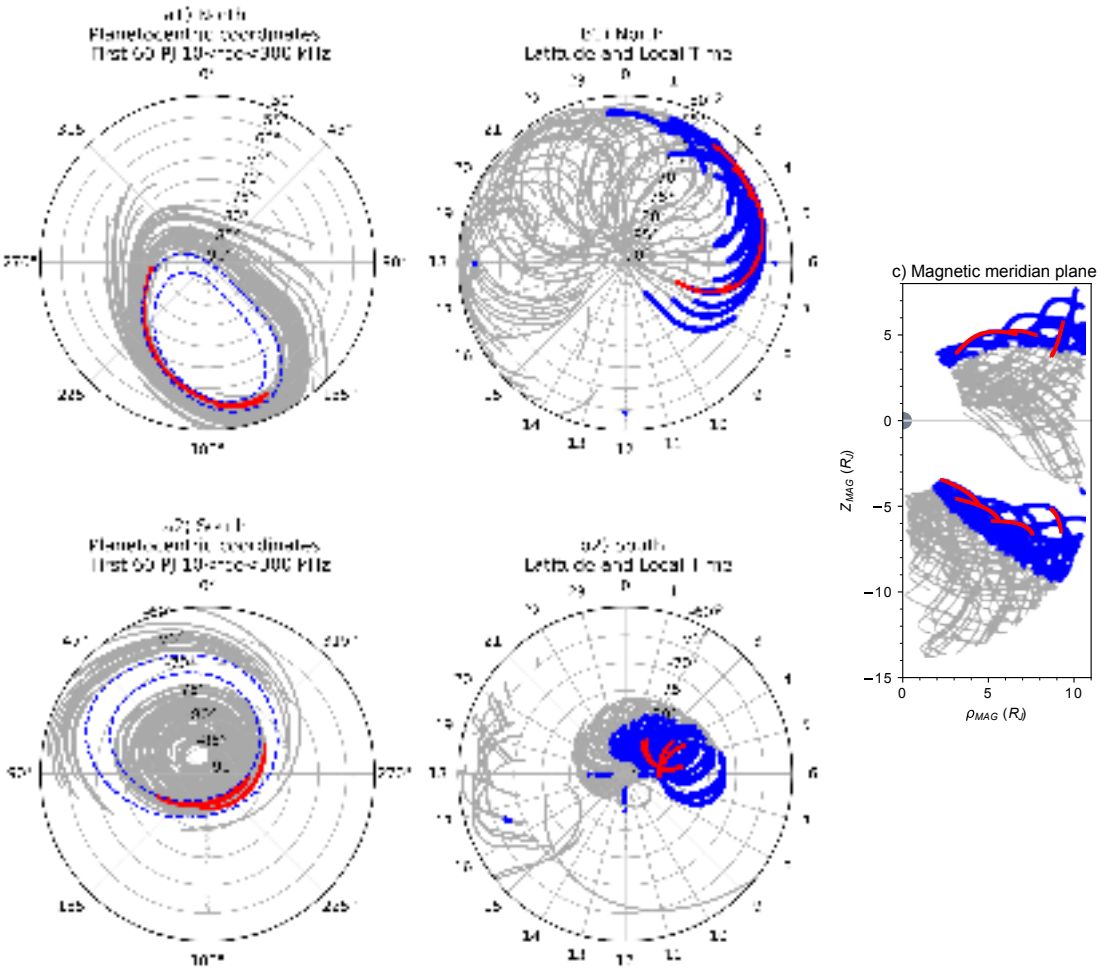


Figure 5.1.: Juno footprint projected 400 km above the 1 bar level (JRM33+CON20) during its first 60 perijoves where $10 < f_{ce} < 400$ kHz. The format is the same as Figure 4.2.

To track bKOM source candidates, I extended the radio survey of HOM/DAM sources presented in Section 4.1 to the 10-400 kHz range over PJ1-60 (Oct 2016-Apr 2024). To do so, I used both Waves Burst and Survey modes measurements obtained with HFR-Low and LFR-High. Unfortunately, bKOM emissions close to the local f_{ce} are detected during intervals when Juno instruments are not necessarily in their high resolution mode, and often, noise on the HFR-Low (for bKOM where $f > 150$ kHz) can prevent the detection of bKOM emissions. I used in priority radio measurements in Burst mode to make sure I tracked emissions $f < f_{ce} + 1\%$. I restricted this study to radio sources where electron measurements were available at a time resolution of 1 or

30 s.

The Juno trajectory restricted to magnetic field amplitude where f_{ce} is in the studied range is shown in black in Figure 5.1. This trajectory does not account for the criteria for high-resolution measurements. The four panels show this trajectory in different coordinates. Panels a1) and a2) (on the left) show this trajectory in planetocentric coordinates, while Panels b1) and b2) (on the right) show it in a Latitude VS local time coordinates. Panels a1) and b1) show the Northern Hemisphere, while panels a2) and b2) show the Southern Hemisphere. In panels a1) and a2), the blue dashed lines represent M-SHELL=15$R_J$and M-SHELL=60R_J. These magnetic apexes correspond to the mean limits of the UV main auroral oval. On panels b1 and b2, the time intervals during which Juno intercepts the flux tubes mapping to the MAO in blue.

Overall, Juno rarely flies over the statistical auroral oval, and does so mostly for longitudes near 200° and on the dawn side. In the Northern Hemisphere, the equatorward part of the oval is favored, while in the Southern Hemisphere, the poleward part is favored.

5.1.2. Tracking bKOM source candidates

5.1.2.1. Location and plasma context of the candidate sources

The radio survey on the interval, resulted in the identification of 7 radio sources candidates out of the 60 first perijoves, 4 in the south (PJ1S, PJ4S, PJ11S, PJ12S) and 3 in the north (PJ5N, PJ7N, PJ9N) whose time intervals and characteristics are listed in Table 5.1. Due to the lack of high resolution data for the Waves and/or JADE-E instruments, PJ7N and PJ12S were left away from the survey.

Figure 5.2 shows an example of a time-frequency spectrogram of the bKOM source crossing candidate on 2017-03-27T02:00-06:00. Figure5.2a shows the Burst mode measurements when available, Figure 5.2b shows the Survey mode measurements in the whole interval. The black box shows the interval during which Burst mode measurements are available. The solid (resp dotted and dashed) black line represents the local f_{ce} (resp $f_{ce}+1\%$ and $f_{ce}/10$) while the white line represents the local f_{pe} such that the usual $\frac{f_{pe}}{f_{ce}} < 0.1$ is verified whenever the white line is below the dashed black line. Red double arrows delimit the identified radio source candidates. The horizontal blue lines at the bottom of Figure5.2 b indicate whenever Juno is connected to the MAO.

PJ	Time	f_{ce} (kHz)	f_{pe}/f_{ce}	R (R_J)	MLat (°)	M Shell (R_J)	Dawn storm	Solar Wind	FAC	Estimated intensity ($Wm^{-2}Hz^{-1}$)	Lat. size ($\times 10^3 km$)	JADE-E	Waves	Cavities	Unstable populations
1S	2016-08-27 21:15 to 22:40	12	0.03 to 0.3	10 to 11	-35 to -30	40 to 50	X	X		3×10^{-11}	650	LR	Survey	X	N/A
4S	2017-02-02 15:30 to 17:15	100 to 300	0.01 to 0.07	4 to 6	-59 to -48	30 to 51			↑	4×10^{-11}	180	HR	Burst		Shell Conics
5N	2017-03-27 02:00 to 03:30	30 to 150	0,01 to 0.5	6 to 8,3	33 to 51	22 to 52	X		↑	1×10^{-11}	400	HR	Burst	X	Conics
9N	2017-10-24 10:20 to 11:30	20 to 30	0,05 to 0.5	8.5	35 to 40	20 to 35	X		↕	1×10^{-11}	450	LR+HR	Survey	X	Conics
11S	2018-02-07 17:30 to 20:00	30 to 120	0.003 to 0.05	5.5 to 8	-54 to -45	52	X	X	↑*	1×10^{-10}	320	LR	Burst		N/A
12S	2018-04-01 15:40 to 18:10	18 to 43	N/A	8 to 10	-49 to -40	50 to 53		X		2×10^{-10}	600	None	Survey	N/A	N/A
7N	2017-07-10 17:15 to 17:55	15	N/A	10	24 to 28	14 to 19		X		5×10^{-11}	500	None	Survey	N/A	N/A

Table 5.1.: Catalog of bKOM source crossings identified from Juno/Waves observations over PJ1-60.

Columns 1 and 2 indicate the perijove and the event time interval. Columns 3-4 give the bKOM frequency and the $\frac{f_{pe}}{f_{ce}}$ ratio (derived from JADE-E and MAG measurements) during the source crossings. Columns 5-6-7 give the radial distance from Jupiter, the magnetic latitude, and M Shell (JRM33+CON20). Columns 8-9 indicate whether dawn storms Bonfond et al. (2021) or if high solar wind parameters were identified less than a day from the source crossings. Column 10 illustrates the direction of field aligned current (FAC). Column 11 gives the source peak spectral flux density as observed by Waves. Column 12 gives the latitudinal extent (defined as the $r\cos\theta_{SIII}$ length with r the radial distance and θ_{SysIII} the latitude) of the source crossings. Columns 13 and 14 indicate whether the electron or radio measurements were in High Resolution mode. The last column indicates the category of unstable population. Column 15 indicates the presence of cavity. Column 16 indicates the identified CMI unstable population. "N/A" indicates that the resolution of either JADE-E or Waves measurements was not sufficient to obtain the corresponding property.

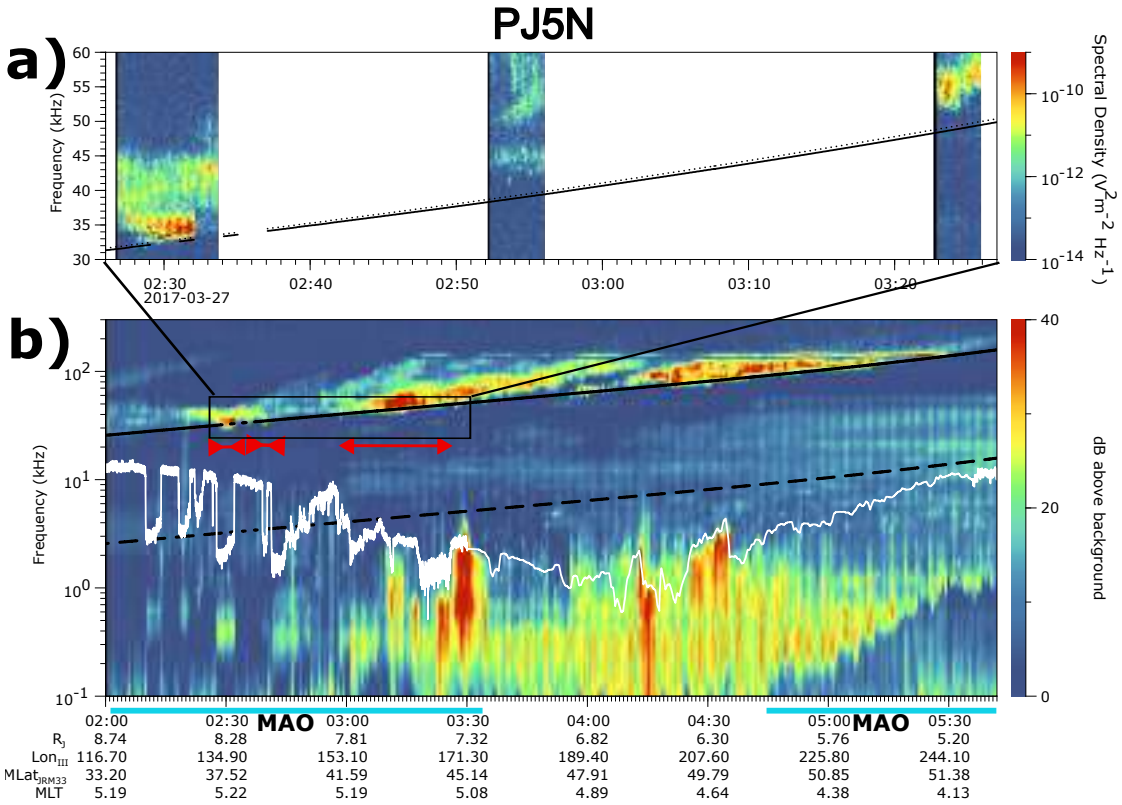


Figure 5.2.: Time-frequency spectrogram of PJ5N bKOM candidate source

These source crossings (shown in red in Figure 5.1) are all located in the Dawn Sector (local time between 02 and 07 hours) and along magnetic flux tubes connected to the statistical main auroral oval, with M-SHELL mapping from 30 to 52R_J. This connection is then verified using UVS images when available, as shown in Figure 5.3. This figure also confirms that these radio source candidates are all connected to the Main Auroral Oval. This list of candidates was also compared with Bonfond et al. (2021)'s list of identified Dawn Storms (see Chapter 1) and found that 3 candidates have not only been identified during Dawn Storms but are also magnetically connected to the characteristic bright spot.

All these sources are located at high radial distances from Jupiter (4 R_J to 11 R_J). At such distances, we can infer from the very rough approximation of a dipole magnetic field (i.e. $B \approx B_0 r^{-3} \Rightarrow \sin^2(\theta_{LC}) \simeq r^{-3}$) that the loss cone angle is in the range [1.6° – 7.2°], which is smaller than JADE-E angular resolution of 7.5°.

These source crossings were all identified during the first 11 perijoves. The precession of Juno's orbits results in a preferential coverage of the dawn side.

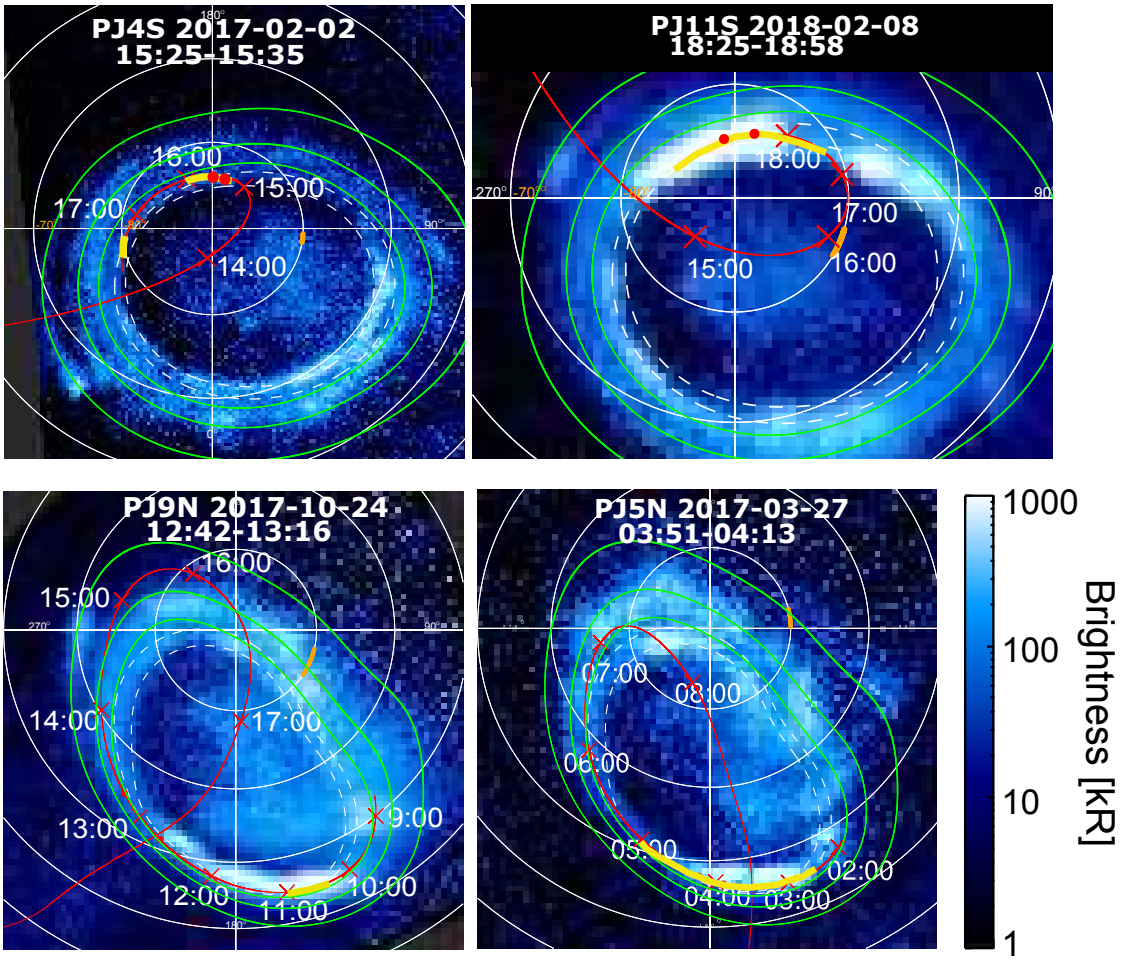


Figure 5.3.: UV images from UVS during or near bKOM source crossing candidates on top of which the trajectory of Juno is plotted in red at 300 km above the 1 bar level. A pair of red dots delimit the UVS observing time interval for each polar map.. The intervals corresponding to the source crossings are indicated by a yellow line.

5.1.2.2. Auroral cavities for bKOM generation

For the 5 bKOM source candidates, the $\frac{f_{pe}}{f_{ce}} < 0.1$ condition is not fulfilled as clearly as in the HOM/DAM cases. Instead, this ratio is often close to this limit and can even be exceeded during some radio source candidate crossings (PJ5N, PJ1S, and PJ9N) In these 3 cases, sudden electron depletions (henceforth referred to as "cavities") have been identified, which have not been previously seen for any HOM/DAM sources. These cavities bear a resemblance to the auroral cavities at Earth. During PJ5N, 5 small-scale cavities (a few tens of km long) were identified, all associated with radio emissions near f_{ce}, thus interpreted as distinct, successive, radio source crossings.

Such cavities were all associated with whistler waves. Such waves are generated by weakly energetic electron beams accelerated along magnetic field lines (Sulaiman et al. 2022; Yoon et al. 2025).

Interestingly, these three cavity cases were identified along with Dawn Storms, suggesting dawn storms provides the necessary acceleration processes to generate such cavities. However, during PJ11S, no cavity was observed, whereas the source candidate was clearly connected to the Dawn Storm bright spot.

5.1.2.3. Solar wind influence

As Solar wind was shown to have a great influence on the bKOM occurrence, I compared the solar wind conditions at Jupiter a few tens of hours before and after the source crossings to assess for any compressions of the magnetosphere during these events. Kim et al. (2016)'s MS-FLUKKS MHD model uses in situ plasma measurement of the solar wind at 1 au either from Stereo-A or OMNI. These measurements are then used to propagate the solar wind properties to Jupiter. The simulated properties have an uncertainty strongly dependent on the Sun-spacecraft-Jupiter alignment.

Figure 5.4 shows the numerically obtained solar wind proton density, radial velocity, proton dynamic pressure, and magnetic field amplitude (from top to bottom) as a function of δT, the time difference (in days), with start time of bKOM source candidates. Pairs of colored dots delimit the intervals during which dawn storms were identified by Bonfond et al. (2021). As dawn storms are due to magnetosphere reconfigurations(which can sometimes be due to solar wind compressions), I investigated the correlation of bKOM with those in this section. The vertical red line corresponds to $\delta T = 0$ day and the 2 vertical blue lines delimit $\delta T = \pm 10$ hours, which is a rough estimation of the temporal incertitude of the model. I either used OMNI (continuous line) or Stereo-A (dashed line) measurements, keeping the data from the spacecraft most aligned (large Sun-Spacecraft-Jupiter angle) with Jupiter (or both in ambiguous cases).

PJ7N, PJ11S, and PJ12S coincide with a significant magnetospheric compression (high density, pressure, and magnetic field intensity), supporting a partial correlation of the bKOM occurrence with the solar wind activity. This also confirms that radio sources identified during dawn storms can also occur in the absence of solar wind compressions.

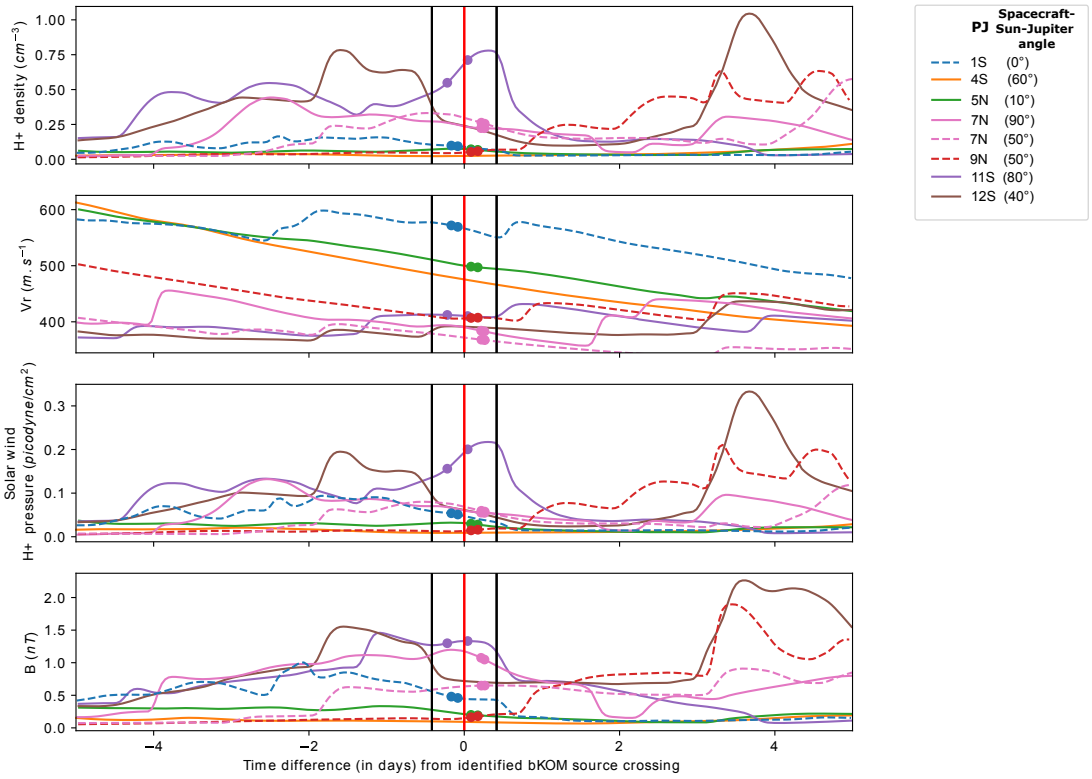


Figure 5.4.: Hourly-averaged solar wind parameters from Kim et al. (2016)'s model for each radio source crossing.
From top to bottom: modeled density of solar wind proton, modeled radial solar wind velocity, modeled solar wind proton dynamic pressure, and modeled magnetic field. These values are shown as a function of the time difference from the identified bKOM source crossing candidates T(in days). Dots delimit the intervals during which dawn storms were identified by Bonfond et al. (2021). The red line corresponds to $\delta T = 0$ days and the double blue line to $\delta T = \pm 10$ hours, which is approximately the temporal incertitude of the model. The precision of the model is strongly dependent on the alignment of Jupiter with the spacecraft whose measurements are used as input. In this figure, we either used OMNI (continuous line) or Stereo-A (dashed line) measurements (or both in ambiguous cases) depending on which spacecraft has the best Spacecraft-Sun-Jupiter alignment (the Spacecraft-Sun-Jupiter angle used for this is shown in the legend).

5.2. Case study: PJ4S

From the 7 source crossing candidates, two of them (PJ5N and PJ4S) were identified while Juno instruments were all in a favorable configuration (high resolution electron and radio measurements for most of the interval) I now propose to study these cases of PJ4S and PJ5N, which show two different types of source crossings. In Section 5.4, I will compare these case studies with the rest of the source crossing candidates.

5.2.1. Radio source and auroral context

Figure 5.5 presents the in situ radio, plasma, and magnetic measurements as well as the results of my growth rate analysis. The format of this figure is similar to Figure 4.8. 5.5 a and b illustrates the identification of the radio source from 15:20 to at least 15:26 (after which only Survey mode low resolution measurements were available), with emissions seen below f_{ce} from 15:23 to 15:26. The Survey mode measurements hint for a source region extending up to 15:40.

5.5 c and d present JADE-E measurements either in a time-energy spectrum for all electrons and a time-pitch angle spectrum for electrons between 1 and 5 keV. An inverted V structure can be seen from 15:15 to 15:20, peaking near 70 keV. Moreover, as mentioned above, the loss cone is not visible in 5.5 d. From 15:22 to 15:37, depletions in the upward and downward directions at pitch angles larger than the loss cone angle are observed. This feature, reminiscent of the conics discussed by Louarn et al. (2018), is delimited by larger pitch angles, near 30° and 150°, and can be a sign of an acceleration below the spacecraft.

5.5 e shows δB_ϕ that allows to derive the FAC. In particular, the radio source is identified mostly during an upward FAC.

5.2.2. Predicted growth rates

5.5s f and g show that the growth rate analysis leads to the identification of 0.3 to 8 keV shell type EDFs (with γ up to 10^{-3} when $f < f_{ce}$ emissions were identified. The energy of these shell is coherent with the associated frequency of the radio emissions. Similarly, to HOM/DAM, the analysis results in the identification of unstable shells (with γ about 10^{-4}) while no $f < f_{ce}$ emissions were detected. Similarly, this discrepancy can be explained by the short time of interaction to amplify waves at Waves' sensitivity.

The sufficiently unstable ($\gamma \sim 10^{-4}$) upward and downward portions of the EDF are identified from 15:25 to 15:27 and from 15:29 to 15:37. These bidirectional CMI-unstable electrons predict emission frequencies between f_{ce} and f_{ce}+1% after 15:25, mostly after Waves stopped operating in Burst mode. Furthermore, the energy of these resonance circles follows the same trend as the inverted V from 15:15 to 15:30 but contrarily to HOM/DAM sources, the energy of these conics trend differs from the one of the inverted V (and of the shell) from 15:30 to 15:36. This suggests that multiple processes are accelerated different parts of the EDF at once.

Figure 5.6 shows representative unstable EDFs corresponding to the $f < f_{ce}$ radio source at 15:25:15 and to the $f_{ce} < f < f_{ce} + 1\%$ at 15:33:17. On both these panels, shell-type EDFs upward electrons yield large growth rates. As expected, the loss cone (red line) is not resolved by JADE-E. The unstable upward population is then identified as conics.

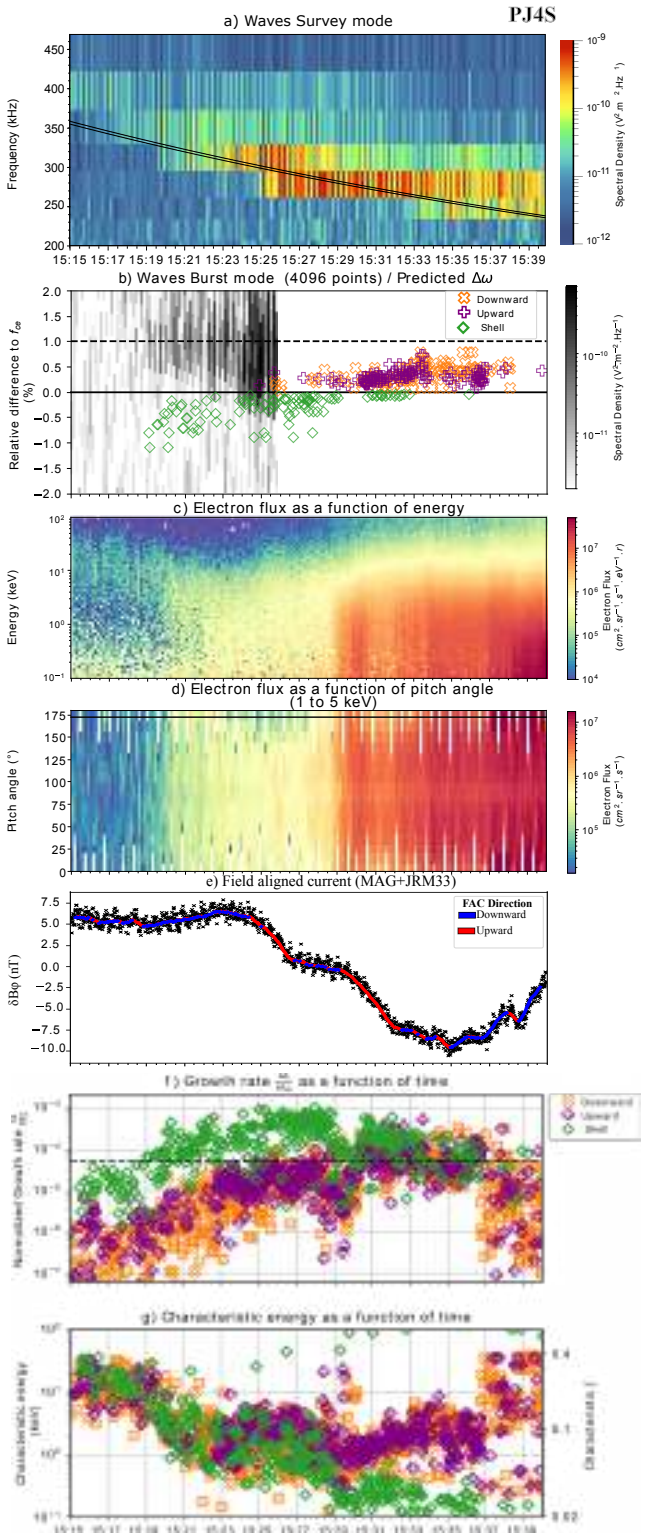


Figure 5.5.: In situ measurements and growth rate analysis as a function of time for the PJ4S bKOM source

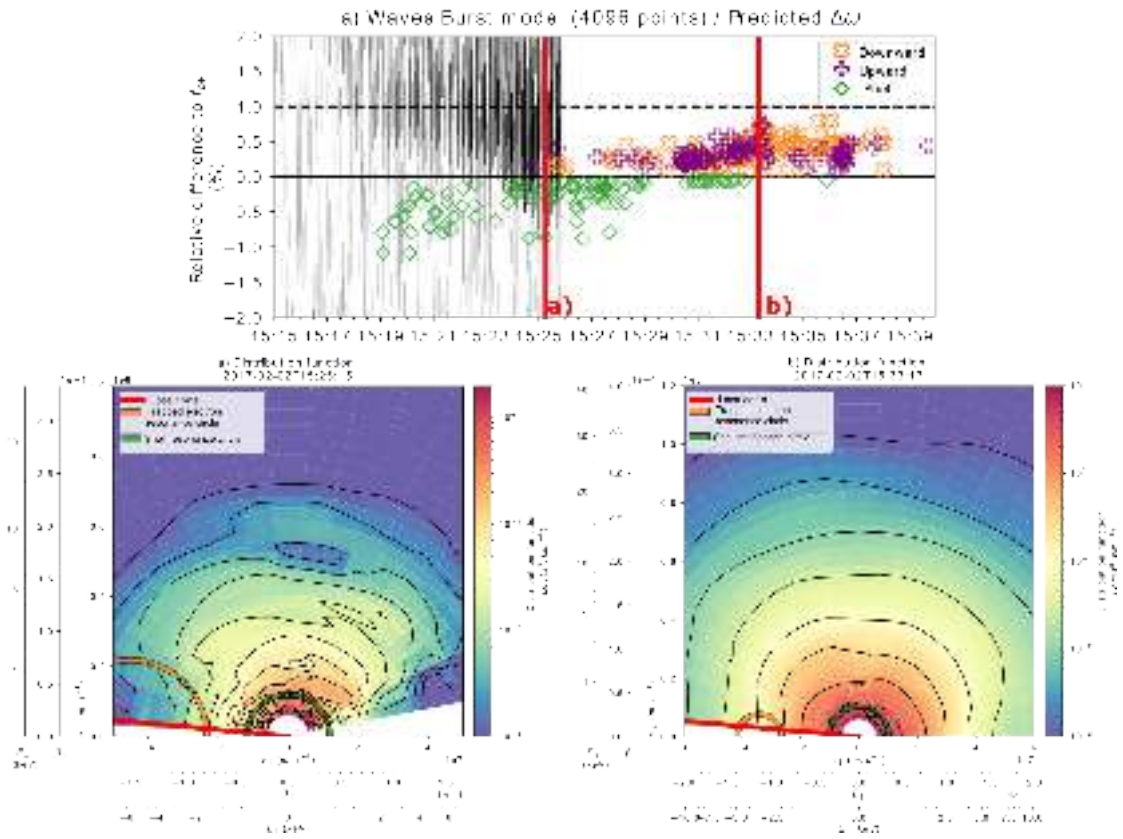


Figure 5.6.: Unstable EDFs from PJ4S bKOM radio source below Figure 5.5b on top of which red lines indicate the intervals corresponding to the shown EDF.

Altogether, the observed radio emissions indicate a first, shell-driven CMI source from 15:22 to 15:28, accounting for the amplification of radio waves below f_{ce}, followed by a second, conics-driven CMI source from 15:30 to 15:37, amplifying waves between f_{ce} and $f_{ce}+1\%$.

5.2.2.1. Emission angles

The investigated bKOM source region displays a large number of positive growth rates for all the tested categories of resonance circles. I took advantage of it to determine the expected emission angles predicted for the different populations.

The emission angles $\theta_{(\vec{\mathbf{B}},\vec{\mathbf{k}})}$ associated with the unstable resonance circles are shown in Figure 5.7. Shell-type resonance circles are not included in this figure as they necessarily amplify waves perpendicular to the magnetic field. These angles are computed from Equation 2.3b supposing $N = 1$. The double blue dashed lines enclose $\theta_{(\vec{\mathbf{B}},\vec{\mathbf{k}})}$ for the largest growth rates, here chosen $\gamma > 5\times10^{-5}$, between 93.1° and 97.5° for upward electrons (upward propagating wave and between 82.5° and 87.3° for downward electrons (downward propagating wave). The latter waves are likely to be reflected onto the iso-f_X surface surrounding the bKOM source.

Interestingly, the scattering of the wave emission angle is larger than the 1.5° thickness of the emission cone measured for HOM emissions (Kaiser et al. 2000).

The circles yielding weaker growth rates correspond to larger electron energies and to lower emission angles. The range of oblique emission angle is consistent with that determined from direction-finding studies (Ladreiter et al. 1994).

Interestingly, this case study of a single bKOM source thus shows that 3 portions of the EDF can be simultaneously CMI-unstable and yield emissions at different frequencies and with different emission angles. As a result, the 3 types of radiated waves may be tracked further away from the source with 3 different arc-shaped structures in the time-frequency planes

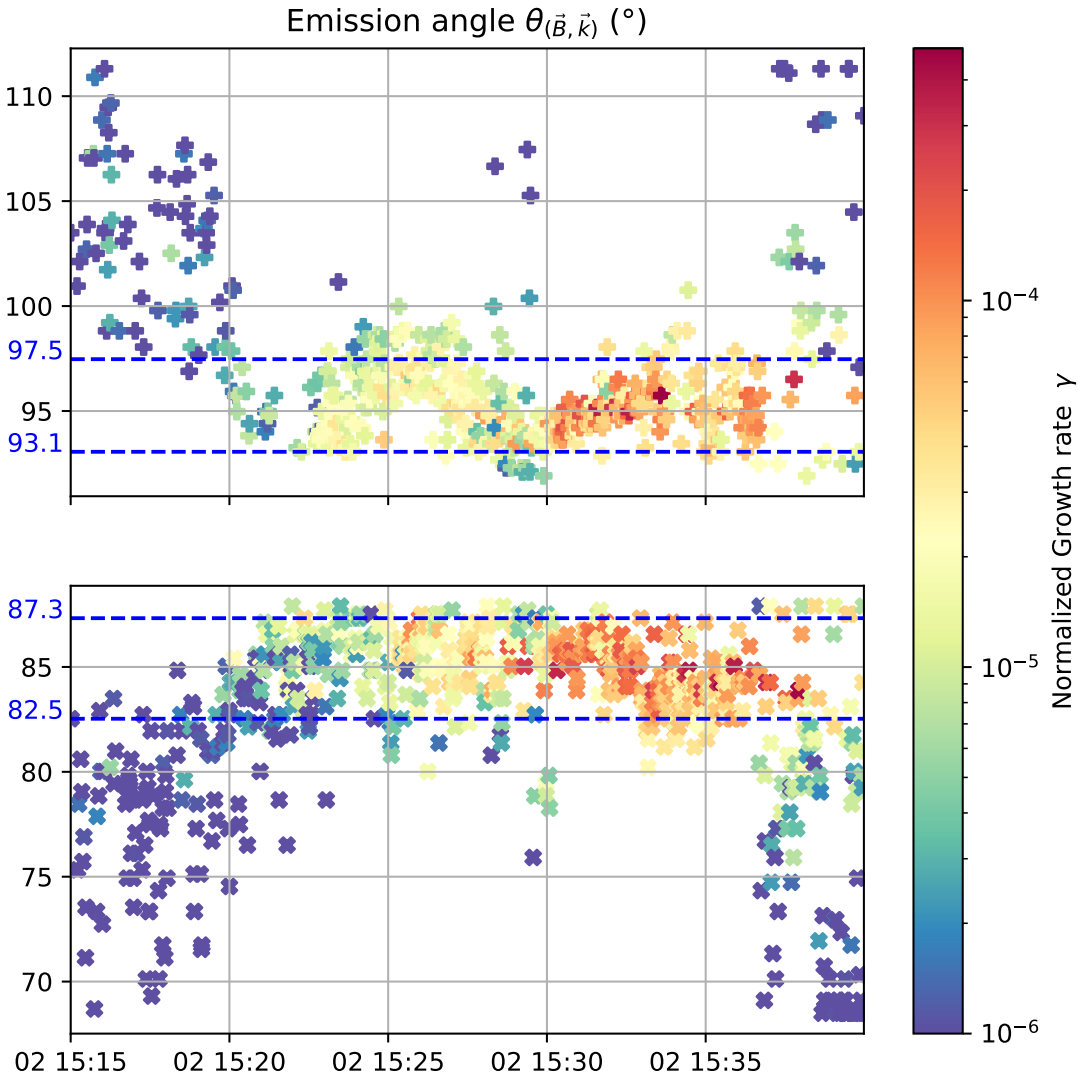


Figure 5.7.: Emission angle associated with the unstable resonance circles during PJ4S source crossing. Top (resp. bottom) panel shows the angles deduced from circles intercepting upward (downward) electrons yielding upward (downward) waves. The color bar indicates the growth rate corresponding to the associated resonance circle. Blue dashed lines enclose the values associated with resonance circles yielding $\gamma > 5 \times 10^{-5}$.

5.3. Case study: PJ5N

Figure 5.8 follows the same format as Figure 5.5 and presents the case of PJ5N with a bKOM source candidate colocated with an auroral cavity.

In Figure 5.8a, radio emissions around f_{ce} are detected only between 02:27:57 and 02:32:05. Notably, the flux density increases across the entire spectrum during this period until dropping suddenly at all frequencies at 02:32:00. Emissions are seen

slightly below f_{ce} from 02:28:50 to 02:29:05, and below $f_{ce}+1\%$ from 02:28:30 to 02:29:00 and again from 02:29:30 to 02:29:45.

It is worth noting that emissions are modulated at the Juno spin period with a phase shift for emissions below and above fce+2%. This indicates a different direction of the incoming waves, which either diagnose different source regions and/or emission angles and/or propagation modes (Roux et al. 1993).

Figure 5.8b presents the JADE-E electron spectrogram processed differently than for PJ5S to better mitigate the residual noise during this interval. Instrumental sub-second fluctuations (addressed in Louarn et al. 2018) produced unphysical results during the nominal background subtraction. To reduce these effects, the electron data were averaged over 3 seconds. The resulting spectrogram reveals a sudden electron depletion from 02:27:38 to 02:32:00, accompanied by a decrease in $\frac{f_{pe}}{f_{ce}}$ from 0.25 to 0.07. This depletion region, marked by a pair of vertical dashed blue lines, roughly coincides with our estimated source region and exactly matches the bright radio emissions seen in Figure 5.8a, particularly at 02:32:00. Between 02:30:00 and 02:32:00, a monoenergetic electron signature with a peak energy decreasing from 30 to 10 keV is clearly visible. This feature likely extends beyond the JADE-E energy range.

Figure 5.8c shows that the monoenergetic signature mentioned above corresponds to bidirectional electron beams observed from 02:30:30 to 02:32:00. Slightly earlier, from 02:27:30 to 02:30:30, weaker bidirectional beams and intermittent depletions are apparent at pitch angles below 30° or above 150°.

Figure 5.8d depicts magnetic data, which are sparse, with gaps from 02:29:00 to 02:31:00 and 02:32:00 to 02:34:00 (not shown here). Despite this, the observed drop in B_ϕ suggests an upward FAC coinciding with the auroral cavity, such as commonly observed at Earth for the AKR source region Roux et al. (1993).

Figures 5.8e-f display the results of the growth rate analysis while excluding shell-type resonance circles for clarity. Indeed, even after averaging the data, frequent monoenergetic shell-like features persisted, likely unphysical, and were left away from the analysis. The remaining resonance circle types show similar growth rates to PJ4S, reaching $\gamma \leq 10 \times 10^{-4}$ within the cavity, corresponding to electron energies between 5-30 keV, consistent with the lower limit of the inverted V feature. The predicted wave frequencies ($f = f_{ce} + 0.7\%$ to 6%) align well with the low frequency cutoff of the observed emissions. The analysis of the CMI-unstable downward and upward portions of the EDF shows that the source of free energy comes from the conics evoked above, overlapping various intensifications and depletions. Between 02:30:30 and 02:32:00, no unstable EDFs were detected, ruling out CMI wave amplification in this interval.

In this case, the high energy unstable electrons amplify waves with $\theta_{(\vec{\mathbf{k}},\vec{\mathbf{B}})}$ in the range $[98°, 114°]$ for downward electrons and as low as 68° and up to 86° for upward electrons.

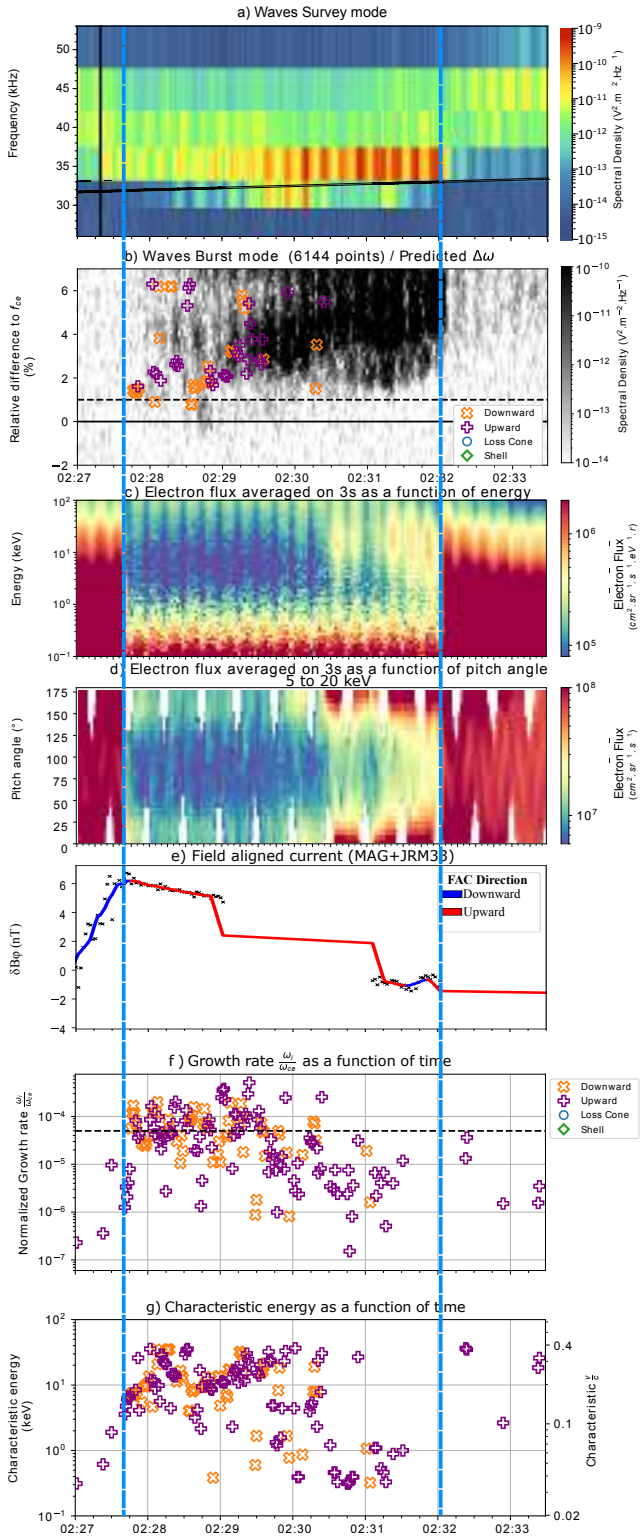


Figure 5.8.: In situ measurements and growth rate analysis as a function of time for the PJ5N bKOM source

5.4. Overall properties of bKOM sources

Among the other source candidates, PJ9N was the only other event sampled with high resolution electron measurements, which yielded positive CMI growth rates. This source was very similar to the PJ5N one. Indeed, this case was also composed of multiple auroral cavities and presented unstable conics from 1 keV to 20 keV(yielding growth rate of the order of 1×10^{-4}) which amplified waves along directions 5° to 22° from the normal to $\vec{\mathbf{B}}$. PJ1S also displayed small-scale auroral cavities associated with small-scale FAC (whose direction reverses at the boundaries of each cavity).

During PJ11S, the angular coverage of the low resolution electron measurements was too poor to assess for either loss cone or conics, but $f < f_{ce}$ radio emissions were here clearly observed, together with upward FAC, were multiple monoenergetic events.

5.5. Summary of bKOM source properties

From this survey of the first 60 Juno perijoves, we only found 7 bKOM source crossing candidates and only 5 of them were confirmed as so with a growth rate analysis. This low number is explained by the biased trajectory of Juno.

The obtained results can be summarized into 2 typical bKOM sources that both enclose emissions from 12 to 300 kHz, 4 to 11 R_J from Jupiter, with a mean intensity of 6×10^{-11} $Wm^{-2}Hz^{-1}$. The first "cavity" category (3 cases) exhibits:

- $\frac{f_{pe}}{f_{ce}} \in [0.01, 0.5]$ and sudden electron depletions reminiscent of AKR sources
- Magnetic connection with the MAO and with dawn storms
- Partial correlation with solar wind compressions
- Unstable bidirectional 5-30 keV conics yielding $\gamma \sim 10^{-4}$
- Upward FAC

The second category more similar to HOM/DAM (2 cases) exhibits:

- $\frac{f_{pe}}{f_{ce}} \in [0.003, 0.07]$
- Unstable 0.2-10 keV shell yielding γ up to 10^{-3}
- Unstable bidirectional 0.5-10 keV conics yielding $\gamma \sim 10^{-4}$
- Magnetic connection with the MAO
- Upward FAC

In these cases, the loss cone was smaller than JADE-E angular resolution thus I couldn't assess for their growth rates.

More source crossings are needed to confirm the statistics.

These characteristics will be discussed and compared to the ones obtained for other Jovian radio components and in a broader context in the next Chapter.

6. The CMI in the context of the Jovian magnetosphere and beyond

Radio, what's new ?

Queen

Contents

6.1. Discussion on the generation of auroral radio emissions at Jupiter . . . 146
6.1.1. Sources of free energy . . . 146
6.1.2. Efficiency of the CMI at weakly relativistic energies: comparison between the resonant and the precipitating electrons . . . 147
6.2. An updated view of the Jovian radio spectra . . . 148
6.2.1. Limitations of the used CMI growth rate analysis . . . 148
6.3. Comparing the Jovian auroral radio emissions with the Terrestrial and Kronian cases . . . 149
6.3.1. Source properties . . . 150
6.3.2. Sources of free energy . . . 150
6.3.3. O-mode and harmonics . . . 151
6.4. Extension to the case of Mercury . . . 152

In the previous chapters, I have used in situ measurements from Juno to locate the radio sources for all the Jovian components to verify the CMI as their generation mechanism, and to identify their sources of free energy. In this chapter, I discuss the universality of the CMI by examining the results obtained in the context of Jupiter's magnetosphere (Section 1), by comparing these properties with those of AKR and SKR (Section 2) and by discussing the implications of these results for the case of Mercury's magnetosphere as a potential source of radio emissions generated by the CMI (Section 3).

6.1. Discussion on the generation of auroral radio emissions at Jupiter

The results obtained in Chapters 4 and 5 are summarized in Table 6.1.

Component	Moon-DAM		DAM/HOM		bKOM	
	Io	Callisto	$f > f_{ce}$	$f < f_{ce}$	"Cavity"	No cavity
Frequency	4-30 MHz		0.3-15 MHz	0.3-5 MHz	10-300 kHz	
$\frac{f_{pe}}{f_{ce}}$	10^{-3}	10^{-4}	$10^{-3} - 10^{-2}$		0.3 (outside) 10^{-2} (inside)	$10^{-3} - 10^{-2}$
Monoenergetic signatures				X	X	X
FAC	↑			↑		↑
Alfvén waves	X		X			
Predicted angles	79°-84°			70°-86°	90°	
Source size (km)	200-600		250-3000		320-650 $\times 10^3$	
UV association	MAW/RAW/TEB		Diffuse aurora Equator MAO		MAO Dawn storms	
Source of free energy	Loss cone	Loss cone?	Loss cone & Conics	Shell	Conics	Conics & Shell
Unstable e- energy (keV)	3-8	1-8	1-5	0.2-5	0.1-30	

Table 6.1.: Characteristics of the Jovian auroral radio components obtained in situ. Callisto's radio emission was not detected.

6.1.1. Sources of free energy

In Chapter 4, I found that less than 20% of the crossed radio sources were generated at $\theta_{\vec{\mathbf{B}},\vec{\mathbf{k}}} = 90°$ below f_{ce} by shell-type EDF. This result is coherent with the low fraction (7%) of monoenergetic EDF reported by Salveter et al. (2022) in the [30-1200 keV] range.

These shells were systematically associated with an enlargement of the loss cone and often with an upward FAC. Thus, these shells are possibly generated by a rare system of FAC at Jupiter.

Furthermore, these EDFs were mostly reported in the South. This asymmetry may be related to the stronger FACs reported in the South (Kotsiaros et al. 2019; Al Saati et al. 2022). This FAC asymmetry is thought to be due to the Northern magnetic anomaly (Al Saati et al. 2022).

The predominance of the loss cone as a source of energy aligns well with the prevailing paradigm, which posits that acceleration processes at Jupiter are linked to Alfvén waves (Lysak et al. 2021). However, no clear correlation was found between the recurring Alfvénic perturbations identified by Gershman et al. (2019) and the radio sources. This absence of Alfvén waves, whereas the distributions are observed to be broadband, was interpreted as a sign of Alfvénic dissipation via a turbulent cascade able to stochastically accelerate electrons (Sulaiman et al. 2022; Lysak et al. 2021; Saur et al. 2018).

My work on Io-DAM generation associated with Louis et al. (2020)'s study on Ganymede-DAM and Louis et al. (2023b) analysis and hypotheses for Ganymede and Europa source crossings showed that the emissions induced by these moons were generated by loss cone EDF in upward FAC. Hence, Moon-DAM appears as a simple case of radio emission driven by one type of EDF whose understanding will help disentangle the various radio emissions associated with HOM/DAM/bKOM emissions unrelated to satellites.

On top of the loss cone and the shell, upward and downward conics were confirmed as a secondary source of energy amplifying oblique emissions for HOM/DAM and main source for bKOM. The origin of these conics is unclear, as some of them correspond to loss cone enlargement, possibly triggered by potentials below the source, while others were theorized to be generated by low-frequency potential, Alfvén waves, or via wave-particle accelerations (Louarn et al. 2018; Muñoz et al. 2022).

The simultaneous identification of the loss cone, upward and downward conics, and shell as sources of free energy, each emitting at different angles and different frequencies, should generate distinct radio signatures in the time-frequency plane. However, the observed wave bandwidth probably makes these arcs indistinguishable. Simulations with the EXPRESS code (Louis et al. 2019) could help verify the presence of these arcs.

6.1.2. Efficiency of the CMI at weakly relativistic energies: comparison between the resonant and the precipitating electrons

As shown in Table 6.1, all Jovian radio components were generated by electrons of the same energy range: 0.1 to 30 keV. This range is coherent with the usual semi-relativistic assumption for the CMI. In the case of Moon-DAM, these energies compare well with those determined from remote observations by Mauduit et al. (2023), Hess et al. (2007, 2008), and Lamy et al. (2022, 2023b). The obtained range suggests that the CMI is particularly efficient for a few keV at Jupiter.

Radio auroral sources were predicted to be located on the same field lines as the UV aurora. However, the energy range of precipitating electrons (few hundreds keV see Benmahi et al. 2024) does not match the energy range of the CMI unstable electrons (discussed above).

On one hand, this is coherent with the identified connection of HOM/DAM with the diffuse aurora equatorward the MAO, where the acceleration processes and mean electron energy differ from the ones at MAO (see Chapter 1 and discussions in Sulaiman et al. 2022). This was verified in a case study magnetically connected to the MAO, during which no radio emissions were identified but >50 keV monoenergetic EDF were identified, I identified that 50-200 keV electrons can be CMI unstable but they yield very weak growth rate ($\sim 10^{-7}$) unable to amplify waves at observable levels.

On the other hand, bKOM sources, who are further away from the planet, were

found to be connected to the MAO and sometimes to the brightest spots of dawn storms. This discrepancy between bKOM and HOM/DAM remains to be studied with more source crossings, but I infer that the electrons on the field lines connected to the MAO are only CMI-unstable at a distance corresponding to regions where f_{ce} is in the bKOM frequency range. Further down the magnetic field lines, electrons might undergo accelerations and/or pitch angle scattering, accelerating them to the observed high energy but removing their unstable characteristics and/or reducing their density to values where they are too weak to amplify radio emissions. at the HOM/DAM frequency range.

6.2. An updated view of the Jovian radio spectra

As mentioned in Chapter 1, the limits of the different radio components are porous so that bKOM is sometimes observed extending up to 1 MHz whereas HOM and DAM components are now thought to be a single component from 0.3 MHz.

In my work, I showed that HOM and DAM sources were located on the same field lines in large-scale highly depleted regions and generated by the same type of unstable EDF confirming this association.

bKOM sources, although less crossed, revealed a complex generation scenario. Indeed, while some source crossings were reminiscent of HOM/DAM sources (generation by shell and conics, low $\frac{f_{pe}}{f_{ce}}$), others were found in short scale sudden depletions reminiscent of AKR auroral cavities, partially associated with solar wind compressions and dawn storms.

Moreover, in the bKOM sources I identified, the wave intensity was stronger than that of HOM/DAM sources generated by the particularly efficient shell distribution. This is contrary to what is observed remotely (see Figure 1.5 and Zarka 1998). This difference could be due to a visibility effect.

6.2.1. Limitations of the used CMI growth rate analysis

The computation of the intensity was shown to be poorly constrained as it requires a precise estimation of the source term and the group velocity, which are highly dependent on the characteristics of the ambient plasma. Yoon et al. (2025) showed that a quasi-linear approach could overcome this problem and compare more accurately the amplified intensity and estimate the relaxation time of the electrons. Such an approach would also enable the evaluation of the saturation of the CMI in Jovian sources and the verification of the effectiveness of the CMI for distributions where multiple unstable features are intercepted by different sets of resonance circles.

The growth rate of >50 keV electrons was computed on resonance ellipses instead of resonance circles to account for the relativistic corrections of the resonance equations. However, I still used an expression of the growth rate based on the weakly relativistic assumption. Zhang et al. (2023) computed the growth rate in a fully relativistic assumption for an analytical model of the unstable (power-law) EDF and found growth

Component	Frequency	$\frac{f_{pe}}{f_{ce}}$	FAC	Emission angle (°)	Source size (km)	UV Association	Source of free energy	Unstable e^- Energy (keV)
AKR	10-1000kHz	$\sim 10^{-2} - 0.14$ Cavities	Upward	84°-90°	<100 km	Main oval	Shell	1-5 keV
SKR	10-1000 kHz	0.05-0.09	Upward	78°-90°	240-3000	Main oval	Shell	6-12 keV

Table 6.2.: Characteristics of AKR and SKR

rates 3 times larger than in the weakly relativistic assumption.

Compared to my method, Zhang et al. (2023) and Yoon et al. (2025) approaches requires to fit the parameters of an analytical model of the EDF to measurements. The diversity and complexity of the observed distributions at Jupiter would probably require multiple models.

Since I considered a homogeneous plasma, the propagation effect of the amplified waves was not studied. Wave refraction is however, expected to strongly affect the wave properties at the edges of the cavities (Louarn and Le Quéau 1996). Investigating wave refraction in the Jovian context will be of interest for future studies, and might help to check in situ the observed oblate DAM beaming pattern (Galopeau and Boudjada 2016).

6.3. Comparing the Jovian auroral radio emissions with the Terrestrial and Kronian cases

Out of Jupiter, only the auroral radio sources of AKR at Earth and SKR at Saturn have been in situ confirmed to be generated by the CMI (Louarn and Le Quéau 1996; Ergun et al. 2000; Mutel et al. 2010; Lamy et al. 2010). In these magnetospheres, the auroral activity is controlled by a static current system and the solar wind activity rather than stochastic processes linked to the enforcement of corotation. At Earth, intense AKR is triggered during substorms when the solar wind's field lines reconnect with the terrestrial field lines (Waters et al. 2022). At Saturn, SKR activity is enhanced during magnetospheric compressions (Desch 1983).

The properties of these different emissions are described in Zarka (1998), Zarka (2004), Lamy (2020), Lamy et al. (2010, 2018), Roux et al. (1993), Louarn and Le Quéau (1996), Ergun et al. (2000), and Mutel et al. (2010) and refs therein. They are summarized with those obtained for the different components of the Jovian spectrum in Table 6.2.

6.3.1. Source properties

The radio sources identified at Earth and Saturn both connect to the brightest auroral emissions, the equivalent of the MAO. Indeed, AKR sources have been identified in regions of 10 – 100 km connected to discrete UV arcs generated by the precipitation of electrons in inverted-Vs generated by upward currents. In addition, these sources were found in cavities which verify $\frac{f_{pe}}{f_{ce}} < 0.14$. Regions outside cavities do not verify this condition.

SKR sources were detected in regions dominated by the hot plasma with upward current and partially magnetically connected to the main UV emissions. However, the SKR sources were 240-3000 km long, and the sources were not detected in cavities.

The range of $\frac{f_{pe}}{f_{ce}}$ in bKOM sources ($\sim 10^{-2} - 10^{-1}$) was also found to be similar to the one of AKR sources. Additionally, cavities reminiscent of the terrestrial auroral cavities were found in some bKOM sources. Some of the identified cavities were found during dawn storms, but the correlation between cavities and dawn storms is not clear yet. At Earth, these cavities diagnose potential, whereas at Jupiter, the processes generating such cavities are unknown.

These similarities suggest that bKOM best compares with AKR and SKR, whereas HOM/DAM are proper to Jupiter.

All shell sources were detected in mostly upward current regions. This feature is probably a universal condition for perpendicular emission. This also means that these perpendicular emissions could be used to remotely sample upward FAC.

The size of the sources was found to be significantly larger than the AKR and SKR sources. This confirms Jupiter to be the ideal case to study the saturation of CMI compared to AKR and SKR.

6.3.2. Sources of free energy

The energy of the rare shells generating high growth rates at Jupiter (0.2-5 keV), although lower, is of the same order as that found at Earth (1-5 keV) and Saturn (6-12 keV). This implies that the CMI is universally efficient for electrons between 0.1 to 15 keV.

The prominence of the loss cone as a source of free energy at Jupiter questions its non-identification at Saturn. A reanalysis of Cassini's SKR source crossings associated with models of the loss cone would allow the verification of whether the loss cone is able to generate strong emissions at Saturn like at Jupiter, or only weak emissions like at Earth.

6.3.3. O-mode and harmonics

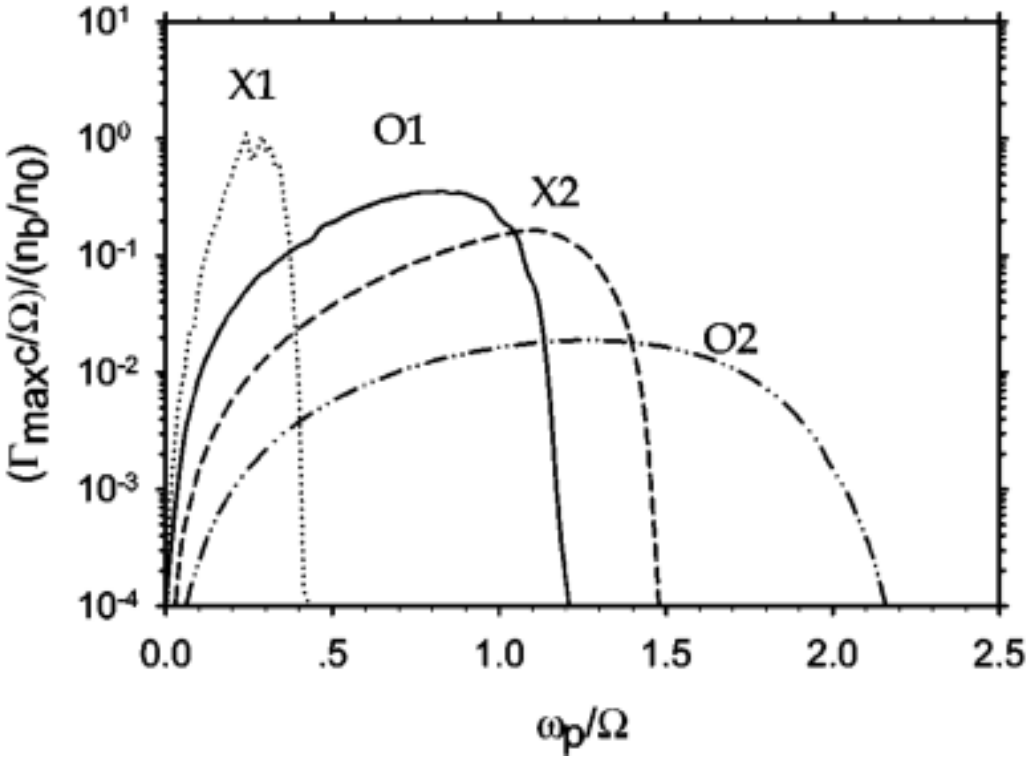


Figure 6.1.: Spatial amplification (proportional to the growth rate) as a function of $\frac{f_{pe}}{f_{ce}}$ computed in the case of beam distribution for the fundamental in X-mode (X1) and O-mode (O1) and for the 1st harmonic in X-mode (X2) and O-mode (O2). Credit: Chen et al. (2002)

At Earth and Saturn, AKR and SKR are regularly seen to be composed of bright X-mode emissions accompanied by 10-100 times weaker O- (and at Earth Z-) mode. In some AKR sources, the O-mode was shown to be dominant (Roux et al. 1993; Lamy et al. 2011). No O-mode was reported in Jovian source crossings while it was detected remotely (Zarka 1998).

The dominant emission mode of the CMI was theoretically shown to depend strongly on $\frac{f_{pe}}{f_{ce}}$ (Winglee 1985). For instance while X-mode dominates at $\frac{f_{pe}}{f_{ce}} \ll 1$, for $0.3 < \frac{f_{pe}}{f_{ce}} < 1$, the O-mode was shown to be dominant.

These theoretical developments led to the assumption that O-mode dominated AKR were produced from regions with large $\frac{f_{pe}}{f_{ce}} > 0.3$ at Earth.

At Jupiter, the lower $\frac{f_{pe}}{f_{ce}}$ (10^{-3}) seen in HOM and DAM sources could further reduce the retained factor 100 between X and O mode intensities.

While the bKOM $\frac{f_{pe}}{f_{ce}}$ ratios were higher and thus slightly more favorable for its amplification, no O-mode emissions were identified in bKOM sources.

At Earth and Saturn, 1st harmonic emissions were detected in association either with fundamental X-mode (86% of harmonics at Saturn and 100% at Earth) or with fundamental O-mode (14% at Saturn) (Benson 1982; Hosotani et al. 2003; Wu et al. 2022). Furthermore, second harmonics were also reported with a polarization opposite to the 1st harmonic at Saturn (11% of harmonics). At Jupiter, I discovered 2 cases of 1st harmonics HOM associated with X-mode fundamental. The mode of these harmonics was not obtained.

Similarly to O-mode, amplification of the 1st harmonic was shown to have larger growth rates at $\frac{f_{pe}}{f_{ce}}$>1.

At Jupiter, the 1st harmonic intensity might be drastically reduced in HOM and DAM sources where $\frac{f_{pe}}{f_{ce}}$ is particularly low. Note that the 2 detected Jovian harmonics were emitted from regions with $\frac{f_{pe}}{f_{ce}} = 10^{-2}$ which is still very low but falls at the upper end of the range identified in HOM/DAM sources. The question of the generation process of harmonics at Jupiter is still open, but the low $\frac{f_{pe}}{f_{ce}}$ suggests these harmonics are emitted on the X-mode.

6.4. Extension to the case of Mercury

Beyond the case of Jupiter, I have paid attention to the possible existence of auroral radio emissions produced by Mercury, in the context of the upcoming radio exploration of the Hermean magnetosphere with Bepi-Colombo.

Mercury's magnetic field has been discovered with in situ measurements by Mariner 10 (Russell et al. 1988) and better characterized by MESSENGER (Slavin et al. 2008). The possibility of radio emissions generated by the CMI at tens of kHz has been discussed by Blomberg et al. (2007), Zarka et al. (2001), and Varela et al. (2016), which predicted a Hermetian radio power of 1×10^6 W if it exists. Contrary to the other magnetized planet, Mercury does not possess a thick atmosphere or ionosphere, making it a unique magnetosphere in the solar system that the Bepi Colombo/Mio polar orbiter will characterize. In addition, rapid reconfigurations of the magnetosphere reminiscent of substorms were observed within Mercury's magnetotail as sudden, regular, electron flux enhancements at energy >30 keV that may precipitate and induce the observed X-ray fluorescence at the surface (Lindsay et al. 2016). This magnetosphere has the peculiarity of being surrounded by a dense solar wind environment which would trap these radiations into the magnetosphere, explaining the absence of remote detection (Zarka 2000). Only Bepi/Mio/PWI radio instrument will be able to discover such waves.

This spacecraft has already completed 6 flybys of Mercury, during which PWI antenna was unfortunately not yet deployed. However, the plasma instrument MEA has already acquired pioneering electron measurements near Mercury's magnetic poles.

By collaborating with N. André and M. Rojo at IRAP, I looked at the MEA-derived plasma density and associated f_{pe} derived for the first 4 Mercury's flybys. I estimated f_{ce} from the magnetic model KTH (Pump et al. 2024). The resulting fpe/fce ratio

is displayed in Figure 6.2. It remains systematically beyond 3, quenching any CMI resonance with local energetic electrons.

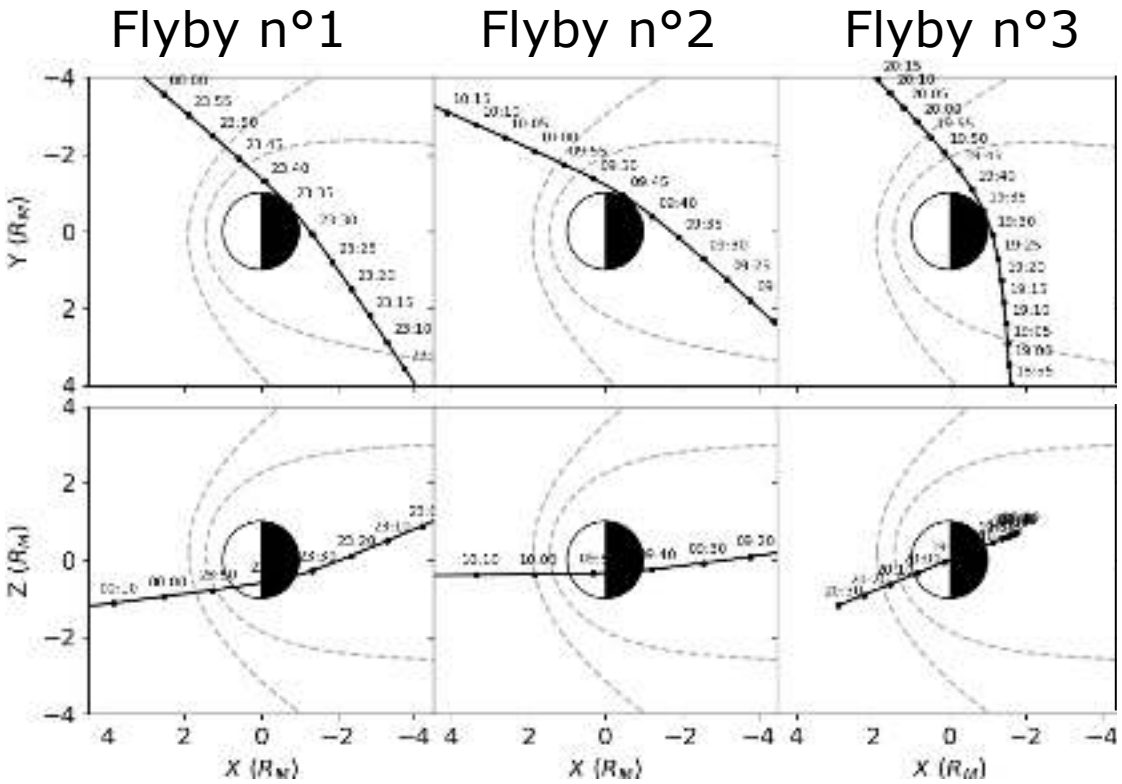


Figure 6.2.: Geometry of the flybys from Bepi-Colombo in the Mercury solar orbital (MSO) coordinate system with average Bow Shock and Magnetopause models displayed with dashed gray lines. Credits: Rojo et al. (2024)

However, auroral radio emissions were predicted to be emitted from eventually highly depleted regions of the polar magnetosphere, which Bepi will investigate.

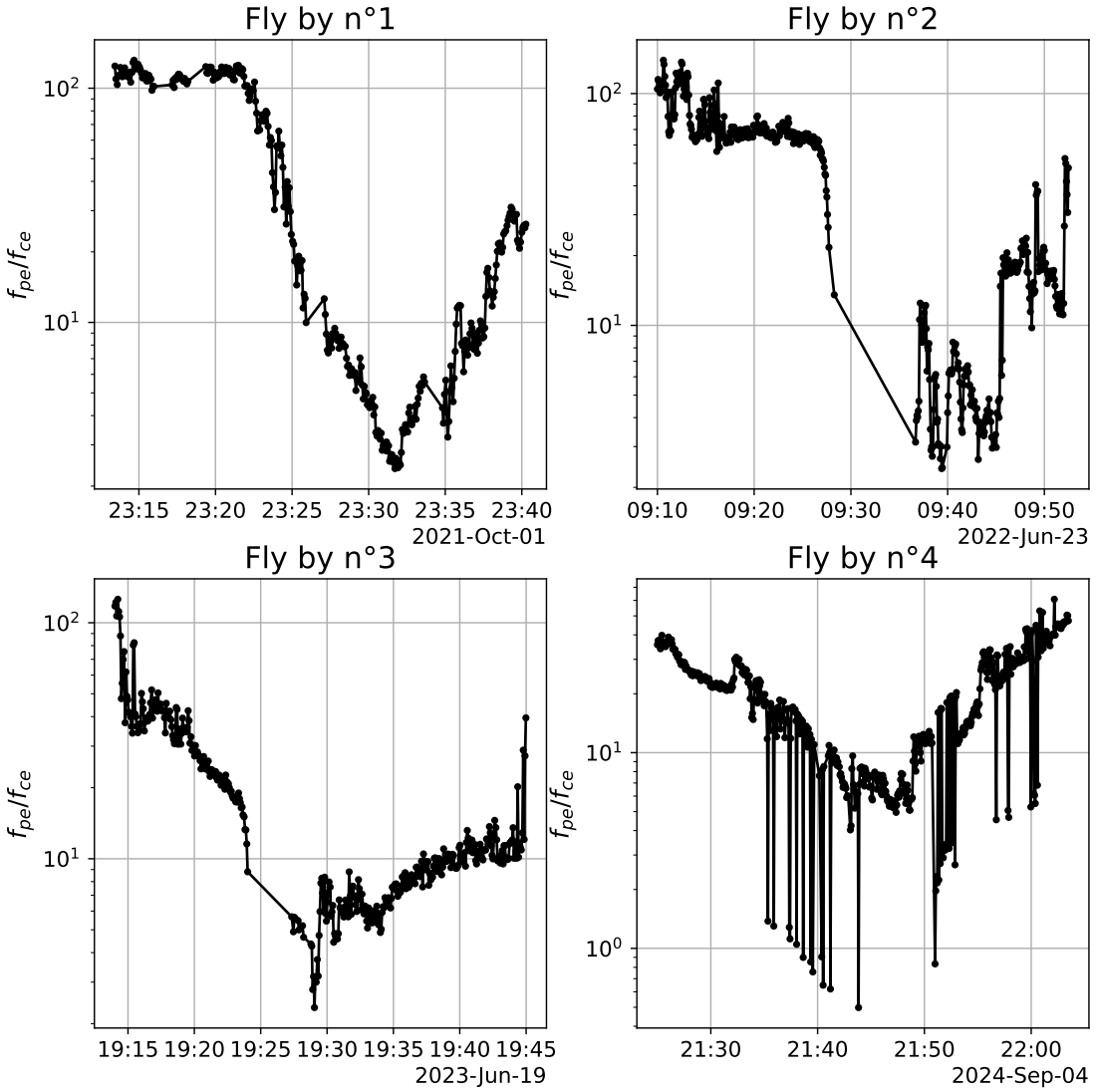


Figure 6.3.: $\frac{f_{pe}}{f_{ce}}$ obtained during Bepi flybys in the Hermetian magnetosphere. Courtesy: M. Rojo

Conclusion

Radio, someone still loves you

Queen

The goal of this thesis was to confirm that Jupiter's auroral radio emissions are indeed generated by the CMI, to characterize the sources of these emissions, and to compare the generation of the different components of the Jovian spectrum.

To do so, I have developed a new expression of the CMI growth rate for the case of Jupiter. Whereas the expressions used previously assumed a plasma dominated by cold or hot electrons, this new expression can account for both cases in the semi-relativistic approximation.

This expression was systematically used with a method to derive the growth rate from Juno's in situ measurements on the sources crossed by Juno, which were identified with Louis et al. (2019) criterion, assuming a source was crossed when emissions were detected below $f_{ce} + 1\%$.

I have surveyed and analyzed all the Jovian radio auroral components and confirmed that they were all generated by the CMI.

For the case of HOM/DAM, I identified 116 source crossings for the first 70 orbits of Juno. I have confirmed the CMI as a generation mechanism and statistically showed that the HOM and DAM component are actually a single component which is emitted from highly depleted regions ($\frac{f_{pe}}{f_{ce}} \sim 10^{-3} - 10^{-2}$), connected to the Diffuse aurora and the equatorward boundary of the MAO at all longitudes. These emissions are mainly generated by loss cone EDF of a few keV and secondarily by conics, both partially correlated with Alfvénic perturbations. I completed these sources of free energy with the 0.2-5 keV shell distributions, newly identified at Jupiter.

These shells were shown to amplify waves down to 2% below f_{ce}. They were specifically identified in regions associated with an upward current, monoenergetic signatures in electron energy spectra. They were systematically associated with an enlargement of the loss cone, a possible sign of acceleration below the spacecraft.

During collaborations (Louis et al. 2023b; Rabia et al. 2025), I investigated the generation of Moon-DAM during crossings of Io's flux tubes and the newly identified Callisto flux tube. Generally, Moon-DAM is emitted in flux tubes connected to the UV auroral footprint associated with the moon.

Using my method, I showed during three flux tube crossings that the auroral radio emissions induced by Io were indeed generated by CMI-unstable loss cone EDF of 3 to 15 keV located in upward currents. In the case of Callisto, no radio emissions were identified. I was nevertheless interested in the possibility that emissions might

be produced below the sensitivity threshold of Waves. I identified unstable loss cone electrons of 1-8 keV, but their growth rate was too low to generate emissions detectable by Waves.

All these unstable electrons have an energy in the range 0.1 to 15 keV, consistent with the weakly relativistic approximation and the association of HOM/DAM with Diffuse aurora. Nonetheless, I investigated electrons in the 50-1000 keV range as a potential source of free energy. These electrons are commonly seen above Jupiter's main auroral emissions, and I showed they can be CMI-unstable and exhibit the same types of unstable EDF, but do not amplify waves at observable levels.

I also reported the first 2 cases of HOM 1st harmonic, whose generation remains to be studied to better understand the energy dissipation processes at Jupiter.

For the bKOM case, I studied the first 60 orbits and found only 7 cases between 10 and 300 kHz, but only 5 of them had high resolution measurements, allowing me to apply my growth rate analysis. This low number can be explained by the fact that these emissions are emitted at higher altitudes where the main oval is not often crossed. Among these 5 crossings, I identified three cases of sudden electron depletion reminiscent of auroral cavities in which AKR is emitted. The source crossings were also partially associated with magnetospheric compressions and dawn storms, which are intensifications of the UV aurora linked to a reconfiguration of the magnetosphere. I then applied my growth rate analysis. Unfortunately, the loss cone was not resolved by the JADE-E electron instrument, so I was unable to verify whether the loss cone distributions were unstable for this component. Nevertheless, I was able to obtain that the bKOM is generated by conical and sometimes shell-like distributions of 1-30 keV.

Finally, I discussed these results with the characteristics of AKR and SKR sources.

6.1. Perspectives

In future studies, I plan to investigate the sources crossed by Juno during its Extended Mission 2 to verify on a larger statistics the results described here.

I also intend to further investigate the generation of the 1st harmonics I identified by looking into more details the plasma and magnetic measurements of these intervals.

Furthermore, the case study on the generation by >50 keV electrons will be extended to other regions connected to the MAO and/or in regions where ubiquitous emissions are seen tens percents above f_{ce}. To do so, I plan to develop a more accurate expression of the growth rate for this range of energy and to use both JADE-E and JEDI measurements to obtain the complete EDF from 0.01 keV to 1200 keV. It would also be interesting to resurvey Juno radio measurements with a criterion accounting for generation by high-energy electrons.

This case study also leads to a reconsideration of the spectrum obtained in the first 70 Juno orbits to search for emission tens percents below f_{ce} that would unambiguously show that high-energy electrons can generate intense waves. Such emission would require a purely hot plasma so that the X-mode cut-off shifts below the emission

frequency.

Furthermore, I plan to apply my methods to other magnetospheres such as Saturn's to study the generation of SKR by loss cone. Also, I plan to take the opportunity of Bepi Columbo mission to study the eventual generation of radio emissions in this magnetosphere.

Below I describe the cases of Ganymede's and Uranus' magnetospheres that would be interesting objects to study the CMI and its conditions.

6.1.1. The case of Ganymede

Ganymede's magnetosphere was exhibited by Galileo during its flyby (Gurnett et al. 1996). A magnetosphere was also confirmed through the observations of radio waves incoming from the satellite. This magnetosphere is categorized with Mercury's as a "mini magnetosphere", but for the case of the embedded magnetosphere of Ganymede inside Jupiter's magnetosphere, the plasma regime is subalfvénic. Among the radio waves observed by Galileo (and later by Juno, see Kurth et al. 2022), no emissions were associated with the CMI. This absence was hypothesized to be due to a large $\frac{f_{pe}}{f_{ce}}$ for which the CMI cannot generate intense X-mode radio emissions. The Jupiter Icy Moons Explorer (JUICE) mission will fly by Ganymede and will in situ measure its auroral regions to verify this hypothesis.

6.1.2. The case of Uranus

The magnetosphere of Uranus is not well understood due to its fast-rotating (17.25h) magnetic field tilted on its rotation axis (59°), making its magnetotail spirals. Moreover, its rotation axis is tilted over 90° relative to its revolution axis. This makes the alignment of the magnetic field with the solar wind very different, whether the planet is at the equinox or the solstice. Uranus' Kilometric Radiation (UKR) were remotely detected by Voyager 2 (Warwick et al. 1986, 1989). Since they exhibit similar properties (beaming, mostly X-mode, circular polarization) to the other planetary auroral radio emissions, they were attributed to the CMI. However, these emissions stand out as they can be emitted from the depleted equatorial regions and in other regions be emitted mostly on the O-mode rather than the X-mode. These emissions have yet to be characterized in situ by a future mission, as the orbiter mission concept, Uranus Orbiter and Probe. I contributed on a proceeding (Lamy et al. 2023a) proposing a High Frequency Receiver in the framework of a Radio and Plasma Wave to study UKR.

Overall, the comparative study of solar system radio sources will refine our understanding of the CMI as a fundamental plasma instability able to efficiently amplify radio waves for a wide range of magnetized objects in the ongoing search for exoplanets and in the larger astrophysical context (blazars, pulsars).

Bibliography

Al Saati, S., N. Clément, C. Louis, et al. (2022). "Magnetosphere-Ionosphere-Thermosphere Coupling Study at Jupiter Based on Juno's First 30 Orbits and Modeling Tools". In: *Journal of Geophysical Research (Space Physics)* 127.10, e2022JA030586, e2022JA030586. DOI: 10.1029/2022JA030586.

Allegrini, F., F. Bagenal, S. Bolton, et al. (2017). "Electron beams and loss cones in the auroral regions of Jupiter". In: *Geophysical Research Letters* 44.14, pp. 7131–7139. DOI: 10.1002/2017GL073180.

Allegrini, F., B. Mauk, G. Clark, et al. (2020). "Energy Flux and Characteristic Energy of Electrons Over Jupiter's Main Auroral Emission". In: *Journal of Geophysical Research (Space Physics)* 125, e27693. ISSN: 0148-0227. DOI: 10.1029/2019JA027693.

André, M. and L. Eliasson (1992). "Electron acceleration by low frequency electric field fluctuations: Electron conics". In: *Geophysical Research Letters* 19.11, pp. 1073–1076. ISSN: 1944-8007. DOI: 10.1029/92gl01022.

Appleton, E. (1932). "Wireless studies of the ionosphere". In: *Journal of the Institution of Electrical Engineers* 71 (430), pp. 642–650. DOI: 10.1049/jiee-1.1932.0144.

Badman, S. V., G. Branduardi-Raymont, M. Galand, et al. (2015). "Auroral Processes at the Giant Planets: Energy Deposition, Emission Mechanisms, Morphology and Spectra". In: *Space Science Reviews* 187.1, pp. 99–179. ISSN: 0038-6308, 1572-9672. DOI: 10.1007/s11214-014-0042-x.

Bagenal, F., A. Adriani, F. Allegrini, et al. (2017). "Magnetospheric Science Objectives of the Juno Mission". In: *Space Science Reviews* 213.1-4, pp. 219–287. DOI: 10.1007/s11214-014-0036-8.

Bagenal, F. and P. A. Delamere (2011). "Flow of mass and energy in the magnetospheres of Jupiter and Saturn". In: *Journal of Geophysical Research (Space Physics)* 116.A5, A05209, A05209. DOI: 10.1029/2010JA016294.

Barrow, C. H. and D. P. Morrow (1968). "The Polarization of the Jupiter Radiation at 18 Mc/s". In: *The Astrophysical Journal* 152, p. 593. DOI: 10.1086/149574.

Barrow, C., A. Lecacheux, R. MacDowall, and M. Kaiser (2001). "The Jovian HOM and bKOM radio emissions observed by Wind/WAVES and by Ulysses/URAP". In: *Planetary and Space Science* 49.3, pp. 377–384. ISSN: 0032-0633. DOI: 10.1016/s0032-0633(00)00158-6.

Bekefi (1969). *Radiation Processes in Plasmas*. John Wiley.

Benmahi, B., B. Bonfond, B. Benne, et al. (2024). "Energy mapping of Jupiter's auroral electrons from Juno/UVS data using a new H2 UV emission model". In: *Astronomy & Astrophysics* 685, A26. ISSN: 1432-0746. DOI: 10.1051/0004-6361/202348634.

Benson, R. F. (1982). "Harmonic auroral kilometric radiation of natural origin". In: *Geophysical Research Letters* 9.9, pp. 1120–1123. DOI: 10.1029/GL009i009p01120.

Bigg, E. K. (1964). "Influence of the Satellite Io on Jupiter's Decametric Emission". In: *Nature* 203.4949, pp. 1008–1010. DOI: 10.1038/2031008a0.

Bingham, R., D. C. Speirs, B. J. Kellett, et al. (2013). "Laboratory astrophysics: Investigation of planetary and astrophysical maser emission". In: *Space Science Reviews* 178.2–4, pp. 695–713. ISSN: 1572-9672. DOI: 10.1007/s11214-013-9963-z.

Blanc, M., R. Kallenbach, and N. V. Erkaev (2005). "Solar System Magnetospheres". In: *Space Science Reviews* 116.1–2, pp. 227–298. ISSN: 1572-9672. DOI: 10.1007/s11214-005-1958-y.

Blomberg, L. G., J. A. Cumnock, K.-H. Glassmeier, and R. A. Treumann (2007). "Plasma Waves in the Hermean Magnetosphere". In: *Space Science Reviews* 132.2–4, pp. 575–591. ISSN: 1572-9672. DOI: 10.1007/s11214-007-9282-3.

Boischot, A., A. Lecacheux, M. L. Kaiser, M. D. Desch, J. K. Alexander, and J. W. Warwick (1981). "Radio Jupiter after Voyager: An overview of the planetary radio astronomy observations". In: *Journal of Geophysical Research: Space Physics* 86.A10, pp. 8213–8226. DOI: 10.1029/JA086iA10p08213.

Bolton, S. J., J. Lunine, D. Stevenson, et al. (2017). "The Juno Mission". In: *Space Science Reviews* 213.1, pp. 5–37. ISSN: 0038-6308, 1572-9672. DOI: 10.1007/s11214-017-0429-6.

Bonfond, B., D. Grodent, J. .-. Gérard, A. Radioti, J. Saur, and S. Jacobsen (2008). "UV Io footprint leading spot: A key feature for understanding the UV Io footprint multiplicity?" In: *Geophysical Research Letters* 35.5, L05107, p. L05107. DOI: 10.1029/2007GL032418.

Bonfond, B., J. Saur, D. Grodent, et al. (2017). "The tails of the satellite auroral footprints at Jupiter". In: *Journal of Geophysical Research (Space Physics)* 122, pp. 7985–7996. ISSN: 0148-0227. DOI: 10.1002/2017JA024370.

Bonfond, B., Z. H. Yao, G. R. Gladstone, et al. (2021). "Are Dawn Storms Jupiter's Auroral Substorms?" In: *AGU Advances* 2.1, e2020AV000275. ISSN: 2576-604X, 2576-604X. DOI: 10.1029/2020AV000275.

Bonfond, B., Z. Yao, and D. Grodent (2020). "Six Pieces of Evidence Against the Corotation Enforcement Theory to Explain the Main Aurora at Jupiter". In: *Journal of Geophysical Research: Space Physics* 125.11, e2020JA028152. ISSN: 2169-9380, 2169-9402. DOI: 10.1029/2020JA028152.

Boudouma, A., P. Zarka, C. K. Louis, C. Briand, and M. Imai (2024). "Generation Mechanism and Beaming of Jovian nKOM From 3D Numerical Modeling of Juno/Waves Observations". In: *Journal of Geophysical Research: Space Physics* 129.4, e2023JA032280. ISSN: 2169-9380, 2169-9402. DOI: 10.1029/2023JA032280.

Boudouma, A., P. Zarka, F. P. Magalhães, et al. (2023). "Localisation of the main HOM source in the dusk side of the Jovian magnetosphere". In: *Planetary, Solar and Heliospheric Radio Emissions IX*. Ed. by C. K. Louis, C. M. Jackman, G. Fischer, A. H. Sulaiman, and P. Zucca, 103094, p. 103094. DOI: 10.25546/103094.

Broadfoot, A. L., B. R. Sandel, D. E. Shemansky, et al. (1981). "Overview of the Voyager ultraviolet spectrometry results through Jupiter encounter". In: *Journal of Geophysical Research* 86.A10, pp. 8259–8284. DOI: 10.1029/JA086iA10p08259.

Burke, B. F. and K. L. Franklin (1955). "Observations of a variable radio source associated with the planet Jupiter". In: *Journal of Geophysical Research* 60.2, pp. 213–217.

Carr, T. D., M. D. Desch, and J. K. Alexander (1983). "Physics of the Jovian magnetosphere. 7. Phenomenology of magnetospheric radio emissions." In: *Physics of the Jovian Magnetosphere*. Ed. by A. J. Dessler, pp. 226–284. DOI: 10.1017/CBO9780511564574.009.

Chen, Y. P., G. C. Zhou, P. H. Yoon, and C. S. Wu (2002). "A beam-maser instability: Direct amplification of radiation". In: *Physics of Plasmas* 9.6, pp. 2816–2821. ISSN: 1089-7674. DOI: 10.1063/1.1481748.

Clarke, J. T., H. W. Moos, S. K. Atreya, and A. L. Lane (1980). "Observations from earth orbit and variability of the polar aurora on Jupiter". In: *The Astrophysical Journal* 241, pp. L179–L182. DOI: 10.1086/183386.

Clarke, J. T., D. Grodent, S. W. H. Cowley, et al. (2004). "Jupiter's aurora". In: *Jupiter. The Planet, Satellites and Magnetosphere*. Ed. by F. Bagenal, T. E. Dowling, and W. B. McKinnon. Vol. 1, pp. 639–670.

Collet, B., L. Lamy, C. K. Louis, V. Hue, and T. K. Kim (2025). "In Situ Analysis of Jupiter's Broadband Kilometric Auroral Radio Emissions With Juno". In: *Geophysical Research Letters* 52.9, e2024GL114447. ISSN: 0094-8276, 1944-8007. DOI: 10.1029/2024GL114447.

Collet, B., L. Lamy, C. K. Louis, et al. (2023). "Characterization of Jovian hectometric sources with Juno: statistical position and generation by shell-type electrons". In: *Planetary, Solar and Heliospheric Radio Emissions IX*. Ed. by C. K. Louis, C. M. Jackman, G. Fischer, A. H. Sulaiman, and P. Zucca, 103095, p. 103095. DOI: 10.25546/103095.

Collet, B., L. Lamy, C. K. Louis, et al. (2024a). "A New Type of Jovian Hectometric Radiation Powered by Monoenergetic Electron Beams". In: *Journal of Geophysical Research: Space Physics* 129.5, e2024JA032422. ISSN: 2169-9380, 2169-9402. DOI: 10.1029/2024JA032422.

Collet, B., L. Lamy, C. Louis, et al. (2024b). *List of HOM/DAM Radio Sources crossings during Juno's 45 first perijoves*. DOI: 10.5281/ZENODO.10869371.

Connerney, J. E. P., M. Benn, J. B. Bjarno, et al. (2017). "The Juno Magnetic Field Investigation". In: *Space Science Reviews* 213.1–4, pp. 39–138. ISSN: 1572-9672. DOI: 10.1007/s11214-017-0334-z.

Connerney, J. E. P., S. Kotsiaros, R. J. Oliversen, et al. (2018). "A New Model of Jupiter's Magnetic Field From Juno's First Nine Orbits". In: *Geophysical Research Letters* 45.6, pp. 2590–2596. DOI: 10.1002/2018GL077312.

Connerney, J. E. P., S. Timmins, M. Herceg, and J. L. Joergensen (2020). "A Jovian Magnetodisc Model for the Juno Era". In: *Journal of Geophysical Research (Space Physics)* 125.10, e28138, e28138. DOI: 10.1029/2020JA028138.

Connerney, J. E. P., S. Timmins, R. J. Oliversen, et al. (2022). "A New Model of Jupiter's Magnetic Field at the Completion of Juno's Prime Mission". In: *Journal of Geophysical Research (Planets)* 127.2, e07055, e07055. DOI: 10.1029/2021JE007055.

Cooper, J. F., R. E. Johnson, B. H. Mauk, H. B. Garrett, and N. Gehrels (2001). "Energetic Ion and Electron Irradiation of the Icy Galilean Satellites". In: *Icarus* 149.1, pp. 133–159. DOI: 10.1006/icar.2000.6498.

Cowley, S. W. H. and E. J. Bunce (2001). "Origin of the main auroral oval in Jupiter's coupled magnetosphere-ionosphere system". In: *Planetary and Space Science* 49.10-11, pp. 1067–1088. DOI: 10.1016/S0032-0633(00)00167-7.

Delory, G. T., R. E. Ergun, C. W. Carlson, et al. (1998). "FAST observations of electron distributions within AKR source regions". In: *Geophysical Research Letters* 25.12, pp. 2069–2072. DOI: 10.1029/98GL00705.

Desch, M. D. (1983). "Radio emission signature of Saturn immersions in Jupiter's magnetic tail". In: *Journal of Geophysical Research* 88.A9, pp. 6904–6910. DOI: 10.1029/JA088iA09p06904.

Desch, M. D. and M. L. Kaiser (1980). "The occurrence rate, polarization character, and intensity of broadband Jovian kilometric radiation". In: *Journal of Geophysical Research* 85, pp. 4248–4256. ISSN: 0148-0227. DOI: 10.1029/JA085iA08p04248.

Dory, R. A., G. E. Guest, and E. G. Harris (1965). "Unstable Electrostatic Plasma Waves Propagating Perpendicular to a Magnetic Field". In: *Physical Review Letters* 14.5, pp. 131–133. ISSN: 0031-9007. DOI: 10.1103/physrevlett.14.131.

Dulk, G. A., W. C. Erickson, R. Manning, and J. .-. Bougeret (2001). "Calibration of low-frequency radio telescopes using the galactic background radiation". In: *Astronomy and Astrophysics* 365, pp. 294–300. DOI: 10.1051/0004-6361:20000006.

Ebert, R. W., T. K. Greathouse, G. Clark, et al. (2021). "Simultaneous UV Images and High-Latitude Particle and Field Measurements During an Auroral Dawn Storm at Jupiter". In: *Journal of Geophysical Research (Space Physics)* 126.12, e29679, e29679. DOI: 10.1029/2021JA02967910.1002/essoar.10503105.2.

Eliasson, L., M. André, R. Lundin, R. Pottelette, G. Marklund, and G. Holmgren (1996). "Observations of electron conies by the Viking satellite". In: *Journal of Geophysical Research: Space Physics* 101.A6, pp. 13225–13238. ISSN: 0148-0227. DOI: 10.1029/95ja02386.

Elliott, S. S., D. A. Gurnett, W. S. Kurth, et al. (2018). "The Acceleration of Electrons to High Energies Over the Jovian Polar Cap via Whistler Mode Wave-Particle Interactions". In: *Journal of Geophysical Research (Space Physics)* 123.9, pp. 7523–7533. DOI: 10.1029/2018JA025797.

Elliott, S. S., A. H. Sulaiman, W. S. Kurth, et al. (2021). "The High-Latitude Extension of Jupiter's Io Torus: Electron Densities Measured by Juno Waves". In: *Journal of Geophysical Research (Space Physics)* 126.8, e29195, e29195. DOI: 10.1029/2021JA029195.

Ergun, R. E., C. W. Carlson, J. P. McFadden, G. T. Delory, R. J. Strangeway, and P. L. Pritchett (2000). "Electron-Cyclotron Maser Driven by Charged-Particle Acceleration from Magnetic Field-aligned Electric Fields". In: *The Astrophysical Journal* 538.1, pp. 456–466. DOI: 10.1086/309094.

Feng, E., B. Zhang, Z. Yao, et al. (2023). "Variation of the Jovian Magnetopause Under Constant Solar Wind Conditions: Significance of Magnetodisc Dynamics". In: *Geophysical Research Letters* 50.12. ISSN: 1944-8007. DOI: 10.1029/2023gl104046.

Fischer, G., U. Taubenschuss, D. Píša, M. Imai, and W. S. Kurth (2025). "Spectral Structures of Jovian Broadband Kilometric Radiation Revealed by Cassini and Juno". In: *Journal of Geophysical Research*.

Galopeau, P. H. M. and M. Y. Boudjada (2016). "An oblate beaming cone for Io-controlled Jovian decameter emission". In: *Journal of Geophysical Research (Space Physics)* 121.4, pp. 3120–3138. DOI: 10.1002/2015JA021038.

Galopeau, P. H. M. and M. Y. Boudjada (2005). "Solar wind control of Jovian auroral emissions". In: *Journal of Geophysical Research (Space Physics)* 110.A9, A09221, A09221. DOI: 10.1029/2004JA010843.

Galopeau, P. H. M., M. Y. Boudjada, and H. O. Rucker (2004). "Evidence of jovian active longitude: 1. Efficiency of cyclotron maser instability". In: *Journal of Geophysical Research (Space Physics)* 109.A12, A12217, A12217. DOI: 10.1029/2004JA010459.

Gautier, A.-L. (2013). "Etude de la propagation des ondes radio dans les environnements planétaires". Thèse de doctorat dirigée par Cecconi, Baptiste et Zarka, Philippe Astronomie et astrophysique Observatoire de Paris (1667-....) 2013. PhD thesis, 1 vol. (X–304 p.)

Genova, F. and M. G. Aubier (1987). "High frequency limit and visibility of the non-Io and Io-dependent Jovian decameter radio emission". In: *Astronomy and Astrophysics* 177.1-2, pp. 303–309.

Genova, F., P. Zarka, and A. Lecacheux (1989). "Jupiter Decametric Radiation". In: *NASA Special Publication*. Ed. by M. J. S. Belton, R. A. West, J. Rahe, and M. Pereyda. Vol. 494, pp. 156–174.

Gerard, J. C., D. Grodent, R. Prange, et al. (1994). "A Remarkable Auroral Event on Jupiter Observed in the Ultraviolet with the Hubble Space Telescope". In: *Science* 266.5191, pp. 1675–1678. DOI: 10.1126/science.266.5191.1675.

Gérard, J.-C., B. Bonfond, D. Grodent, et al. (2014). "Mapping the electron energy in Jupiter's aurora: Hubble spectral observations". In: *Journal of Geophysical Research: Space Physics* 119.11, pp. 9072–9088. DOI: 10.1002/2014JA020514.

Gershman, D. J., J. E. P. Connerney, S. Kotsiaros, et al. (2019). "Alfvénic Fluctuations Associated With Jupiter's Auroral Emissions". In: *Geophysical Research Letters* 46.13, pp. 7157–7165. ISSN: 0094-8276, 1944-8007. DOI: 10.1029/2019GL082951.

Gladstone, G. R., S. C. Persyn, J. S. Eterno, et al. (2017). "The Ultraviolet Spectrograph on NASA's Juno Mission". In: *Space Science Reviews* 213.1-4, pp. 447–473. DOI: 10.1007/s11214-014-0040-z.

Greathouse, T., R. Gladstone, M. Versteeg, et al. (2021). "Local Time Dependence of Jupiter's Polar Auroral Emissions Observed by Juno UVS". In: *Journal of Geophysical Research (Planets)* 126, e06954. ISSN: 0148-0227. DOI: 10.1029/2021JE00695410.1002/essoar.10507057.1.

Grodent, D., J. T. Clarke, J. Kim, J. H. Waite, and S. W. H. Cowley (2003). "Jupiter's main auroral oval observed with HST-STIS". In: *Journal of Geophysical Research (Space Physics)* 108.A11, 1389, p. 1389. DOI: 10.1029/2003JA009921.

Gurnett, D. A., W. S. Kurth, A. Roux, S. J. Bolton, and C. F. Kennel (1996). "Evidence for a magnetosphere at Ganymede from plasma-wave observations by the Galileo spacecraft". In: *Nature* 384.6609, pp. 535–537. DOI: 10.1038/384535a0.

Head, L. A., D. Grodent, B. Bonfond, et al. (2024). "Effect of magnetospheric conditions on the morphology of Jupiter's ultraviolet main auroral emission as observed by Juno-UVS". In: *Astronomy &; Astrophysics* 688, A205. ISSN: 1432-0746. DOI: 10.1051/0004-6361/202450253.

Heidari, N., I. Boisse, N. C. Hara, et al. (2024). "The SOPHIE search for northern extrasolar planets: XIX. A system including a cold sub-Neptune potentially transiting a V = 6.5 star HD 88986". In: *Astronomy and Astrophysics* 681, A55, A55. DOI: 10.1051/0004-6361/202347897.

Hess, S., B. Cecconi, and P. Zarka (2008). "Modeling of Io-Jupiter decameter arcs, emission beaming and energy source". In: *Geophysical Research Letters* 35.13, L13107, p. L13107. DOI: 10.1029/2008GL033656.

Hess, S., P. Delamere, V. Dols, B. Bonfond, and D. Swift (2010). "Power transmission and particle acceleration along the Io flux tube". In: *Journal of Geophysical Research (Space Physics)* 115.A6, A06205, A06205. DOI: 10.1029/2009JA014928.

Hess, S., F. Mottez, and P. Zarka (2007). "Jovian *S* burst generation by Alfvén waves:" in: *Journal of Geophysical Research: Space Physics* 112 (A11). ISSN: 01480227. DOI: 10.1029/2006JA012191.

Hess, S., F. Mottez, and P. Zarka (2009). "Effect of electric potential structures on Jovian S-burst morphology". In: *Geophysical Research Letters* 36.14. DOI: 10.1029/2009GL039084.

Higgins, C. A. (2007). "Satellite control of Jovian 2-6 MHz radio emission using Voyager data". In: *Journal of Geophysical Research (Space Physics)* 112.A5, A05213, A05213. DOI: 10.1029/2006JA012100.

Higgins, C. A., J. D. Menietti, and I. W. Christopher (2006). "Europa control of Jovian radio emission: A Galileo study". In: *Geophysical Research Letters* 33.14, L14110, p. L14110. DOI: 10.1029/2006GL026218.

Hill, T. W. (1979). "Inertial limit on corotation". In: *Journal of Geophysical Research* 84.A11, pp. 6554–6558. DOI: 10.1029/JA084iA11p06554.

Hosotani, A., T. Ono, M. Iizima, and A. Kumamoto (2003). "Second harmonics of auroral kilometric radiation observed by the Akebono satellite". In: *National Institute of Polar Research*.

Huff, R. L., W. Calvert, J. D. Craven, L. A. Frank, and D. A. Gurnett (1988). "Mapping of auroral kilometric radiation sources to the aurora". In: *Journal of Geophysical Research* 93.A10, pp. 11445–11454. DOI: 10.1029/JA093iA10p11445.

Imai, M., T. K. Greathouse, W. S. Kurth, et al. (2019). "Probing Jovian Broadband Kilometric Radio Sources Tied to the Ultraviolet Main Auroral Oval With Juno". In: *Geophysical Research Letters* 46.2, pp. 571–579. DOI: 10.1029/2018GL081227.

Jácome, H. R. P., M. S. Marques, P. Zarka, E. Echer, L. Lamy, and C. K. Louis (2022). "Search for Jovian decametric emission induced by Europa on the extensive Nançay Decameter Array catalog". In: *Astronomy and Astrophysics* 665, A67, A67. DOI: 10.1051/0004-6361/202244246.

Kaiser, M. L., P. Zarka, W. S. Kurth, G. B. Hospodarsky, and D. A. Gurnett (2000). "Cassini and Wind stereoscopic observations of Jovian nonthermal radio emissions: Measure-

ment of beam widths". In: *Journal of Geophysical Research* 105.A7, pp. 16053–16062. DOI: 10.1029/1999JA000414.

Khurana, K. K., M. G. Kivelson, V. M. Vasyliunas, et al. (2004). "The configuration of Jupiter's magnetosphere". In: *Jupiter. The Planet, Satellites and Magnetosphere*. Ed. by F. Bagenal, T. E. Dowling, and W. B. McKinnon. Vol. 1, pp. 593–616.

Kim, T. K., N. V. Pogorelov, G. P. Zank, H. A. Elliott, and D. J. McComas (2016). "MODELING THE SOLAR WIND AT THE ULYSSES, VOYAGER, AND NEW HORIZONS SPACECRAFT". In: *The Astrophysical Journal* 832.1, p. 72. ISSN: 1538-4357. DOI: 10.3847/0004-637x/832/1/72.

Kimura, T., F. Tsuchiya, H. Misawa, A. Morioka, and H. Nozawa (2008). "Occurrence and source characteristics of the high-latitude components of Jovian broadband kilometric radiation". In: *Planetary and Space Science* 56.8, pp. 1155–1168. ISSN: 0032-0633. DOI: 10.1016/j.pss.2008.03.001.

Knight, S. (1973). "Parallel electric fields". In: *Planetary and Space Science* 21.5, pp. 741–750. ISSN: 00320633. DOI: 10.1016/0032-0633(73)90093-7.

Kotsiaros, S., J. E. P. Connerney, G. Clark, et al. (2019). "Birkeland currents in Jupiter's magnetosphere observed by the polar-orbiting Juno spacecraft". In: *Nature Astronomy* 3, pp. 904–909. DOI: 10.1038/s41550-019-0819-7.

Kurth, W. S., D. D. Barbosa, F. L. Scarf, D. A. Gurnett, and R. L. Poynter (1979). "Low frequency radio emissions from Jupiter: Jovian kilometric radiation". In: *Geophysical Research Letters* 6.9, pp. 747–750. ISSN: 0094-8276, 1944-8007. DOI: 10.1029/GL006i009p00747.

Kurth, W. S., D. A. Gurnett, and F. L. Scarf (1980). "Spatial and temporal studies of Jovian kilometric radiation". In: *Geophysical Research Letters* 7.1, pp. 61–64. ISSN: 0094-8276, 1944-8007. DOI: 10.1029/GL007i001p00061.

Kurth, W. S., D. A. Gurnett, and F. L. Scarf (1989). "Jovian Type III radio bursts". In: *Journal of Geophysical Research* 94.A6, pp. 6917–6924. DOI: 10.1029/JA094iA06p06917.

Kurth, W. S., G. B. Hospodarsky, D. L. Kirchner, et al. (2017). "The Juno Waves Investigation". In: *Space Science Reviews* 213.1–4, pp. 347–392. ISSN: 1572-9672. DOI: 10.1007/s11214-017-0396-y.

Kurth, W. S., B. H. Mauk, S. S. Elliott, et al. (2018). "Whistler Mode Waves Associated With Broadband Auroral Electron Precipitation at Jupiter". In: *Geophysical Research Letters* 45.18, pp. 9372–9379. DOI: 10.1029/2018GL078566.

Kurth, W. S., A. H. Sulaiman, G. B. Hospodarsky, et al. (2022). "Juno Plasma Wave Observations at Ganymede". In: *Geophysical Research Letters* 49.23, e2022GL098591, e2022GL098591. DOI: 10.1029/2022GL098591.

Kurth, W. S., M. M. Baumback, and D. A. Gurnett (1975). "Direction-finding measurements of auroral kilometric radiation". In: *Journal of Geophysical Research* 80.19, pp. 2764–2770. ISSN: 01480227. DOI: 10.1029/JA080i019p02764.

Ladreiter, H., P. Zarka, and A. Lecacheux (1994). "Direction finding study of Jovian hectometric and broadband kilometric radio emissions: evidence for their auroral origin". In: *Planetary and Space Science* 42.11, pp. 919–931. ISSN: 00320633. DOI: 10.1016/0032-0633(94)90052-3.

Lamy, L. (2020). "Auroral emissions from Uranus and Neptune". In: *Philosophical Transactions of the Royal Society of London Series A* 378.2187, 20190481, p. 20190481. DOI: 10.1098/rsta.2019.0481.

Lamy, L., B. Cecconi, M. Dekkali, et al. (2023a). "Re-exploring the radio spectrum of Uranus in orbit: science case and digital high-frequency receiver". In: *Planetary, Solar and Heliospheric Radio Emissions IX*. Ed. by C. K. Louis, C. M. Jackman, G. Fischer, A. H. Sulaiman, and P. Zucca, 103105, p. 103105. DOI: 10.25546/103105.

Lamy, L., B. Cecconi, P. Zarka, et al. (2011). "Emission and propagation of Saturn kilometric radiation: Magnetoionic modes, beaming pattern, and polarization state". In: *Journal of Geophysical Research (Space Physics)* 116.A4, A04212, A04212. DOI: 10.1029/2010JA016195.

Lamy, L., L. Colomban, P. Zarka, et al. (2022). "Determining the Beaming of Io Decametric Emissions: A Remote Diagnostic to Probe the Io-Jupiter Interaction". In: *Journal of Geophysical Research (Space Physics)* 127.4, e30160, e30160. DOI: 10.1029/2021JA030160.

Lamy, L., A. Duchêne, E. Mauduit, et al. (2023b). "Probing Jupiter-satellite interactions from the beaming of their decametric emissions: the case of Europa and Ganymede". In: *Planetary, Solar and Heliospheric Radio Emissions IX*. Ed. by C. K. Louis, C. M. Jackman, G. Fischer, A. H. Sulaiman, and P. Zucca, 103097, p. 103097. DOI: 10.25546/103097.

Lamy, L., R. Prangé, F. Henry, and P. Le Sidaner (2015). "The Auroral Planetary Imaging and Spectroscopy (APIS) service". In: *Astronomy and Computing* 11, pp. 138–145. DOI: 10.1016/j.ascom.2015.01.005.

Lamy, L., P. Schippers, P. Zarka, et al. (2010). "Properties of Saturn Kilometric Radiation measured within its source region". In: *Geophysical Research Letters*. DOI: 10.1029/2010gl043415.

Lamy, L., P. Zarka, B. Cecconi, et al. (2018). "The low-frequency source of Saturn's kilometric radiation". In: *Science* 362.6410, aat2027, aat2027. DOI: 10.1126/science.aat2027.

Le Queau, D. and P. Louarn (1989). "Analytical study of the relativistic dispersion: Application to the generation of the auroral kilometric radiation". In: *Journal of Geophysical Research: Space Physics* 94 (A3), pp. 2605–2616. ISSN: 2156-2202. DOI: 10.1029/JA094iA03p02605.

Le Quéau, D., R. Pellat, and A. Roux (1984). "Direct generation of the auroral kilometric radiation by the maser synchrotron instability: An analytical approach". In: *Physics of Fluids* 27.1, p. 247. ISSN: 00319171. DOI: 10.1063/1.864520.

Leblanc, Y. and G. Daigne (1985). "Broadband Jovian kilometric radiation: New results on polarization and beaming". In: *Journal of Geophysical Research: Space Physics* 90 (A12), pp. 12073–12080. ISSN: 0148-0227. DOI: 10.1029/JA090iA12p12073.

Lecacheux, A. (1978). "Direction Finding of a Radiosource of Unknown Polarization with Short Electric Antennas on a Spacecraft". In: *Astronomy and Astrophysics* 70, p. 701. ISSN: 0004-6361.

Lecacheux, A., B. M. Pedersen, P. Zarka, et al. (1992). "In ecliptic observations of Jovian radio emissions by Ulysses comparison with Voyager results". In: *Geophysical Research Letters* 19.12, pp. 1307–1310. ISSN: 1944-8007. DOI: 10.1029/92gl01037.

Lee, L. C. and C. S. Wu (1980). "Amplification of radiation near cyclotron frequency due to electron population inversion". In: *The Physics of Fluids* 23.7, pp. 1348–1354. ISSN: 0031-9171. DOI: 10.1063/1.863148.

Lindsay, S. T., M. K. James, E. J. Bunce, et al. (2016). "MESSENGER X-ray observations of magnetosphere-surface interaction on the nightside of Mercury". In: *Planetary and Space Science* 125, pp. 72–79. DOI: 10.1016/j.pss.2016.03.005.

Louarn, P. (1992). "Auroral planetary radio emissions, theoretical aspects". In: *Advances in Space Research* 12.8, pp. 121–134. ISSN: 02731177. DOI: 10.1016/0273-1177(92)90385-B.

Louarn, P., F. Allegrini, D. J. McComas, et al. (2017). "Generation of the Jovian hectometric radiation: First lessons from Juno". In: *Geophysical Research Letters* 44.10, pp. 4439–4446. DOI: 10.1002/2017GL072923.

Louarn, P., F. Allegrini, D. J. McComas, et al. (2018). "Observation of Electron Conics by Juno: Implications for Radio Generation and Acceleration Processes". In: *Geophysical Research Letters* 45.18, pp. 9408–9416. DOI: 10.1029/2018GL078973.

Louarn, P. and D. Le Quéau (1996). "Generation of the Auroral Kilometric Radiation in plasma cavities—II. The cyclotron maser instability in small size sources". In: *Planetary and Space Science* 44.3, pp. 211–224. ISSN: 0032-0633. DOI: 10.1016/0032-0633(95)00122-0.

Louarn, P., A. Roux, H. de Féraudy, D. Le Quéau, M. André, and L. Matson (1990). "Trapped electrons as a free energy source for the auroral kilometric radiation". In: *Journal of Geophysical Research: Space Physics* 95.A5, pp. 5983–5995. ISSN: 0148-0227. DOI: 10.1029/ja095ia05p05983.

Louarn, P., A. Roux, S. Perraut, W. Kurth, and D. Gurnett (1998). "A study of the large-scale dynamics of the Jovian magnetosphere using the Galileo Plasma Wave Experiment". In: *Geophysical Research Letters* 25.15, pp. 2905–2908. ISSN: 1944-8007. DOI: 10.1029/98gl01774.

Louis, C. K., C. M. Jackman, G. Hospodarsky, et al. (2023a). "Effect of a Magnetospheric Compression on Jovian Radio Emissions: In Situ Case Study Using Juno Data". In: *Journal of Geophysical Research (Space Physics)* 128.9, e2022JA031155, e2022JA031155. DOI: 10.1029/2022JA031155.

Louis, C. K., L. Lamy, P. Zarka, B. Cecconi, and S. L. G. Hess (2017). "Detection of Jupiter decametric emissions controlled by Europa and Ganymede with Voyager/PRA and Cassini/RPWS". In: *Journal of Geophysical Research (Space Physics)* 122.9, pp. 9228–9247. DOI: 10.1002/2016JA023779.

Louis, C. K., P. Louarn, F. Allegrini, W. S. Kurth, and J. R. Szalay (2020). "Ganymede-Induced Decametric Radio Emission: In Situ Observations and Measurements by Juno". In: *Geophysical Research Letters* 47.20. ISSN: 0094-8276, 1944-8007. DOI: 10.1029/2020GL090021.

Louis, C. K., P. Louarn, B. Collet, et al. (2023b). "Source of Radio Emissions Induced by the Galilean Moons Io, Europa and Ganymede: In Situ Measurements by Juno". In:

Journal of Geophysical Research: Space Physics 128.12. ISSN: 2169-9380, 2169-9402. DOI: 10.1029/2023JA031985.

Louis, C. K., R. Prangé, L. Lamy, et al. (2019). "Jovian Auroral Radio Sources Detected In Situ by Juno/Waves: Comparisons With Model Auroral Ovals and Simultaneous HST FUV Images". In: *Geophysical Research Letters* 46.21, pp. 11606–11614. ISSN: 0094-8276, 1944-8007. DOI: 10.1029/2019GL084799.

Louis, C. K., P. Zarka, K. Dabidin, et al. (2021). "Latitudinal Beaming of Jupiter's Radio Emissions From Juno/Waves Flux Density Measurements". In: *Journal of Geophysical Research: Space Physics* 126.10, e2021JA029435. ISSN: 2169-9380, 2169-9402. DOI: 10.1029/2021JA029435.

Louis, C. K. (2018). "Les émissions radio aurorales de Jupiter : observations à distance, in-situ et simulations". PhD thesis. Université Paris Sciences et Lettres; Observatoire de Paris – LESIA.

Lysak, R. L., Y. Song, S. Elliott, W. Kurth, A. H. Sulaiman, and D. Gershman (2021). "The Jovian Ionospheric Alfvén Resonator and Auroral Particle Acceleration". In: *Journal of Geophysical Research (Space Physics)* 126.12, e29886, e29886. DOI: 10.1029/2021JA02988610.1002/essoar.10507765.1.

Lysak, R. L. (1993). "Generalized model of the ionospheric Alfvén resonator". In: *Geophysical Monograph Series* 80, pp. 121–128. DOI: 10.1029/GM080p0121.

MacDowall, R. J., M. L. Kaiser, M. D. Desch, W. M. Farrell, R. A. Hess, and R. G. Stone (1993). "Quasiperiodic Jovian Radio bursts: observations from the Ulysses Radio and Plasma Wave Experiment". In: *Planetary and Space Science* 41.11-12, pp. 1059–1072. DOI: 10.1016/0032-0633(93)90109-F.

Manning, R. and G. A. Dulk (2001). "The Galactic background radiation from 0.2 to 13.8 MHz". In: *Astronomy and Astrophysics* 372, pp. 663–666. DOI: 10.1051/0004-6361:20010516.

Mauduit, E., P. Zarka, L. Lamy, and S. L. G. Hess (2023). "Drifting discrete Jovian radio bursts reveal acceleration processes related to Ganymede and the main aurora". In: *Nature Communications* 14, 5981, p. 5981. DOI: 10.1038/s41467-023-41617-8.

Mauk, B. H., G. Clark, G. R. Gladstone, et al. (2020). "Energetic Particles and Acceleration Regions Over Jupiter's Polar Cap and Main Aurora: A Broad Overview". In: *Journal of Geophysical Research (Space Physics)* 125.3, e27699, e27699. DOI: 10.1029/2019JA027699.

Mauk, B. H., D. K. Haggerty, S. E. Jaskulek, et al. (2017). "The Jupiter Energetic Particle Detector Instrument (JEDI) Investigation for the Juno Mission". In: *Space Science Reviews* 213.1-4, pp. 289–346. DOI: 10.1007/s11214-013-0025-3.

Mauk, B. H., D. K. Haggerty, C. Paranicas, et al. (2018). "Diverse Electron and Ion Acceleration Characteristics Observed Over Jupiter's Main Aurora". In: *Geophysical Research Letters* 45.3, pp. 1277–1285. ISSN: 0094-8276, 1944-8007. DOI: 10.1002/2017GL076901.

McComas, D. J., N. Alexander, F. Allegrini, et al. (2013). "The Jovian Auroral Distributions Experiment (JADE) on the Juno Mission to Jupiter". In: *Space Science Reviews* 213.1–4, pp. 547–643. ISSN: 1572-9672. DOI: 10.1007/s11214-013-9990-9.

McConville, S. L., D. C. Speirs, K. Ronald, et al. (2008). "Demonstration of auroral radio emission mechanisms by laboratory experiment". In: *Plasma Physics and Controlled Fusion* 50.7, 074010, p. 074010. DOI: 10.1088/0741-3335/50/7/074010.

Mellott, M. M., R. L. Huff, and D. A. Gurnett (1986). "DE 1 observations of harmonic auroral kilometric radiation". In: *Journal of Geophysical Research: Space Physics* 91.A12, pp. 13732–13738. ISSN: 0148-0227. DOI: 10.1029/ja091ia12p13732.

Menietti, J. D. (1995). "Absence of magnetic field constraints on the source region of Jovian decametric radiation". In: *Geophysical Research Letters* 22.11, pp. 1389–1392. DOI: 10.1029/95GL00702.

Menietti, J. D. and J. L. Burch (1985). ""Electron conic" signatures observed in the nightside auroral zone and over the polar cap". In: *Journal of Geophysical Research: Space Physics* 90 (A6), pp. 5345–5353. ISSN: 0148-0227. DOI: 10.1029/JA090iA06p05345.

Menietti, J. D., D. A. Gurnett, and I. Christopher (2001). "Control of Jovian radio emission by Callisto". In: *Geophysical Research Letters* 28.15, pp. 3047–3050. DOI: 10.1029/2001GL012965.

Menietti, J. D., D. A. Gurnett, and J. B. Groene (1998). "Second harmonic hectometric radio emission at Jupiter". In: *Geophysical Research Letters* 25.24, pp. 4425–4428. DOI: 10.1029/1998GL900193.

Menietti, J. D., R. L. Mutel, I. W. Christopher, K. A. Hutchinson, and J. B. Sigwarth (2011). "Simultaneous radio and optical observations of auroral structures: Implications for AKR beaming". In: *Journal of Geophysical Research (Space Physics)* 116.A12, A12219, A12219. DOI: 10.1029/2011JA017168.

Menietti, J. D., P. H. Yoon, T. F. Averkamp, et al. (2023). "Wave and Particle Analysis of Z-Mode and O-Mode Emission in the Jovian Inner Magnetosphere". In: *Journal of Geophysical Research: Space Physics* 128.5. ISSN: 2169-9402. DOI: 10.1029/2022ja031199.

Menietti, J. and D. Curran (1990). "Instantaneous Io flux tube as the source of Jovian DAM: Possible second harmonic emissions". In: *Journal of Geophysical Research: Space Physics* 95.A12, pp. 21273–21280. DOI: 10.1029/JA095iA12p21273.

Mottez, F., S. Hess, and P. Zarka (2010). "Explanation of dominant oblique radio emission at Jupiter and comparison to the terrestrial case". In: *Planetary and Space Science* 58.10, pp. 1414–1422. DOI: 10.1016/j.pss.2010.05.012.

Muñoz, J. R., F. Allegrini, R. W. Ebert, et al. (2022). "A Survey of Electron Conics at Jupiter Utilizing the JADE-E Data During Science Orbits 01, 03-30". In: *Journal of Geophysical Research: Space Physics* 127.10. ISSN: 2169-9402. DOI: 10.1029/2022ja030418.

Mutel, R. L., J. D. Menietti, D. A. Gurnett, et al. (2010). "CMI growth rates for Saturnian kilometric radiation". In: *Geophysical Research Letters* 37.19, 2010GL044940. ISSN: 0094-8276, 1944-8007. DOI: 10.1029/2010GL044940.

Nichols, J. D., J. T. Clarke, J. C. Gérard, D. Grodent, and K. C. Hansen (2009). "Variation of different components of Jupiter's auroral emission". In: *Journal of Geophysical Research (Space Physics)* 114.A6, A06210, A06210. DOI: 10.1029/2009JA014051.

Ning, H., Y. Chen, C. Li, S. Ye, A. Kuznetsov, and S. Wu (2023). "Excitation of extraordinary modes inside the source of Saturn's kilometric radiation". In: *Astronomy*

& Astrophysics 678, A94. ISSN: 0004-6361, 1432-0746. DOI: 10.1051/0004-6361/202347149.

Pallier, L. and R. Prangé (2001). "More about the structure of the high latitude Jovian aurorae". In: *Planetary and Space Science* 49.10-11, pp. 1159–1173. DOI: 10.1016/S0032-0633(01)00023-X.

Pan, D.-X., Z.-H. Yao, H. Manners, et al. (2021). "Ultralow Frequency Waves in Driving Jovian Aurorae Revealed by Observations From HST and Juno". In: *Geophysical Research Letters* 48.5, e91579, e91579. DOI: 10.1029/2020GL091579.

Prange, R., P. Zarka, G. E. Ballester, et al. (1993). "Correlated variations of UV and radio emissions during an outstanding Jovian auroral event". In: *Journal of Geophysical Research* 98.E10, pp. 18779–18792. DOI: 10.1029/93JE01802.

Prange, R. (1992). "The UV and IR Jovian aurorae". In: *Advances in Space Research* 12.8, pp. 379–389. DOI: 10.1016/0273-1177(92)90413-R.

Prangé, R., G. Chagnon, M. G. Kivelson, T. A. Livengood, and W. Kurth (2001). "Temporal monitoring of Jupiter's auroral activity with IUE during the Galileo mission. Implications for magnetospheric processes". In: *Planetary and Space Science* 49.3-4, pp. 405–415. DOI: 10.1016/S0032-0633(00)00161-6.

Pritchett, P. L. (1984). "Relativistic dispersion and the generation of auroral kilometric radiation". In: *Geophysical Research Letters* 11.2, pp. 143–146. ISSN: 1944-8007. DOI: 10.1029/GL011i002p00143.

Pritchett, P. L. (1986). "Electron-cyclotron maser instability in relativistic plasmas". In: *The Physics of Fluids* 29.9, pp. 2919–2930. ISSN: 0031-9171. DOI: 10.1063/1.865492.

Pump, K., D. Heyner, D. Schmid, W. Exner, and F. Plaschke (2024). "Revised Magnetospheric Model Reveals Signatures of Field-Aligned Current Systems at Mercury". In: *Journal of Geophysical Research (Space Physics)* 129.3, e2023JA031529, e2023JA031529. DOI: 10.1029/2023JA031529.

Rabia, J., V. Hue, C. K. Louis, et al. (2025). "In situ and remote observations of the ultraviolet footprint of the moon Callisto by the Juno spacecraft". In: *Nature Communications* 16.1. ISSN: 2041-1723. DOI: 10.1038/s41467-025-62520-4.

Reiner, M. J., J. Fainberg, and R. G. Stone (1994). "A new component of Jovian kilometric radio emission". In: *Journal of Geophysical Research* 99.A4, pp. 6137–6144. DOI: 10.1029/93JA03398.

Reiner, M. J., M. L. Kaiser, and M. D. Desch (2000). "Long-term behavior of Jovian bKOM and nKOM radio emissions observed during the Ulysses-Jupiter encounter". In: *Geophysical Research Letters* 27.3, pp. 297–300. ISSN: 0094-8276, 1944-8007. DOI: 10.1029/1999gl003710.

Rojo, M., N. André, S. Aizawa, et al. (2024). "Structure and dynamics of the Hermean magnetosphere revealed by electron observations from the Mercury electron analyzer after the first three Mercury flybys of BepiColombo". In: *Astronomy & Astrophysics* 687, A243. ISSN: 1432-0746. DOI: 10.1051/0004-6361/202449450.

Ronald, K., D. C. Speirs, S. L. McConville, et al. (2008). "Radio frequency resonator structure and diagnostic measurements for a laboratory simulation of Auroral Kilometric Radiation)". In: *Physics of Plasmas* 15.5, 056503, p. 056503. DOI: 10.1063/1.2856649.

Roux, A., A. Hilgers, H. De Feraudy, et al. (1993). "Auroral kilometric radiation sources: In situ and remote observations from Viking". In: *Journal of Geophysical Research: Space Physics* 98 (A7), pp. 11657–11670. ISSN: 0148-0227. DOI: 10.1029/92JA02309.

Russell, C. T., D. N. Baker, and J. A. Slavin (1988). "The magnetosphere of Mercury." In: *Mercury, University of Arizona Press*. Ed. by F. Vilas, C. R. Chapman, and M. S. Matthews, pp. 514–561.

Salveter, A., J. Saur, G. Clark, and B. H. Mauk (2022). "Jovian Auroral Electron Precipitation Budget—A Statistical Analysis of Diffuse, Mono-Energetic, and Broadband Auroral Electron Distributions". In: *Journal of Geophysical Research: Space Physics* 127.8. _eprint: https://onlinelibrary.wiley.com/doi/pdf/10.1029/2021JA030224, e2021JA030224. ISSN: 2169-9402. DOI: 10.1029/2021JA030224.

Saur, J., T. Grambusch, S. Duling, F. M. Neubauer, and S. Simon (2013). "Magnetic energy fluxes in sub-Alfvénic planet star and moon planet interactions". In: *Astronomy and Astrophysics* 552, A119, A119. DOI: 10.1051/0004-6361/201118179.

Saur, J., S. Janser, A. Schreiner, et al. (2018). "Wave-Particle Interaction of Alfvén Waves in Jupiter's Magnetosphere: Auroral and Magnetospheric Particle Acceleration". In: *Journal of Geophysical Research: Space Physics* 123.11, pp. 9560–9573. ISSN: 2169-9380, 2169-9402. DOI: 10.1029/2018JA025948.

Saur, J., A. Pouquet, and W. H. Matthaeus (2003). "An acceleration mechanism for the generation of the main auroral oval on Jupiter". In: *Geophysical Research Letters* 30.5, 1260, p. 1260. DOI: 10.1029/2002GL015761.

Scarf, F. L., D. A. Gurnett, and W. S. Kurth (1979). "Jupiter Plasma Wave Observations: An Initial Voyager 1 Overview". In: *Science* 204.4396, pp. 991–995. DOI: 10.1126/science.204.4396.991.

Slavin, J. A., M. H. Acuña, B. J. Anderson, et al. (2008). "Mercury's Magnetosphere After MESSENGER's First Flyby". In: *Science* 321.5885, p. 85. DOI: 10.1126/science.1159040.

Strangeway, R. J. (1986). "On the applicability of relativistic dispersion to auroral zone electron distributions". In: *Journal of Geophysical Research: Space Physics* 91 (A3), pp. 3152–3166. ISSN: 0148-0227. DOI: 10.1029/JA091iA03p03152.

Sulaiman, A. H., B. H. Mauk, J. R. Szalay, et al. (2022). "Jupiter's Low-Altitude Auroral Zones: Fields, Particles, Plasma Waves, and Density Depletions". In: *Journal of Geophysical Research: Space Physics* 127.8, e2022JA030334. ISSN: 2169-9380, 2169-9402. DOI: 10.1029/2022JA030334.

Szalay, J. R., F. Allegrini, F. Bagenal, et al. (2020). "A New Framework to Explain Changes in Io's Footprint Tail Electron Fluxes". In: *Geophysical Research Letters* 47.18, e89267, e89267. DOI: 10.1029/2020GL089267.

Szalay, J. R., F. Allegrini, F. Bagenal, et al. (2021). "Proton Outflow Associated With Jupiter's Auroral Processes". In: *Geophysical Research Letters* 48.1, e91627, e91627. DOI: 10.1029/2020GL091627.

Szalay, J. R., F. Allegrini, R. W. Ebert, et al. (2024). "Oxygen production from dissociation of Europa's water-ice surface". In: *Nature Astronomy* 8, pp. 567–576. DOI: 10.1038/s41550-024-02206-x.

Treumann, R. A. (2006). "The electron–cyclotron maser for astrophysical application". In: *The Astronomy and Astrophysics Review* 13.4, pp. 229–315. ISSN: 0935-4956, 1432-0754. DOI: 10.1007/s00159-006-0001-y.

Varela, J., V. Reville, A. S. Brun, F. Pantellini, and P. Zarka (2016). "Radio emission in Mercury magnetosphere". In: *Astronomy and Astrophysics* 595, A69, A69. DOI: 10.1051/0004-6361/201628607.

Warwick, J. W., J. B. Pearce, A. C. Riddle, et al. (1979). "Voyager 1 Planetary Radio Astronomy Observations Near Jupiter". In: *Science* 204.4396, pp. 995–998. DOI: 10.1126/science.204.4396.995.

Warwick, J. W., D. R. Evans, G. R. Peltzer, et al. (1989). "Voyager Planetary Radio Astronomy at Neptune". In: *Science* 246.4936, pp. 1498–1501. ISSN: 1095-9203. DOI: 10.1126/science.246.4936.1498.

Warwick, J. W., D. R. Evans, J. H. Romig, et al. (1986). "Voyager 2 Radio Observations of Uranus". In: *Science* 233.4759, pp. 102–106. ISSN: 1095-9203. DOI: 10.1126/science.233.4759.102.

Waters, J. E., C. M. Jackman, D. K. Whiter, et al. (2022). "A Perspective on Substorm Dynamics Using 10 Years of Auroral Kilometric Radiation Observations From Wind". In: *Journal of Geophysical Research (Space Physics)* 127.9, e30449, e30449. DOI: 10.1029/2022JA030449.

Winglee, R. M. (1985). "Fundamental and harmonic electron cyclotron maser emission". In: *Journal of Geophysical Research* 90.A10, pp. 9663–9674. DOI: 10.1029/JA090iA10p09663.

Wong, H. K., C. S. Wu, F. J. Ke, R. S. Schneider, and L. F. Ziebell (1982). "Electromagnetic cyclotron-loss-cone instability associated with weakly relativistic electrons". In: *Journal of Plasma Physics* 28.3, pp. 503–525. ISSN: 0022-3778, 1469-7807. DOI: 10.1017/S0022377800000453.

Wu, C. S. and L.-C. Lee (1979). "A theory of the terrestrial kilometric radiation". In: *The Astrophysical Journal* 230, pp. 621–626. DOI: 10.1086/157120.

Wu, C. S. and X. M. Qiu (1983). "Emissions of second-harmonic auroral kilometric radiation". In: *Journal of Geophysical Research* 88.A12, pp. 10072–10080. DOI: 10.1029/JA088iA12p10072.

Wu, C. (1985). "Kinetic cyclotron and synchrotron maser instabilities: Radio emission processes by direct amplification of radiation". In: *Space Science Reviews* 41.3. ISSN: 0038-6308, 1572-9672. DOI: 10.1007/BF00190653.

Wu, S., P. Zarka, L. Lamy, et al. (2022). "Observations of the First Harmonic of Saturn Kilometric Radiation During Cassini's Grand Finale". In: *Journal of Geophysical Research (Space Physics)* 127.9, e30776, e30776. DOI: 10.1029/2022JA030776.

Yao, Z. H., B. Bonfond, D. Grodent, et al. (2022). "On the Relation Between Auroral Morphologies and Compression Conditions of Jupiter's Magnetopause: Observations From Juno and the Hubble Space Telescope". In: *Journal of Geophysical Research (Space Physics)* 127.10, e2021JA029894, e2021JA029894. DOI: 10.1029/2021JA029894.

Yoon, P. H., J. D. Menietti, F. Allegrini, et al. (2025). "Quasilinear Analysis in the Source Region of Jovian Hectometric Emission Associated With Upward Electron Beams".

In: *Journal of Geophysical Research (Space Physics)* 130.2, 2024JA033241. DOI: 10.1029/2024JA033241.

Zarka, P. (2000). "Radio Emissions from the Planets and their Moons". In: *Geophysical Monograph Series* 119, pp. 167–178. DOI: 10.1029/GM119p0167.

Zarka, P. (2004). "Radio and plasma waves at the outer planets". In: *Advances in Space Research* 33.11, pp. 2045–2060. ISSN: 02731177. DOI: 10.1016/j.asr.2003.07.055.

Zarka, P., D. Le Quéau, and F. Genova (1986). "The maser synchrotron instability in an inhomogeneous medium: Determination of the spectral intensity of auroral kilometric radiation". In: *Journal of Geophysical Research: Space Physics* 91.A12, pp. 13542–13558. ISSN: 0148-0227. DOI: 10.1029/ja091ia12p13542.

Zarka, P., F. P. Magalhães, M. S. Marques, et al. (2021). "Jupiter's Auroral Radio Emissions Observed by Cassini: Rotational Versus Solar Wind Control, and Components Identification". In: *Journal of Geophysical Research: Space Physics* 126.10, e2021JA029780. ISSN: 2169-9380, 2169-9402. DOI: 10.1029/2021JA029780.

Zarka, P., M. S. Marques, C. Louis, et al. (2017). "Radio emission from satellite-Jupiter interactions (especially Ganymede)". In: *Planetary Radio Emissions VIII*. Ed. by G. Fischer, G. Mann, M. Panchenko, and P. Zarka, pp. 45–58. DOI: 10.1553/PRE8s45.

Zarka, P. (1998). "Auroral radio emissions at the outer planets: Observations and theories". In: *Journal of Geophysical Research: Planets* 103 (E9), pp. 20159–20194. ISSN: 0148-0227. DOI: 10.1029/98JE01323.

Zarka, P. (2007). "Plasma interactions of exoplanets with their parent star and associated radio emissions". In: *Planetary and Space Science* 55.5, pp. 598–617. DOI: 10.1016/j.pss.2006.05.045.

Zarka, P., J. Queinnec, and F. J. Crary (2001). "Low-frequency limit of Jovian radio emissions and implications on source locations and Io plasma wake". In: *Planetary and Space Science* 49.10-11, pp. 1137–1149. DOI: 10.1016/S0032-0633(01)00021-6.

Zhang, L., J. Tang, J. Shen, D. Wu, and L. Chen (2023). "Effects of Fully Relativistic Condition on Electron Cyclotron Maser Emission". In: *The Astrophysical Journal* 944.1, 37, p. 37. DOI: 10.3847/1538-4357/acaef9.

APPENDIXES

A. Expression of the relativistic dispersion tensor

I recall the expression of the $\vec{N}\otimes\vec{N}-N^2$ term that appears in the dispersion relation of waves in plasma (Bekefi 1969). These expressions are given in the $(\vec{e_x},\vec{e_y},\vec{e_z}) = \left(\frac{\vec{k}}{k},\frac{\vec{B}\times\vec{k}}{Bk_\perp},\frac{\vec{B}}{B}\right)$ space and in the $(\vec{e_+},\vec{e_-},\vec{e_z})$ space defined by $\vec{e_\pm}=\vec{e_x}\pm i\vec{e_y}$ where e_+ (resp e_-) represents the right-handed (resp. left-handed) polarized component.

$$\vec{N} = \frac{\vec{k}c}{\omega} = \begin{pmatrix} N_\perp \\ 0 \\ N_\parallel \end{pmatrix} \tag{A.1a}$$

$$\vec{N}\otimes\vec{N} = \begin{pmatrix} N_\perp^2 & 0 & N_\perp N_\parallel \\ 0 & 0 & 0 \\ N_\perp N_\parallel & 0 & N_\parallel^2 \end{pmatrix} \qquad \text{(in } (x,y,z) \text{ space)} \tag{A.1b}$$

$$\vec{N}\otimes\vec{N}-N^2 = \frac{1}{2}\begin{pmatrix} -N_\parallel^2-N^2 & N_\perp^2 & 2N_\perp N_\parallel \\ N_\perp^2 & -N_\parallel^2-N^2 & 2N_\perp N_\parallel \\ N_\perp N_\parallel & N_\perp N_\parallel & -2N_\perp^2 \end{pmatrix} \qquad \text{(in } (+,-,\parallel) \text{ space)} \tag{A.1c}$$

The expression of $\overleftrightarrow{\boldsymbol{\sigma}}$ in the fully relativistic case for the X-mode assumption writes (Le Quéau et al. 1984):

$$\frac{\overleftrightarrow{\boldsymbol{\sigma}}}{2\pi i\omega\epsilon_0} = \frac{\omega_{\mathrm{pe}}^2}{\omega^2}\int_0^\infty p_\perp \mathrm{d}p_\perp \int_{-\infty}^\infty \mathrm{d}p_\parallel \frac{\overleftrightarrow{\boldsymbol{S}}/\gamma}{\omega - k_\parallel p_\parallel/m_{\mathrm{e}}\gamma - \omega_{\mathrm{ce}}/\gamma} \tag{A.2a}$$

where the tensor $\overleftrightarrow{\boldsymbol{S}}$ is represented by the following matrix

$$\overleftrightarrow{\boldsymbol{S}} = \begin{pmatrix} v_\perp U\left(\frac{J_1(x)}{x}\right)^2 & iv_\perp U\frac{J_1(x)J_1'(x)}{x} & v_\perp W\frac{J_1(x)^2}{x} \\ -iv_\perp U\frac{J_1(x)J_1'(x)}{x} & v_\perp U\left(J_1'(x)\right)^2 & -iv_\perp W J_1(x)J_1'(x) \\ v_\parallel U\frac{J_1(x)^2}{x} & iv_\parallel U J_1(x)J_1'(x) & v_\parallel W J_1(x)^2 \end{pmatrix} \tag{A.2b}$$

with $x=\Gamma\overline{k_\perp}\beta_\perp$, J_1 the Bessel function of first order and U and W given by:

$$U = m_{\mathrm{e}}\gamma\omega\partial_{p_\perp}F_e + k_\parallel\left(p_\perp\partial_{p_\parallel} - p_\parallel\partial_{p_\perp}\right)F_e, \tag{A.2c}$$

$$W = m_{\mathrm{e}}\gamma\omega\partial_{p_\parallel}F_e - m_{\mathrm{e}}l\frac{\omega_{\mathrm{ce}}}{p_\perp}\left(p_\perp\partial_{p_\parallel} - p_\parallel\partial_{p_\perp}\right)F_e \tag{A.2d}$$

B. Influence of the parallel gradient term

In certain expressions of the growth rate in the literature, the $k_\parallel v_\perp\frac{\partial F_e}{\partial v_\parallel}$ in Equation 2.14 is sometimes taken into account. This term only affects non-centered resonance circles as they drive emissios with $k_\parallel\neq 0$. In order to verify that this term is negligible in Jovian sources, I derived a modified expression of the growth rate that take this term

into account:

$$\gamma = \frac{\omega_i}{\omega_{ce}} = \frac{\left(\frac{\pi\omega_{ph}/\omega_{ce}}{2}\right)^2}{1+\left(\frac{\omega_{pc}/\omega_{ce}}{2\Delta\omega}\right)^2} c^2 \frac{1}{n_e} \int_0^\pi d\phi v_r^2 \sin^2\alpha \left(\frac{\partial F_e}{\partial v_\perp} + \beta_0 r_\perp \sin(\alpha) \frac{\partial F_e}{\partial v_\parallel}\right) \tag{B.3}$$

I have then compared the growth rates obtained with this expression and the usual one (Equation 2.23) for the case of PJ6S on 19 May 2017 from 06:52:00 to 06:52:10 with the methods described in Chapter 3. This example is representative the prominent generation of hectometric emission by loss-cone type EDF.

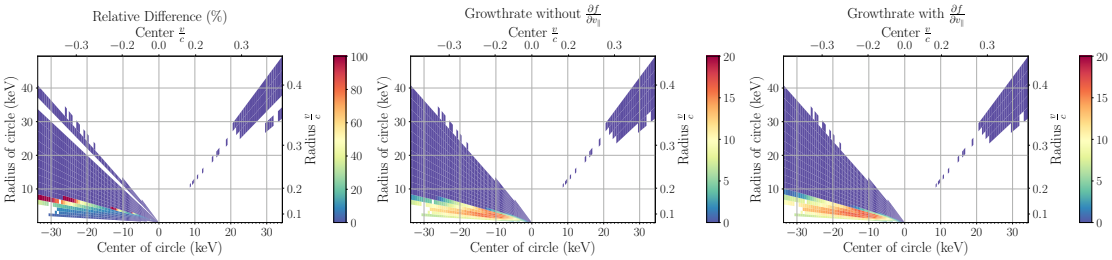


Figure 1.: Comparison of the growth rate provided by Equations 2.23 and B.3 (respectively without and with the contribution of $\frac{\partial F_e}{\partial v_\parallel}$) applied to Juno/JADE-E measurements obtained on 2017-05-19 06:52:10

Figure 1 shows an example of the analysis of a single JADE-E measurement. Panel a shows the relative difference between each expression for each circles as a function of β_0 and r. Panel b (resp c) shows the growth rate obtained with the growth rate that does (resp. does not) take into account the parallel gradient contribution. The difference between the 2 obtained growth rates becomes important only where the growth rates (computed with $\frac{\partial F_e}{\partial v_\parallel}$) are low. Nevertheless, the position of the maximal growth rates and associated CMI resonance circles do not change. As the growth rate analysis presented in chapter 3 supposes that the final radio wave is prominently amplified by the resonance circle leading to the maximal growth rate, this large difference is not important in the amplification of the wave.

Figure 2 a shows the maximal growth rates for each second of measurement either for centered circles (shell) or non centered circles (loss cone and conics), for both expression of the growth rate while Panel b shows the relative difference between each expression. This figure shows that taking into account the parallel gradient only increases the obtained growth rate by a few percent. As the wave intensity depends on the exponential of the growth rate, this difference is not significant.

A larger sample of source crossing with different properties is necessary.

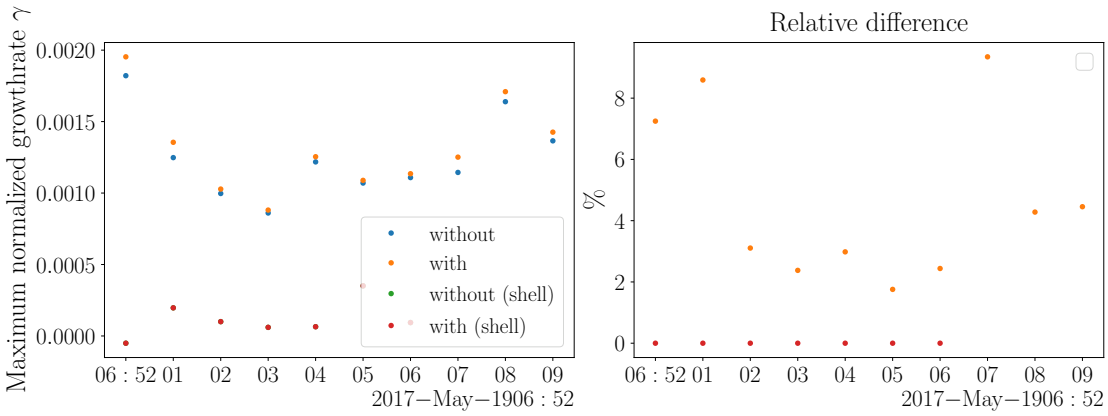


Figure 2.: Comparison of the growth rate with and without taking into account the parallel gradient term on 2017-05-19 between 06:52:00 and 06:52:10.

C. Expression of θ_{chara} and v_{chara} for an ellipse

For an ellipse defined by Equation C.4 with $\beta_{0e} > r_{\parallel}$.

$$\frac{(v_{\parallel} - \beta_{0e})^2}{r_{\parallel}^2} + \frac{v_{\perp}^2}{r_{\perp}^2} = 1 \tag{C.4}$$

The tangent of such ellipse can be found from by deriving the equation of an ellipse. As I am interested in the equation of this tangent crossing the origin, I suppose $v_{\perp} > 0$ and $v_{\parallel} - \beta_{0e} < 0$ which corresponds to a left-handed shifted circle. Equation C.4 simplifies to Equation C.5 from which the slope of tangent can be obtained by computing $\frac{\partial v_{\perp}}{\partial v_{\parallel}}$.

$$v_{\perp}(v_{\parallel}) = r_{\perp}\sqrt{1 - \frac{(v_{\parallel} - \beta_{0e})^2}{r_{\parallel}^2}} \tag{C.5}$$

v_{chara} can thus be obtained by finding $(v_{\parallel,1}, v_{\perp,1})$ for which the tangent crosses the origin. After computation, I obtain $\left(v_{\parallel,1} = \frac{\beta_{0e}^2 - r_{\parallel}^2}{\beta_{0e}}, v_{\perp,1} = \frac{r_{\perp}}{\beta_{0e}}\sqrt{\beta_{0e}^2 - r_{\parallel}^2}\right)$.

Thus, by using $r_{\parallel}^2 = \beta_{0e}^2 \frac{r_{\perp}^2}{r_{\perp}^2 - 1}$

$$v_{chara}^2 = v_{\parallel,1}^2 + v_{\perp,1}^2 = \frac{\beta_{0e}^2}{(1 - r_{\perp}^2)^2} - \frac{r_{\perp}^2}{1 - r_{\perp}^2} \tag{C.6}$$

$$\sin^2\theta_{chara} = \frac{r_{\perp}^2}{\beta_{0e}^2}(1 - r_{\perp}^2) \tag{C.7}$$

D. Comparison between growth rate expressions on a case study

In this section I compare the 3 expressions of the growth rate presented in Section 2.3.4. I took the case of PJ32S (detailed in Chp 4) as the $\frac{n_h}{n_{tot}}$ ratio runs from 0.2 to 0.9 (Figure 4a) and the case of PJ5N (detailled in Chp 5) which is the source crossing with the largest $\frac{\omega_{pe}}{\omega_{ce}} = 0.08$ I identified (Figure 3a). Both these ratios can thus lead to the most important differences between my expression and the hot plasma expression (Equation 2.17). I used the methods described in Chapter 3 to obtain these. In Figure 3 a and Figure 4 a, provide the plasma context of each case and show $\frac{f_{pe}}{f_{ce}}$ for the total electron population derived from JADE-E and MAG measurements in black and for the > 1 keV population in red, while the green line represents $\frac{n_h}{n_{tot}}$. Panels b-c-d present the obtained growth rate with the hot plasma (Equation 2.17), new (Equation 2.23)and cold plasma (Equation 2.21) expressions the same way as in Figure 4.7. Their associated characteristic energies are shown in panels f-h. Panels e shows the JADE-E energy spectrum for each case.

In the case of PJ5N (Fig. 3), the growth rates obtained in the cold plasma approximation are 2 orders of magnitude below those obtained with the other expressions, as expected. Also, I notice that the characteristic energy of the associated circles often reach the maximal energy of the tested set of resonance circles suggesting that the maximal growth rate was perhaps not reached yet. The difference between the "cold plasma" growth rate and the other two expressions result from the inclusion of the $\Delta\omega^2$ term in the latest two.

The growth rates obtained with the hot plasma expression are on average less than one order of magnitude larger than the one obtained with Equation 2.23.

In terms of characteristic energy, the high energy part of both the hot "plasma" and "new" panels match well especially between 02:29:00 and 02:29:30 where the upward high energy follows a monoenergetic rising trend. In the same way as in the cold plasma approximation, the hot plasma expression is not accurate as it favors circles with low energies. This preference is particularly visible for energies below 10 keV in Figure 3f and between 18:40:00 and 18:42:00 in Figure 4f.

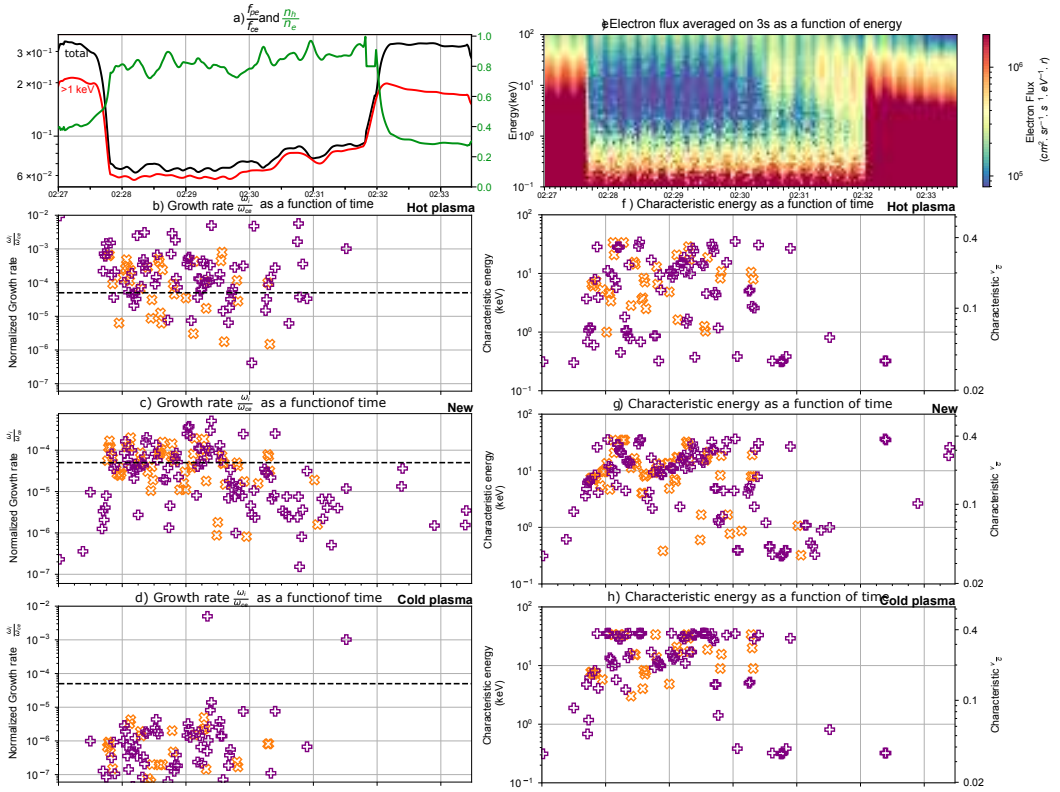


Figure 3.: Comparison of the different growth rate expressions for the bKOM case of PJ5N a) $\frac{f_{pe}}{f_{ce}}$ and $\frac{n_h}{n_{tot}}$ b-d) Computed growth rates for the different expressions e)Electron flux f-h)Associated characteristic energy

In the case of PJ32S, I retrieve the same conclusion with the cold plasma approximation providing unphysical results (see Panel h) for large $\frac{\omega_{pc}}{\omega_{ce}}$.

For both cases, the “new” expression of the growth rate was shown in Chapter 4 and 5 to yield wave predicted intensities compliant with the observed ones, and therefore more reliable than by using the other two types of growth rates.

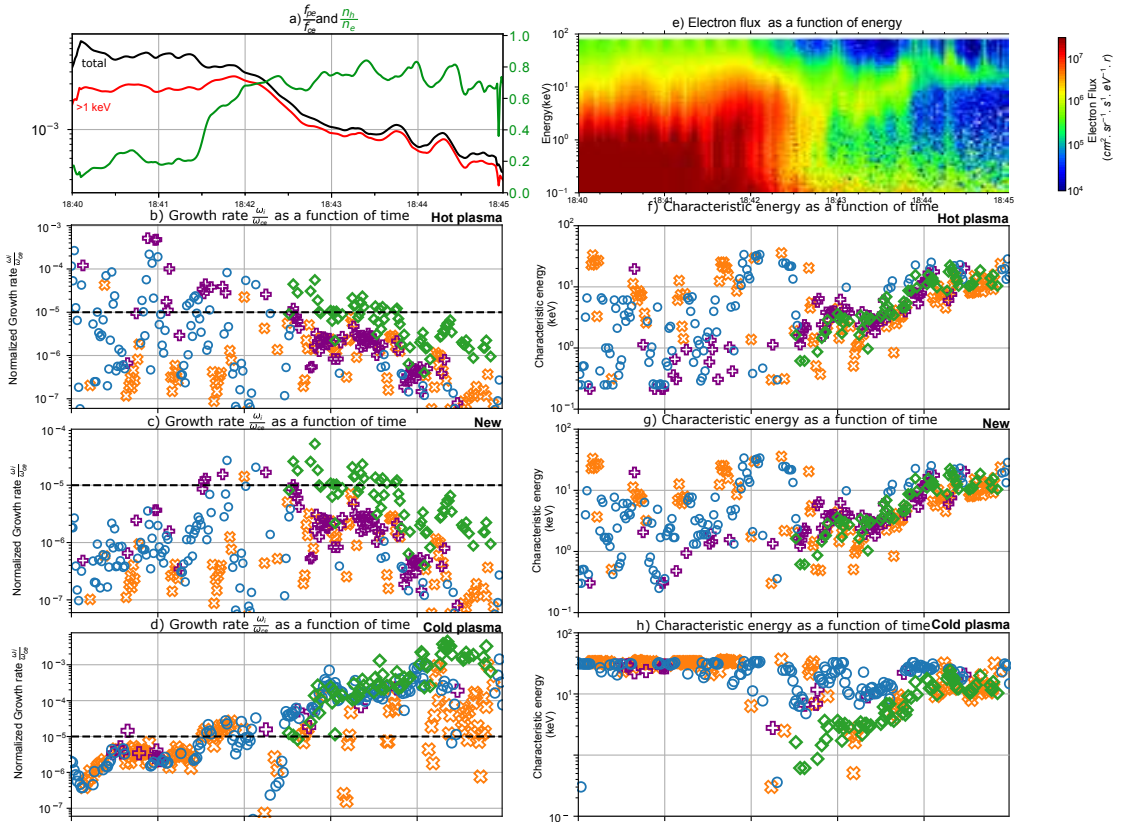


Figure 4.: Comparison of the different growth rate expression. Same as Figure 3 for the HOM source crossing of PJ32S.

E. List of HOM/DAM sources in the first 70 Juno orbits

PJ	Start $f \leq f_{ce}+1\%$	End $f \leq f_{ce}+1\%$	Start $f \leq f_{ce}$	End $f \leq f_{ce}$	f_{ce} (kHz)	M-SHELL (R_J)	LT (h)	Lon (°)
1S	2016-08-27 13:29:00	2016-08-27 13:30:52	2016-08-27 13:29:29	2016-08-27 13:30:51	4.9	17	18:00	119
3N	2016-12-11 16:24:02	2016-12-11 16:26:16			4.8	14-26	21:00	341
3S	2016-12-11 17:36:23	2016-12-11 17:37:41			6.2	15-26	17:00	26
4S	2017-02-02 13:36:17	2017-02-02 13:38:14			4.7	14-30	17:00	300
5S	2017-03-27 09:40:15	2017-03-27 09:41:00			3.4	20-35	16:00	219
6S	2017-05-19 06:43:00	2017-05-19 06:52:43	2017-05-19 06:51:46	2017-05-19 06:52:27	3.6	8-48	17:00	174

6S	2017-05-19 06:43:00	2017-05-19 06:50:00			3.7	8-20	17:00	173
7N	2017-07-11 01:16:08	2017-07-11 01:22:40			5.3	9-51	02:00-21:00	14
7S	2017-07-11 02:30:07	2017-07-11 02:33:56			5.3	15-47	16:00	76
8N	2017-09-01 20:23:00	2017-09-01 20:31:00			1.2	16-47	01:00	97
8S	2017-09-01 21:16:15	2017-09-01 21:19:03			6.8	12-45	18:00	289
8S	2017-09-01 22:26:29	2017-09-01 22:27:57			5.1	18	16:00	348
9N	2017-10-24 16:36:00	2017-10-24 16:44:00			2.0	13-30	19:00-22:00	26
9N	2017-10-24 17:19:40	2017-10-24 17:21:18			13.1	12-52	17:00	208
9S	2017-10-24 18:27:00	2017-10-24 18:31:00			3.6	15	15:00	267
9N	2017-10-24 18:27:13	2017-10-24 18:30:50			3.6	13	15:00	267
10S	2017-12-16 17:25:32	2017-12-16 17:28:49			7.4	27-55	18:00	261
10S	2017-12-16 18:36:44	2017-12-16 18:42:10			4.2	11-53	15:00	331
11N	2018-02-07 12:55:00	2018-02-07 12:57:00	2018-02-07 12:57:23	2018-02-07 12:57:38	2.5	17	14:00	16
11S	2018-02-07 14:43:00	2018-02-07 14:45:20	2018-02-07 14:44:52	2018-02-07 14:45:20	2.9	18-41	13:00	256
12N	2018-04-01 07:20:00	2018-04-01 08:27:00			0.8	21-42	04:00	215-261
12N	2018-04-01 09:08:40	2018-04-01 09:14:07			5.8	13-51	09:00-13:00	28-65
12S	2018-04-01 10:44:00	2018-04-01 10:47:00			2.2	49	14:00	179
13N	2018-05-24 05:06:19	2018-05-24 05:08:12			6.2	14-39	21:00	323
13N	2018-05-24 06:18:22	2018-05-24 06:21:13			4.6	13-39	14:00	62
14N	2018-07-16 02:53:36	2018-07-16 03:03:37			0.4	22	02:00	174
14S	2018-07-16 04:41:09	2018-07-16 04:44:15			5.6	14-46	00:00-24:00	337-357
15N	2018-09-06 23:48:00	2018-09-06 23:54:00			1.3	16-44	24:00	127

15N	2018-09-07 00:40:51	2018-09-07 00:43:54			7.3	21-53	19:00	280
15S	2018-09-07 01:52:48	2018-09-07 01:55:00			4.2	14-48	13:00	21
16N	2018-10-29 20:14:00	2018-10-29 20:17:00			3.2	17	20:00	75
16N	2018-10-29 20:44:41	2018-10-29 20:45:20			13.4	27-52	16:00	216
16S	2018-10-29 21:56:00	2018-10-29 21:58:20			3.0	17-39	12:00	303
17N	2018-12-21 16:13:03	2018-12-21 16:35:47			6.4	13-24	02:00-14:00	1-357
17N	2018-12-21 16:19:03	2018-12-21 16:31:12			6.0	20	13:00	24-100
18N	2019-02-12 16:47:33	2019-02-12 16:50:47			3.7	17	19:00	74
18N	2019-02-12 17:14:48	2019-02-12 17:16:21			15.7	23-55	15:00	205
18S	2019-02-12 18:30:00	2019-02-12 18:31:33			2.5	48	11:00	299
19N	2019-04-06 11:14:00	2019-04-06 11:39:00			3.7	13-27	00:00-24:00	273-355
19N	2019-04-06 11:34:04	2019-04-06 11:38:44			4.8	17	23:00	325-348
19S	2019-04-06 13:22:00	2019-04-06 13:27:00			1.6	16-42	11:00	184
20N	2019-05-29 06:28:00	2019-05-29 06:36:00			0.9	15-30	23:00	149
20N	2019-05-29 07:36:22	2019-05-29 07:38:11			6.5	16-45	19:00	296
20S	2019-05-29 08:57:00	2019-05-29 08:59:00			3.1	23-46	12:00	62
21N	2019-07-21 03:05:00	2019-07-21 03:08:28	2019-07-21 03:08:05	2019-07-21 03:08:28	2.7	15-33	20:00	100
21S	2019-07-21 04:57:50	2019-07-21 05:00:09			2.5	28-52	11:00	339
22N	2019-09-12 03:13:52	2019-09-12 03:14:35			7.9	22-39	17:00	268
23N	2019-11-03 21:46:08	2019-11-03 21:54:07			8.4	10-47	15:00	83-124
23S	2019-11-03 23:26:00	2019-11-03 23:27:40			1.6	27	08:00	277
24S	2019-12-26 18:59:45	2019-12-26 19:06:15	2019-12-26 19:03:25	2019-12-26 19:04:55	1.0	19-45	08:00	191

24S	2019-12-26 18:59:52	2019-12-26 19:06:48			1.0	19-45	08:00	191
25S	2020-02-17 19:11:12	2020-02-17 19:13:12	2020-02-17 19:11:46	2020-02-17 19:11:55	1.2	25-43	07:00	247
26N	2020-04-10 13:02:53	2020-04-10 13:08:25			4.4	22	21:00	260
26S	2020-04-10 15:07:07	2020-04-10 15:11:40			1.2	24-41	09:00	159
27S	2020-06-02 11:10:25	2020-06-02 11:12:25			2.9	16-32	09:00	45
28N	2020-07-25 05:34:06	2020-07-25 05:36:08			4.9	17	17:00	103
28S	2020-07-25 07:13:31	2020-07-25 07:15:09	2020-07-25 07:14:06	2020-07-25 07:14:53	2.2	16-31	08:00	324
29S	2020-09-16 03:26:00	2020-09-16 03:29:25			1.3	21-46	07:00	258
30N	2020-11-08 01:15:52	2020-11-08 01:19:13			6.4	10-21	14:00	74-95
30S	2020-11-08 02:53:47	2020-11-08 02:58:22			1.7	12-29	07:00	285
31S	2020-12-30 23:06:30	2020-12-30 23:09:40	2020-12-30 23:08:22	2020-12-30 23:09:23	1.1	18-31	07:00	214
32N	2021-02-21 17:13:00	2021-02-21 17:14:39			8.0	18	17:00	300
32S	2021-02-21 18:40:15	2021-02-21 18:43:43	2021-02-21 18:42:40	2021-02-21 18:43:01	2.1	22	09:00	92
33N	2021-04-15 22:41:52	2021-04-15 22:44:58			3.5	15	18:00	116
33S	2021-04-16 00:27:57	2021-04-16 00:31:01			2.4	14-45	08:00	355
34N	2021-06-08 06:58:33	2021-06-08 07:00:59			4.0	16	18:00	120
34S	2021-06-08 08:41:23	2021-06-08 08:42:46			2.5	17	08:00	355
35N	2021-07-21 07:26:17	2021-07-21 07:27:42	2021-07-21 07:27:30	2021-07-21 07:27:40	3.9	16	18:00	124
35S	2021-07-21 09:09:30	2021-07-21 09:10:58			2.5	15	08:00	1
36S	2021-09-03 00:06:14	2021-09-03 00:09:18			1.0	18-30	07:00	192
37N	2021-10-16 16:46:54	2021-10-16 16:49:35			8.5	13-45	16:00	293-319
37S	2021-10-16 18:22:34	2021-02-21 18:26:22	2021-10-16 18:22:34	2021-02-21 18:22:50	1.6	20	08:00	114

37S	2021-10-16 18:22:34	2021-02-21 18:26:22	2021-10-16 18:24:10	2021-02-21 18:25:34	1.6	20	08:00	114
38N	2021-11-29 13:33:07	2021-11-29 13:47:54			6.4	14-24	19:00	266-330
38S	2021-11-29 15:34:05	2021-11-29 15:37:17	2021-11-29 15:34:33	2021-11-29 15:34:44	1.1	21	07:00	161
38S	2021-11-29 15:34:05	2021-11-29 15:37:17	2021-11-29 15:36:09	2021-11-29 15:36:34	1.1	21	07:00	161
39N	2022-01-12 09:55:20	2022-01-12 10:02:58			6.0	16	19:00	278-300
39N	2022-01-12 10:04:10	2022-01-12 10:09:06			8.1	14	17:00	90-352
39S	2022-01-12 11:57:00	2022-01-12 12:00:39			1.0	19-33	07:00	172
40N	2022-02-25 01:21:15	2022-02-25 01:24:15			5.7	14-47	16:00	109
40S	2022-02-25 03:02:45	2022-02-25 03:03:48			1.9	22-35	07:00	339
41N	2022-04-09 14:59:41	2022-04-09 15:08:27			4.1	14-50	20:00	229
41N	2022-04-09 17:04:11	2022-04-09 17:08:08			1.3	19-35	07:00	125
41S	2022-04-09 17:04:37	2022-04-09 17:07:52	2022-04-09 17:05:39	2022-04-09 17:06:44	1.3	23	07:00	124
42N	2022-05-23 01:32:05	2022-05-23 01:37:17			4.7	13-24	20:00	244
42N	2022-05-23 01:52:03	2022-05-23 01:54:04			9.4	16	16:00	325-349
43N	2022-07-05 08:33:32	2022-07-05 08:35:40			4.8	16	17:00	127
44N	2022-08-17 14:21:23	2022-08-17 14:25:46			9.4	15	07:00-17:00	20-75
44N	2022-08-17 14:21:33	2022-08-17 14:25:00			9.4	15	07:00-17:00	20-75
44S	2022-08-17 16:14:22	2022-08-17 16:17:36	2022-08-17 16:17:11	2022-08-17 16:17:36	0.9	18	05:00	222
45N	2022-09-29 16:43:00	2022-09-29 16:45:46			7.6	13	13:00	73
46N	2022-11-06 20:47:10	2022-11-06 20:52:00			4.1	12-39	17:00	153
46S	2022-11-06 22:39:30	2022-11-06 20:41:00			2.0	16	06:00	39
47N	2022-12-15 03:00:00	2022-12-15 03:05:30			10.3	12-27	07:00-13:00	27-95

47S	2022-12-15 04:56:00	2022-12-15 04:59:30			0.8	18-29	04:00	235
48S	2023-01-22 07:09:01	2023-01-22 07:11:59	2023-01-22 07:09:50	2023-01-22 07:11:38	1.0	18	04:00	272
48N	2023-01-22 05:21:07	2023-01-22 05:22:40			9.6	18	10:00	72
49S	2023-03-01 07:27:41	2023-03-01 07:32:34			0.8	17-42	04:00	246
50S	2023-04-08 09:40:54	2023-04-08 09:43:00			0.9	19-40	04:00	283
50N	2023-04-08 07:47:34	2023-04-08 07:51:29			8.7	11	12:00	49-71
53S	2023-07-31 10:53:21	2023-07-31 10:57:11	2023-07-31 10:54:00	2023-07-31 10:56:00	0.6	21	04:00	211
54N	2023-09-07 11:36:34	2023-09-07 11:40:01			10.5	14	08:00-13:00	38-83
55S	2023-10-15 12:49:30	2023-10-15 12:55:45			0.5	21-45	03:00	202
56S	2023-11-22 14:14:42	2023-11-22 14:18:53			0.5	23	03:00	213
58N	2024-02-03 21:18:28	2024-02-03 21:21:18			8.9	11-44	13:00	122
58S	2024-02-03 23:09:08	2024-02-03 23:11:35			1.1	19-32	03:00	359
60S	2024-04-09 10:32:39	2024-04-09 10:38:32			0.6	19	05:00	121
61S	2024-05-12 05:39:29	2024-05-12 05:44:24			0.4	18	20:00	234
62S	2024-06-13 22:03:50	2024-06-13 22:07:22			0.4	29-46	19:00	246
63S	2024-07-16 16:14:06	2024-07-16 16:16:45	2024-07-16 16:14:19	2024-07-16 16:16:43	0.7	22-35	14:00	317
64N	2024-08-18 06:38:27	2024-08-18 06:39:22			11.4	11	04:00	99
64S	2024-08-18 08:32:05	2024-08-18 08:34:42	2024-08-18 08:33:08	2024-08-18 08:33:48	0.7	16	14:00	324
65S	2024-09-20 04:15:33	2024-09-20 04:29:46	2024-09-20 04:20:51	2024-09-20 04:28:23	0.6	20-48	06:00	102
66S	2024-10-22 19:57:36	2024-10-22 20:21:41	2024-10-22 20:08:20	2024-10-22 20:21:24	0.5	42-53	07:00	92
70S	2025-03-02 18:06:13	2025-03-02 18:09:42			0.4	19	16:00	297

Table 1.

Note that the local time is unphysical for trajectory near the pole.